NASA/CR—2005-213585

Probabilistic Fracture Mechanics Analysis of the Orbiter's LH_2 Feedline Flowliner

Stephen J. Hudak, Jr., Luc Huyse, Graham Chell, Yi-Der Lee,
David S. Riha, Ben Thacker, Craig McClung, Brian Gardner,
Gerald R. Leverant, Jim Unruh, and Jason Pleming
Southwest Research Institute, San Antonio, Texas

June 2005

The NASA STI Program Office . . . in Profile

Since its founding, NASA has been dedicated to the advancement of aeronautics and space science. The NASA Scientific and Technical Information (STI) Program Office plays a key part in helping NASA maintain this important role.

The NASA STI Program Office is operated by Langley Research Center, the Lead Center for NASA's scientific and technical information. The NASA STI Program Office provides access to the NASA STI Database, the largest collection of aeronautical and space science STI in the world. The Program Office is also NASA's institutional mechanism for disseminating the results of its research and development activities. These results are published by NASA in the NASA STI Report Series, which includes the following report types:

- TECHNICAL PUBLICATION. Reports of completed research or a major significant phase of research that present the results of NASA programs and include extensive data or theoretical analysis. Includes compilations of significant scientific and technical data and information deemed to be of continuing reference value. NASA's counterpart of peer-reviewed formal professional papers but has less stringent limitations on manuscript length and extent of graphic presentations.

- TECHNICAL MEMORANDUM. Scientific and technical findings that are preliminary or of specialized interest, e.g., quick release reports, working papers, and bibliographies that contain minimal annotation. Does not contain extensive analysis.

- CONTRACTOR REPORT. Scientific and technical findings by NASA-sponsored contractors and grantees.

- CONFERENCE PUBLICATION. Collected papers from scientific and technical conferences, symposia, seminars, or other meetings sponsored or cosponsored by NASA.

- SPECIAL PUBLICATION. Scientific, technical, or historical information from NASA programs, projects, and missions, often concerned with subjects having substantial public interest.

- TECHNICAL TRANSLATION. English-language translations of foreign scientific and technical material pertinent to NASA's mission.

Specialized services that complement the STI Program Office's diverse offerings include creating custom thesauri, building customized databases, organizing and publishing research results . . . even providing videos.

For more information about the NASA STI Program Office, see the following:

- Access the NASA STI Program Home Page at ***http://www.sti.nasa.gov***

- E-mail your question via the Internet to help@sti.nasa.gov

- Fax your question to the NASA Access Help Desk at 301–621–0134

- Telephone the NASA Access Help Desk at 301–621–0390

- Write to:
  NASA Access Help Desk
  NASA Center for AeroSpace Information
  7121 Standard Drive
  Hanover, MD 21076

NASA/CR—2005-213585

Probabilistic Fracture Mechanics Analysis of the Orbiter's LH_2 Feedline Flowliner

Stephen J. Hudak, Jr., Luc Huyse, Graham Chell, Yi-Der Lee,
David S. Riha, Ben Thacker, Craig McClung, Brian Gardner,
Gerald R. Leverant, Jim Unruh, and Jason Pleming
Southwest Research Institute, San Antonio, Texas

Prepared under Contract NAS1–00135

National Aeronautics and
Space Administration

Glenn Research Center

June 2005

Acknowledgments

The authors gratefully acknowledge Charlie Harris (NESC), Bob Piascik (NESC), and Pete Bonacuse (U.S. Army Research Laboratory) for their vision, support, and encouragement during the course of this research. Charlie Harris recognized the need for probabilistic analysis of the flowliner cracking and served as the ITA Team Lead for most of the investigation; Clinton Cragg (NESC) ably took over for Charlie during the latter portion of the program. Bob Piascik introduced us to the flowliner problem and encouraged us to pursue a probabilistic analysis of the problem. Pete Bonacuse got us up to speed on the flowliner problem and provided useful technical comments throughout the program and during the review of the final report; he also served as the contracting officer's technical representative and facilitated the publication of this report.

The report would not have been possible without the support and generous sharing of information from our numerous ITA teammates. In this regard we are particularly indebted to Ivatury Raju (NESC/NASA LaRC), Mark James (NIA), and David Dawicke (NASA LaRC) for stimulating discussions and results on application of fracture mechanics to this complex dynamic problem; to Gary Halford (NASA GRC) for helping us understand the essence of the flowliner fatigue problem; to Kenny Elliot (NASA LaRC) for providing strain data needed for uncertainty modeling of loading; to Daniel Kaufman (NASA GSFC) and his team at Swales Aerospace, including Bill Haile, Steve Brodeur, Avi Gopstein, and Michael Kaiser for providing input on strain transfer factors and characterization of loading spectra; to Eric Madaras (NASA LaRC) for helpful discussions on flowliner NDE methods.

We would also like to acknowledge the efforts of Linda Tufino and Roxanne Kerr for invaluable help in preparing two major reports under this program on a very challenging schedule.

Stephen J. Hudak, Jr., would also like to thank SwRI management including Walt Downing, Executive Vice President, Bob Bass, Division Vice President, and Jim Lankford, Deputy Director for relieving him of his institutional duties so that this program could be completed on schedule.

Available from

NASA Center for Aerospace Information
7121 Standard Drive
Hanover, MD 21076

National Technical Information Service
5285 Port Royal Road
Springfield, VA 22100

Available electronically at http://gltrs.grc.nasa.gov

TABLE OF CONTENTS

TABLE OF CONTENTS

1.0 INTRODUCTION

When performing deterministic engineering analyses, it is common practice to employ conservative assumptions in those areas where hard data are lacking, or where the accuracy of analytical or computational models are unknown. This approach leads to satisfactory conclusions when results are positive—*i.e.,* the functionality, durability, or safety of the system is demonstrated. In this instance, the conservative assumptions are accepted as additional, but often unquantified, safety factors. However, this approach is unsatisfactory when the outcome of the analysis is negative—*i.e.,* the functionality, durability or safety cannot be demonstrated. The questions then are: Is the component really unsafe? Or alternatively, is the analysis just unrealistically conservative?

The above scenario typified the situation with regard to the feedline flowliners that supply liquid hydrogen (LH_2) fuel to the low-pressure hydrogen turbo pumps (LPHTPs) of the Space Shuttle Main Engines (SSMEs). Cracks were first discovered in June of 2002 at the slots in the flowliner at the locations illustrated in Figure 1-1. Uncertainty in key input parameters in initial analyses led to multiple conservative assumptions regarding: 1) initial defect sizes due to uncertainties in inspection capability, 2) load/stress history due to uncertainties in fluid-structure interactions, transient thermal stress, and welding residual stress, and 3) rate of fatigue crack growth due to the uncertain influence of the cryogenic environment (LH_2 at – 423ºF). In addition, uncertainties also existed in modeling of the crack driving forces needed to predict the remaining fatigue life that resulted in conservative assumptions regarding crack shape, as well as other factors. The combined effect of these multiple conservative assumptions has been predicted flowliner lives as low as 0.8 of a flight, or about 1.6 million flow-induced vibratory cycles.

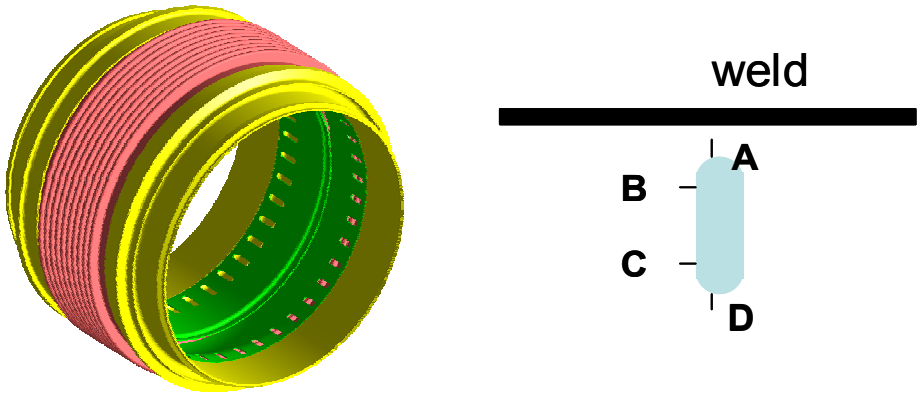

Figure 1-1: Liquid hydrogen feedline (yellow) showing bellows (red) and flowliner (green) along with schematic of designated crack locations at flowliner slots. Welds at either end of the feedline serve to connect the feedline to flanges (not shown). Not all locations exhibit cracking; in fact only eleven cracks were observed in the entire Space Shuttle fleet.

This over-conservatism can be remedied either by a) acquiring new data and knowledge, b) explicitly accounting for the uncertainties by performing probabilistic analysis, or c) by a combination of the above—the approach taken in the effort summarized in the current report.

In response to the above situation, NASA's Engineering and Safety Center (NESC) has embarked on an Independent Technical Assessment (ITA) to determine the safety implications of observed and repaired fatigue cracks in the flowliners in the feedlines that supply liquid hydrogen fuel to the Space Shuttle Main Engine. The objective of the ITA is to assess the impact of the cracking and repairs on the safety and reliability of the SSME and shuttle fleet. Southwest Research Institute® (SwRI®), as part of this multidisciplinary team, is focusing on both deterministic and probabilistic fracture mechanics analyses of the flowliner. This report summarizes work performed over a four-month period.

Under a Phase 1 of this ITA, SwRI laid out the general approach, performed preliminary probabilistic analyses to scope the problem, identified gaps in the knowledge and technology base, and provided recommendations to remedy these gaps [Hudak et. al. 2004]. The current report addresses these gaps by providing a more complete probabilistic analysis that included enhanced crack driving forces for the fatigue analysis and more robust modeling of uncertainty associated with materials crack growth rates and flow-induced dynamic loads/stress in the flowliner.

2. DETERMINSTIC FATIGUE CRACK GROWTH MODEL

The Flowliner Fatigue Life (FFL) program was designed and written by SwRI to directly interface with the NESSUS probability code in order to increase the computational efficiency in probability analyses and to provide greater flexibility in analysis options than are presently available by running NASGRO. The program calculates the fatigue growth and lifetimes of quarter-elliptical corner cracks and through-wall cracks at slots in the liners. A description of a preliminary version of the program is given in Hudak et al (2004). Since then significant enhancements have been made to the code and extensive verification has been performed. For example, verification of the weight function approach used in the FFL program for calculating the stress intensity factors of corner cracks in bivariant stress fields and through-wall cracks in bivariant stress fields is presented in sub-sections 2.9.2.3 and 2.9.3.3, respectively. In addition, verification of the crack growth integration routines was accomplished by reproducing some of the fatigue analysis results derived by NASA-LaRC using NASGRO (see Section 3.1).

This section summarizes the capabilities of the latest version of the FFL program

2.1 Crack Growth Models

The present version of FFL can perform fatigue crack growth calculations for eight crack models consisting of four corner and four through crack geometries (corresponding to circumferentially oriented cracks at Locations B and C on a liner slot, and axially oriented cracks at Locations A and D, see Figure 1-1). The crack models A and B are nearest the attachment weld. The stress intensity factors (SIFs) for the four corner crack models in bivariant stress fields are calculated using the weight function (WF) method described in Section 2.8. (An example of a bivariant stress distribution is given by Equation 2.26.) A similar approach to this is adopted for through cracks, although in these cases the WF formulation is somewhat simpler, since only univariant stressing is considered. (An example of a univariant stress distribution is given by Equation 2.32.)

The WF solutions contained in FFL are applicable to cracks that develop in either the upstream or downstream liners, and, in the case of corner cracks, that emanate from either the outside or inside diameters. Combining the WF solutions with the appropriate local stress gradient make them specific to the various crack locations at the flowliner slots.

2.2 Applied Stress Distributions

Cracks in the liners are subjected to a number of different sources of stressing. These can be divided into static stresses, which remain unchanged during a flight, and cyclic stresses. Static stresses can result, for example, from system loads (such as internal pressure), and residual stresses associated with machining or welding. The cyclic stresses are due to power variations during take-off, which causes resonant vibration modes in the liners.

The various stress types are characterized by magnitude (A) and normalized bivariant spatial distribution (Σ). This distribution can be different for each source of stress (e.g. system or vibration) and, in the case of cyclic stresses, for different vibration modes. In addition, the full

capability of the program allows each of the foregoing distributions to vary from slot ligament to slot ligament.

The actual bivariant stresses ($\sigma(x,y)$) are taken as the magnitudes multiplied by the corresponding distributions, as shown in the equations below.

$$\sigma_{static}^{system}(x,y) = A_{static}^{system}\Sigma_{static}^{system}(x,y) \tag{2.1}$$

$$\sigma_{static}^{residual}(x,y) = A_{static}^{residual}\Sigma_{static}^{residual}(x,y) \tag{2.2}$$

$$\Delta\sigma_{cyclic}^{vib}(j,k,x,y) = A_{cyclic}^{vib}(j,k)\Delta\Sigma_{cyclic}^{vib}(k,x,y) \tag{2.3}$$

In these equations, x is the circumferential distance through the ligament (in the cases of cracks B and C) or the axial distance through the remaining section (in the cases of cracks A and D) measured from the crack origin, y is the distance through the liner thickness measured from the origin (see Figure 2-12 for a schematic of the coordinate system), j refers to the $j^{'}th$ load step in the $k^{'}th$ vibration mode (e.g. 5ND). The superscript identifies the source of the stress, and the subscript whether it is a static or cyclic stress.

The static stresses (excluding residual stresses) are further assumed to be composed of two components, through wall bending and membrane. These local ligament stress components are assumed to result from remote bend and tensile stressing, the magnitude of the remote stresses being given by the value of A_{static}^{system}.

The relative contribution of the bending and membrane components to the stresses is determined by bending and membrane factors (T^b and T^m, respectively). When expressed in terms of these factors, the static stresses become:

$$\sigma_{static}^{system}(x,y) = \frac{T_{static}^{b}}{T_{static}^{b}+T_{static}^{m}} A_{static}^{system}\Sigma_{static\ bend}^{system}(x,y) + \frac{T_{static}^{m}}{T_{static}^{b}+T_{static}^{m}} A_{static}^{system}\Sigma_{static\ \mathrm{membrane}}^{system}(x,y) \tag{2.4}$$

Examples of the normalized stress distributions corresponding to bending and membrane loading are shown in Figures 2-1 and 2-2, respectively. These bivariant axial stress distributions appropriate to Location B on the slot were determined from a static finite element stress analysis using ABAQUS (see sub-section 2.8.2.4). In these analyses, the liner was modeled as a plate containing three slots with symmetric boundary conditions applied to simulate an infinite array of slots. One of the plate ends was fixed to represent the attachment weld, and the other (free) end was subjected to out-of-plane bending (through thickness bending) and tension stressing. The boundary conditions applied to the model are shown in Figure 2-17. The slot results in stress concentration factors (local stresses divided by remote stresses) of 1.63 and 1.93 for the bending and membrane cases, respectively.

The effect of having cyclic stresses resulting from mixed bending and tension on fatigue lives can be considerable. Through-wall cyclic bending is indicated whenever the OD and ID stresses corresponding to a specific vibration mode differ at the same location through the

ligament. If the OD and ID stresses are equal, then there is no through thickness bending at that ligament location. The effects of this through wall bending on crack growth are illustrated by the FFL analysis results shown in Figures 2-3 and 2-4. These figures, based on using a two-degree of freedom analysis (see sub-section 2.6) and the bending and membrane loading shown in Figures 2-1 and 2-2, respectively, demonstrate how the number of predicted flights to cause failure could be reduced drastically as the through-wall tension component of the cyclic loading increases. The crack geometry analyzed in this example application of FFL is shown in Figure 2-5. In this hypothetical example based on a flight-loading spectrum derived by GSFC using a rainflow counting method the predicted life is around 46 flights when the cyclic stresses are derived solely from remote bending. This reduces to 22 flights when the cyclic loads are composed equally of bending and tension, and reduces further to 15 flights when only remote cyclic tension loads are assumed.

The effect of combined bending and tension on the predicted evolution of the crack shape with flights is also dramatic, as can be seen from the results displayed in Figure 2-4. As expected, when the cyclic loading is predominantly through thickness bending, most of the crack growth from fatigue occurs through the ligament (at the c-tip) rather than through the liner thickness (at the a-tip). When the predominant cyclic loading is tension, almost equal amounts of crack extension occur through the ligament and through the thickness during most of the fatigue lifetime, and it is only after a crack has penetrated the liner wall that growth through the ligament becomes dominant.

It is re-iterated that the foregoing discussion and results apply only to through wall bending and tension. Vibration induced cyclic stresses also generally vary significantly through the ligaments between slots. Drastic spatial changes in stresses through the ligament will also influence crack shape development, but since these changes are over a distance of 0.75 inches they are less likely to control the way corner crack shapes evolve for crack sizes less than the liner wall thickness (0.05 inches) compared to through wall changes in stress (which occur over distances comparable to these sizes of flaws).

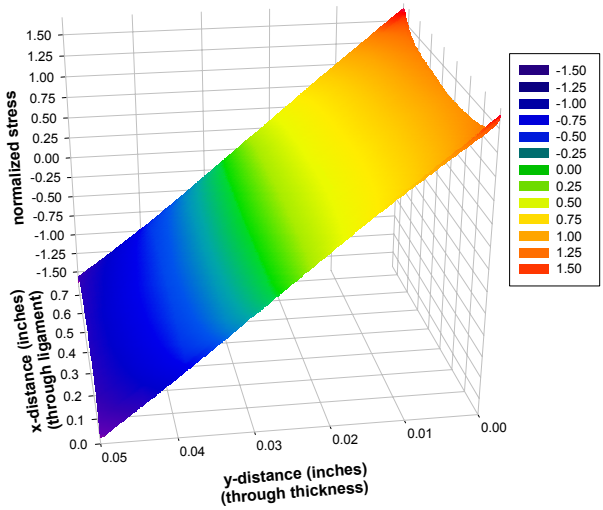

Figure 2-1: Example of normalized bivariant axial stress distribution in a ligament between two slots. This axial stress at Location B results from remote out-of-plane bending.

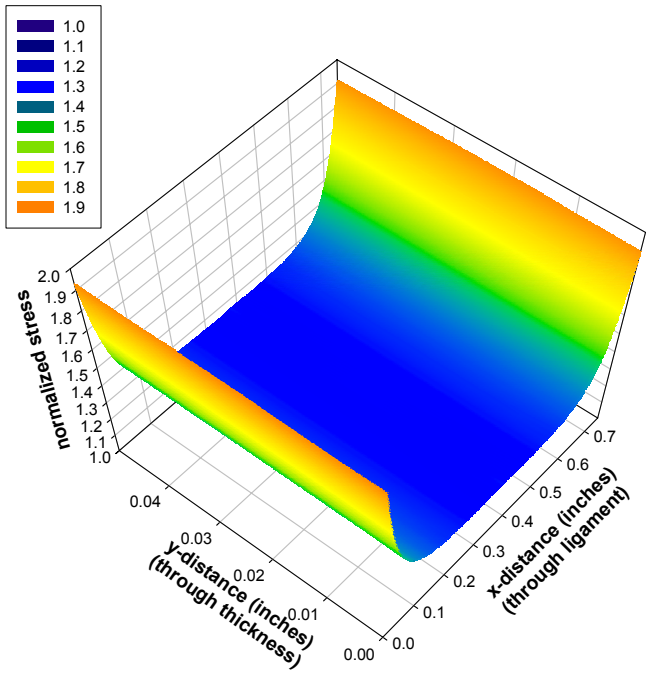

Figure 2-2: Example normalized bivariant axial stress distribution in a ligament between two slots. This axial stress at Location B results from remote uniform tension.

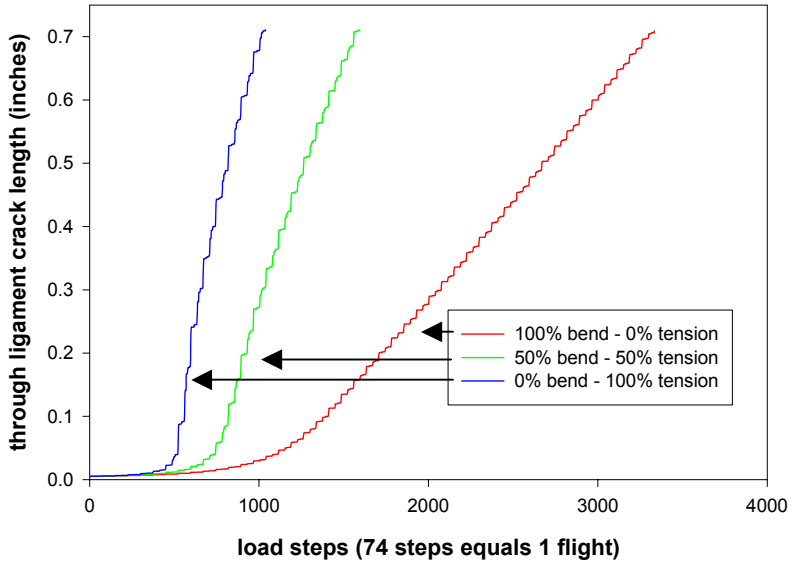

Figure 2-3: Example application of the FFL program to predict the effect of combined cyclic bending and tension loads on the number of flights to failure and the amount of crack growth through the ligament between two slots at the *c*-tip.

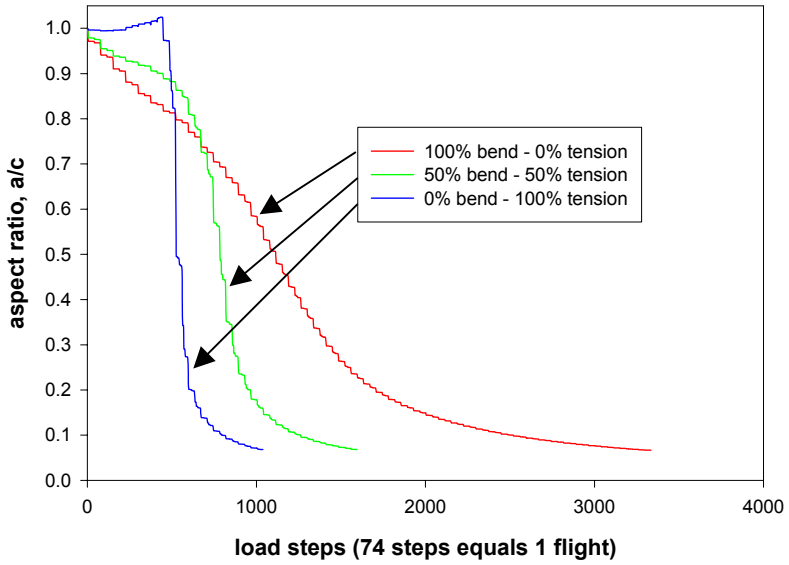

Figure 2-4: Example application of the FFL program to predict the effect of combined cyclic bending and tension loads on the number of flights to failure and crack shape evolution, characterized by the aspect ratio *a/c* where *a* is the crack length through the thickness and *c* the length through the ligament.

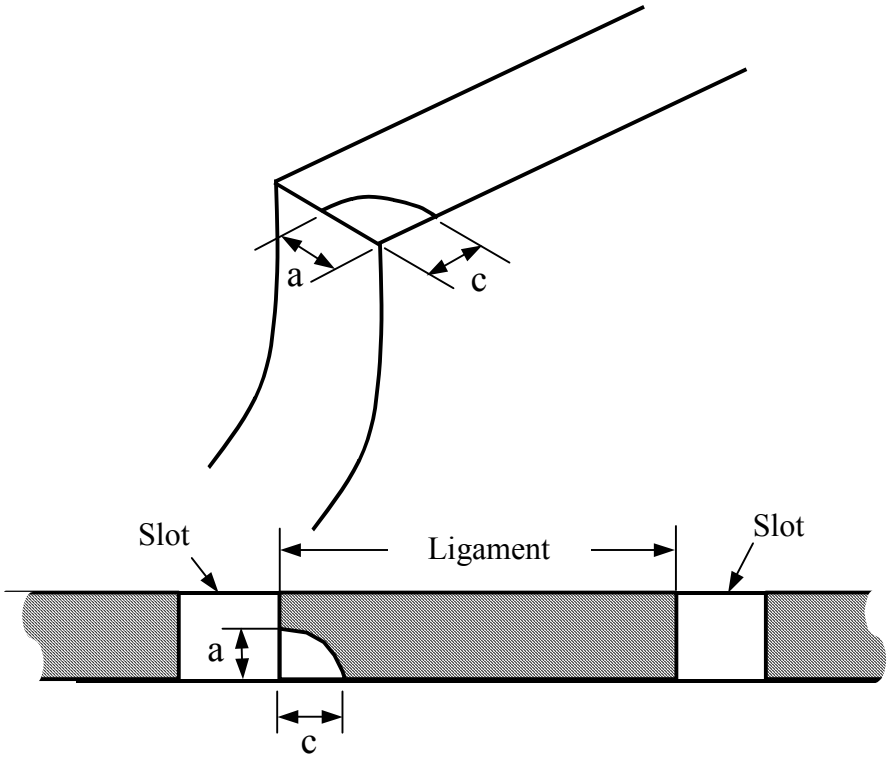

Figure 2-5: Schematic of a corner crack at Location B on a slot.

2.3 Plastic Shakedown of Stresses

In addition to the applied stresses, the FFL program can estimate the shakedown stress distribution if the total applied stress, $\sigma_{total}(x,y)$, at any point in the ligament between slots or in the remaining section exceeds yield. The total stress associated with any slot is defined as:

$$\sigma_{total}(x,y) = \sigma_{static}^{system}(x,y) + \sigma_{static}^{residual}(x,y) + Max\left[\frac{\Delta\sigma_{cyclic}^{vib}(x,y)}{2}\right] \tag{2.5}$$

In this equation, *Max* indicates the maximum cyclic stress in the load steps that define the flight load spectrum.

In the shakedown analysis, a Neuber-based routine is used to derive an approximate elastic-plastic stress distribution, $\sigma_{total}^{elastic-plastic}(x,y)$, that results from plastic stress relaxation and redistribution over the load bearing section (ligament between adjacent slots for axial stresses, or remaining section for hoop stresses). The shakedown stress is then given by:

$$\sigma_{static}^{shakedown}(x,y) = \sigma_{total}^{elastic-plastic}(x,y) - \sigma_{total}(x,y) \tag{2.6}$$

This stress remains in the liner after all loads are removed and is equivalent to an additional static residual stress. Thus, the total stress distribution at maximum load for the *j'th* load step after shakedown is given by:

$$\sigma_{total}^{j}(x,y) = \sigma_{static}^{system}(x,y) + \sigma_{static}^{residual}(x,y) + \sigma_{static}^{shakedown}(x,y) + \left[\frac{\Delta\sigma_{cyclic}^{vib}(x,y)}{2}\right]^{j} \tag{2.7}$$

An example of the results of a shakedown analysis is shown in Figure 2-6. In this figure, a total stress distribution derived from elastic stress analysis consisting of a static membrane stress of peak local value 50 ksi is superposed on a residual stress consisting of a through-wall bend stress of peak value 80 ksi and a peak maximum alternating membrane stress of 60 ksi. The total value of all the peak stress values is 190 ksi, which is significantly higher than the yield stress (taken in this example to be 100 ksi for illustrative purposes). As a consequence, plastic stress relaxation and redistribution occurs, as shown in Figure 2-6. After all stresses are removed (including the residual stress), the shakedown stress remains and is shown in Figure 2-8.

In the example given, the shakedown stress is beneficial, since it results in a compressive stress at the site of a corner crack at Location B on a slot. This compressive static stress will reduce the local stress ratio, *R*, and hence reduce fatigue crack growth rates with respect to the value of *R* in the absence of the shakedown stress.

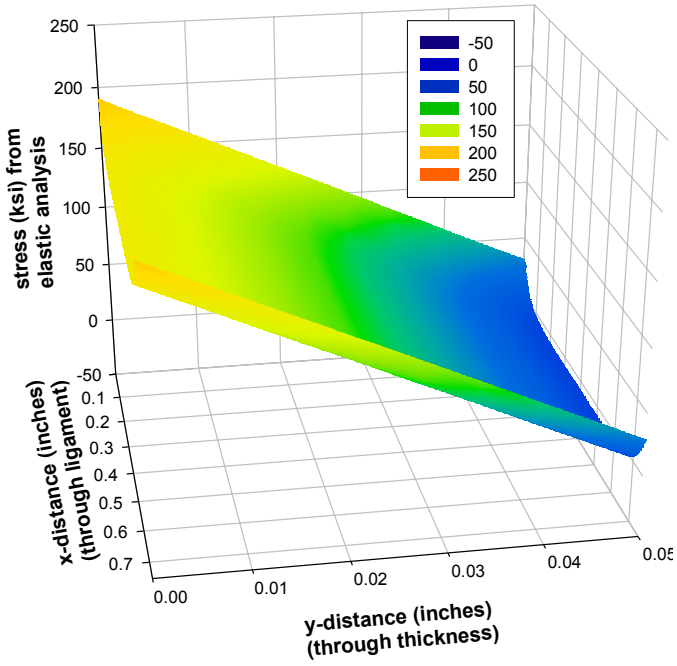

Figure 2-6: Example of a peak axial stress distribution in the ligament between two slots derived from a linear elastic stress analysis. The stress is the superposition of the system, residual and maximum alternating stress.

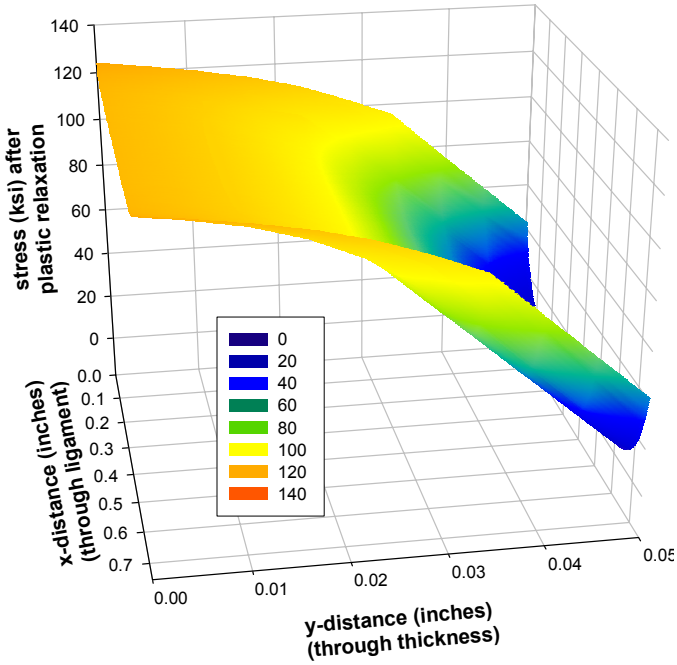

Figure 2-7: As shown in this figure, yielding results in plastic relaxation (from a maximum value of 190 ksi down to around 124 ksi) and redistribution of the linear elastic peak axial stress distribution shown in Figure 2-6. In this illustrative result, the yield stress was assumed to be 100 ksi.

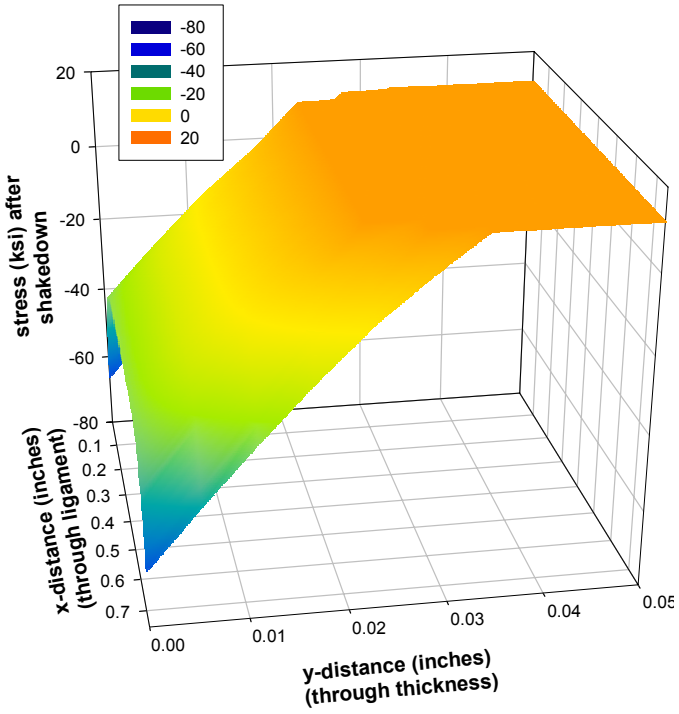

Figure 2-8: A shakedown stress (equivalent to an additional static residual stress) remains in the ligament after all loads are removed. This shakedown stress is equal to the calculated elastic-plastic stresses shown in Figure 2-7 minus the elastically derived stress in Figure 2-6. In this example, tensile yielding has resulted in a compressive stress at the location of a corner crack at B (centered at the origin of coordinates).

2.4 Flowliner Stress Intensity Factors (SIFs)

FFL computes SIFs for corner and through-wall cracks using the weight function (WF) method (see Section 2.8). The bivariant stress distribution is read from a file containing a table of stress values as a function of x and y. Interpolation is performed to obtained stress values at specific positions during the double integration performed as part of the WF method for corner cracks, and the single integration that is performed for through wall cracks. The integration itself (particularly for corner cracks with two degrees of freedom) is a computationally intensive process that would severely hamper deterministic fatigue crack growth calculations (not to mention probability based calculations) due to the time taken in evaluating SIFs. In order to reduce this computational burden, tables of normalized SIFs are generated for corner cracks for specific stress gradients before fatigue growth calculations are performed. These tables are then interpolated during the fatigue calculations to derive the required SIF values. This computationally efficient scheme uses the normalized stresses [*e.g.*, $\Sigma_{static}^{system}(x,y)$, $\Sigma_{static}^{residual}(x,y)$, $\Delta\Sigma_{cyclic}^{vib}(x,y)$] when generating the tables of normalized SIFs. The SIFs are de-normalized by first multiplying the table values for the a-tip by $\sqrt{\pi a}$ and for the c-tip by $\sqrt{\pi \frac{a^2}{c}}$ and then multiplying the results for both tips by the appropriate magnitude of the stress [compare Equations (2.1) through (2.3)]. Since the normalized stress distributions for the system stresses,

residual stresses, and cyclic stresses do not change during the fatigue calculations for a given vibration mode (even during a probability calculation only the magnitudes A vary), the set-up of the normalized SIF tables need only be performed once per vibration mode during deterministic or probability evaluations.

The exception to this efficient scheme for corner cracks occurs when a shakedown analysis is invoked. In these cases, a "look-up" table of SIF solutions has to be generated after each shakedown analysis because the spatial distributions for the shakedown stresses are not known a priori.

A look-up table is also employed for through-crack SIF computations. In these cases, a one-dimensional integral is evaluated using a univariant stress distribution through the ligament derived from the bivariant stress field. This univariant field is derived as the value of the bivariant stress at the midpoint of the liner wall. The through wall distribution in stress is approximately allowed for by using the SIF solution for through wall bending, based on the assumption that the through wall stress distribution will be linear in the thin-walled liners. The bending stress, taken as half the difference between the ID and OD stresses, will be a function of distance through the ligament. The actual bending stress used in the SIF calculations is taken as a value obtained by averaging the bending stress, determined as a function of distance, over the crack length. The sign of the bending stress is taken as the sign of this stress on the liner ID. More details are given in sub-section 2.8.3.2.

2.5 Effective Cyclic Stress Intensity Factors

The fatigue crack growth calculations use values for the total cyclic SIF ($\Delta K = K_{\max} - K_{\min}$, where subscripts *max* and *min* signify maximum and minimum loads, respectively) and an effective SIF (ΔK_{eff}). The effective SIF takes into account stress ratio dependent crack closure effects and a surface interaction term, β_R, as described in the NASGRO user manual. The recommended procedure in NASGRO for determining ΔK_{eff} is adopted, with the constraint term α specified by the user (normally with a value of 2 to 2.5) and the normalized maximum stress ratio, $\frac{S_{\max}}{\sigma_0}$, set to 0.3, where σ_0 is the flow stress. However, these closure corrections are only applied if a flag (Nclosure) is set to 1. If Nclosure is set to 0 the full range, ΔK, is used when R is positive, and $\Delta K = K_{\max}$ is used for negative stress ratios. This latter approach - setting Nclosure=0 - is conservative and is consistent with assuming cyclic loading occurs under high-R conditions, the assumption made in flowliner fatigue life computations performed by other ITA Team members.

2.6 Degrees of Freedom for Growth of Corner Cracks

In general, growth at quarter-elliptical corner cracks develops and the crack shape evolves with two degrees of freedom corresponding to propagation at points on the crack fronts near the free surfaces. This facilitates the size and shape of propagating cracks to be predicted as they grow though the liner thickness at the a-tip and across the ligaments between the slots

(circumferential cracks at B and C) or axially towards the ends of the liners (cracks at A and D) at the c-tip.

When the a-tip is 97.5% of the liner thickness, further growth is prevented at this tip and the a-tip is assumed to have penetrated the liner wall. After penetrating the wall (*i.e.*, satisfying the 97.5% criterion for the crack depth) the corner crack can be constrained to remain as a corner crack but to grow only at the c-tip (designated as the first scenario in sub-section 3.2.2) or to transition to a through-wall crack with a straight crack front (designated as the second scenario in sub-section 3.2.2). In either case, further crack growth is assumed to occur only through the ligament (at the c-tip) and no further extension at the a-tip is allowed, reducing the degrees of freedom governing crack growth from two (for the quarter-elliptical corner crack) to one. However, note that the SIF determined for the c-tip in the first scenario is influenced by crack-front curvature, since this SIF is determined using the WF for a corner crack of length c and constant depth equal to $0.975t$. The conditions governing the transitioning from a corner to a through-wall crack (the second scenario) are described in Section 2.8.

Fatigue calculations can be constrained to occur with one degree of freedom governed by conditions at the c-tip. If this option is exercised, then growth through the liner wall at the a-tip is set equal to the amount of growth determined for the c-tip (*i.e.*, the crack shape remains constant) until the a-tip is 97.5% through the thickness. When this condition is attained, no further growth at the a-tip is allowed.

The effect of using either two or one degree(s) of freedom on calculated lifetimes is illustrated in Table 2-1. In this table, failure implies that the c-tip length exceeded 95% of the ligament width between slots. This table shows calculated liner fatigue lives determined assuming cyclic stresses arising from different combinations of bending and tension. In the case of pure bending, there is a significant difference in the predicted number of flights to failure between the one and two degree of freedom assumptions. This difference is substantially reduced when bending and tension contribute equally to the cyclic stresses, and becomes almost negligible when the cyclic stresses are composed of only tension loading. This is understandable because when the stressing on the ligament is almost uniform (except for the concentration along the slot through the liner thickness, see Figure 2-2) then a quarter-circular corner crack will tend to remain a quarter-circular crack as it propagates, making the assumption that its growth is governed by one degree freedom a realistic one.

Table 2-1: Effect of assumed degree of freedom on predicted flights to failure.

Degree of Freedom	Predicted Flights to Failure		
	100%Bending 0%Tension	**50%Bending 50%Tension**	**0%Bending 100%Tension**
1	29	19	14
2	46	22	15

2.7 Fatigue Crack Growth Rate Equations

The FFL program has the option of using either of two fatigue crack growth equations. The first is compatible with NASGRO and is given by:

$$\frac{da}{dN} = C\Delta K_{eff}^{n} \frac{\left(1 - \frac{\Delta K_{th}}{\Delta K}\right)^{p}}{\left(1 - \frac{K_{\max}}{K_c}\right)^{q}} \tag{2.8}$$

In this NASGRO equation, C, n, p and q are constants fitted to measured crack growth rate data, ΔK_{th} is the cyclic threshold stress intensity factor, and K_c is the fracture toughness.

The second equation, a three-component growth rate equation (see Saxena and Hudak**,** 1979, 1980), is of the form:

$$\frac{da}{dN} = \left[\frac{1}{C_1 \Delta K_{eff}^{n_1}} + \frac{1}{C_2 \Delta K_{eff}^{n_2}} - \frac{1}{C_2 \left((1-R) U K_c \right)^{n_2}} \right]^{-1} \tag{2.9}$$

In this equation, C_1 and n_1 are constants in a term that describes crack growth near threshold, C_2 and n_2 are constants in a term that describes crack growth in the classic Paris regime, and the third term allows for accelerated growth near instability due to the onset of monotonic failure modes. U is equal to the ratio $\frac{\Delta K_{eff}}{\Delta K}$ and R is the stress ratio, $\frac{K_{\min}}{K_{\max}}$. Note that this three-component model does not require a threshold to be used.

The forms of the NASGRO and three component growth rate equations are compared in Figure 2-9.

The form of the three-component model is better suited to probabilistic fatigue life calculations since it avoids problems often encountered with asymptotic models in statistical characterization of uncertainty in the near-threshold fatigue crack growth regime (see Section 4.2.2).

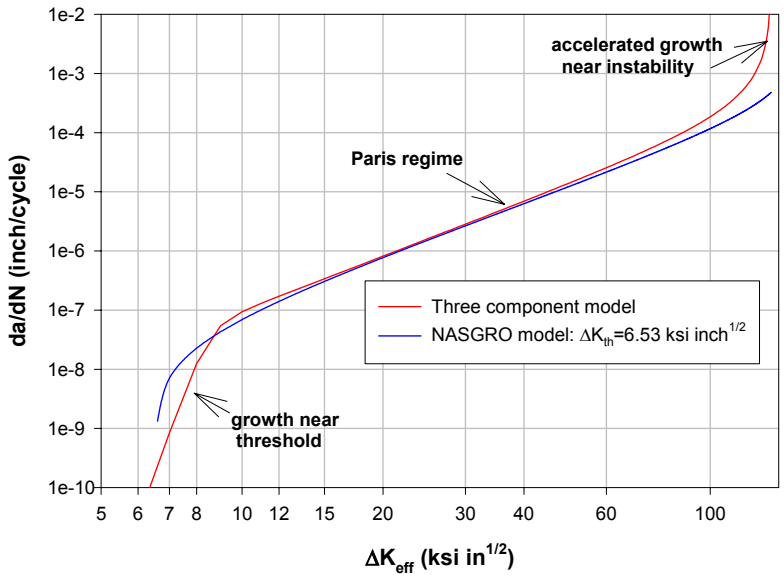

Figure 2-9: Illustration of the form of the three-component and NASGRO growth rate equations, showing the threshold growth region, the classical Paris regime, and accelerated growth near instability.

The small crack effect on the threshold, as specified in NASGRO, is included in the NASGRO equation but not when the three-component growth rate equation is used. In the latter case, the current fatigue lifetime calculations were all made assuming no threshold. However, the effective SIF corresponding to a growth rate of 10^{-9} inch/cycle determined from the three component equation is similar to the threshold value used in the NASGRO equation, as can be seen from Figure 2-9.

The threshold value used in NASGRO is also corrected for the so-called "fanning" of the da/dN curve near threshold as R changes. This effect is included in the FFL program, but only when the NASGRO growth rate equation is selected.

2.8 Crack Transitioning

An option is available in the FFL code to allow transitioning of corner cracks into through wall cracks. Transitioning is implemented when the following conditions are simultaneously satisfied:

$$a \geq 0.975t \qquad c \geq c_{tran} \tag{2.10a}$$

or when

$$K_{\max} \geq K_c \tag{2.10b}$$

where c_{tran} is specified by the user, K_{max} is the SIF at maximum load in a fatigue cycle and K_c is the fracture toughness. The through-wall crack length after transitioning is set equal to c. If c_{tran}

is specified as zero, then transitioning will occur immediately when the a-tip of the crack penetrates the liner wall. If c_{tran} is specified as, say, $2t$, then transitioning will not be activated when the a-tip penetrates the wall until the crack length in the ligament equals $2t$. In these cases, the crack depth is held constant at $0.975t$ but the crack is allowed to grow according to the conditions at the c-tip calculated using the corner crack model until a length of c_{tran} is reached.

If the toughness criterion for transitioning is activated, then transitioning to a through crack of length c is performed irrespective of the value of c_{trans}.

2.9 Weight Function Solutions for Corner and Through-Thickness Cracks at Various Locations in the Flowliner

2.9.1 Introduction

Stress intensity factors (SIFs) for corner and straight-fronted through thickness cracks at Locations A, B, C and D on the flowliner slots subjected to bivariant and univariant stressing are required for the deterministic fatigue crack growth life module, Flowliner Fatigue Life (FFL), described above. Solutions for circumferential (Locations B and C) and axial (Locations A and D) cracks are of interest for a complete analysis of fatigue cracking in the flowliner.

The approach adopted for calculating the SIFs is based on the weight function (WF) method. This method was chosen because: it is extremely versatile; it employs stress distributions derived from an un-cracked structural analysis; it can be applied independent of the source of the stressing (*e.g.*, whether the stresses are induced by pressure loads, thermal strains, welding residual stresses or vibratory stresses). SwRI has extensive experience in applying this approach and also has the computational tools to verify it (*e.g.*, ABAQUS and FADD3D). Essentially, the WF is the SIF solution corresponding to unit point loads symmetrically applied to the top and bottom surfaces at any location (x,y) on the crack surfaces. By applying the principle of linear superposition, the point load solutions can be integrated over the surfaces of the crack to determine the SIF for any arbitrary distribution of point loads, $P(x,y)$.

The detailed development of weight functions (WFs) for corner and through-thickness cracks and the validation of the approach is presented in Sections 2.9.2 and 2.9.3, respectively.

2.9.2 Weight Functions for Corner Cracks

2.9.2.1 General: The WF, $W(x, y, a, c, t, w, R_{liner}, D_{slot})$ is a function of crack size and shape (characterized by the corner crack dimensions, a and c), the geometry of the structure (characterized, for the flowliner, by the liner thickness, t, the ligament or section width, w, the radius of the liner, R_{liner}, and the slot dimensions, D_{slot}), and displacement imposed boundary conditions (*e.g.,* the constraints imposed on flowliner deformation by the weld). Once determined for the crack configurations of interest, the WF can be used to evaluate corner crack SIFs for any arbitrary stressing.

The SIF determination can be accomplished by performing the following integration:

$$K(a,\frac{a}{c},\phi) = \iint_A \sigma(x,y) W\left(x,y,a,\frac{a}{c},\phi\right) dA \qquad (2.11)$$

In this equation, A, is the area of the crack surfaces, $\sigma(x,y)$, is an arbitrary bivariant stress distribution, ϕ is an angle defining a position on the crack front, and, for simplicity, the dependencies of the SIF, K, and WF, W, on t, w, R_{liner} and D_{slot}, have been omitted. In the present analyses, corner cracks are allocated two degrees of freedom (DOF) during fatigue crack growth calculations determined by the SIFs evaluated at two very near surface breaking points on the crack front corresponding to $\phi=90°$ (the through-thickness a-tip) and $\phi=0°$ (the through-ligament c-tip).

More details regarding the theory behind the WF approach to corner cracks are given in sub-section 2.9.2.2. Validation of the approach for corner cracks is detailed in sub-section 2.9.2.3. The finite element models used to determine key parameters appearing in the weight function formulation are described in sub-section 2.9.2.4.

2.9.2.2 Theoretical Approach: At the start of this project, a limited number of corner crack SIF solutions for cracks in plates subject to bivariant stressing were available for use by the team members. However, these solutions were considered either too limited or not directly applicable to corner cracks at slots in the flowliner because of the differences in geometry (plate versus slotted cylinder), loading conditions, and because of the potential for stress re-distribution in the liner from a ligament containing a crack onto adjacent un-cracked ligaments. Examples of these solutions are: the CC01 corner crack solution in NASGRO [NASGRO, 2003] (limited to linear stress variations); NASCRAC solutions [Harris et al, 1987] (uses an RMS-averaged effective stress intensity factor for the entire crack boundary that does not provide information on the specific local variation in K, and has accuracy limitations, especially for deep cracks [Favanesi et al, 1994]); and the slice synthesis method (SSM) solutions of Zhao et al [1995] (accuracy was considered an issue for this approximate method in addition to computational speed which limits its practicality for some fatigue crack growth applications).

Highly accurate SIF solutions for cracks in structural components subject to arbitrary bivariant stress distributions are possible using the point load weight function (WF) formulation described in sub-section 2.9.2.1. Several WF formulations have been proposed for elliptically shaped cracks (*e.g.*, Oore and Burns [1980] and Orynyak [1994,1995]) and the current version of NASGRO [NASGRO, 2003] includes a limited number of bivariant SIF solutions based on a hybrid approach developed by Fujimoto [2000] (although some inconsistencies have been discovered in this approach for deep cracks). Recently, a new and powerful bivariant weight function formulation for a corner crack in a rectangular plate of finite width and thickness has been developed at SwRI [McClung et al, 2004]. The corner crack is assumed to have a quarter-elliptical shape that can be characterized by two degrees of freedom, the crack dimensions c and a in the width and thickness directions, respectively (Figure 2-10). This new formulation is the one used herein to develop WFs for corner cracks at flowliner slots.

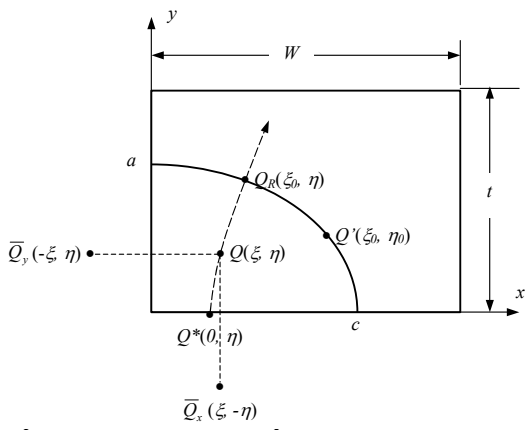

Figure 2-10: Geometry configuration and nomenclature for corner crack in plate.

The new formulation uses the WF proposed by Onynyak for an elliptical crack in an infinite body written in the form:

$$W_{QQ'} = \frac{\sqrt{R^2 - r^2}}{\pi \ell_{QQ'}^2 \sqrt{\pi R}} \tag{2.12}$$

This equation represents the weighting effects on any point Q' along the crack front contributed by a point unit load applied at Q on the elliptical crack surface. Here, R is the distance between Q^* and Q_R, r the distance between Q and Q^*, and $\ell_{QQ'}$ the distance between Q and Q'. Expressions for Q, Q', Q_R, and Q^* can be concisely formulated using an elliptical coordinate notation in which $Q = (\xi, \eta)$, $Q' = (\xi_0, \eta_0), Q_R = (\xi_0, \eta)$ and $Q^* = (0, \eta)$ where ξ and η are elliptical coordinates with origin at the center of the crack. It can be seen that Q, Q_R, and Q^* are defined along the same elliptical angle η (see Figure 2-10). ξ_0 is the "elliptical radius" defining the elliptical crack front.

To account for the free boundary correction for a quarter-elliptical corner crack in a quarter-infinite body, Eq. (2.12) was modified to include two additional length parameters, $\ell_{\overline{Q}_x Q'}$ and $\ell_{\overline{Q}_y Q'}$, as shown in Eq. (2.13)

$$W_{QQ'} = \frac{\sqrt{R^2 - r^2}}{\pi \ell_{QQ'}^2 \sqrt{\pi R}} \left(1 + \frac{\ell_{QQ'}^2}{\ell_{\overline{Q}_x Q'}^2} + \frac{\ell_{QQ'}^2}{\ell_{\overline{Q}_y Q'}^2} \right) \tag{2.13}$$

In reference to Figure 2-10, $\ell_{\overline{Q}_x Q'}$ is the distance between $\overline{Q}_x$ and Q', and $\ell_{\overline{Q}_y Q'}$ the distance between $\overline{Q}_y$ and Q'. The locations, $\overline{Q}_x$ and $\overline{Q}_y$, are points symmetrical to the location of point load Q with respect to the x- and y-axes.

The final form of the WF equation taking into account finite width and thickness effects, is:

$$W_{QQ'} = \frac{\sqrt{R^2 - r^2}}{\pi \ell^2_{QQ'} \sqrt{\pi R}} \left(1 + \frac{\ell^2_{QQ'}}{\ell^2_{\overline{Q}_x Q'}} + \frac{\ell^2_{QQ'}}{\ell^2_{\overline{Q}_y Q'}} \right) \left[1 + \Pi_1 \sqrt{1 - \frac{r}{R}} + \Pi_2 \left(1 - \frac{y}{y'} \right) + \Pi_3 \left(1 - \frac{x}{x'} \right) \right] \tag{2.14}$$

where x and y define the Cartesian coordinates of Q, $x' = c\sqrt{1 - y^2/a^2}$, $y' = a\sqrt{1 - x^2/c^2}$, and Π_1, Π_2, and Π_3 are parameters correcting for free surface effects whose values have to be determined for the a-tip and c-tip from three known reference SIF solutions. Assuming Π_1, Π_2, and Π_3 are known, the SIF can be evaluated by performing surface integration across the crack area, as shown in the equations below

$$K = \int_0^a \int_0^{c\sqrt{1 - \frac{y^2}{a^2}}} \sigma(x, y) \cdot W_{QQ'} \, dx dy \tag{2.15}$$

$$K^{a,c} = \int_0^a \int_0^{c\sqrt{1 - \frac{y^2}{a^2}}} \sigma(x, y) \frac{\sqrt{R^2 - r^2}}{\pi \ell^2_{QQ^{a,c}} \sqrt{\pi R}} \left(1 + \frac{\ell^2_{QQ^{a,c}}}{\ell^2_{\overline{Q}_x Q^{a,c}}} + \frac{\ell^2_{QQ^{a,c}}}{\ell^2_{\overline{Q}_y Q^{a,c}}} \right) \left[1 + \Pi_1^{a,c} \sqrt{1 - \frac{r}{R}} + \Pi_2^{a,c} \left(1 - \frac{y}{y'} \right) + \Pi_3^{a,c} \left(1 - \frac{x}{x'} \right) \right] dx dy \tag{2.16}$$

where the superscripts a and c denote parameters associated with a- and c-crack tips, respectively.

To facilitate the computation, Eq. (2.16) is preferably written in terms of elliptical coordinate parameters instead of Cartesian. For $\alpha = a/c \le 1$, the relationships between Cartesian and elliptical coordinates (ξ, η) are as follows:

$$x = b \cosh \xi \cos \eta \,, \quad y = b \sinh \xi \sin \eta \,, \quad b = \sqrt{c^2 - a^2} \tag{2.17}$$

For any point along the crack front, the "elliptical radius" in the elliptical coordinate system is the same and is given by

$$\xi_0 = \frac{1}{2} \ln \left(\frac{1 + \alpha}{1 - \alpha} \right) \tag{2.18}$$

The Cartesian coordinates for Q, Q_R, Q^*, Q', $\overline{Q}_x$, and $\overline{Q}_y$ in terms of elliptical coordinate parameters, are as follows:

$$Q = (b\cosh\xi\cos\eta, b\sinh\xi\sin\eta) \tag{2.19}$$
$$Q_R = (b\cosh\xi_0\cos\eta, b\sinh\xi_0\sin\eta) \tag{2.20}$$
$$Q^* = (b\cos\eta, 0) \tag{2.21}$$
$$Q' = (b\cosh\xi_0\cos\eta, b\sinh\xi_0\sin\eta) \tag{2.22}$$
$$\overline{Q}_x = (-b\cosh\xi\cos\eta, b\sinh\xi\sin\eta) \tag{2.23}$$
$$\overline{Q}_y = (b\cosh\xi\cos\eta, -b\sinh\xi\sin\eta) \tag{2.24}$$

and the infinitesimal area becomes

$$dxdy = b^2(\sinh^2\xi + \sin^2\eta)d\eta d\xi \tag{2.25}$$

Furthermore, the integration limits are converted from $y: 0 \to a\sqrt{1-x^2/c^2}$ and $x: 0 \to c$ to $\xi: 0 \to \xi_0$ and $\eta: 0 \to \pi/2$. The integration sequence is now interchangeable.

The weight function method adopted herein requires an accurate set of reference solutions for known stress distributions for a matrix of crack geometries so that the parameters Π_1, Π_2, and Π_3 can be determined. These reference solutions were numerically generated for the liner slot cracks at Locations A, B, C and D using the finite element code ABAQUS.

Reference solutions for corner cracks at each of the four Locations, A, B, C and D, were generated for a matrix of 36 combinations of geometrical aspect ratios: *a/c*=0.125, 0.25, 0.5, 0.75, 1.0, 1.25; and *a/t*=0.1, 0.2, 0.3, 0.5, 0.7 and 0.85. For any arbitrary combination of aspect ratio and crack depth, the reference solutions are determined from the matrix of specific solutions through Hermite interpolation.

Three sets of reference SIF solutions were determined corresponding to unit tension, unit bending along the *x*-axis, and unit bending along the *y*-axis. Mathematically, the three reference stresses are given by $\sigma_0 = 1$, $\sigma_1 = -y/a + 1$, and $\sigma_2 = -x/c + 1$. More details concerning the finite element modeling of the corner cracks at Locations A, B, C and D are given in sub-section 2.9.2.4. Validation of the weight function methodology for bivariant stressing of corner cracks is presented in 2.9.2.3.

2.9.2.3 Validation: The WF formulation contains three parameters that are unknown and have to be determined using three reference SIF solutions. In the present case, these reference solutions correspond to the SIFs for corner cracks subjected to uniform stressing, and linear in-plane and out-of-plane stressing. Validation of the approach is therefore accomplished by applying the developed WFs to evaluate the SIFs for corner cracks subjected to a bivariant stress distribution that is dissimilar to the stresses used to generate the reference solutions. These solutions are then compared with independently derived solutions for the same bivariant stress field obtained using ABAQUS. Agreement between these two sets of solutions will confirm the accuracy of the WF approach and the software developed to implement it.

The applied stress chosen for validation is given by the following equation:

$$\sigma(x,y) = \left(1 - \frac{x}{W}\right)^3 \left(1 - \frac{y}{t}\right)^3 \tag{2.26}$$

Figure 2-11 shows that this bivariant stress has steep gradients that cause the stress to fall rapidly away from the origin of coordinates in both the x and y directions. In this plot, the liner thickness t=0.05 inches and the ligament W=0.75 inches. Figure 2-12 shows the local coordinate system used for each of the four crack Locations, A, B, C and D, analyzed.

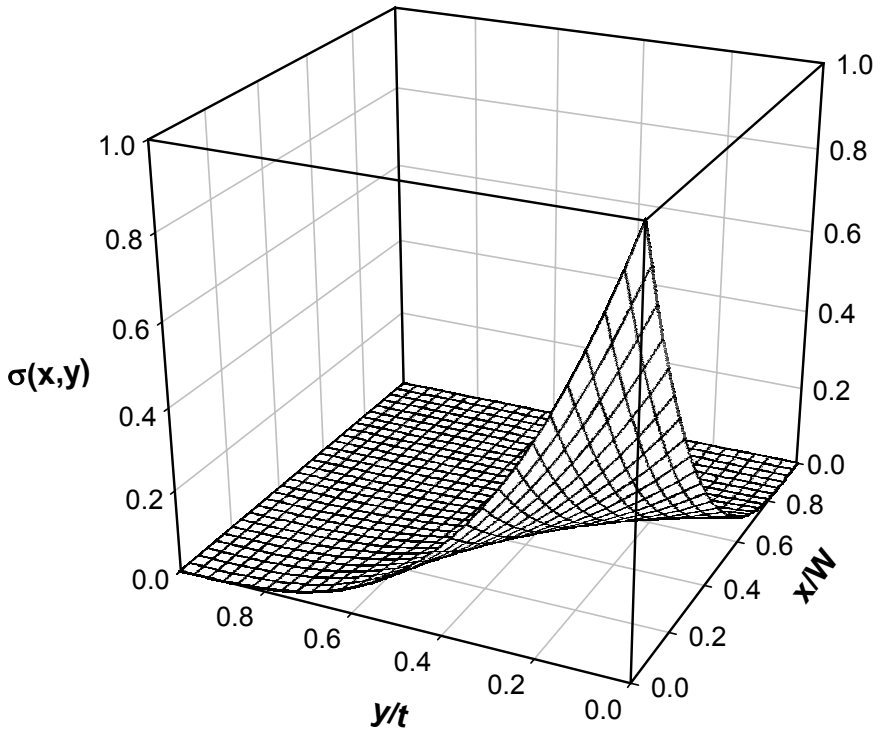

Figure2-11: Illustration of the steep third-order polynomial bivariant stress used for validation.

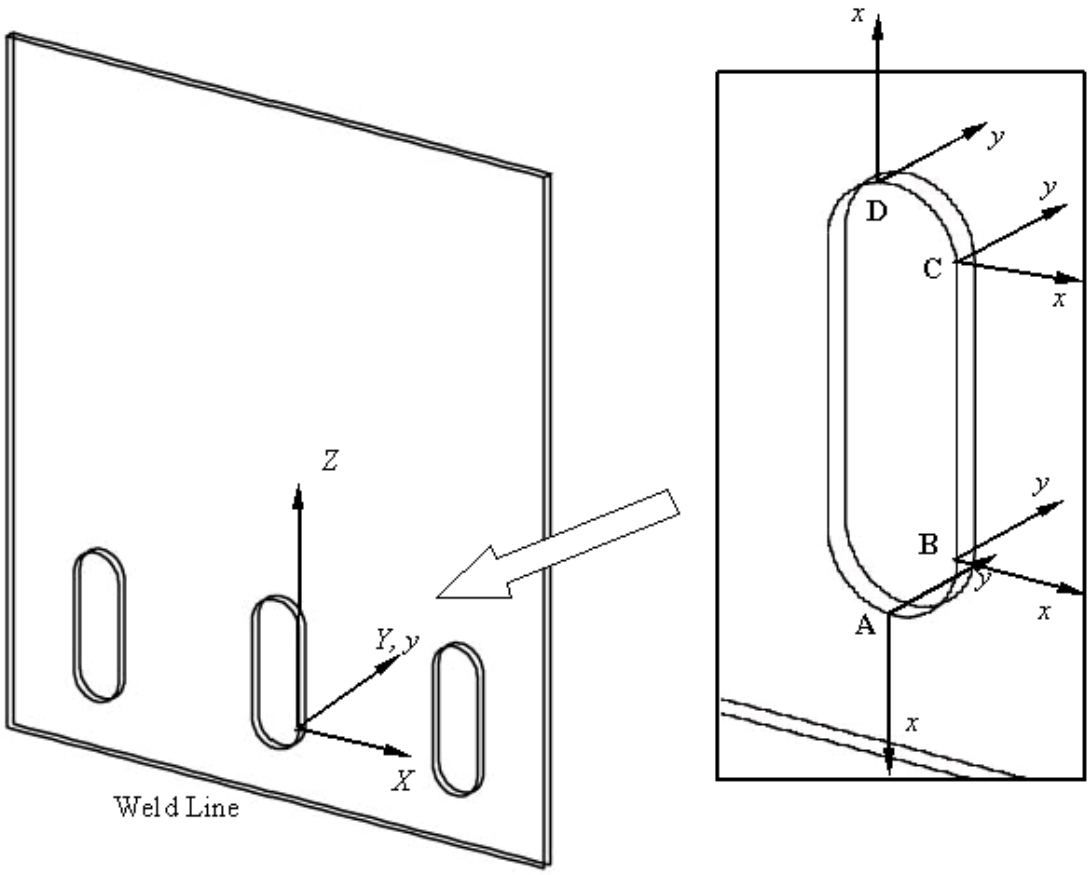

Figure 2-12: Potential crack sites A, B, C and D and the associated local coordinate system (*xy*) and the global coordinate system (*XYZ*) for the plate.

SIFs corresponding to the stresses defined by Equation (2.26) were determined for a matrix of corner crack sizes and Locations A, B, C, and D on a slot in the liner (see sub-section 2.8.2.4). The crack size matrix used is specified in Table 2-2. The matrix corresponds to *a/t* ratios of 0.1 and 0.5 (*t*=0.05 inches), and aspect ratios *a/c* of 0.5 and 1.0. The finite element models used in the ABAQUS computations were the same as those used to generate the reference SIF solutions. Typical finite element models of the cracks are shown in Figures 2-21 through 2-24.

Table 2-2: Matrix of crack dimensions used for validation.

a (*inch*)	*c* (*inch*)	$\sigma(x,y)$
0.005	0.005	$\left(1-\frac{x}{c}\right)^3\left(1-\frac{y}{a}\right)^3$
0.025	0.025	
0.005	0.01	
0.025	0.05	

Figures 2-13 to 2.16 show the predicted WF results expressed in terms of normalized stress intensity factors F_a $(=\frac{K}{\frac{\sqrt{\pi a}}{\Phi}})$ for the a-tip and c-tip plotted against the finite element results, where *a* is the crack depth through the thickness, and Φ is a shape factor approximated by $\sqrt{1+1.464(a/c)^{1.65}}$ for *a/c*<1. The numerical values for F_a for both sets of results can be found in Table 2.3.

The excellent agreement between the WF predicted SIFs for the bivariant cubic stress distribution and the ABAQUS derived solutions validates the accuracy of the WF solutions derived herein for corner cracks at Locations A, B, C and D.

Table 2.3: Numerical values for F_a ($= \frac{K}{\frac{\sqrt{\pi a}}{\Phi}}$) computed using FEA and the WF Method and shown in Figures 2-13 through 2-16.

Crack Site	*a* (inch)	*c* (inch)	F_a Computed Using FEA		F_a Predicted by Weight Function Method	
			c-tip	*a*-tip	*c*-tip	*a*-tip
A	0.005	0.005	1.0610	0.9228	1.0600	0.9159
	0.025	0.025	0.7848	0.3602	0.7846	0.3735
	0.005	0.01	0.7451	0.8987	0.7445	0.8990
	0.025	0.05	0.4869	0.4162	0.4860	0.4212
B	0.005	0.005	1.0970	0.9366	1.0810	0.9131
	0.025	0.025	0.9288	0.3974	0.9314	0.4140
	0.005	0.01	0.7985	0.9203	0.7981	0.9201
	0.025	0.05	0.6947	0.4855	0.6951	0.4898
C	0.005	0.005	1.0970	0.9367	1.095	0.9356
	0.025	0.025	0.9301	0.3987	0.9328	0.4152
	0.005	0.01	0.7985	0.9204	0.7980	0.9205
	0.025	0.05	0.6969	0.4919	0.6975	0.4940
D	0.005	0.005	1.0920	0.9242	1.0910	0.9241
	0.025	0.025	0.9154	0.3825	0.9197	0.3997
	0.005	0.01	0.7950	0.9109	0.7946	0.9109
	0.025	0.05	0.6867	0.4675	0.6874	0.4684

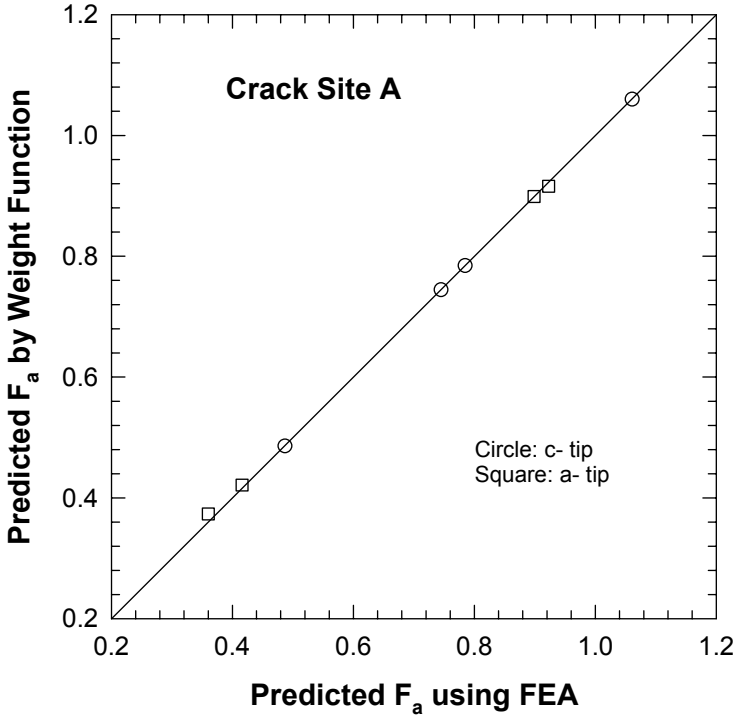

Figure 2-13: Comparison of normalized stress intensity factors determined using FEA with WF results for crack site A.

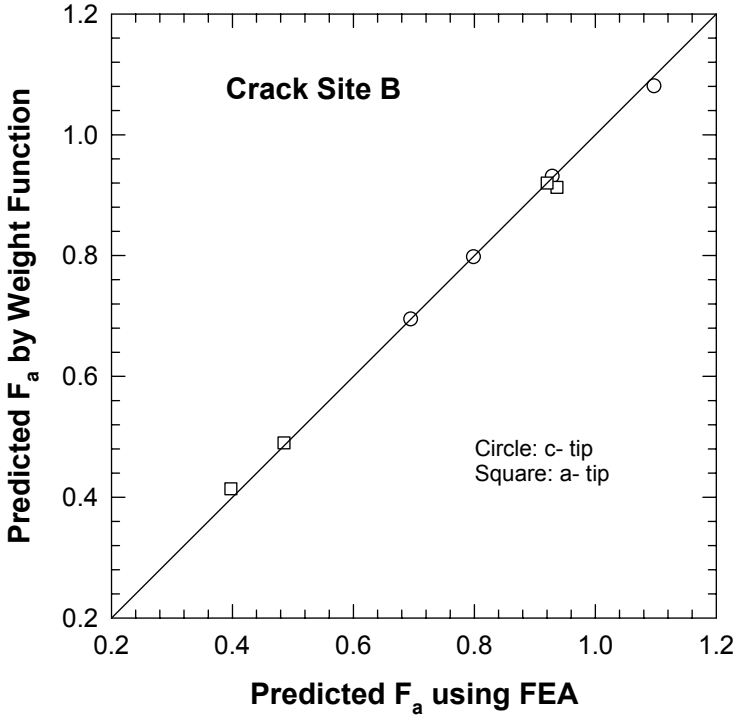

Figure 2-14: Comparison of normalized stress intensity factors determined using FEA with WF results for crack site B.

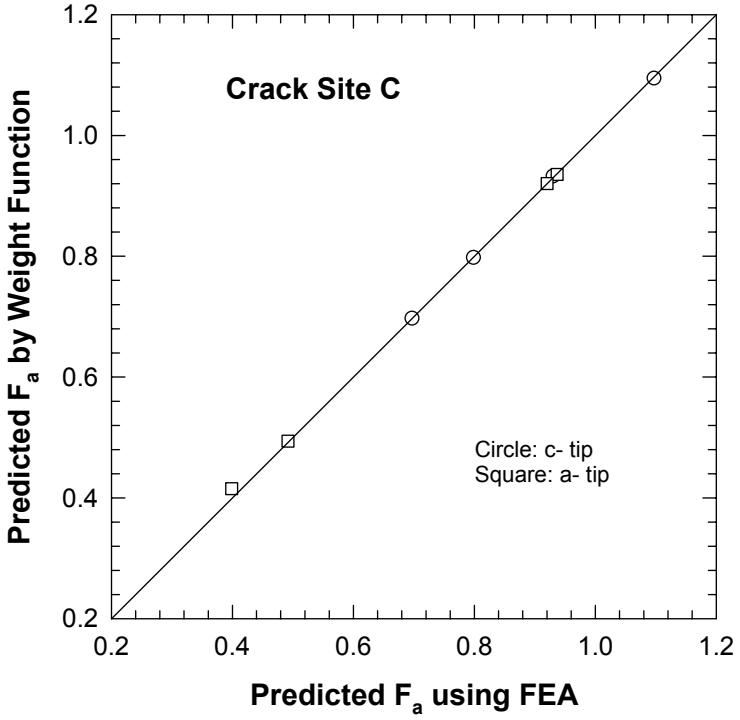

Figure 2-15: Comparison of normalized stress intensity factors determined using FEA with WF results for crack site C.

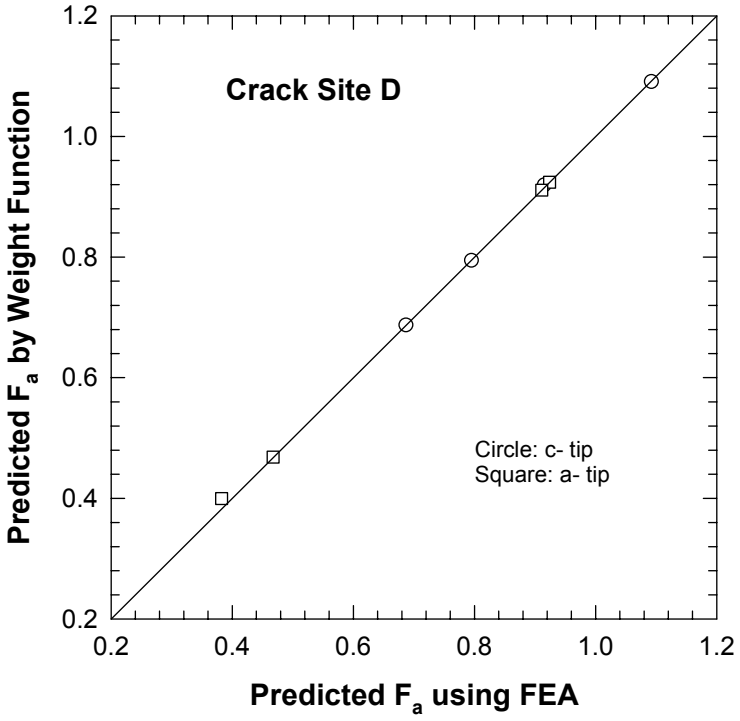

Figure 2-16: Comparison of normalized stress intensity factors determined using FEA with WF results for crack site D.

2.9.2.4 Finite Element Modeling: The upstream and downstream flowliners were assumed equivalent for analysis purposes and were modeled as flat plates containing three slots with boundary conditions representative of an infinite array of slots. The attachment weld was simulated by fixed displacements at the end of the liner representing the welded flowliner to flange, the other end was free to deform. The boundary conditions applied to the three-dimensional model are summarized schematically in Figure 2-17.

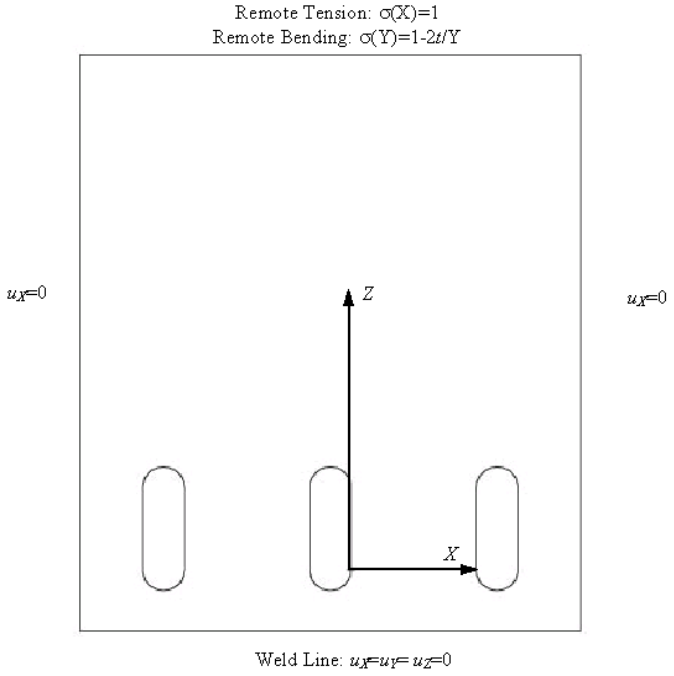

Figure 2-17: Boundary conditions applied to the finite element modeling of the flowliner.

The three-dimensional model shown in Figure 2-17 was analyzed using ABAQUS employing solid elements with the free ends of the liner subjected to bending and uniform tension stressing. In order to verify that the boundary conditions and the stiffness response of the modeling were accurate, a thin shell model of the liner was also analyzed for comparison with the results of the finite element model and the independent thin shell analysis performed by NASA MSFC [Allen, 2004].

Figure 2-18 shows a comparison of remote tension results derived from the solid and thin shell models. The stress distributions are almost identical except at those locations where the semi-circular notches at the ends of the slots transition into straight segments. The discrepancy is attributed to the different extrapolation schemes used for determining the stresses at the surface from results determined from internal integration points. The stress concentration factor, k_t, predicted by the 3D model is 1.93, while that for the thin shell model is 1.82.

The equivalent remote bending results are plotted in Figure 2-19. In this case, the 3D solid model and the thin shell results show quite consistent behaviors with the k_t for the former being 1.63 while for the latter it is 1.61.

Comparing the present results with those obtained by NASA MSFC, it appears that the NASA results under-predict the k_t value for remote tension compared to the present results while the mid-ligament stress distributions for both are similar. The results for remote bending indicate that the NASA analysis may have slightly over-predicted the k_t value compared to the current results and also predicts a higher mid-ligament stress distribution. The mid-ligament stress given in the current analysis is consistent with the expected ligament stress deduced from force balance considerations, while the NASA stresses are higher than would be expected.

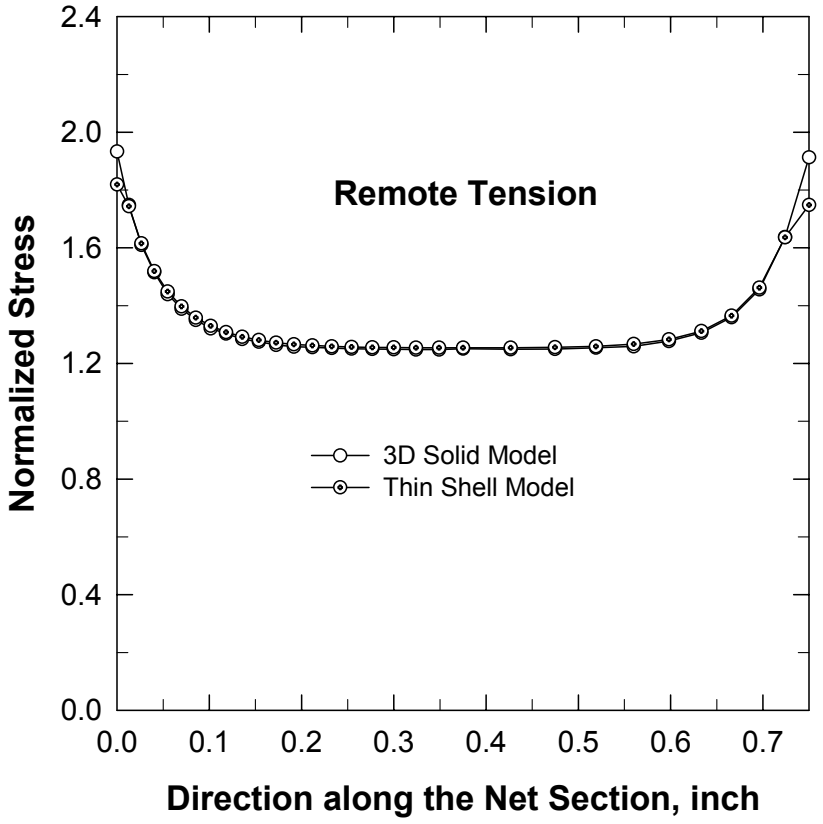

Figure 2-18: Comparison of predicted axial stress distributions across the ligament between two slots obtained from the 3D solid model and the thin shell model when the free end of the liner is subject to uniform stressing.

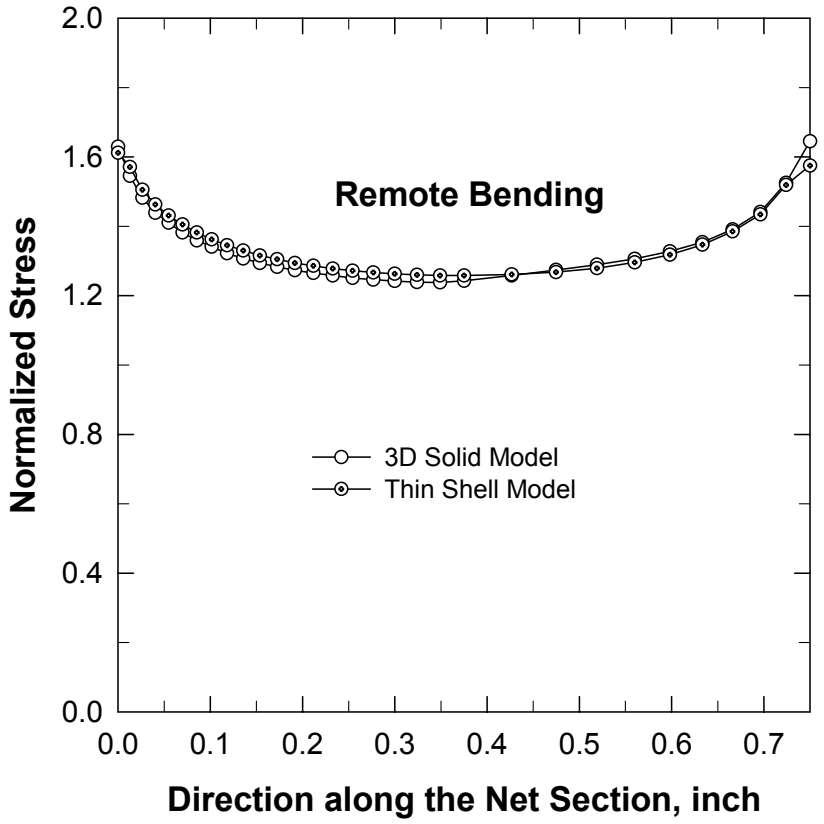

Figure 2-19: Comparison of predicted axial stress distributions across the ligament between two slots obtained from the 3D solid model and the thin shell model when the free end of the liner is subject to bend stressing.

The foregoing results, and the agreement between the 3D solid model and the thin shell model, indicate that the stiffness of the 3D solid model accurately captures the stiffness predicted from thin shell analysis, and that both sets of results are in reasonable agreement with an independent analysis performed by NASA. This conclusion is important, because it is necessary to employ a 3D solid model when analyzing corner cracks in the liner, and inaccuracies in the stiffness of the modeling will result in inaccuracies in the crack solutions.

The 3D solid model was used as the basis for building finite element models of the liner slots containing corner cracks. An overview of the locations of the four types of cracks analyzed (circumferential corner cracks at B and C and axial corner cracks at A and D) is shown in Figure 2-20. More detailed representations of modeling for the four cracks are illustrated in Figures 2-21 (axial crack at A), 2-22 (circumferential crack at B), 2-23 (circumferential crack at C) and 2-24 (axial crack at D).

Crack models similar to those shown in Figures 2-21 (axial crack at Location A) and 2-22 (circumferential crack at Location B) were used in the determination of reference SIF solutions for use in the weight function formulation. In these cases, uniform tension, and linear in-plane and out-of-plane stress distributions were used. The same crack models were also used in the validation of the WF approach, as described in sub-section 2.9.2.3.

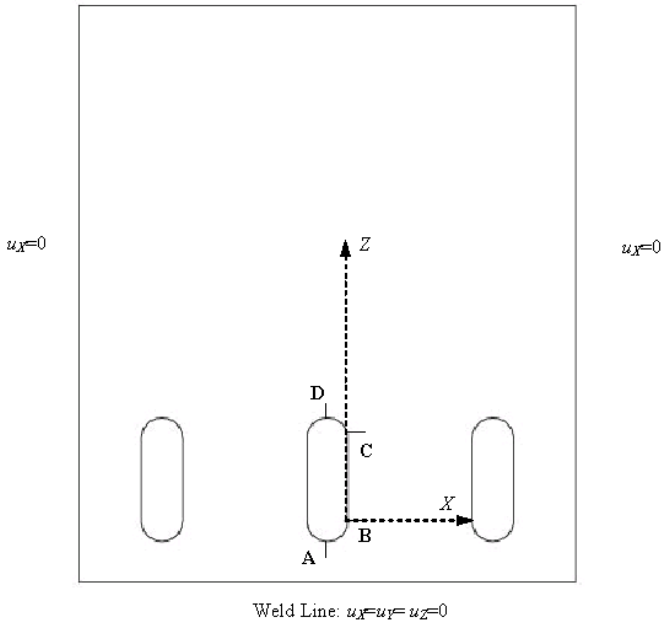

Figure 2-20: Boundary conditions applied to the finite element modeling of the cracked flowliner and the locations of the corner cracks at A, B, C, and D.

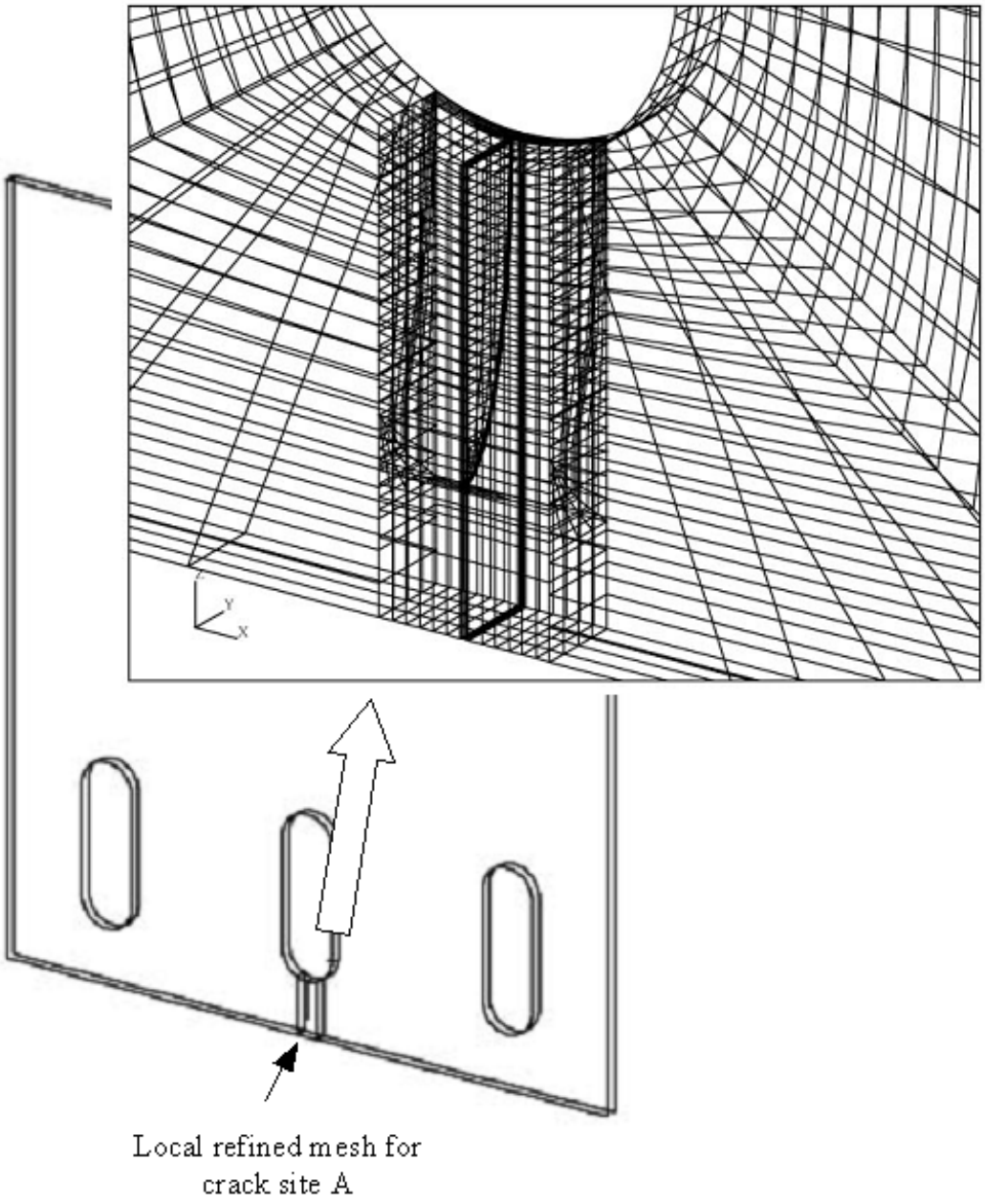

Figure 2-21: Typical details of the 3D solid element modeling of an axial corner crack at Location A.

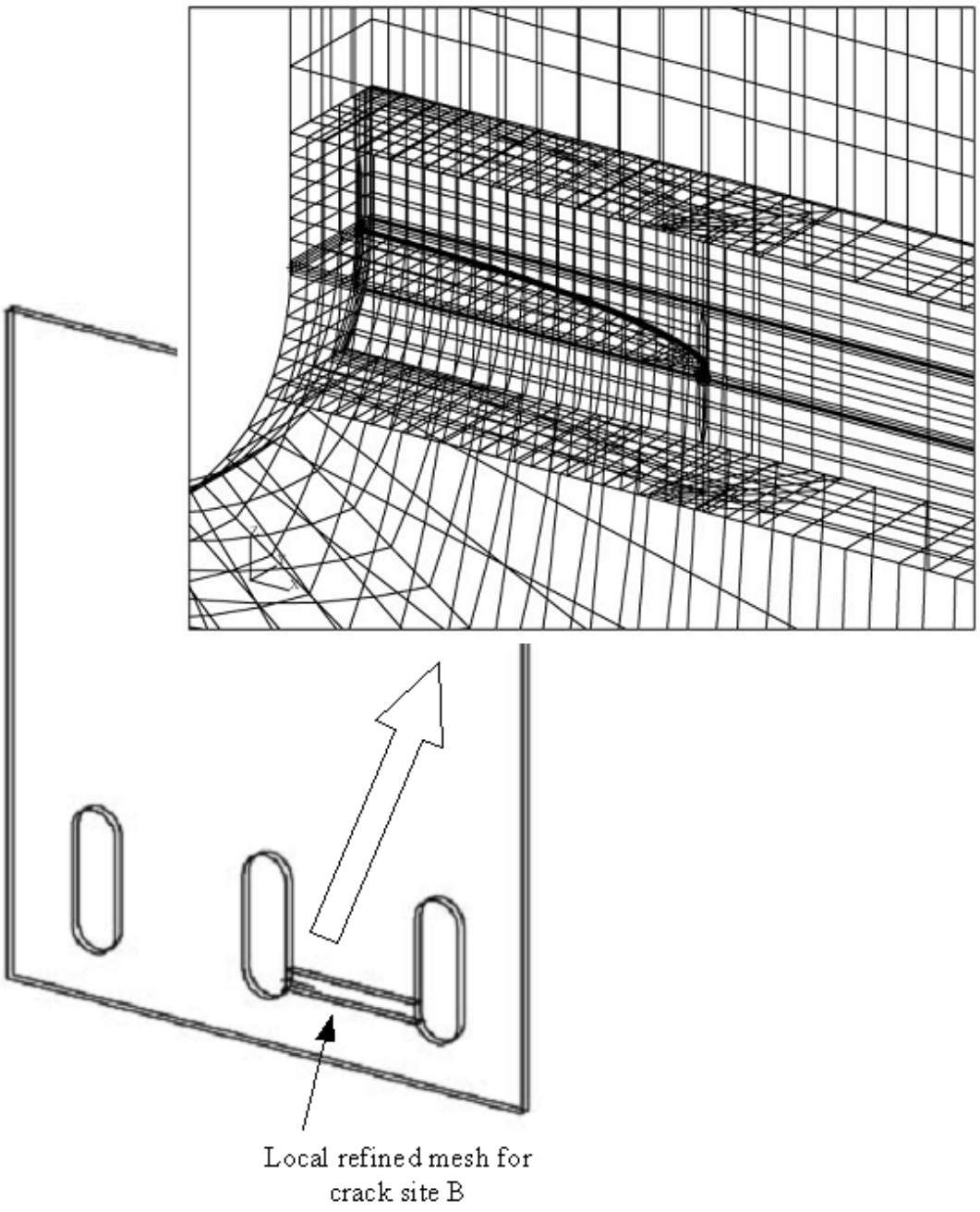

Figure 2-22: Typical details of the 3D solid element modeling of a circumferential corner crack at Location B.

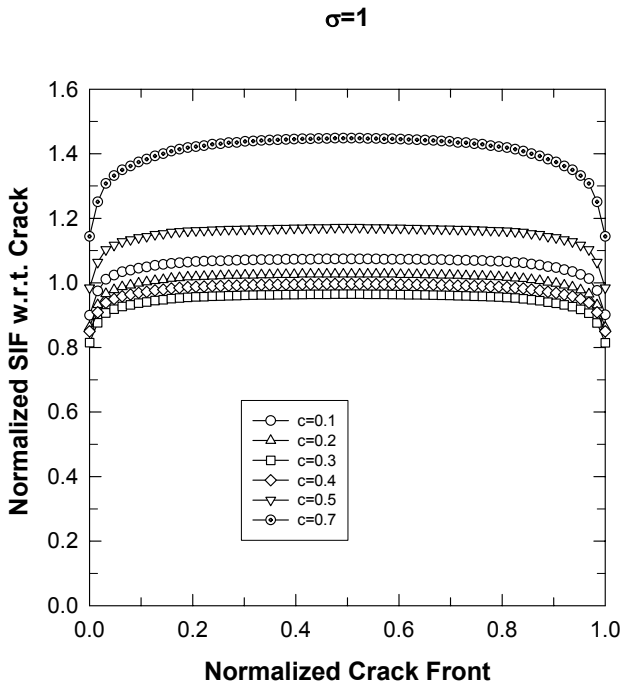

Figure 2-23: Finite element results showing the through thickness variation in normalized SIF along the front of a through wall crack at Location B subjected to uniform stressing. The maximum SIF values always occur at the mid-wall

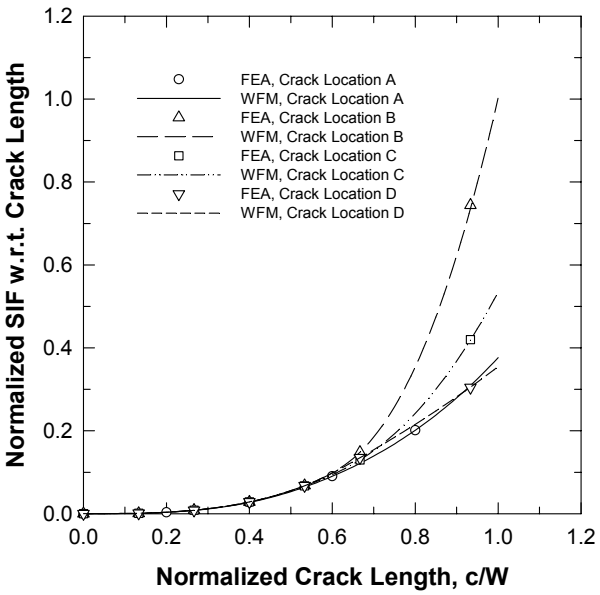

Figure 2-24: Comparison of WF derived normalized SIF values for through cracks subjected to a cubic stress variation with SIFs obtained from *J* contour integral solutions generated using finite element models of cracks at Locations A, B, C and D on a liner slot.

2.9.3 Weight Functions for Through Thickness Cracks

2.9.3.1 General: WFs were developed for through-thickness cracks at Locations A and D (axial) and B and C (circumferential) on a slot. These solutions were developed primarily to provide SIF solutions for use in fatigue crack growth computations once a corner crack breaks through the thickness and transitions into a through crack. In order to capture the bivariant nature of ligament stresses, the solution scheme is based on a one-dimensional weight function for univariant stressing combined with explicit SIF solutions corresponding to through-thickness bending. The complete SIF solution is determined by integrating over the crack length the product of a univariant stress distribution and the weight function (to capture the effects of stress changes in the ligament direction) and evaluation of a through-thickness bending SIF solution (to capture the effects of through-thickness stress variations).

In the current analysis, the WFs, $m(x, c, t, w, R_{liner}, D_{slot})$, for through cracks are limited to one degree of freedom and are applicable to arbitrary univariant stressing where the stress variation is assumed independent of the through-wall location, y, and is a function only of the through ligament distance, x. In terms of the WF for univariant stressing, $m(x, c)$ (the arguments $t, w, R_{liner}, D_{slot}$ are omitted hereafter) , the SIF for through cracks is calculated from the equation:

$$K(c) = \int_c \sigma(x) m(x,c) dx \tag{2.27}$$

where the integral is performed over the crack length, c.

Approximations have to be made to reduce the bivariant stress distribution in the liner to a univariant stress distribution, $\sigma(x)$, that can be used in Equation (2.27). This is done by setting $\sigma(x) = \sigma(x,y=t/2) = \sigma_{mid}(x)$, the value of the bivariant stress mid-way through the liner wall.

The bivariant nature of the liner stresses is captured by combining the univariant SIF, $K(c)$, with the solution for a unit through thickness bend, $\kappa_b(c)$, where the bend stress, $\sigma_b(c)$ is evaluated as a function of crack length and is derived from the difference between the mid-wall stress and the stresses at the ID and OD.

More details regarding the evaluation of WFs for through thickness cracks are given in sub-section 2.9.3.2. Validation of the approach is given in sub-section 2.9.3.3.

2.9.3.2 Theoretical Approach: The through thickness crack WF, $m(\xi,c)$, is one-dimensional, where ξ is the location on the crack measured from the surface of the slot, and c is the crack length. The SIF for a univariant stress is evaluated from the WF as shown in Equation (2.27). As was the case for corner crack WFs, the formulation for the WFs for through thickness cracks involves unknown parameters that are determined from reference SIF solutions corresponding to specific stress distributions. The procedure for computing the reference SIF solutions involves computing J contour integral values along circular paths around the crack tip using the finite element program ABAQUS. In the present case, three stress distributions were used to calculate

three reference SIF solutions. These three stresses were a uniform stress, a linear stress, *x/W*, and a quadratic stress, $(x/W)^2$, respectively, where *W* is a normalizing ligament length depending on the crack location. For crack Locations B, C, and D, *W*=0.75" was used, and for crack Location A, *W*=0.25"- the distance from the slot root to the weld line. The reference solutions were generated at the crack lengths of 0.1", 0.2", 0.3", 0.4", 0.5", and 0.7" (93.3% of the ligament width) for crack Locations B, C, and D, and crack lengths of 0.05", 0.1", 0.15", and 0.2" (80% of ligament width) for crack Location A.

Additional computations with the same crack configurations were performed to determine the SIF solutions at Locations A, B, C and D for a through thickness (out-of-plane) bending stress (=1-2*y*/*t*).

As expected, since the SIF computations were made using a three-dimensional finite element model, the SIF values vary along the crack front through the liner thickness, even though the univariant stress does not. This is due to the effects of the free surfaces at the ID and OD. In order to reduce the problem to a single degree of freedom, the reference SIF solution were equated to the maximum SIF values observed along the crack front. In all the cases analyzed, these maximum SIF values were observed to occur at the mid-wall position, as illustrated in Figure 2-23. In this figure, normalized SIF values are plotted as a function of normalized through wall location on the crack front for cracks of various lengths subjected to uniform stressing.

In the through crack WF formulation, the WF is represented by a five-term expansion around the singularity of the crack tip at $\xi=c$ and is given by

$$m\left(\bar{\xi},\bar{c}\right)=\frac{1}{\sqrt{2\pi\bar{\xi}}}\sum_{i=0}^{4}\beta_i\left(\bar{c}\right)\left(1-\frac{\bar{\xi}}{\bar{c}}\right)^{i-\frac{1}{2}} \tag{2.28}$$

where $\bar{c}$ and $\bar{\xi}$ are crack lengths normalized with respect to the ligament width and $0 \le \bar{\xi} \le \bar{c}$. The parameters, $\beta_i(\bar{c})$ are determined using the three reference SIF solutions for uniform, linear and quadratic stressing. The stress intensity factor for a crack length *c* subjected to univariant stressing can thus be determined from the equation

$$K_{mid}=\sqrt{\pi c}\int_0^{\bar{c}}\sigma_{mid}\left(\bar{\xi}\right)m\left(\bar{\xi},\bar{c}\right)d\bar{\xi}=\sqrt{\pi c}\int_0^{\bar{c}}\frac{\sigma_{mid}\left(\bar{\xi}\right)}{\sqrt{2\pi\bar{\xi}}}\sum_{i=0}^{4}\beta\left(\bar{c}\right)\left(1-\frac{\bar{\xi}}{\bar{c}}\right)^{i-\frac{1}{2}}d\bar{\xi} \tag{2.29}$$

where σ_{mid} is the univariant stress variation over the ligament equal to the stress at mid-wall. In general, for thin shells, the through thickness stress variation is linear and σ_{mid} can be approximated as the average value of the stress on the ID and the OD.

The SIFs for through cracks subjected to through wall bending was also computed to enable the effects of variations in through thickness stressing to be approximated. The SIF factor was taken as the maximum value (e.g. the value at the ID), as the SIF values vary approximately in a linear manner through the thickness, from positive to negative values.

In practice, the ligaments at Locations A, B, C and D on the slots are subjected to a through wall bend stress that varies as a function of the distance through the ligament, reflecting the reduction in stresses away from the stress concentrating influence of a slot. The SIF module for the FFL program allows for this variation in an approximate way by making the through-wall bend stress a function of crack length. This is accomplished by averaging the bend stress over the crack. This averaging process is performed using the following equation

$$\sigma_b^{avg} = \frac{\int_0^c [\sigma_{ID}(x) - \sigma_{mid}(x)]dx}{c} \tag{2.30}$$

The SIF solution for the through-thickness stress variation is approximated by $\sigma_b^{avg}\kappa_b$ where κ_b is the computed SIF results for unit through-thickness bending with the tensile stress at the ID of the liner.

The SIF solutions for straight-fronted through thickness cracks subjected to bivariant stressing can thus be determined from the equation

$$K(c) = \int_c \sigma_{mid}(x) m(x,c) dx + \sigma_b^{avg}\kappa_b(c) \tag{2.31}$$

2.9.3.3 Validation: The validation of the derived WFs for through thickness cracks was accomplished by comparing SIFs calculated using the WF approach with the results of finite element computations for cracks subjected to the same applied stress. The applied stress chosen in the validation exercise for cracks at Locations A, B, C and D had a cubic variation through the ligament of the form shown in equation (2.32), where *x* is the distance from the slot surface, and the width parameter, *W*, was taken as 0.75" for crack Locations B, C, and D, and 0.25" for crack Location A.

$$\sigma(x) = \left(\frac{x}{W}\right)^3 \tag{2.32}$$

The results of the WF and finite element computations are summarized in Figure 2-24. It can be seen that there is excellent agreement between the WF and finite element results, validating the newly developed WF solution.

Additional validation was performed for through wall circumferential cracks at Location B, since the fatigue life analyses performed herein concentrate on cracks at this location. The applied stress distribution in this case corresponds to the OD stress variation resulting from the dynamic 3ND vibration mode. The results from applying the WF approach

and performing independent finite element computations are shown in Figure 2-25. There is again excellent agreement between the two sets of results.

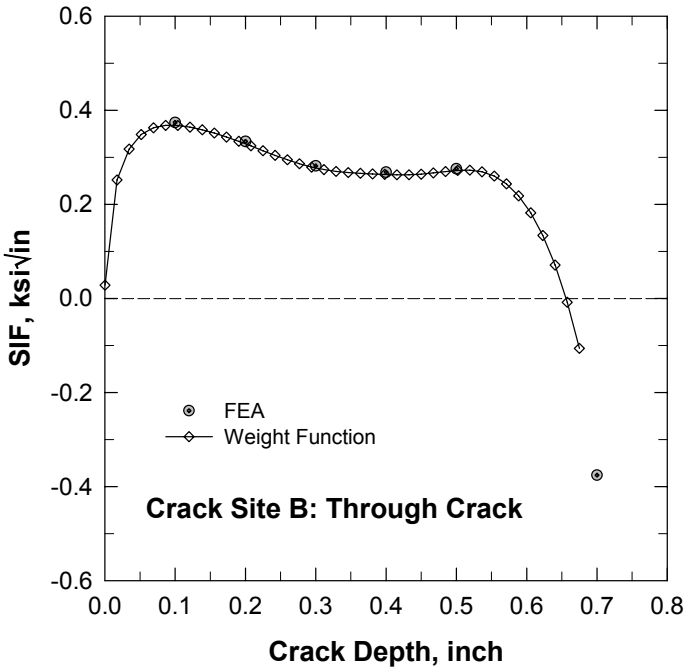

Figure 2-25: Comparison of SIF solutions derived for cracks at Location B using the WF approach with computed SIF results obtained from finite element analysis. The applied stress used was provided and identified by NASA-LaRC. It corresponds to the stress variation through a critical ligament in a flowliner at the OD surface when the liner is subjected to the dynamic 3ND vibration mode.

3. DETERMINISTIC FATIGUE CRACK GROWTH RESULTS

This section summarizes deterministic calculation of flowliner fatigue life performed using the fatigue crack growth models and WF developed SIF solutions described in Section 2. First, computed lives are compared to those obtained by NASA-LaRC under identical loading spectra and input assumptions, except with finite element derived SIF solutions. These results provide additional verification for the WF developed SIF solutions developed in Section 2. Then computational results are obtained for various flowliner loading spectra developed by the Program Office and ITA Team using the deterministic models developed in Section 2. Predicted crack shape evolution at location B is also compared to that observed during a previous MPTA test performed at NASA-MSFC, although the location of that crack was between the A and B locations and hence it would have experienced somewhat different stress fields to those at location B. These results are used to further verify the WF developed SIF solutions.

3.1 Comparison of SwRI and NASA-LaRC Fatigue Lives

The section summarizes the calculations performed to compare the fatigue lives computed by SwRI for through thickness cracks at Location B using the FFL program with the results reported by NASA-LaRC employing NASGRO. In these comparisons, the bivariant stress distributions across the critical ligament section, the load spectra as a combination of various representative dynamic vibration modes, and the material fatigue behavior employed in SwRI fatigue life computation are the same as those developed and identified by NASA-LaRC from modal dynamic structural analysis (James et al, 2004).

The WF approach used by SwRI will produce different SIF solutions to those computed by NASA-LaRC. In the latter case, SIF solutions were derived using dynamic thin shell finite element analysis to compute strain energy release rates based on the virtual crack closure technique. Although the virtual crack closure method produces static SIFs, the dynamic finite element analysis of the cracked liner provides some dynamic interaction effects between the crack and the vibration modes set up in the liner. Although this particular dynamic interaction is absent from the WF approach, the method employs the stress results from a dynamic analysis of the crack-free liner, and captures dynamic effects by using these stresses, which can be significantly different from statically determined stresses.

There are three separate load spectra associated with upstream and downstream flowliners used in this comparison, NESC-1, NESC-2 and NESC-3. The dynamic stress gradients corresponding to these spectra were provided to SwRI by NASA-LaRC in the form of NASGRO compatible input files and are used in the WF analysis, enabling a direct comparison with the lifetime results obtained by James et al (2004). In their fatigue life computation, James et al assumed that the mean stress distribution is the same as the alternating stress distribution, a restriction imposed by the need to use the tabular input form of SIF input to NASGRO. To facilitate comparison, SwRI made the same assumption.

3.1.1 Baseline Comparison

As baseline verification for the input data and to confirm the accuracy of the crack growth integration routines employed in FFL, the SIF solutions derived by NASA-LaRC that included Mode I, II and III contributions were hard coded into FFL software and fatigue lives of upstream and downstream liners were computed using these solutions. The results are shown in Table 3-1 where they can be compared with the results reported by NASA-LaRC using NASGRO. The NASGRO code will terminate fatigue growth calculations when the crack length exceeds the maximum crack length for which the SIF tabular solutions are defined. This limit was 0.3 inches in the NASA-LaRC runs. The FFL program does not have this restriction, and hence in some instances, as can be seen in Table 3-1, the SwRI and NASA-LaRC results differ. However, in general, there is excellent agreement between the two sets of results.

Table 3-1: Comparison of fatigue lives computed using the SwRI program FFL based on tabular SIF solutions with results reported by NASA-LaRC. Both sets of computations used the total SIF derived by NASA-LaRC for combined Modes I, II and III. The crack length defining failure was 0.3" in NASA-LaRC calculations, corresponding to the limit of the SIF solutions used in NASGRO.

Initial Crack Size	Upstream Liner		Downstream Liner	
	Final Crack Lengths and Missions		Final Crack Lengths and Missions	
	SwRI	NASA-LaRC	SwRI	NASA-LaRC
	NESC-1		NESC-1	
0.02"	0.31"	0.3"	0.31"	0.3"
	39	39	1	1
0.075"	0.31"	0.3"	0.31"	0.3"
	21	21	1	0.2
	NESC-2		NESC-2	
0.02"	0.34"	0.3"	0.34"	0.3"
	21	21	28	27
0.075"	0.33"	0.3"	0.33"	0.3"
	12	11	11	10
	NESC-3		NESC-3	
0.02"	0.30"	0.3"	0.30"	0.3"
	71	72	11	10
0.075"	0.31"	0.3"	0.31"	0.3"
	36	35	5	4

The FFL code only computes Mode I SIFs, so it is of interest to compare the differences in fatigue lives calculated using a total SIF that includes contributions from Modes I, II and III with results based only on the Mode I SIFs. The results of this comparison are displayed in Table 3-2. As expected, the Mode I predicted lives exceed those of the combined mode lives. In general, the calculated Mode I lives are about a factor of two greater than the combined mode lives.

Table 3-2: Comparison of fatigue lives computed using the SwRI program FFL based on tabular SIF solutions with results reported by NASA-LaRC. The NASA-LaRC results were based on the total SIF for combined Modes I, II and III. The SwRI calculations used only the Mode I SIF solutions derived by NASA-LaRC. The crack length defining failure was 0.3" in NASA-LaRC calculations, corresponding to the limit of the SIF solutions used in NASGRO.

Initial Crack Size	Upstream Liner		Downstream Liner	
	Final Crack Lengths and Missions		Final Crack Lengths and Missions	
	SwRI (Mode I only)	NASA-LaRC (Modes I, II and III)	SwRI (Mode I only)	NASA-LaRC (Modes I, II and III)
	NESC-1		NESC-1	
0.02"	0.30"	0.3"	0.31"	0.3"
	66	39	2	1
0.075"	0.30"	0.3"	0.31"	0.3"
	40	21	1	0.2
	NESC-2		NESC-2	
0.02"	0.30"	0.3"	0.34"	0.3"
	33	21	35	27
0.075"	0.31"	0.3"	0.33"	0.3"
	21	11	15	10
	NESC-3		NESC-3	
0.02"	0.30"	0.3"	0.30"	0.3"
	121	72	13	10
0.075"	0.30"	0.3"	0.31"	0.3"
	69	35	7	4

3.1.2 Comparison of Fatigue Lives

In this section, fatigue lives determined using the WF method are compared with those generated by NASA-LaRC in order to illustrate the sensitivity of the results to the fracture mechanics modeling. To this end, the fatigue lives of through cracks at Location B in upstream and downstream liners were evaluated for the three load spectra, NESC-1, NESC-2 and NESC-3. The results are presented in Table 3-3.

In the downstream flowliner, the fatigue life results predicted by the WF method are about a factor of two greater than those calculated by NASA-LaRC. However, the predicted lives determined by SwRI are shorter than the NASA-LaRC lives for the upstream flowliner. This outcome reflects the difference in the derived K solutions by SwRI and by NASA-LaRC, as can be seen from the discussion below.

Figure 3-1 shows the dynamic stress gradients for mode shapes 3ND, C4ND, 5ND and C9ND provided to SwRI by NASA-LaRC on the OD surface, mid-plane, and ID surface for slot Location B. Using these stress variations, the weight function derived SIFs for crack depths up to

Table 3-3: Comparison of fatigue lives computed using the SwRI program FFL based on the WF approach with results reported by NASA-LaRC. The NASA-LaRC results were based on the total SIF for combined Modes I, II and III. The SwRI WFs are applicable only to Mode I. The crack length defining failure was 0.3" in NASA-LaRC calculations, corresponding to the limit of the SIF solutions used in NASGRO.

Initial Crack Size	Upstream Liner		Downstream Liner	
	Final Crack Lengths and Missions		Final Crack Lengths and Missions	
	SwRI (Mode I only)	NASA-LaRC (Modes I, II and III)	SwRI (Mode I only)	NASA-LaRC (Modes I, II and III)
	NESC-1		NESC-1	
0.02"	0.33"	0.3"	0.33"	0.3"
	10	39	2	1
0.075"	0.32"	0.3"	0.35"	0.3"
	6	21	2	0.2
	NESC-2		NESC-2	
0.02"	0.35"	0.3"	0.30"	0.3"
	6	21	42	27
0.075"	0.35"	0.3"	0.30"	0.3"
	4	11	24	10
	NESC-3		NESC-3	
0.02"	0.30"	0.3"	0.31"	0.3"
	15	72	16	10
0.075"	0.31"	0.3"	0.31"	0.3"
	9	35	10	4

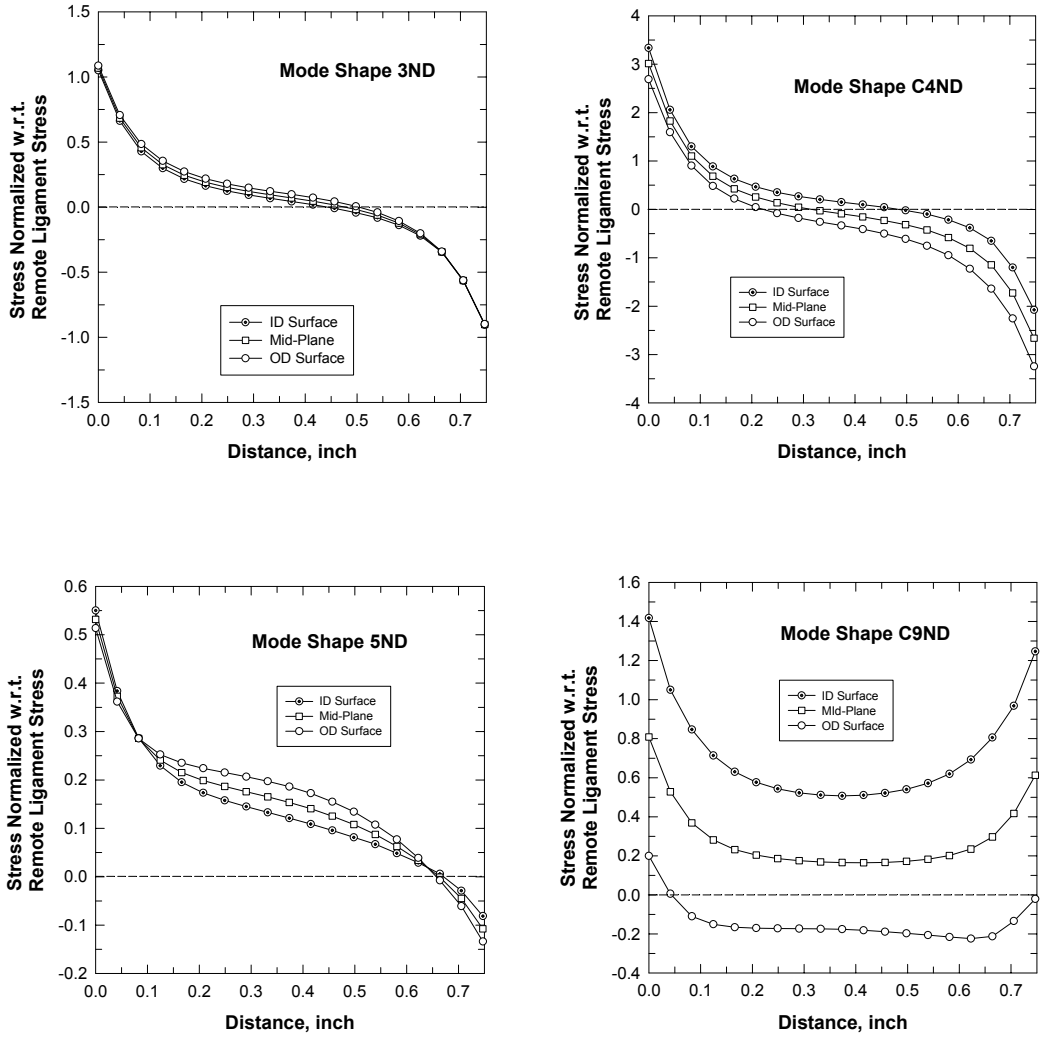

Figure 3-1: Variations of stress component normal to anticipated crack plane at circumferential crack Location B based on dynamic structural analysis for mode shapes 3ND, C4ND, 5ND and C9ND.

0.6" were generated and are plotted in Figure 3-2 for mode shapes 3ND, C4ND, 5ND and C9ND. For consistency with James et al (2004), the SIF values presented in these figures were scaled with respect to a unit value of the far field mid-ligament stress. Thus, actual SIF values are obtained by multiplying the values shown in the figures by the far-field mid-ligament stress in units of ksi.

Also in Figure 3-2 is shown the FEM SIF results for the Mode I crack component generated by NASA-LaRC using thin shell finite elements. The comparison of these results with those produced using the WF approach indicates that for small cracks (crack lengths less than 0.1") the WF derived SIFs based on the mid-plane stress are in reasonable good agreement with those generated by NASA-LaRC. However, once the crack grows deeper the two sets of results

begin to diverge but with the results for some dynamic modes distinctively remaining in better agreement than those for other modes. For example, the agreement is especially good for the C9ND mode shape, but not particularly good for the 3ND mode shape. The reason for these differences is presently not known. However, the SIFs calculated by the WF method appear in some cases to behave in a more consistent manner than those calculated using thin shell finite elements. For example, the spatial distributions of the dynamic stresses for the 3ND and C4ND modes are similar, with the magnitude of the C4ND mode being about three times greater than the 3ND mode. This is reflected in the SIFs calculated using the WF approach, with the variation of the SIFs with crack length being similar for the 3ND and C4ND modes. In contrast, the behaviors of the SIFs calculated using the thin shell method is significantly different between the 3ND and C4ND modes, as can be seen from the results in Figure 3-2. Indeed, not only do the SIFs evaluated using the WF and thin shell approaches show similar variations with crack length for the C4ND mode, but the magnitudes of the SIFs are also similar, especially for the case when the mid-wall stress is used in the WF calculations.

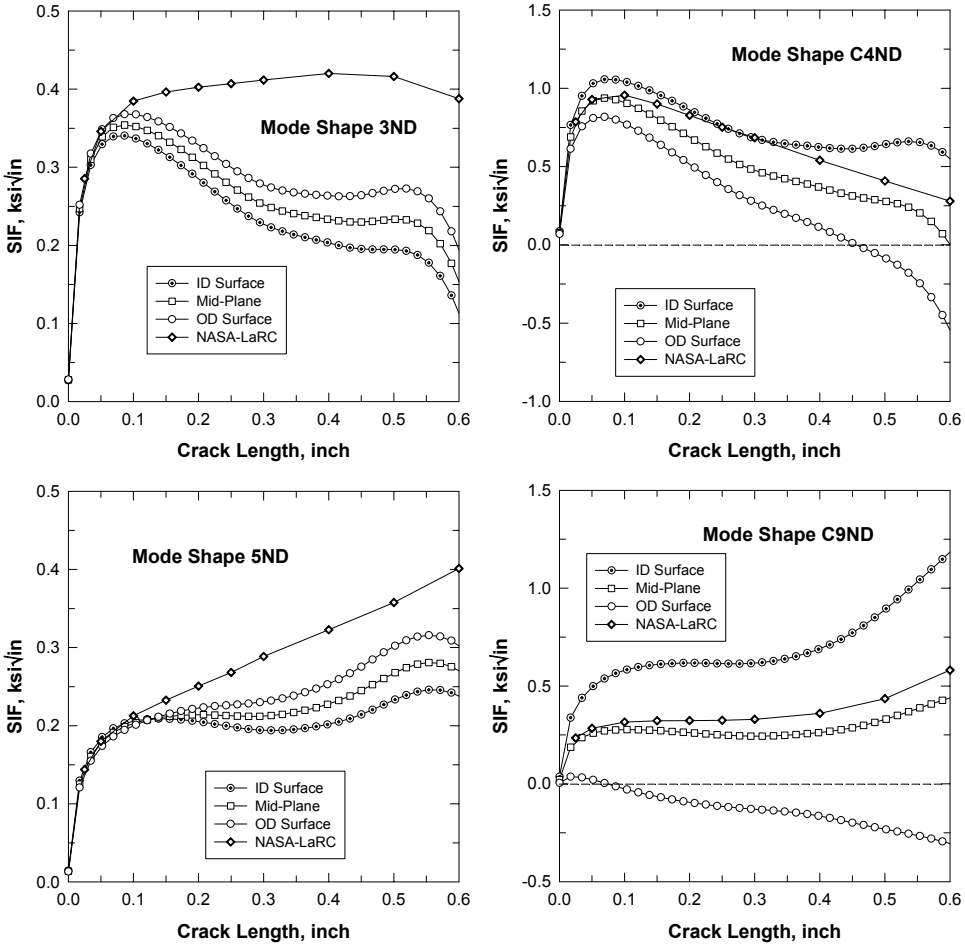

Figure 3-2: Comparison of SIFs from SwRI's weight functions and NASA-LaRC's FEM analysis for the dynamic stresses from the 3ND, C4ND, 5ND and C9ND mode shapes depicted in Figure 3-1.

In summary, the WF derived *K* solutions tend to be smaller than those generated by NASA-LaRC for the dominant vibration modes inherent in downstream flowliner: 3ND, C4ND, and 5ND. However, for the dominant mode in upstream flowliner, C9ND, the WF based *K* solutions are larger than those by NASA-LaRC FEA analysis. These differences will be reflected in the calculated fatigue lives based on the two approaches, and will add to the differences that also arise from the fact that NASA-LaRC considered the effects of Modes I, II and III loading, while SwRI consider only the influence of Mode I loading.

Similar differences between fatigue lives calculated using the NASA-LaRC approach and the WF method for NESC-1, NESC-2 and NESC-3 spectra are also observed in flowliner cracks at Location B due to the certification spectra. Typical results for a downstream liner are given in Table 3-4.

Table 3-4: Comparison of SwRI predicted fatigue lives based on the WF method with those determined by NASA-LaRC for downstream flowliners subjected to the certification spectra. Failure is defined when the crack length exceeds 0.3".

Spectrum	Missions	
	SwRI (Mode I only)	NASA-LaRC (Modes I, II and III)
1.8 E1 Nominal	< 2	< 1 (0.24)
1.3 E2 Nominal	< 2	< 1 (0.21)
1.34 E1 Engine Out	< 12	< 4 (3.48)
1.1b E1 Nominal -1Sig	<2	< 1 (0.26)
1.28 E1 Engine Out -1Sig	< 3	< 1 (0.55)
1.17 E3 Engine Out -1Sig	< 3	< 1 (0.54)
FCV Failed Open 1.66	< 2	< 1 (0.13)
FCV Failed Closed 1.63	< 3	< 1 (0.3)

3.2 Fatigue Lives for NESC-2 and NESC-3 Spectra

3.2.1 General

Several sets of calculations were performed to exercise the deterministic FFL code for corner cracks and through thickness cracks at Locations B on downstream liner slots. The cracks were assumed to be on the ID, either at the slot on the left or the slot on the right of a given ligament (Figure 3-3). Cracks on the OD were considered to be less life-limiting as they are subjected to a compressive stress arising from a mean stress that is assumed to be a through-wall bend stress with the tensile component on the ID, consistent with residual stress measurements.

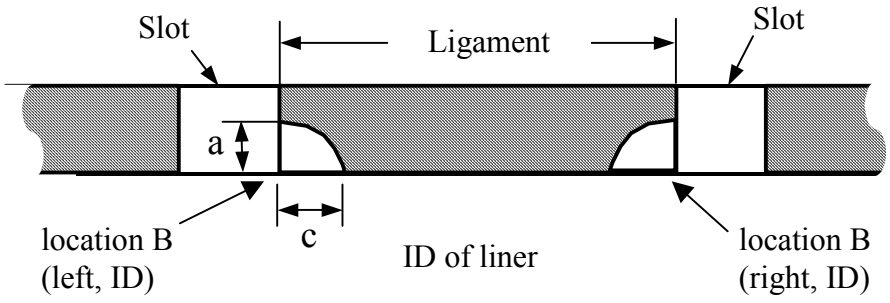

Figure 3-3: Schematic showing the locations of the cracks analyzed.

The fatigue life computations were made for load spectra NESC-2 and NESC-3, which for downstream liners are composed of two modes, C4ND and 5ND. Bivariant stress distributions were derived for each of the thirty-eight slots from the results of dynamic stress analysis based on the C4ND and 5ND modes. Figures showing the bivariant nature of the maximum (or minimum) axial stresses in a fatigue cycle are given in Section 4, where, in the figures, the origin of coordinates is at the ID and is located at the slot on the left side of a ligament. (Note that after half a cycle, the maximum stress becomes the minimum and vice versa.) The numbering of the slots is consistent with the slot number scheme adopted in the modal analysis performed by Swales [private communication]. A more complete description of how the stress distributions for each slot were determined is presented in Section 4.

A static mean stress was assumed present in all the calculations to simulate the effects of residual and system stressing. This mean stress was characterized as by a remote through-wall bend stress of magnitude 70 ksi, with the tensile stress at the ID [Warren, 2004, and Elliot, 2004]. Thus, the ID is assumed to be the preferred location of cracking. The distribution of this mean stress in the ligament is similar to that shown in Figure 2-1, with the magnitudes shown in that figure multiplied by 70.

All the calculations were made using the three-component fatigue crack growth rate model with the following values used for the constants appearing in equation (2.9):

$$C_1 = 1.61\times10^{-28} \quad n_1=22.16$$
$$C_2 = 8.59\times10^{-11} \quad n_2=3.05$$
$$K_c=150 \text{ ksi inch}^{1/2}$$

The initial crack shapes in all the computations involving corner cracks were assumed to be quarter-circular. Thereafter, the cracks changed shape in response to the bi-variant stress gradients.

3.2.2 NESC Spectrum-2: Crack Location B (Left, ID)

A number of scenarios (different sets of calculations) were investigated. In the first scenario, the initial crack size was taken as a corner crack with *a=c=0.02* inches and the transition option in FFL was turned off. This means that the a-tip of the crack was allowed to grow through the thickness until it reached 0.975*t*, after which it was maintained at this value while the c-tip was allowed to grow through the ligament The second scenario consisted of allowing the corner crack to transition to a straight-fronted through crack when the a-tip reached a depth of 0.975*t*. The third scenario assumed that the initial cracks were straight-fronted through thickness flaws of length 0.05 inches. The crack models represented by these three scenarios are illustrated in Figure 3-4.

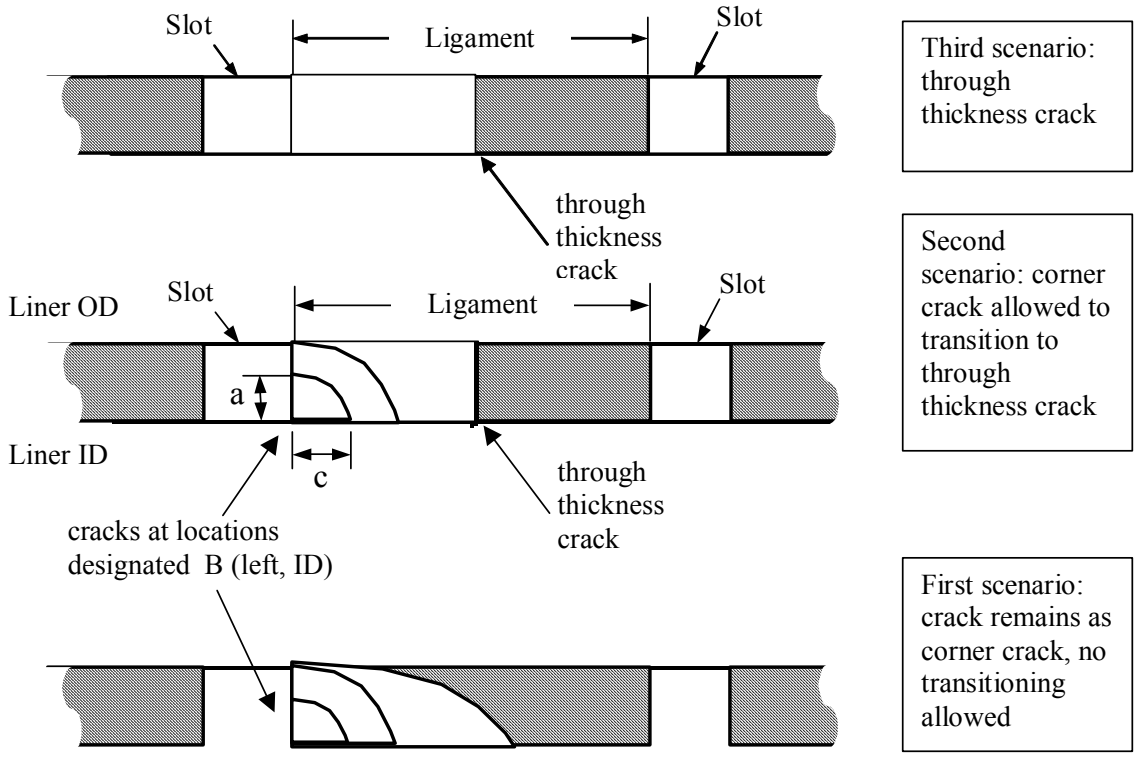

Figure 3-4: Schematic showing the locations of the cracks analyzed and how crack transitioning in crack shape is modeled.

The first scenario modeling approximately simulates the behavior of the observed MPTA crack. This crack penetrated the liner wall but did not become a straight-fronted through crack, maintaining a shape similar to that of a corner crack with a fixed depth equal to the liner thickness (see Figure 3-5).

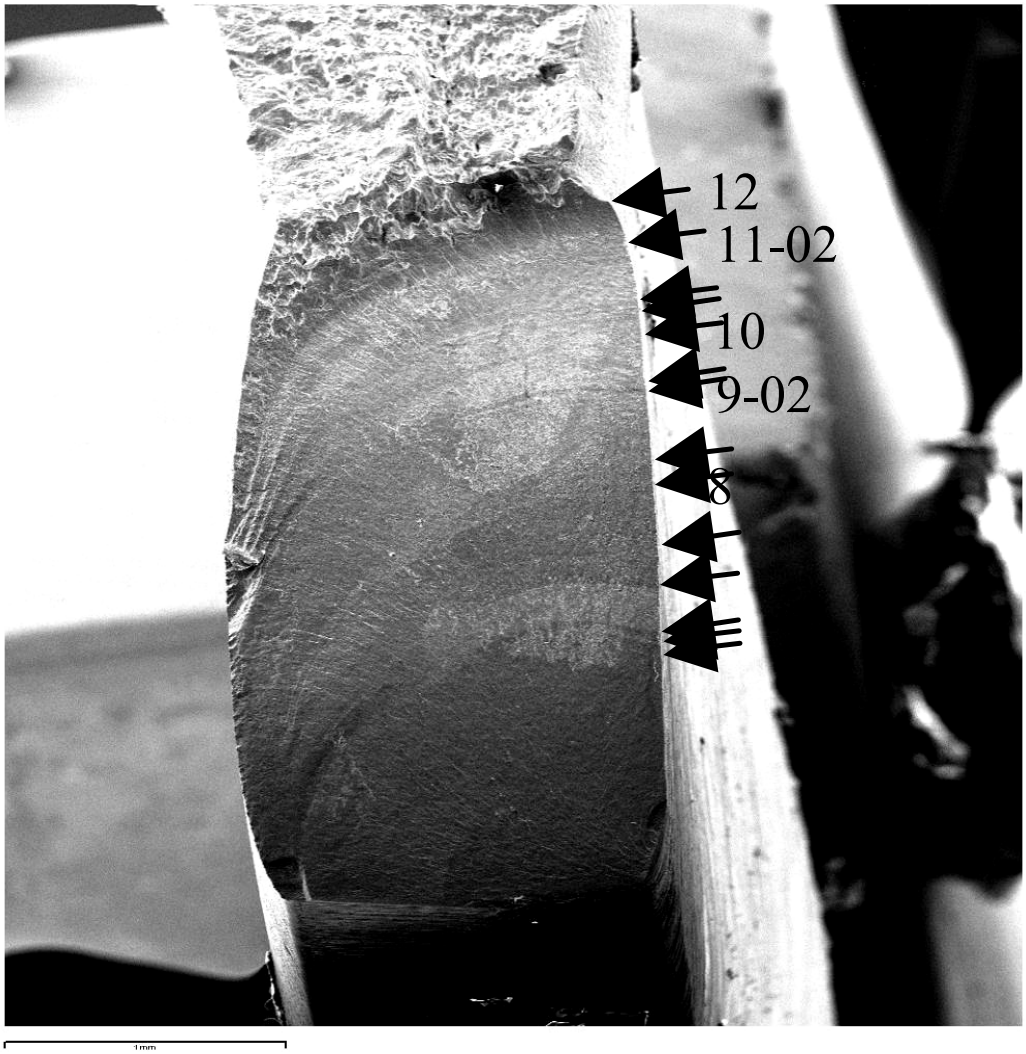

Figure 3-5: Observed cracking behavior in the MPTA. Note that the crack shape remains approximately quarter circular until it penetrates the liner wall, after which it continues to grow at the c-tip while the a-tip lags behind, resulting in a curved crack front and a crack shape that more resembles a corner crack than a through wall crack with a straight front.

Failure was not predicted at any of the slots for the first scenario, even after 1000 missions (taken as runout, when the fatigue life computations were terminated). The results for each slot are presented in Table 3-5. Cracks at some of the slots were predicted not to grow perceptibly, even though no cyclic threshold is specified in the three-component crack growth model. A few cracks grew but did not penetrate the liner wall at runout. The slots with the most severe cyclic stressing resulted in cracks growing and breaking through the thickness, but not many had succeeded in growing more than 0.4 inches through the ligament at runout. Pairs of slots appear to have been subjected to similar cyclic stressing (probably due to the symmetric nature of the vibration modes set up in the liner) and produced almost identical crack sizes at runout. For example, slots 9 and 28 appear to be "paired", as do slots 16 and 35, and so on for the rest of the slots. (In general, if n is less than or equal to 19, then slot n is paired with slot n+19 located 180º away, a distance of half of the circumference of the liner.) Based on the

predicted final crack lengths at runout scenario one, the most onerous 16 slots ranked according to severity are 9 (and 28), 5 (and 24), 13 (and 32), 17 (and 36), 2 (and 21), 1 (and 20), 6 (and 25), and 10 (and 29).

The results of the second scenario calculations are also shown in Table 3-5. The eight most severe slots identified from the first scenario are now predicted to cause failure within 1000 missions, a direct consequence of allowing transitioning from corner to through crack. The lowest lifetime of 30 missions is predicted for cracks at slots 13 (and 32). However, slots 17 (and 36) and 9 (and 28) are predicted to have lifetimes of 32 and 38 missions, respectively, comparable to the 30 missions calculated for slots 13 and 36.

The calculated evolution in crack shapes for second scenario cracks is shown in Figure 3-6 for the eight severest slots. The results in Figure 3-6 (a) illustrate that when the initiating crack is quarter circular in shape, it will tend to maintain this shape. This is because the differences in the ID and OD values of the cyclic dynamic stresses in these eight slots are small and hence there is only a small through-wall bend component at any point in the ligament. These results are consistent with the stress distributions for these slots (see Section 4.3.5) and the aspect ratio results in Figure 2-4.

The prediction that quarter-circular cracks approximately maintain their shape during through thickness crack growth is a very important result as it agrees with the observed cracking behavior in the MPTA crack evolution shown in Figure 3-5. This agreement supports the form of the dynamic stress distributions used in this fatigue analysis, as these distributions mainly govern crack shape development. The agreement also validates the fracture mechanics modeling used in the FFL program and confirms that this modeling captures the salient features of flowliner slot cracking.

The results in Figure 3-6(b) show that the relative rates of through-ligament crack propagation between the slots can vary with missions. For example, the crack length for slot 10 is predicted to be longer than that in slot 5 after 30 missions (around 2000 load steps) but is shorter than it after 80 missions (around 5000 load steps). Consequently, the crack at slot 10 is calculated to have a lifetime of 392 missions while the life for slot 5 is 64 missions. This outcome could not have been predicted based on crack size observations made after only a few missions.

Table 3-5: Predicted missions to failure or runout (1000 missions) for corner cracks of initial size 0.02 inches and through-thickness cracks of initial size 0.05 inches at Location B (left, ID) in a downstream liner subjected to NESC-2 Spectrum. Two corner crack cases: no crack transition allowed and crack transition to through thickness crack allowed when $a>0.975t$. The results for slot n+19 are the same as those for slot n, as these slots are paired.

Slot No.	Crack Scenario 1 Initial Corner Crack (No transition allowed)			Crack Scenario 2 Initial Corner Crack (Transition allowed)			Crack Scenario 3 Initial Through Crack	
	Missions to failure or runout	Final crack depth (inches)	Final crack length (inches)	Missions to failure or runout	Final crack depth (inches)	Final crack length (inches)	Missions to failure or runout	Final crack length (inches)
1	runout	breakthrough	0.3523	182	breakthrough	ligament failure	26	ligament failure
2	runout	breakthrough	0.3625	49	breakthrough	ligament failure	38	ligament failure
3	runout	breakthrough	0.1820	runout	breakthrough	0.1820	runout	0.2923
4	runout	0.02	0.0200	runout	0.02	0.0200	runout	0.1436
5	runout	breakthrough	0.4001	64	breakthrough	ligament failure	19	ligament failure
6	runout	breakthrough	0.3414	101	breakthrough	ligament failure	88	ligament failure
7	runout	0.04357	0.1055	runout	0.04357	0.1055	runout	0.2052
8	runout	0.02001	0.0200	runout	0.02001	0.0200	runout	0.1340
9	runout	breakthrough	0.4071	38	breakthrough	ligament failure	16	ligament failure
10	runout	breakthrough	0.3156	392	breakthrough	ligament failure	374	ligament failure
11	runout	0.02003	0.0200	runout	0.02003	0.0200	runout	0.1116
12	runout	0.02	0.0200	runout	0.02	0.0200	200	ligament failure
13	runout	breakthrough	0.3975	30	breakthrough	ligament failure	16	ligament failure
14	runout	breakthrough	0.2713	runout	breakthrough	0.6135	runout	0.6143
15	runout	0.02	0.0200	runout	0.02	0.0200	runout	0.0500
16	runout	0.02435	0.0217	runout	0.02435	0.0217	49	ligament failure
17	runout	breakthrough	0.3817	32	breakthrough	ligament failure	20	ligament failure
18	runout	breakthrough	0.2300	runout	breakthrough	0.4222	runout	0.4267
19	runout	0.02	0.0200	runout	0.02	0.0200	runout	0.0537

The foregoing behavior is a direct result of the variation in the dynamic cyclic stresses through the ligament. In slot 10, the ranges in these cyclic stresses decrease sharply from relatively high values to zero before increasing again as the crack propagates through the ligament, while for slot 5, although the cyclic stresses are lower at the slot surface than those for slot 10, they always remain non-zero as shown in Figure 3-7.

The results for the third scenario are also presented in Table 3-5. Based on the predicted number of missions to failure, the severest 16 slots are 9 (and 28), 13 (and 32), 5 (and 24), 17 (and 36), 1 (and 20), 2 (and 21), 16 (and 35), and 6 (and 25). The severity for the third scenario is similar to that for the second scenario, although in several instances the order is reversed for the slots of similar severity.

Table 3-6 summarizes the slot severity rankings for each of the three scenarios analyzed here. An interesting conclusion to be drawn from the results presented in this table is that the severity of a slot with regard to cracking is dependent on the fracture mechanics/crack modeling used to represent crack growth and transitioning behavior. This is a consequence of the constraints imposed on crack shape in the various scenarios, as well as the significant differences in dynamic stress gradients at the flowliner slots.

Table 3-6: Slot severity rankings for the three scenarios analyzed.

Severity ranking	**Slot No. First Scenario (corner crack, no transition)**	**Slot No. Second Scenario (corner crack, transition)**	**Slot No. Third Scenario (through crack)**
1	9 (and 28)	13 (and 32)	9 (and 28)
2	5 (and 24)	17 (and 36)	13 (and 32)
3	13 (and 32)	9 (and 28)	5 (and 24)
4	17 (and 36)	2 (and 21)	17 (and 36)
5	2 (and 21)	5 (and 24)	1 (and 20)
6	1 (and 20)	6 (and 25)	2 (and 21)
7	6 (and 25)	1 (and 20)	16 (and 35)
8	10 (and 29)	10 (and 29)	6 (and 25)

3.2.3 NESC Spectrum-3: Crack Location B (Left, ID)

A set of calculations was performed similar to those described in sub-section 3.2.2 using the NESC-3 spectrum instead of the NESC-2 spectrum. The results for the equivalent three scenarios are presented in Table 3-7 and demonstrate that the NESC-3 spectrum is more severe than the NESC-2 spectrum. In all other respects, the trends in results from the NESC-3 spectrum are the same as those from the NESC-2 spectrum (Table 3-5).

Table 3-7: Predicted missions to failure or runout (1000 missions) for corner cracks of initial size 0.02 inches and through-thickness cracks of initial size 0.05 inches at Location B (left, ID) in a downstream liner subjected to NESC-3 Spectrum. Two corner crack cases: no crack transition allowed and crack transition to through-thickness crack allowed when $a>0.975t$. The results for slot n+19 are the same as those for slot n, as these slots are paired.

	Crack Scenario 1			Crack Scenario 2			Crack Scenario 3	
	Initial Corner Crack (No transition allowed)			Initial Corner Crack (Transition allowed)			Initial Through Crack	
Slot No.	Missions to failure or runout	Final crack depth (inches)	Final crack length (inches)	Missions to failure or runout	Final crack depth (inches)	Final crack length (inches)	Missions to failure or runout	Final crack length (inches)
1	runout	breakthrough	0.6668	39	breakthrough	ligament failure	12	ligament failure
2	runout	breakthrough	0.4156	18	breakthrough	ligament failure	15	ligament failure
3	runout	breakthrough	0.2241	runout	breakthrough	0.3544	runout	0.3564
4	runout	0.02017	0.0204	runout	0.02017	0.0204	592	ligament failure
5	runout	breakthrough	0.6002	19	breakthrough	ligament failure	9	ligament failure
6	runout	breakthrough	0.3859	35	breakthrough	ligament failure	31	ligament failure
7	runout	breakthrough	0.1652	runout	breakthrough	0.1652	runout	0.2454
8	runout	0.02044	0.0204	runout	0.02044	0.0204	208	ligament failure
9	runout	breakthrough	0.5377	13	breakthrough	ligament failure	8	ligament failure
10	runout	breakthrough	0.3580	97	breakthrough	ligament failure	93	ligament failure
11	runout	0.0226	0.0214	runout	0.0226	0.0214	runout	0.1542
12	runout	0.02028	0.0200	runout	0.02028	0.0200	51	ligament failure
13	runout	breakthrough	0.4883	12	breakthrough	ligament failure	8	ligament failure
14	runout	breakthrough	0.3288	runout	breakthrough	0.6688	runout	0.6690
15	runout	0.02	0.0200	runout	0.02	0.0200	runout	0.0522
16	runout	breakthrough	0.5923	159	breakthrough	ligament failure	19	ligament failure
17	runout	breakthrough	0.4494	13	breakthrough	ligament failure	9	ligament failure
18	runout	breakthrough	0.2755	runout	breakthrough	0.5487	runout	0.5494
19	runout	0.02	0.0200	runout	0.02	0.0200	runout	0.1075

3.2.4 NESC Spectrum-2: Crack Location B (Right, ID)

Fatigue life computations were performed for assumed corner cracks at the ID position of slots on the right sides of ligaments in order to compare the severity of cracking at these locations with the severity of cracking at the left sides. Corner cracks were considered that were allowed to transition to through thickness cracks. The results for this scenario are displayed in Table 3-8. By comparing these results with those presented in Table 3-5, it can be seen that for the NESC-2 spectrum, cracks that develop at Locations B (left, ID) are more life limiting than the equivalent cracks that develop at Locations B (right, ID).

Table3-8: Predicted missions to failure or runout (1000 missions) for corner cracks of initial size 0.02 inches at Location B (right, ID) in a downstream liner subjected to NESC-2 Spectrum. Corner crack transition to through thickness crack allowed when $a>0.975t$. The results for slot n+19 are the same as those for slot n, as these slots are paired.

Slot No.	Missions to failure or runout	Final crack depth (inches)	Final crack length (inches)
1	runout	0.02041	0.0201
2	runout	0.02001	0.0200
3	runout	breakthrough	0.6163
4	33	breakthrough	ligament failure
5	runout	0.02	0.0200
6	runout	0.02022	0.0201
7	runout	breakthrough	0.6525
8	44	breakthrough	ligament failure
9	runout	0.02	0.0200
10	runout	0.04587	0.1365
11	runout	breakthrough	0.6816
12	85	breakthrough	ligament failure
13	runout	0.02	0.0200
14	runout	breakthrough	0.3042
15	169	breakthrough	ligament failure
16	317	breakthrough	ligament failure
17	runout	0.02001	0.0200
18	runout	breakthrough	0.4765
19	31	breakthrough	ligament failure

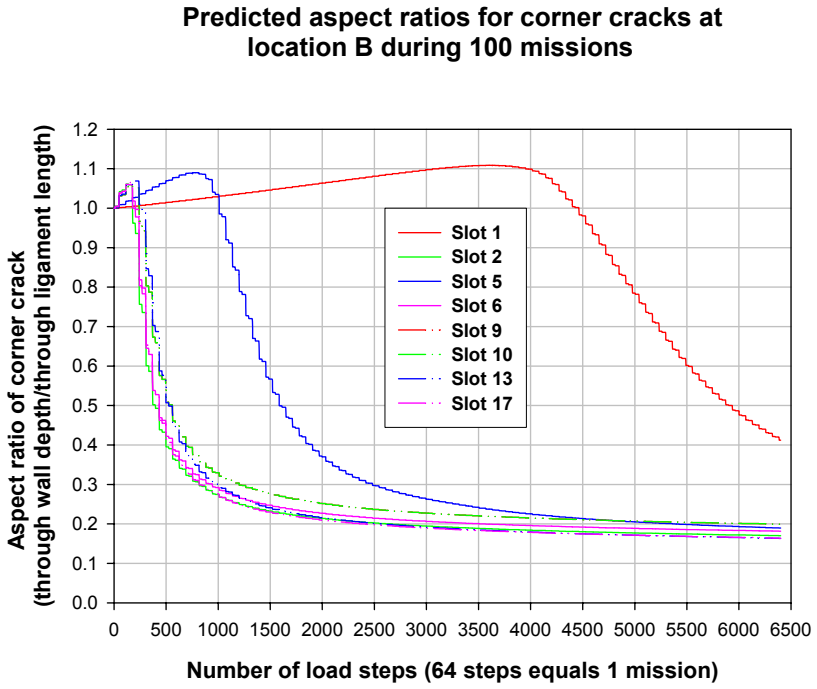

(a) Variation of corner crack aspect ratio as a function of missions.

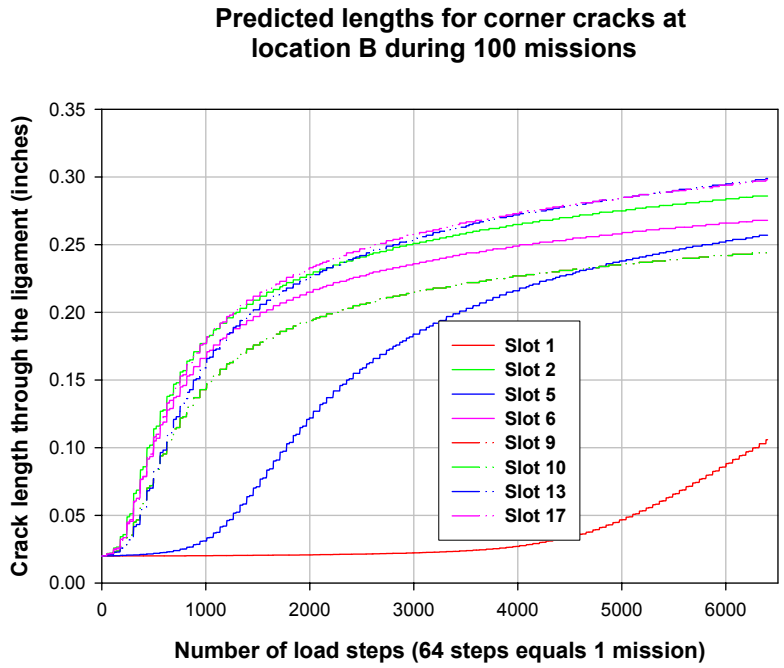

(b) Variation of through-ligament crack length as a function of missions.

Figure 3-6: Predicted crack shape development for corner cracks of initial size 0.02 inches at Location B (left, ID) in eight of the most severe slots for the NESC-2 spectrum.

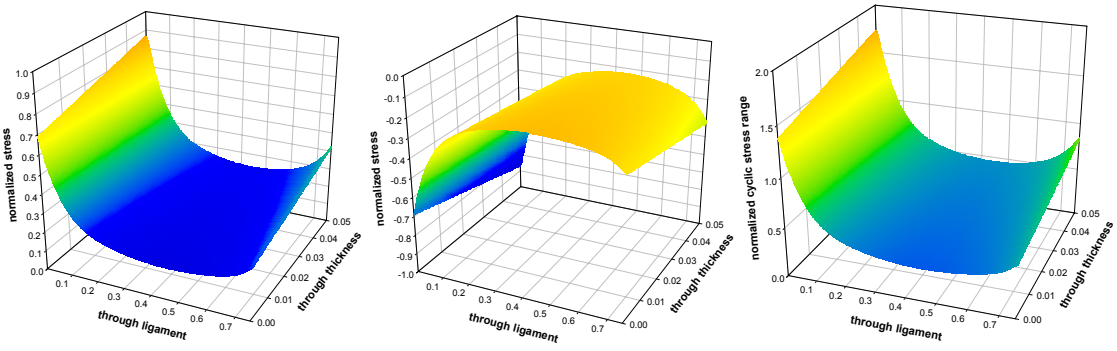

(a) Slot 5: maximum stress (b) Slot 5: minimum stress (c) Slot 5: cyclic stress range (maximum stress – minimum stress)

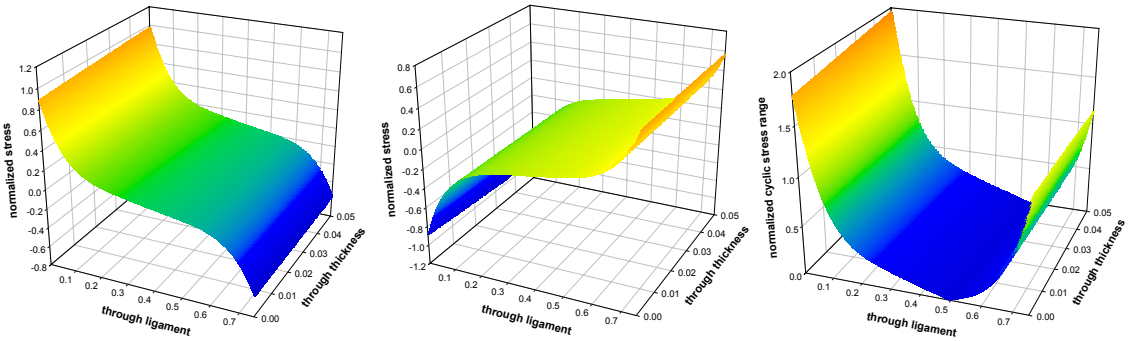

(d) Slot 10: maximum stress (e) Slot 10: minimum stress (f) Slot 10: cyclic stress range (maximum stress – minimum stress)

Figure 3-7: Cyclic stress distributions at maximum and minimum loads and cyclic stress ranges for slots 5 and 10 corresponding to the 5ND vibration mode that dominates crack growth behavior for the NESC-2 spectrum.

3.3 Fatigue Lives for Certification Spectra

Eight different load spectra have been specified by the Program Team at NASA-MSFC as the basis for certification spectra for use in assessing the fatigue lifetimes of flowliners. The eight certification spectra for the downstream liners are composed of three modes, 3ND, C4ND and 5ND and are signified as:

1) 1.8 E1 Nominal
2) 1.3 E2 Nominal
3) 1.34 E1 Engine Out
4) 1.1b E1 Nominal –1Sig
5) 1.28 E1 Engine Out –1Sig
6) 1.17 E3 Engine Out –1Sig
7) FCV Failed Open 1.66
8) FCV Failed Closed 1.63

The fatigue program FFL was used to compute the lives for initial cracks at Location B (left, ID) at each of the 38 slots based on the eight certification spectra. Three analyses were performed based on the three scenarios described in sub-section 3.2.2, even though they were analyzed in a different order. In the first analysis (second scenario of sub-section 3.2.2), an initial quarter circular corner crack of radius 0.02 inches was assumed, and this crack was allowed to transition to a straight-fronted through thickness crack when its depth, a, exceeded 97.5% of the wall thickness. In the second analysis (third scenario of sub-section 3.2.2), a initial through thickness crack of length, c, equal to 0.05 inches, was assumed. In the last analysis (the first scenario in sub-section 3.2.2), the behavior of an initial corner crack of radius 0.02 inches was investigated. The corner crack was restrained to remaining as a corner crack with a fixed depth of $0.975t$ after the a-tip was predicted to breakthrough the liner wall. The three scenarios equivalent to these three analyses are shown schematically in Figure 3-4.

In the first and second analyses, detailed life computations were made for each of the 38 slots, while the third analysis was only performed for the predicted three severest certification spectra and the six severest slots. In all the calculations, a mean stress equal to a remote through wall bending stress of 70 ksi was assumed, and the tensile component of the bending was assumed to be at the ID.

The fatigue life computations were made using bivariant stress distributions derived for each of the thirty-eight slots from the results of dynamic stress analysis based on the vibration modes (*e.g.*, 3ND, C4ND, 5ND) set up in the liners. Figures showing the bivariant nature of the maximum (or minimum) axial stresses in a fatigue cycle are given in Section 4.

All calculations were made using the three-component fatigue crack growth rate model with the same constants employed as in sub-section 3.2.2.

The results for the two analyses performed for the certification spectra are displayed in Tables 3-9 through 3-16. It is clear from these results that in some cases failure is predicted for a through thickness crack of initial length 0.05 inches after only one or two missions. Modeling the

cracking as an initial corner crack of size 0.02 inches that is allowed to transition to a through crack provides some mitigation in some cases, but failures are still predicted after only a few missions. The certification spectra designated as 1.28 E1 Engine Out –1Sig, 1.17 E3 Engine Out –1Sig, and FCV Failed Open 1.66, are the severest of the spectra with respect to fatigue life. Slots numbered 2, 5, 6, 9, 13 and 17 appear to be the worst locations for cracking.

Due to the foregoing results, an additional set of analyses was performed assuming that a corner crack remains a corner crack with transitioning to a through thickness crack prohibited. These calculations were made for the three severest certification spectra and the six severest slots. The results are shown in Table 3-17 and demonstrate all the severest slots are now predicted to be relatively innocuous, with either runout or fatigue lives of several hundred missions.

The results presented in Tables 3-9 through 3-16 display some interesting differences in predicted crack size developments between corner cracks and through cracks. For example, in Table 3-13, although the initial corner and through-thickness cracks at slot number 19 for the certified spectrum 1.28 E1 Engine Out are predicted not to fail after 1000 missions, the final crack length after runout for the through crack is smaller than that for the corner crack that is allowed to transition to a through crack. This is the case even though straight-fronted through cracks are generally considered more severe than corner cracks and the initial size of the through crack was 0.05 inches compared to 0.02 inches for the corner crack. The reason for this unexpected behavior can be traced to the fact that the dominant contribution to crack growth at slot 19 comes from the C4ND mode. The distribution of stress arising from this mode for slot 19 is illustrated in Figure 3-8. In this figure, the bivariant stress is shown for the minimum load in a cycle, the stress corresponding to the maximum load being equal to minus the minimum load stress. The important aspect of the stress distribution is the fact that it shows a significant amount of through thickness bending at the crack origin (0,0). This bend component will result in a corner crack that is initially quarter circular in shape propagating more through the ligament than through the thickness. This behavior is demonstrated in Figure 3-9 that shows the calculated variations of crack depth [Figure 3-9 (a)], crack length [Figure 3-9(b)] and aspect ratio [Figure 3-9(c)] with missions. From these figures, it is clear that a corner crack will break through the liner wall and transition into a through crack after around 40 missions (8000 load steps). When this occurs, the crack length through the ligament is approximately 0.25 inches, well in excess of the crack length at runout predicted for a through crack (0.0508 inches). Figure 3-9(c) illustrates how the aspect ratio of the initial quarter circular crack drops rapidly with missions, similar to the behavior predicted for through wall cyclic bending (see Figure 2-4).

Although the lowest deterministically computed lives occur for the 1.17_E3_engine_out spectrum (Table 3-14) this failure is conditional upon one of the engines being out. Since the probability of an engine being out is about 1/800, the unconditional probability of failure is similar to that for a reduced NESC-2 spectrum as shown in shown in Section 5.8. A similar reduction in the probability of failure also occurs for the other engine out spectra. Consequently, the 1.3 E2 Nominal + 3 s trajectory spectrum is actually the most severe certification spectrum (See Section 5.8).

Table 3-9: Predicted missions to failure or runout (1000 missions) for corner cracks of initial size 0.02 inches and through thickness cracks of initial size 0.05 inches at Location B (left, ID) in a downstream liner subjected to Certification Spectrum **1.8_E1_nominal**. Corner crack transition to through thickness crack allowed when $a>0.975t$. The results for slot numbers n greater than 19 are equal to those for slot number n-19.

Slot No.	Initial Corner Crack			Initial Through Crack	
	Missions to failure or runout	Final crack depth (inches)	Final crack length (inches)	Missions to failure or runout	Final crack length (inches)
1	runout	0.02	0.0200	374	ligament failure
2	812	breakthrough	ligament failure	805	ligament failure
3	runout	breakthrough	0.6110	runout	0.6110
4	10	breakthrough	ligament failure	9	ligament failure
5	29	breakthrough	ligament failure	4	ligament failure
6	runout	0.02	0.0200	runout	0.0805
7	runout	breakthrough	0.3497	runout	0.3497
8	782	breakthrough	ligament failure	781	ligament failure
9	runout	breakthrough	0.3229	runout	0.3227
10	runout	breakthrough	0.3786	runout	0.1701
11	runout	0.02039	0.0200	runout	0.5944
12	runout	breakthrough	0.6030	runout	0.6030
13	98	breakthrough	Ligament failure	97	ligament failure
14	6	breakthrough	ligament failure	3	ligament failure
15	runout	0.02014	0.0398	12	ligament failure
16	runout	breakthrough	0.2278	runout	0.2294
17	runout	breakthrough	0.5747	runout	0.5747
18	runout	breakthrough	0.5700	runout	0.5700
19	runout	breakthrough	0.2498	runout	0.0590

Table 3-10: Predicted missions to failure or runout (1000 missions) for corner cracks of initial size 0.02 inches and through thickness cracks of initial size 0.05 inches at Location B (left, ID) in a downstream liner subjected to Certification Spectrum **1.3_E2_nominal**. Corner crack transition to through thickness crack allowed when $a>0.975t$. The results for slot numbers n greater than 19 are equal to those for slot number n-19.

Slot No.	Initial Corner Crack			Initial Through Crack	
	Missions to failure or runout	Final crack depth (inches)	Final crack length (inches)	Missions to failure or runout	Final crack length (inches)
1	runout	0.02	0.0200	295	ligament failure
2	42	breakthrough	ligament failure	38	ligament failure
3	175	breakthrough	ligament failure	175	ligament failure
4	9	breakthrough	ligament failure	8	ligament failure
5	18	breakthrough	ligament failure	3	ligament failure
6	runout	0.02008	0.0200	486	ligament failure
7	runout	breakthrough	0.3554	runout	0.3554
8	796	breakthrough	ligament failure	795	ligament failure
9	runout	breakthrough	0.3367	runout	0.3366
10	runout	breakthrough	0.3274	runout	0.3113
11	runout	breakthrough	0.5940	runout	0.5963
12	runout	breakthrough	0.6037	runout	0.6037
13	11	breakthrough	ligament failure	11	ligament failure
14	4	breakthrough	ligament failure	2	ligament failure
15	runout	0.02125	0.0481	8	ligament failure
16	525	breakthrough	ligament failure	490	ligament failure
17	runout	breakthrough	0.5767	runout	0.5767
18	runout	breakthrough	0.5711	runout	0.5711
19	runout	breakthrough	0.2513	runout	0.1546

Table 3-11: Predicted missions to failure or runout (1000 missions) for corner cracks of initial size 0.02 inches and through thickness cracks of initial size 0.05 inches at Location B (left, ID) in a downstream liner subjected to Certification Spectrum **1.34_E1_engine_out**. Corner crack transition to through thickness crack allowed when $a>0.975t$. The results for slot numbers n greater than 19 are equal to those for slot number n-19.

Slot No.	Initial Corner Crack			Initial Through Crack	
	Missions to failure or runout	Final crack depth (inches)	Final crack length (inches)	Missions to failure or runout	Final crack length (inches)
1	runout	0.02	0.0200	983	ligament failure
2	runout	breakthrough	0.5938	runout	0.5935
3	runout	breakthrough	0.6045	runout	0.6046
4	34	breakthrough	ligament failure	27	ligament failure
5	239	breakthrough	ligament failure	29	ligament failure
6	runout	0.02	0.0200	runout	0.0500
7	runout	breakthrough	0.3191	runout	0.3194
8	655	breakthrough	ligament failure	652	ligament failure
9	runout	breakthrough	0.2913	runout	0.2904
10	runout	0.0472	0.3181	runout	0.0500
11	runout	0.02004	0.0200	runout	0.5868
12	runout	breakthrough	0.6139	runout	0.6153
13	runout	breakthrough	0.6455	runout	0.6455
14	45	breakthrough	ligament failure	26	ligament failure
15	runout	0.02	0.0242	98	ligament failure
16	runout	breakthrough	0.1331	runout	0.1353
17	runout	breakthrough	0.5716	runout	0.5716
18	runout	breakthrough	0.5349	runout	0.5349
19	runout	breakthrough	0.2477	runout	0.0511

Table 3-12: Predicted missions to failure or runout (1000 missions) for corner cracks of initial size 0.02 inches and through thickness cracks of initial size 0.05 inches at Location B (left, ID) in a downstream liner subjected to Certification Spectrum **1.1b_E1_nominal**. Corner crack transition to through thickness crack allowed when $a>0.975t$. The results for slot numbers n greater than 19 are equal to those for slot number n-19.

Slot No.	Initial Corner Crack			Initial Through Crack	
	Missions to failure or runout	Final crack depth (inches)	Final crack length (inches)	Missions to failure or runout	Final crack length (inches)
1	runout	0.02	0.0200	runout	0.5704
2	runout	breakthrough	0.5977	runout	0.5978
3	runout	breakthrough	0.6066	runout	0.6061
4	runout	breakthrough	0.6815	runout	0.6815
5	48	breakthrough	ligament failure	5	ligament failure
6	runout	0.02	0.0200	runout	0.0500
7	runout	breakthrough	0.3449	runout	0.3449
8	runout	breakthrough	0.5849	runout	0.5849
9	runout	breakthrough	0.3166	runout	0.3165
10	runout	breakthrough	0.4237	runout	0.0500
11	runout	0.02022	0.0200	runout	0.5931
12	runout	breakthrough	0.5958	runout	0.5958
13	runout	breakthrough	0.6455	runout	0.6455
14	8	breakthrough	ligament failure	5	ligament failure
15	runout	0.02002	0.0350	18	ligament failure
16	runout	breakthrough	0.1425	runout	0.1447
17	runout	breakthrough	0.5723	runout	0.5723
18	runout	breakthrough	0.5658	runout	0.5658
19	runout	breakthrough	0.2508	runout	0.0553

Table 3-13: Predicted missions to failure or runout (1000 missions) for corner cracks of initial size 0.02 inches and through thickness cracks of initial size 0.05 inches at Location B (left, ID) in a downstream liner subjected to Certification Spectrum **1.28_E1_engine_out**. Corner crack transition to through thickness crack allowed when $a>0.975t$. The results for slot numbers n greater than 19 are equal to those for slot number n-19.

Slot No.	Initial Corner Crack			Initial Through Crack	
	Missions to failure or runout	Final crack depth (inches)	Final crack length (inches)	Missions to failure or runout	Final crack length (inches)
1	6	breakthrough	ligament failure	2	ligament failure
2	2	breakthrough	ligament failure	2	ligament failure
3	runout	breakthrough	0.6038	runout	0.6038
4	11	breakthrough	ligament failure	7	ligament failure
5	4	breakthrough	ligament failure	2	ligament failure
6	3	breakthrough	ligament failure	3	ligament failure
7	runout	breakthrough	0.3170	runout	0.3171
8	8	breakthrough	ligament failure	5	ligament failure
9	2	breakthrough	ligament failure	1	ligament failure
10	runout	breakthrough	0.6545	runout	0.6545
11	runout	0.02014	0.0200	135	ligament failure
12	12	breakthrough	ligament failure	5	ligament failure
13	3	breakthrough	ligament failure	2	ligament failure
14	7	breakthrough	ligament failure	6	ligament failure
15	runout	0.02	0.0230	63	ligament failure
16	44	breakthrough	ligament failure	2	ligament failure
17	2	breakthrough	ligament failure	2	ligament failure
18	runout	breakthrough	0.5497	runout	0.5498
19	runout	breakthrough	0.2521	runout	0.0508

Table 3-14: Predicted missions to failure or runout (1000 missions) for corner cracks of initial size 0.02 inches and through thickness cracks of initial size 0.05 inches at Location B (left, ID) in a downstream liner subjected to Certification Spectrum **1.17_E3_engine_out**. Corner crack transition to through thickness crack allowed when $a>0.975t$. The results for slot numbers n greater than 19 are equal to those for slot number n-19.

Slot No.	Initial Corner Crack			Initial Through Crack	
	Missions to failure or runout	Final crack depth (inches)	Final crack length (inches)	Missions to failure or runout	Final crack length (inches)
1	5	breakthrough	ligament failure	2	ligament failure
2	2	breakthrough	ligament failure	2	ligament failure
3	runout	breakthrough	0.6008	runout	0.6009
4	40	breakthrough	ligament failure	22	ligament failure
5	3	breakthrough	ligament failure	2	ligament failure
6	3	breakthrough	ligament failure	3	ligament failure
7	runout	breakthrough	0.3050	runout	0.3054
8	20	breakthrough	ligament failure	6	ligament failure
9	2	breakthrough	ligament failure	1	ligament failure
10	runout	breakthrough	0.6547	runout	0.6547
11	runout	0.02000	0.0214	393	ligament failure
12	31	breakthrough	ligament failure	6	ligament failure
13	2	breakthrough	ligament failure	2	ligament failure
14	14	breakthrough	ligament failure	13	ligament failure
15	runout	0.02000	0.0214	231	ligament failure
16	64	breakthrough	ligament failure	2	ligament failure
17	1	breakthrough	ligament failure	1	ligament failure
18	runout	breakthrough	0.5451	runout	0.5451
19	runout	breakthrough	0.2484	runout	0.0504

Table 3-15: Predicted missions to failure or runout (1000 missions) for corner cracks of initial size 0.02 inches and through thickness cracks of initial size 0.05 inches at Location B (left, ID) in a downstream liner subjected to Certification Spectrum **FCV_failed_open**. Corner crack transition to through thickness crack allowed when $a>0.975t$. The results for slot numbers n greater than 19 are equal to those for slot number n-19.

Slot No.	Initial Corner Crack			Initial Through Crack	
	Missions to failure or runout	Final crack depth (inches)	Final crack length (inches)	Missions to failure or runout	Final crack length (inches)
1	10	breakthrough	ligament failure	2	ligament failure
2	3	breakthrough	ligament failure	2	ligament failure
3	24	breakthrough	ligament failure	23	ligament failure
4	5	breakthrough	ligament failure	3	ligament failure
5	4	breakthrough	ligament failure	2	ligament failure
6	4	breakthrough	ligament failure	4	ligament failure
7	runout	breakthrough	0.3386	runout	0.3387
8	5	breakthrough	ligament failure	4	ligament failure
9	3	breakthrough	ligament failure	2	ligament failure
10	runout	breakthrough	0.6555	runout	0.6555
11	193	breakthrough	ligament failure	43	ligament failure
12	7	breakthrough	ligament failure	4	ligament failure
13	3	breakthrough	ligament failure	2	ligament failure
14	5	breakthrough	ligament failure	3	ligament failure
15	runout	0.02	0.0302	20	ligament failure
16	24	breakthrough	ligament failure	3	ligament failure
17	3	breakthrough	ligament failure	2	ligament failure
18	runout	breakthrough	0.5629	runout	0.5629
19	runout	breakthrough	0.2546	runout	0.2246

Table 3-16: Predicted missions to failure or runout (1000 missions) for corner cracks of initial size 0.02 inches and through thickness cracks of initial size 0.05 inches at Location B (left, ID) in a downstream liner subjected to Certification Spectrum **FCV_failed_closed**. Corner crack transition to through thickness crack allowed when $a>0.975t$. The results for slot numbers n greater than 19 are equal to those for slot number n-19.

Slot No.	Initial Corner Crack			Initial Through Crack	
	Missions to failure or runout	Final crack depth (inches)	Final crack length (inches)	Missions to failure or runout	Final crack length (inches)
1	runout	0.02	0.0200	382	ligament failure
2	45	breakthrough	ligament failure	18	ligament failure
3	15	breakthrough	ligament failure	14	ligament failure
4	14	breakthrough	ligament failure	12	ligament failure
5	11	breakthrough	ligament failure	6	ligament failure
6	234	breakthrough	ligament failure	84	ligament failure
7	runout	breakthrough	0.3191	runout	0.3191
8	115	breakthrough	ligament failure	113	ligament failure
9	275	breakthrough	ligament failure	283	ligament failure
10	runout	breakthrough	0.6241	runout	0.6241
11	runout	breakthrough	0.5897	runout	0.5897
12	runout	breakthrough	0.5946	runout	0.5947
13	10	breakthrough	ligament failure	9	ligament failure
14	11	breakthrough	ligament failure	5	ligament failure
15	runout	0.02002	0.0232	17	ligament failure
16	41	breakthrough	ligament failure	20	ligament failure
17	runout	breakthrough	0.6177	runout	0.6177
18	runout	breakthrough	0.5517	runout	0.5517
19	runout	breakthrough	0.3160	runout	0.3155

Table 3-17: Predicted missions to failure or runout (1000 missions) and final crack lengths for corner cracks of initial size 0.02 inches at Location B (left, ID) in a downstream liner three Certification Spectra. Corner crack transition to through thickness crack not allowed. In all cases, the crack a-tip grew to 0.975*t* and was prohibited from further growth.

Slot No.	Load Spectrum					
	1.17_E3_Engine_Out		1.28_E1_Engine_Out		FCV_Failed_Open	
	Missions to failure or runout	Final crack length (inches)	Missions to failure or runout	Final crack length (inches)	Missions to failure or runout	Final crack length (inches)
2	runout	0.4010	runout	0.3991	runout	0.4082
5	runout	0.6472	runout	0.6947	373	Ligament failure
6	runout	0.3729	runout	0.3714	runout	0.3788
9	runout	0.5238	runout	0.5198	runout	0.5475
13	runout	0.4706	runout	0.4671	runout	0.4843
17	runout	0.4330	runout	0.4305	runout	0.4426

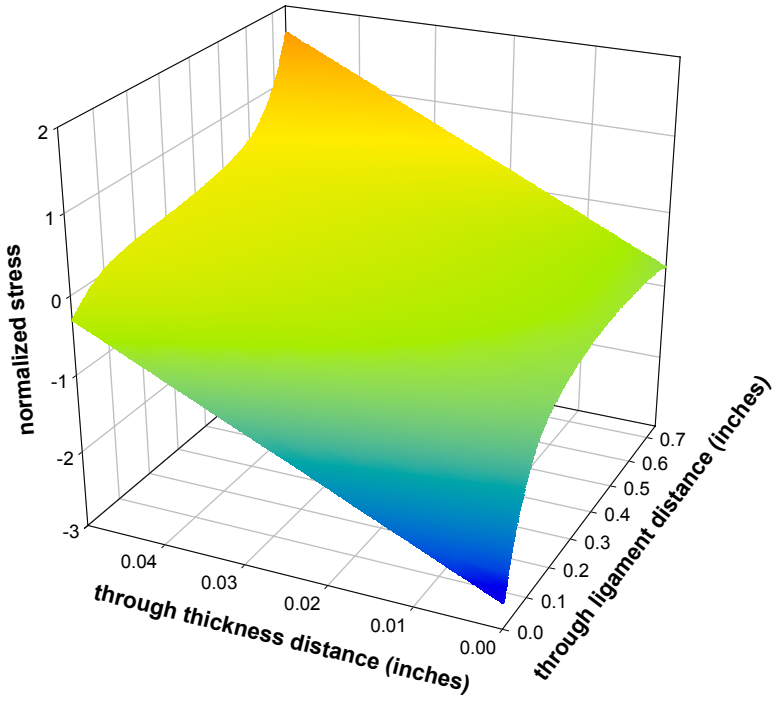

Figure 3-8: Stress distribution at the minimum cyclic load at slot 19 due to Mode C4ND. The distribution shows that through thickness bending is the dominant loading at this slot for this mode.

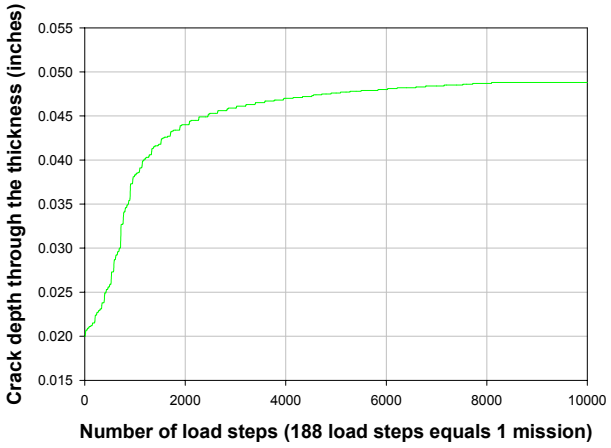

(a)

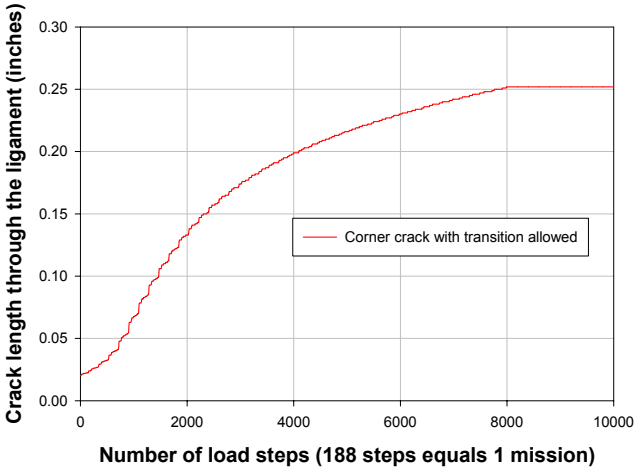

(b)

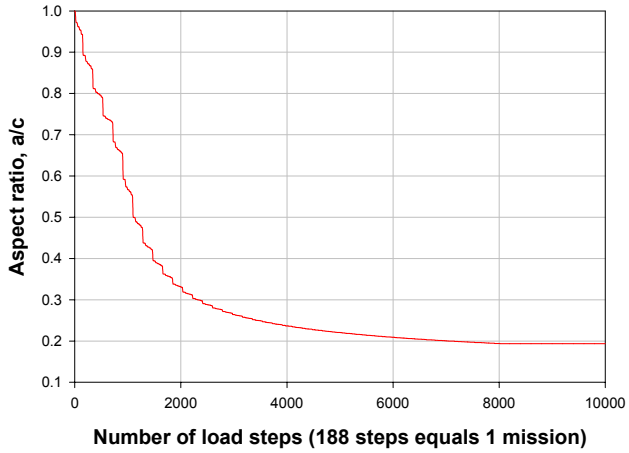

(c)

Figure 3-9: Variation of crack depth (a), crack length (b) and aspect ratio (c) for an initial quarter circular corner crack at slot 19 subjected to the certified spectrum 1.28 E1 Engine Out.

4. UNCERTAINTY MODELING

During Phase II, a more detailed uncertainty model for the load and crack growth properties was implemented. The initial defect distribution is assumed equal to the POD. If an inspection is performed, the POD curve is a conservative probabilistic upper bound to the actual flaw sizes.

The fatigue crack growth (FCG) model in Phase 1 was based on an asymptotic equation. Least square fitting to this equation tends to underestimate the threshold value ΔK_{th}. Because of the importance of the threshold value in the flowliner analysis, an improved probabilistic FCG model, that does not use the asymptotic equation, was developed. Although this model does not include an explicit threshold, the steep slope in the near threshold regime results in an effective threshold when lives in this regime get considerably longer than the service history of the component of interest.

The load spectrum is built upon the flight stage description of shuttle flight STS-110, Engine #1 [ITA Phase 1 Report, Appendix D.2.2]. These flight stages (7 stages for downstream flowliner) form the basis for the deterministic NESC-2 and NESC-3 spectra. (The NESC-1 spectrum is the old Boeing spectrum). The NESC-2 spectrum is derived from the B132 strain gauge data whereas NESC-3 uses the B161 strain data.

The strain measurements provide a means to directly quantify the uncertainty on the structural response. Since the strain data represent a measured structural response, they contain information about the combined effect of the uncertainty on both the loading and the structure. It is therefore not required to perform an explicitly probabilistic structural dynamics analysis. If one assumes that the deterministic structural dynamics analysis predicts the correct trends (*i.e.,* relative values of strains for all modes), then it is most expedient to use the strain data to derive the probability density function (PDF) of a scaling factor on the deterministic stresses from the structural analysis.

4.1 NESSUS Interface

The fracture mechanics software was interfaced with the NESSUS Version 8.1 software. The crack growth module was integrated as a subroutine in NESSUS to achieve maximum performance. The problem statement defines the flowliner fatigue life as a function of the crack site, the crack growth properties, the Flight Stage uncertainty and the initial flaw sizes at the crack site (Figure 4-1).

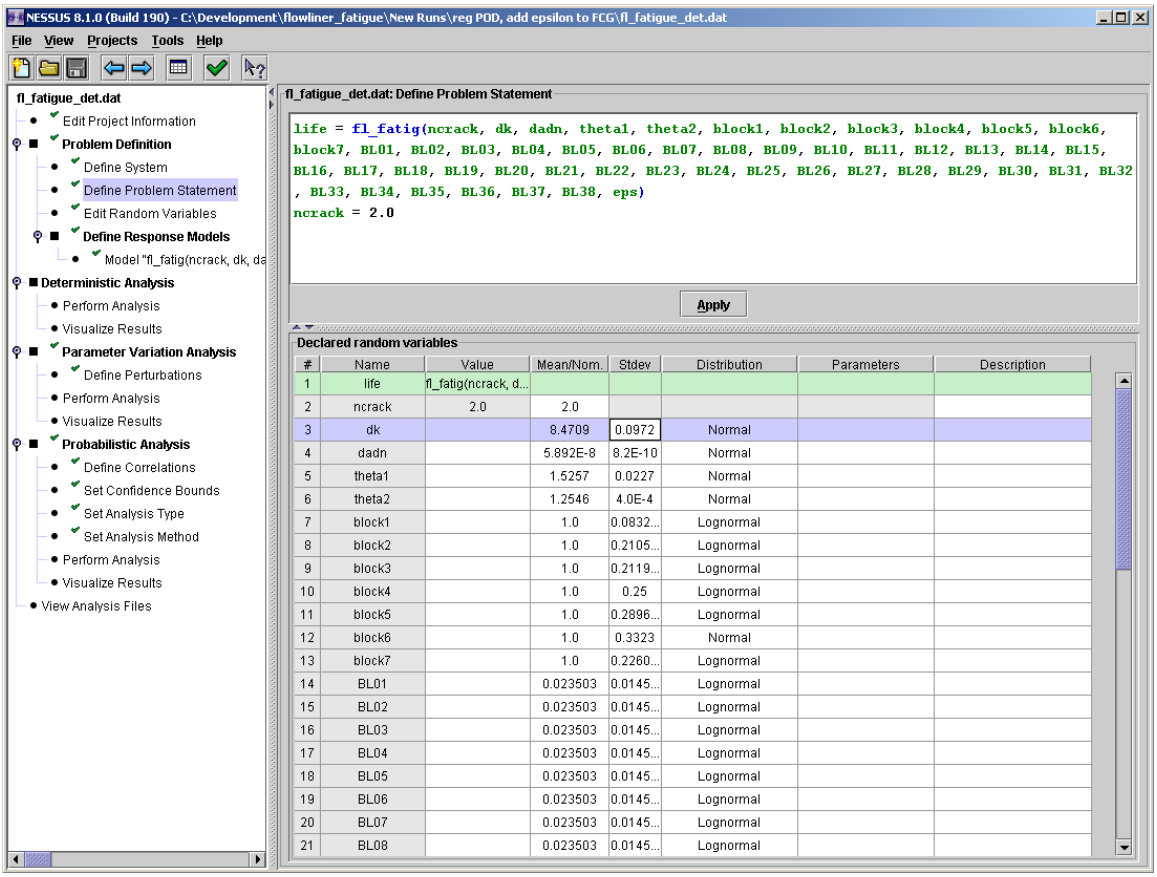

Figure 4-1: Model setup screen in NESSUS.

NESSUS calls the user-defined limit state function subroutine, which in turn calls the fatigue life code. The fatigue life routine computes the life at a specific ligament for given loads, material properties and initial flaw size. The user-defined limit state determines which ligament is the most critical and returns this information to NESSUS.

4.2 Initial Defect Distribution

The current probabilistic analysis assumes that the defect distribution after each inspection is given by the initial POD curve. This assumption is analogous to (but not the same as) the assumption made in deterministic fracture mechanics analyses that the initial defect size is given by the maximum undetectable crack size. Although both assumptions are conservative, the assumption involving the POD curve in a probabilistic analysis is on average less conservative in that it enables crack sizes to be detected below the maximum undetectable crack size used in deterministic analyses.

Currently, the inspection technique of choice for the flowliner slots after each flight is based on eddy current measurement of surface defects. The uncertainty in eddy current measurements is typically modeled using lognormal POD curves [MIL-STD 1823]. Rigorously determined POD curves are presently being measured for an enhanced eddy current procedure

being developed for the flowliner inspections. When available, these POD curves can be utilized in follow-on probabilistic fracture mechanics analyses using the methods developed herein.

Since POD curves have not yet been established for these eddy current inspections of the flowliners, it has been assumed that most defects greater than 75 mils will be detected. This value is several times larger than the typical inspection sensitivity for depot-based eddy current inspections, which is, for example, typically 20-30 mils for inspection of advanced military engines.

Three lognormal POD curves were established for use in the current probabilistic analysis: the baseline curve for eddy current has a median value of 20 mils and has a "high POD" value for a 0.075" flaw—to be defined below. The second curve has its median value at 40 mils and has the same "high POD" value for a 0.15" crack. A third, conservative inspection curve is also used: its median value is 75 mils, which implies that only 50% of the 75 mil flaws will be detected. The same high POD value is then assumed to be 75/20*75=281.25 mils=0.28".

Consideration has been given to the choice of the "high POD" value; typical values are 90%, 95% or even 99% are employed. Although this may seem a fairly small difference in POD, Figure 4-2 shows that this choice has important ramifications on the risk. Each curve in Figure 4-2 has a 50% detectability for 75 mil flaws, but the detectability of the 0.28" flaw is different for each curve (Table 4-1). Each flowliner ligament is assumed 0.75" long. The probability of not detecting a flaw size of length 0.75" is therefore equivalent to not detecting an initial crack that has grown all the way through the ligament length. Based on these risk numbers, the 99% POD curve was selected. The POD curves are shown in Figure 4-3.

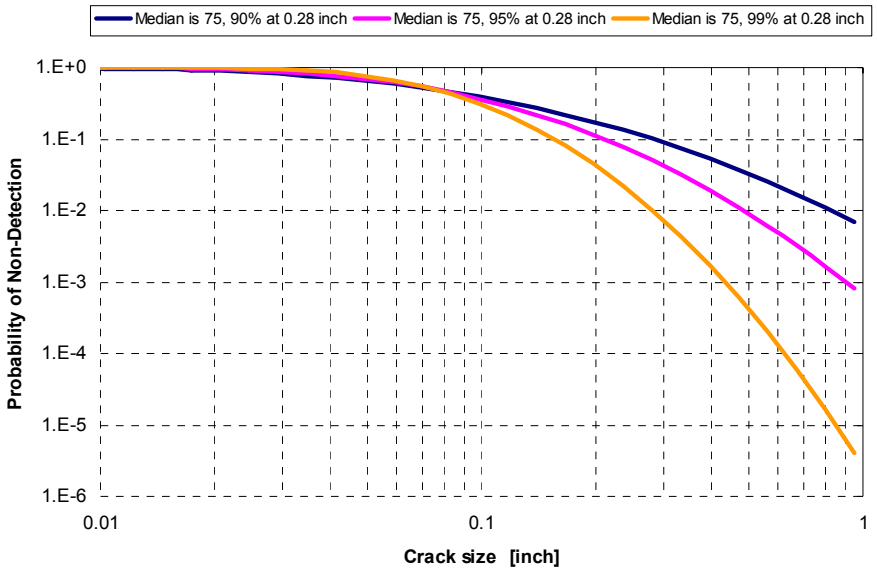

Figure 4-2: Probability for non-detection of large defects if median defect is 75 mils.

Table 4-1: Probability of not detecting an initial flaw through the ligament

High POD value	Prob(initial flaw > 0.75")
90%	0.013
95%	0.002
99%	$2.5\ 10^{-5}$

The lognormal defect distribution is in principle used for both the crack length *c* and crack depth *a*. However, since the flowliner is only 0.05" thick, the initial crack depth is limited to at most 97.5% of the flowliner thickness: $a = \min(c, 0.04875)$. The dashed line in Figure 4-3 indicates this bounding. When the median crack size is 20 mils (blue curve in Figure 4-3), the initial crack depth is limited to 97.5% of the thickness in only 6% of the cases. For the 75 mil median curve (pink curve in Figure 4-3), the initial crack depth is limited to 97.5% of the thickness in about 3 out of 4 cases.

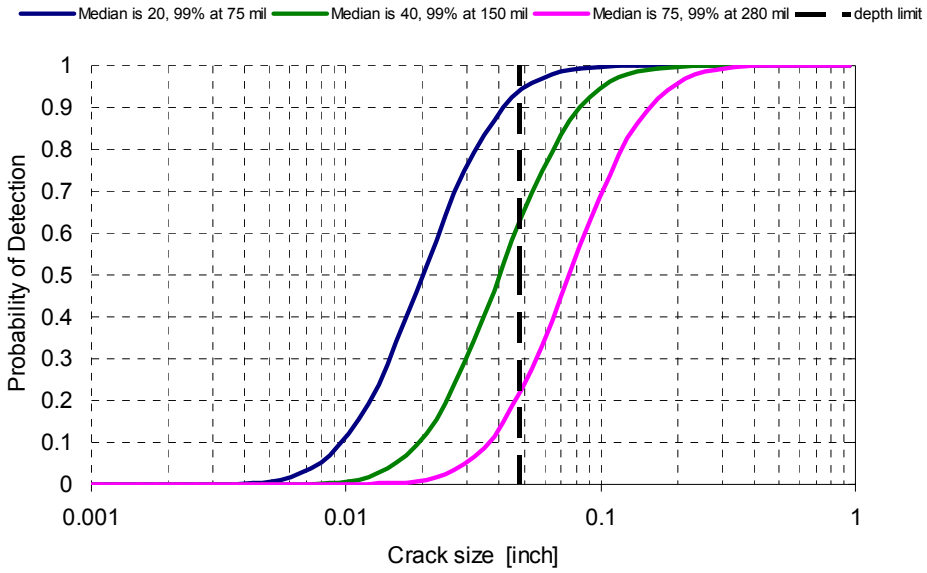

Figure 4-3: Three POD curves considered as initial defect distribution.

4.3 Crack Growth Rate Modeling Uncertainty

4.3.1 Sources of Uncertainty

Uncertainty in the fatigue crack growth rates arises from the following sources:

1. Indirect measurement of crack length (e.g. compliance changes or potential drop) and loading in the experiment
2. Data processing of discrete a vs. N to da/dN vs. ΔK values
3. Closure modeling to collapse data at various R-values (in this case the accuracy and sufficiency of Newman's plasticity-induced crack closure model)

4. Lack of fit between da/dN(ΔK) and the analytical crack growth rate representation
5. Specimen-to-specimen variability within the same heat
6. Heat-to-heat variability

All but the final source of uncertainty are present in the uncertainty modeling. The data set provided to SwRI by NASA Marshall/Langley contained the effects of sources 1, 2 and 5. The closure modeling (source 3) was performed by SwRI and is described in the Phase 1 report [ITA Phase 1 Report, Appendix D.3.4]. A comprehensive lack of fit assessment is the subject of this section.

4.3.2 Crack Growth Model Description

In Phase I, the crack growth model employed was an asymptotic crack growth equation. Because of its asymptotic nature, low values were obtained for ΔK_{th}. The uncertainty modeling is based on the same data set as used in Phase I, but a so-called three-component model was used for the crack growth equation, where each of the n components is modeled by a Paris-like equation. The n-component model is characterized by n Paris-like regimes with n-1 transition zones.

$$\left(\frac{da}{dN}\right)^{-1} = \sum_{i=1}^{n} \left(\frac{da}{dN}_i\right)^{-1} \quad where \quad \frac{da}{dN}_i = C_i(\Delta K)^{m_i} \tag{4.1}$$

Since the instability region of the crack growth relationship is not important in the current application, only two components are used. Only data with $\Delta K_{eff} < 60$ ksi$\sqrt{}$in were included in the curve fit (see Figure 4-4).

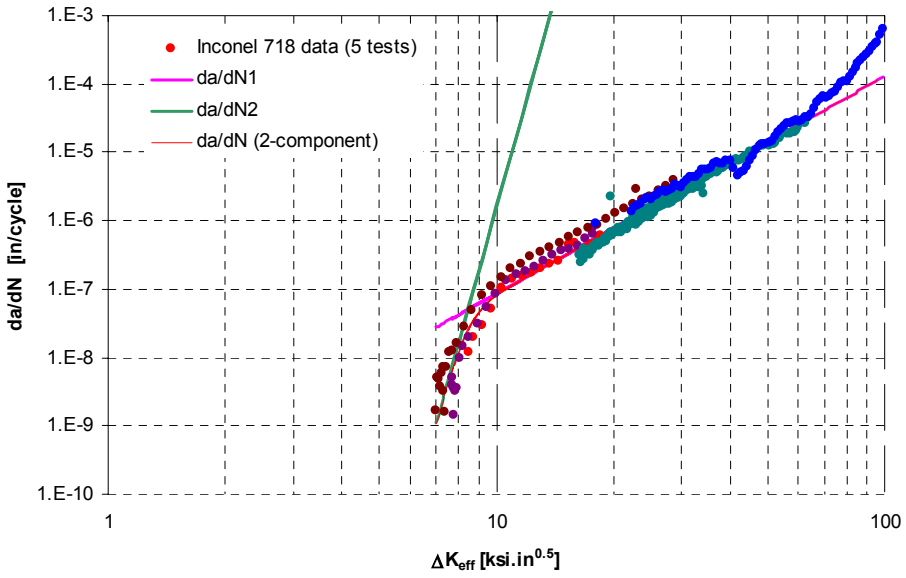

Figure 4-4: Three-component model fit to Inconel 718 data.

4.3.3 Determining Crack Growth Model Parameters

Direct ordinary least squares estimation of the coefficients is numerically ill-conditioned. The coefficients in the two power laws in Equation (4.1) differ by multiple orders of magnitude and appropriate scaling is difficult because of the very steep slope in the first part of the model. To overcome this ill-conditioning the equation was re-parameterized in terms of the intersection of the two power laws (this point will be referred to as the "knee" of the model) and the two slopes of the power laws (the angles of the "legs" of the model). The 4 new parameters are (see Figure 4-5):

- ΔK^*: value of ΔK_{eff} where the two power law regimes intersect, typically less than 10;
- da/dN^*: typically around 10^{-7} in./cycle;
- $\theta_1 = \text{atan}(m_1)$: measured in log(ksi$\sqrt{}$in)-log(in/cycle) space; typically between 85 and 90 degrees (m_1 is typically around 20);
- $\theta_2 = \text{atan}(m_2)$: measured in log(ksi$\sqrt{}$in)-log(in/cycle) space; typically around 70 degrees (m_2 is typically around 3).

The position of the knee anchors the equation and removes the ill-conditioning from the least squares estimation. The value of ΔK^* determines the start of the Paris regime. If the ΔK_{eff}-axis is translated over a distance ΔK^*, the parameter da/dN^* represents the intercept for the Paris law in the new (red) coordinate system (Figure 4-5). The leg-angles θ are used instead of the actual slopes m_i because whereas it is reasonable to assume normality for the distribution of the leg-angle; the distribution of the slopes must necessarily be highly skewed (long right tail).

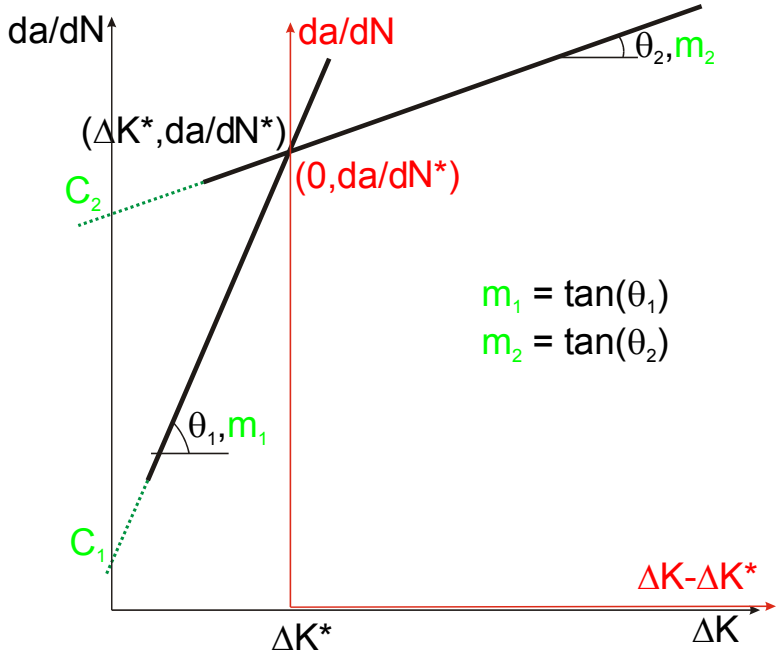

Figure 4-5: Parameterization of Fatigue Crack Growth Curve

Orthogonal distance least squares estimation is a mathematically elegant way to assess the lack-of-fit model uncertainty on highly non-linear equations where uncertainty arises from with both the dependent and independent variables. This is the case with crack growth data since both ΔK and da/dN are measured indirectly. However, from a practical engineering point of view one is usually interested in the uncertainty on the crack growth rate da/dN except near the left end of the curve, where the uncertainty on the threshold ΔK_{th} becomes of interest. In the later regime the crack growth rate is so small (less than 10^{-9} as per ASTM standard) that it is effectively zero for all practical purposes. In this region the uncertainty on the threshold value ΔK_{th} is a more useful metric for the scatter on the model. Consequently, in a first step, ordinary least squares were fit using the following measures for the residuals:

- If da/dN for a data point exceeds da/dN* then measure the error in terms of da/dN. It should be noted that da/dN* is determined iteratively and that the optimal value of da/dN* follows from the least squares procedure itself;
- If da/dN for a data point is less than da/dN* then measure the error in terms of ΔK. To this extend ΔK is solved using an iterative procedure using the current estimates of the 4 model parameters.

Using the above procedure along with the new (three-component) model the least squares fit shown in Figure 4-6 was obtained for the Inconel 718 data. The parameter estimates for this fit are: $\Delta K^* = 8.47$ ksi$\sqrt{\text{in}}$, da/dN* = $5.89\ 10^{-8}$ in/cycle, $\theta_1 = 1.53$ (=87.4 degrees), $\theta_2 = 1.25$ (=71.9 degrees). In terms of the actual Paris equation parameters, these are: $C_1 = 1.67\ 10^{-28}$, $m_1 = 22.1$, $C_2 = 8.62\ 10^{-11}$, $m_2 = 3.05$. The threshold value $\Delta K_{th} = 7.06$, corresponding to a crack growth rate da/dN = 10^{-9}, which is computed from the following equation:

$$\Delta K_{th} = \frac{\Delta K^*}{10^{\frac{9+\log(da/dN^*)}{\tan(\theta_1)}}} \tag{4.2}$$

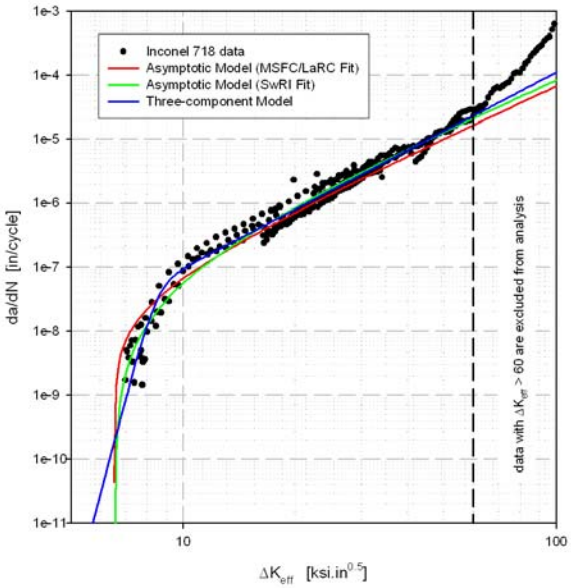

Figure 4-6: Comparison of various crack growth curve fits.

Figure 4-6 also compares the three-component model with two different fits of the asymptotic crack growth rate model contained in NASGRO and fit at MSFC/LaRC and SwRI. Notice that the fits differ significantly in the near-threshold regime where the three-component model has no threshold but the asymptotic models use a threshold, which in this case is about 6.53 ksi√in. The threshold for the asymptotic model is generally about 5 % below the lowest crack growth rate data point, which can lead to non-conservative thresholds when the range of data are inadequate.

4.3.4 Quantification of Crack Growth Rate Uncertainty

The lack of fit between the data and the model equation (1) depends on the value of ΔK and can be described by means of an error process ε(ΔK) in the log-log domain:

$$\log\left(\frac{da}{dN}\right) = -\log\left[\sum_{i=1}^{n}\frac{da}{dN_i}^{-1}\right] + \varepsilon \quad where \quad \frac{da}{dN_i} = C_i\left(\Delta K\right)^{m_i} \tag{4.3}$$

It is important to note that the error process is introduced for the sole purpose of assessing the lack of fit between the crack growth data and the three-component model. It will be used to estimate the variance of the crack growth parameters C_i and m_i but is not an explicit part of the crack growth integration. In other words, the crack growth integration is performed using Eq.(4.1) and not on the basis of Eq.(4.3). This is justifiable since a crack size is an integral measure and the error process has a zero mean value.

The error process ε(ΔK) is assumed to be weakly stationary with zero mean and total variance $\sigma^2 = E(\varepsilon^2)$ equal to 0.011, where E is used to denote the expectation operator. The asymptotic model used in Phase I had a total variance of 0.023. The three-component model therefore seems to provide a slightly better overall fit than the asymptotic model used in Phase 1. As outlined in the Phase 1 report, 5 test results were available at the cryogenic temperature of interest to the flowliner (-423ºF). The relative error between the model prediction and the experimentally recorded crack growth rates is shown in Figure 4-7.

It is immediately clear from Figure 4-7 that the errors associated with neighboring data points are not independent, but that rather strong correlations exist. This correlation is introduced when the measured crack size data (a vs. N) are converted to crack growth rates (da/dN vs. ΔK). This observation leads to the consideration of models in which the correlation between ε_i and ε_j decreases as the distance between the points *i* and *j* increases. The long stretches of either overestimation or underestimation of the experimental growth rate indicates a positive auto-correlation. Because the da/dN vs. ΔK data are derived from a vs. N data, a first-order auto-regressive model seems appropriate for the model error ε. In this model, the model prediction error at a point is only explicitly correlated to the error at the previous point. In a first order auto-regressive model the correlated errors ε_i can be reduced to uncorrelated errors e_i:

$$e_i = \varepsilon_i - \phi \quad \varepsilon_{i-1} \tag{4.4}$$

where ϕ is the correlation coefficient, e_i are zero-mean, uncorrelated normal random variables (each variable e_i has a different variance) and the correlation coefficient $|\phi| < 1$.

Figure 4-7: Relative prediction error for all 5 tests.

Since the data are not collected at equal ΔK intervals, Eq. (4.4) must be generalized:

$$e_i = \varepsilon_i - \phi^{|\Delta K_i - \Delta K_j|} \quad \varepsilon_{i-1} \tag{4.5}$$

The variance for each of the independent e_i variables is given by

$$\sigma_e^2 = \sigma_\varepsilon^2 \left[1 - \phi^{2|\Delta K_i - \Delta K_j|} \right] \tag{4.6}$$

where σ_ε^2 is the total variance due to lack of fit. The covariance structure of the model error ε is determined by ϕ. Direct estimation of the correlation coefficient ϕ cannot readily be performed because the data were not collected at equal ΔK intervals. However, in this application only the uncertainty on the 4 crack growth parameters is of interest. In the statistical literature ϕ is referred to as a nuisance parameter because its value is important only to the extent that it affects the variance on the 4 material model parameters. Therefore a crude estimate of ϕ is likely to be sufficient. In this analysis, the amount of correlation was estimated indirectly, by assuming a value for ϕ and plotting the resulting errors and comparing the rates of fluctuation with the observed misfit patterns, shown in Figure 4-7.

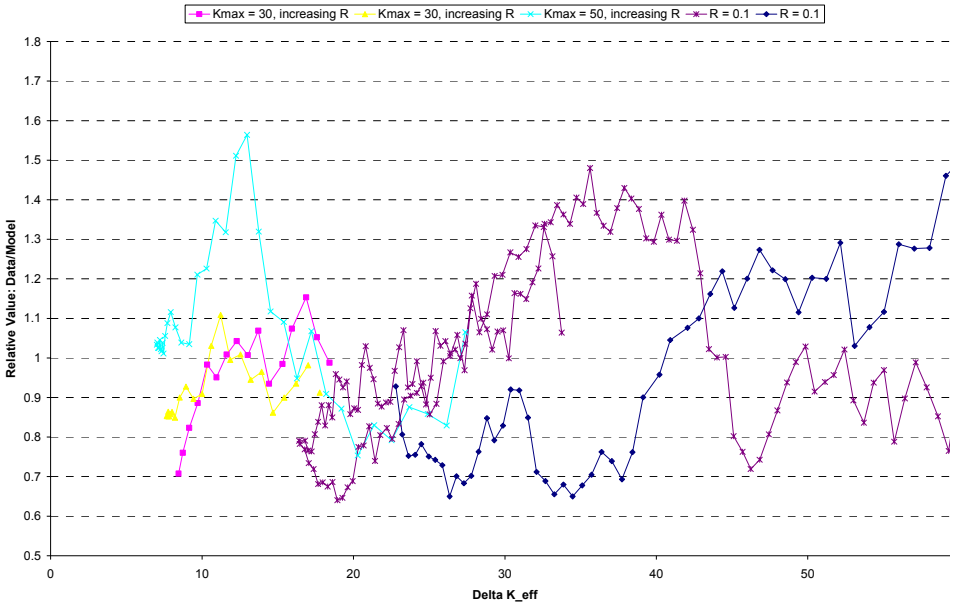

Figure 4-8: Model misfit assuming correlation with $\phi = 0.9$.

When the assumed amount of correlation is too high, not enough fluctuation is observed in the misfit measure "data/model". For insufficient correlation, the misfit measure jumps around too erratically when compared to the observed misfit behavior in Figure 4-7. The experimental data suggest a substantial amount of auto-regressive correlation; a value $\phi = 0.9$ was used in subsequent analysis, since as shown in Figure 4-8, this value gives a misfit pattern similar to that which was observed in the experimental data of Figure 4-7.

Since the correlation structure of the model error process ε is approximately known, one may argue that a more appropriate estimate for the mean value of the 4 material parameters would be given by a generalized least squares estimation which takes this correlation into account. However, a mathematical argument can be made that the mean value obtained using weighted least squares is similar to the ordinary least squares estimate [Seber & Wild, 2003].

It is assumed that, upon re-parameterization of the crack growth law, the uncertainty on the material properties is approximately normally distributed [Kendall and Stuart, 1987]. The asymptotic variance-covariance matrix is given by:

$$\Sigma = \sigma_\varepsilon^2 \left(F^T F\right)^{-1} F^T V F \left(F^T F\right)^{-1} \tag{4.7}$$

where V is the correlation matrix for the error process ε: $v(i,j) = \phi^{|\Delta K(i) - \Delta K(j)|}$. F represents the n x 4 matrix with the derivatives of the crack growth rate da/dN with respect to each of the 4 material parameters for all data points. Table 4-2 shows the estimated uncertainties for various assumptions of the model error process correlation. It can be concluded that improperly ignoring the effect of the correlation between the crack growth at successive data points causes a substantial underestimation of the total crack growth parameter uncertainty. The results also

confirm that the estimate used for ϕ is sufficiently accurate since the uncertainties are not very sensitive to ϕ around $\phi = 0.9$.

Table 4-2: Uncertainty quantification of crack growth parameters

		$\phi = 0$	$\phi = 0.85$	$\phi = 0.9$	$\phi = 0.95$
	Mean value	Standard deviation			
ΔK^*	8.471	0.0163	0.0924	0.0972	0.1024
da/dN^*	0.589×10^{-7}	0.001×10^{-7}	0.007×10^{-7}	0.008×10^{-7}	0.009×10^{-7}
θ_1	1.526	0.0081	0.0224	0.0227	0.0228
θ_2	1.255	0.0001	0.0004	0.0004	0.0005

For the asymptotic model used in Phase 1, the correlations between the material parameters were all very strong. In fact all material parameter pairs are strongly correlated. The correlations for the new model are given in Table 4-3. The correlation structure reflects the two components in the model. As expected, there is a strong negative correlation between ΔK^* and θ_1 and between da/dN^* and θ_2, but only modest correlation between ΔK^* and θ_2, θ_1 and θ_2 or da/dN^* and θ_1. In other words, the knee separates the crack growth model into two parts. For instance, a lower than average value for θ_1 results in a higher than average ΔK^*, but does not reverberate beyond that. This contrasts with the asymptotic model where a change in one parameter caused changes in all material parameters. We believe this more accurately reflects the clear physical distinction between the threshold and Paris crack growth rate regimes.

Table 4-3: Correlations between parameter models

	ΔK^*	da/dN^*	θ_1	θ_2
ΔK^*	1			*sym*
da/dN^*	-0.187	1		
θ_1	-0.8834	0.1786	1	
θ_2	0.1930	-0.9978	-0.1848	1

4.3.5 Quantification of Crack Growth Threshold Uncertainty (ΔK_{th})

The threshold parameter ΔK_{th} is an important factor in the high cycle fatigue assessment since it defines the regime of stress and defect size above which cracks will grow and below which the will arrest. Since it is not feasible to experimentally determine a level below which cracks will never grow, the ASTM Standard for measurement of ΔK_{th} is operationally defined as the ΔK value corresponding to a crack growth rate of 10^{-9} in/cycle [ASTM E647]. As discussed in the Phase 1 report, the threshold value obtained by least squares estimation using an asymptotic crack growth model is always less than the smallest ΔK value observed during the test. The three-component model in Eq. (3.2), however, forces the crack growth curve through the middle of the data cloud near $da/dN = 10^{-9}$ in/cycle. In the three-component model the ΔK

value corresponding to a crack growth rate of 10^{-9} in/cycle is used as an operational definition of ΔK_{th} (as per ASTM practice), even though the model does not mathematically have a threshold. Figure 4-9 compares the CDF for the threshold ΔK_{th} obtained using an asymptotic model with the operational ΔK_{th} definition in the three-component model.

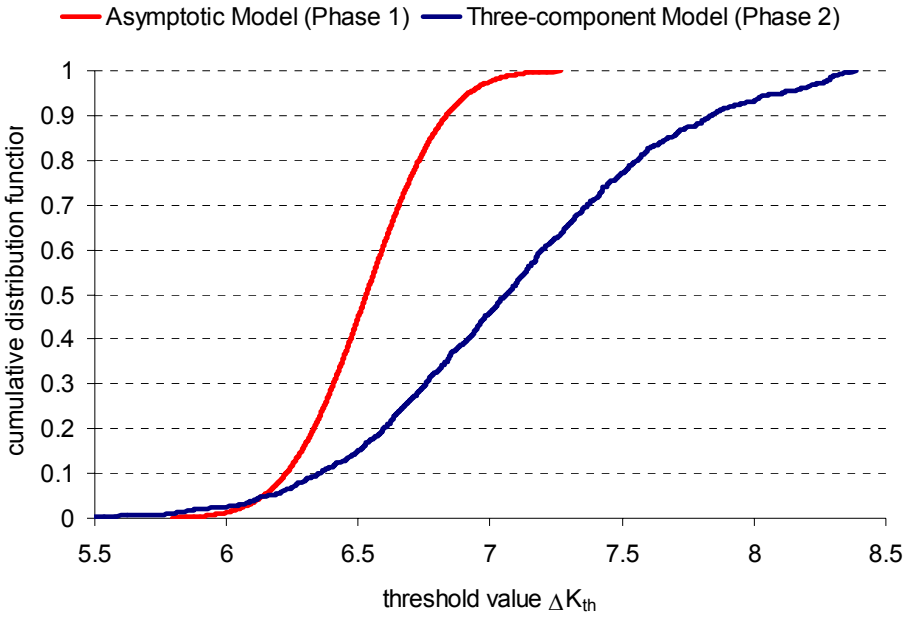

Figure 4-9: Comparison of threshold values ΔK_{th}.

There is no need to explicitly enforce a threshold level in the three-component model. If the ΔK values are much less than the operational ΔK_{th}, the crack growth rate will be minuscule due to the steep slope in the da/dN (ΔK) of about 20 in the near-threshold regime. On the other hand, appreciable crack growth may be obtained using the three-component model for a given Flight Stage with many cycles and a ΔK value slightly less than ΔK_{th}, whereas the asymptotic threshold-based model would have ignored this crack growth contribution. It should be noted that the ΔK_{th} levels in Figure 4-9 are reported for illustrative purposes only; they demonstrate the improvement the three-component model represents over the asymptotic model. Thus, as indicated in Eq. 4.1, no explicit threshold values are used in the Phase II crack growth computations.

4.4 Load Modeling Uncertainty

The objective of this section is to develop a probabilistic load model for the downstream flowliner that on the one hand removes the built-in conservatism in the deterministic load spectrum, while at the same time explicitly accounts for the variability in the shuttle loading including the possibility of loads more extreme than used in the generally conservative deterministic spectrum.

It was beyond the scope of the current effort to perform an extensive probabilistic structural dynamics analysis. Such an analysis would require a detailed probabilistic model of the loads as well as the flowliner geometry and material properties. In addition, the need for such an analysis is reduced by the availability of dynamic structural response measurements provided by NASA. These experimental strain data, which are available for many locations in the flowliner, can be used to directly quantify the uncertainty on the alternating stresses.

The probabilistic load modeling is based on the results of the structural dynamics analysis in the Phase 1 report [ITA Phase 1 Report, Appendix D.2.2]. It should be noted, however, that the uncertainty quantification and subsequent risk analysis is likely to be affected by some key assumptions and limitations of the structural analysis, namely, a stationary single-mode response for each flight stage, which imply time-independent statistics.

The implications of these assumptions will be further discussed in Section 6.

4.4.1 Approach to Modeling Load/Stress Uncertainty

The development of the probabilistic load/stress model consists of the following steps:

1) Use the experimental strain data collected during the BTA ground tests to quantify the uncertainty on the strains or stresses at the strain gauge location. It is assumed that the same strain uncertainty applies to the flowliner during actual flight conditions.
2) Compute the stresses at all locations of interest using transfer factors. The transfer factors vary from slot to slot. For each flight stage and slot they depend on the mode, which is assumed to govern the structural response in that particular flight stage.
3) Obtain the ligament stresses ahead of the hypothesized cracking by scaling the "worst-case gradient" (to be defined later) to match the stresses at the crack site location, as computed using transfer factors.

4.4.2 Baseline Loading Spectrum

Each Shuttle flight results in a different flowliner excitation. The ITA Team has used and developed several spectra. Specifically, a probabilistic load model was developed for the NESC-2 spectrum based on STS-110, engine 1, strain gauge B132. Swales Aerospace provided SwRI with 10kHz sampling rate test data for the BTA test specimens. Eighteen strain gauges were placed on the downstream flowliner, 11 of them in consecutive slots and 7 more at random locations along the perimeter (Figure 4-10).

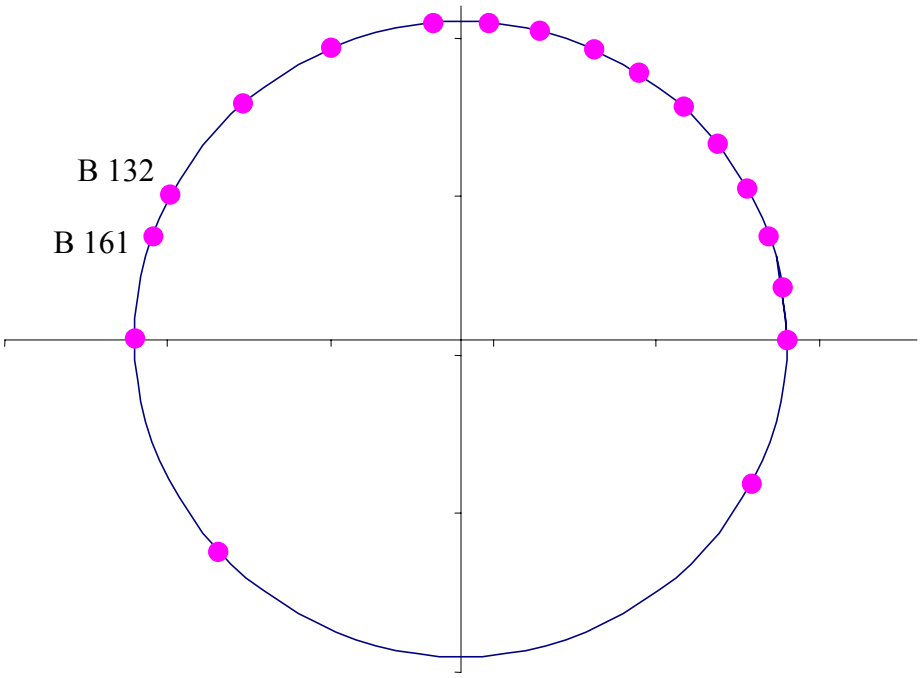

Figure 4-10: Strain gauge locations along the circumference of the downstream flowliner.

The NESC-2 spectrum was chosen for the present analysis on the following grounds:

- SwRI did not have access to the detailed data for the Boeing spectrum
- The Boeing spectrum (NESC-1) represents a "worst case", whereas the NESC-2 and NESC-3 spectra are believed to represent a "nominal" flight conditions.
- Based on the Swales stress and spectra data most damage seems to be accumulated in Flight Stage 6 (total time of 389.5 sec). More severe RMS strains are observed in the B132 strain gauge than in B161 for Flight Stage 6.

For illustration purposes the snoopy diagram for Flight Stage 6 for the STS-110 flight as well as the 5 relevant parts of the BTA tests is represented in Figure 4-11 [ITA Phase 1 Report, Appendix D.2.2]. Since no BTA trajectory represents the bucket in Flight Stage 4, it is taken identical to the Boeing data. Ref [ITA Phase 1 Report, Appendix D.2.2.] notes that Flight Stage 4 does not have a first-order effect on the predicted fatigue life.

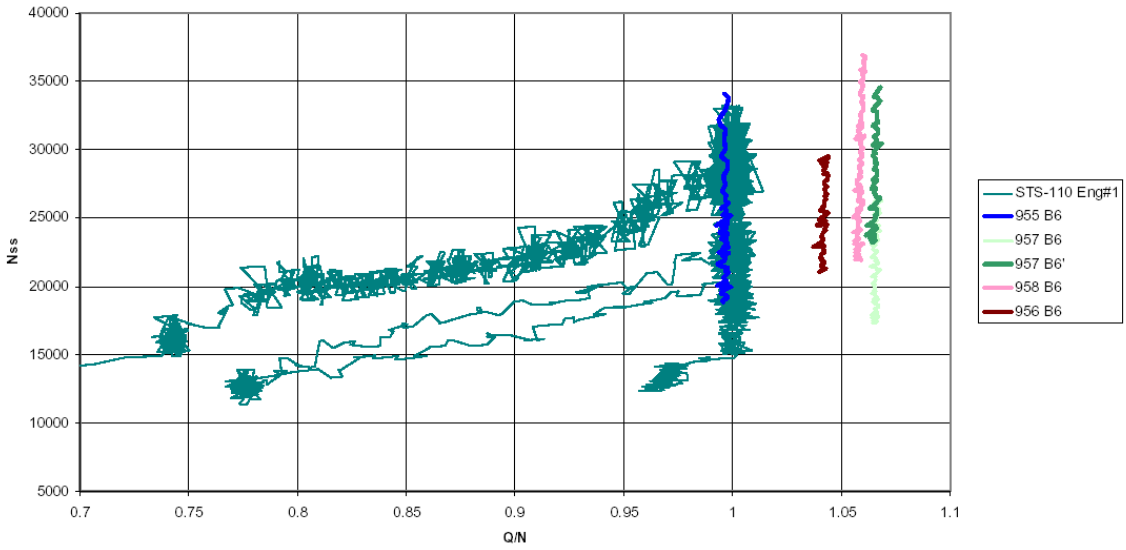

Figure 4-11: STS 110 - Engine 1 - Block 6 - Flight Powered Level/Accelerated Flight [ITA Phase 1 Report, Appendix D.2.2].

Swales Aerospace developed a spectrum on the basis of the following observations and assumptions [ITA Phase 1 Report, Appendix D.2.4]:

- Significant fluctuations in RMS strain levels are observed between tests (for example, RMS levels for B132 varied between 48 and 107 με for Flight Stage 6).
- The spectrum is built from the test with the highest overall RMS value (for Flight Stage 6, strain gauge B132). This is test 958, which is represented with a pink line in Figure 4-11.
- A short time window of this test—in which the maximum overall RMS value is observed—is selected and subsequently rainflow cycle counted.
- The cycle counts are then scaled to match the durations of each flight stage in STS-100. It is thus assumed that the high RMS loading is sustained for the entire duration of the Flight Stage.

This approach essentially assumes a stationary process with a single response mode per Flight Stage. Subsequent analyses by both Swales and SwRI raise questions regarding these assumptions (see discussion in Section 6). However, to maintain compatibility with Swales' rainflow results (and the NESC-2 spectrum), the current probabilistic model necessarily builds upon these same assumptions.

Since the strain levels for the deterministic spectrum were determined on the basis of RMS values, SwRI used the same RMS metric to determine the uncertainty on the load levels. It would be prudent to consider multiple response modes in the future so that more refined deterministic and probabilistic fatigue analyses could be performed.

Figure 4-13 through Figure 4-15 show the RMS values using moving windows of 0.5-second length. RMS amplitudes are for approximately completely-reversed loading since the overall mean strain is small (about με) compared to the amplitude values in Figures 4-12 through 4-15. Often a large fluctuation of the RMS values can be observed between tests and also between different times during the same test. Even though all 5 BTA tests correspond to vertical lines in the Snoopy diagram (Figure 4-11), it seems that while the RMS values remain fairly constant for the biggest portion of Tests 955, 956 and 957, they exhibit strong transient behavior in Test 957 and a gradual drop-off in Test 958. The strain time histories for all five tests are shown in Figure 4-16.

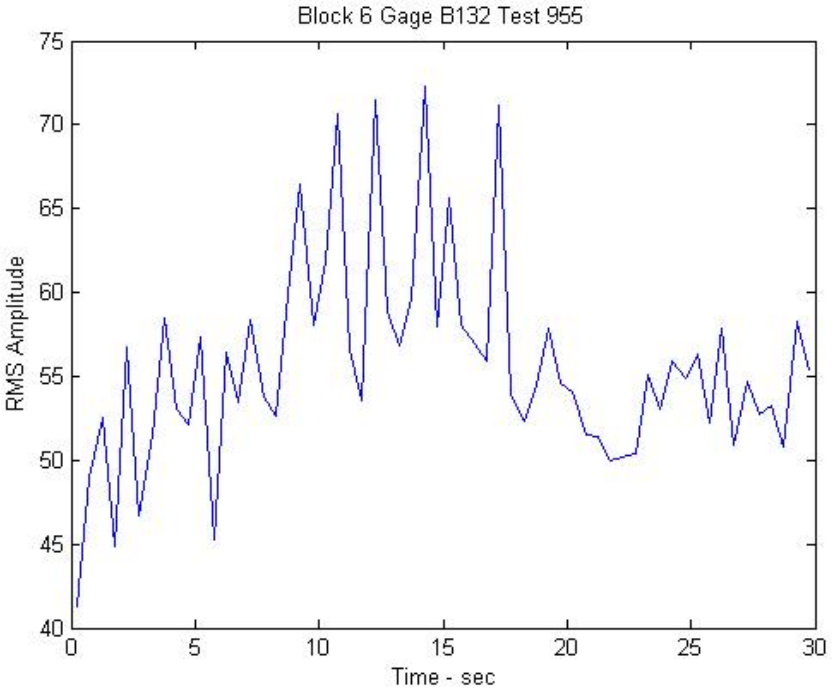

Figure 4-12: Test 955 - RMS values for Flight Stage 6 (0.5 sec time window). RMS amplitudes are in microstrain (με).

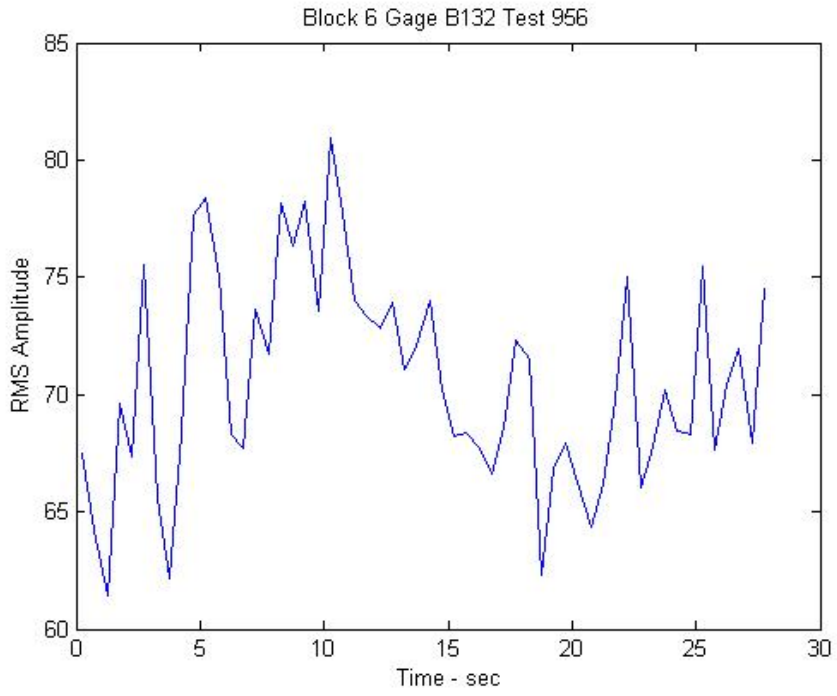

Figure 4-13: Test 956 – Flight Stage 6 RMS values (0.5 sec time window). RMS amplitudes are in microstrain (με).

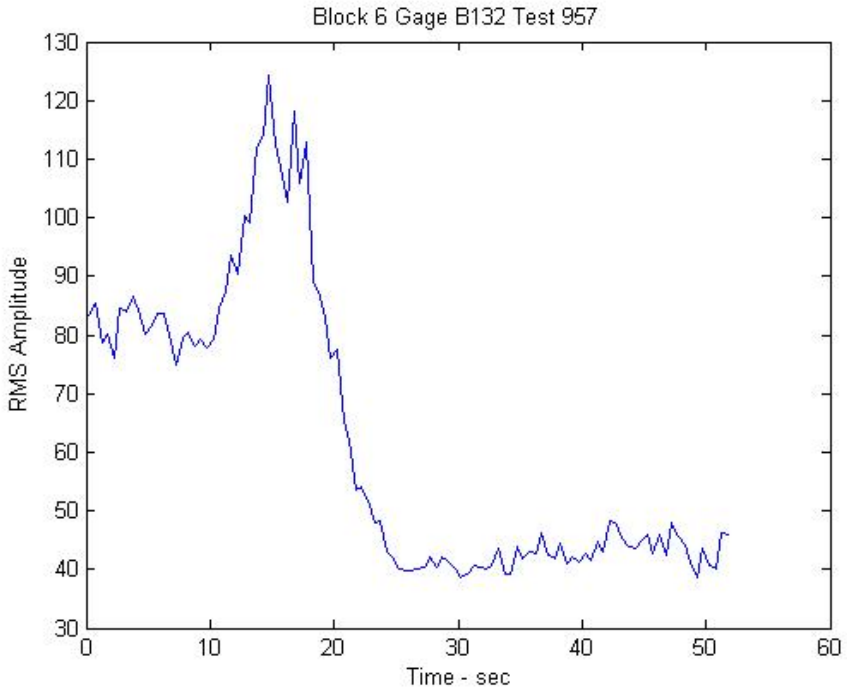

Figure 4-14: Test 957 – Flight Stage 6 RMS values (0.5 sec time window). RMS amplitudes are in microstrain (με).

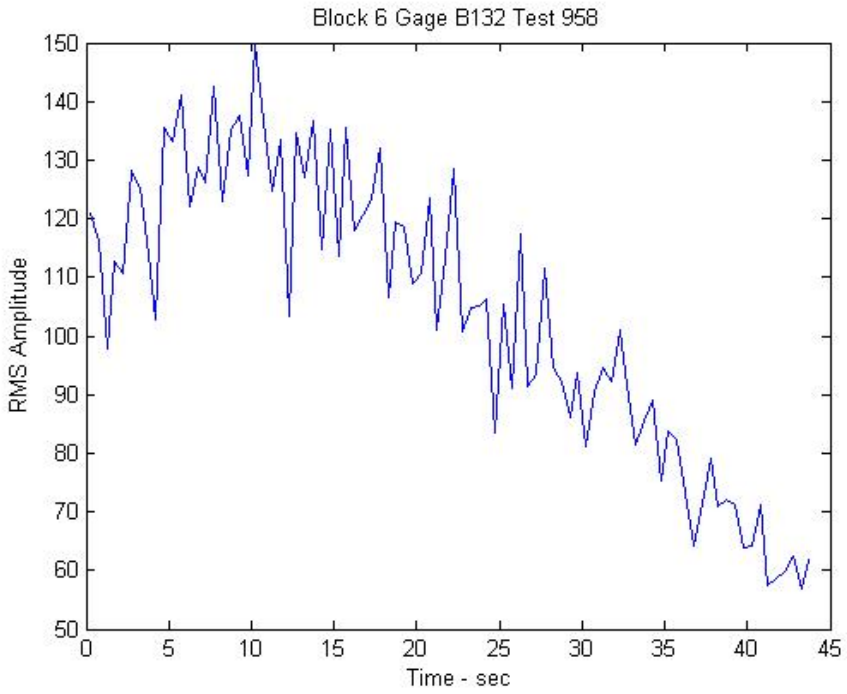

Figure 4-15: Test 958 - RMS values for Flight Stage 6 (0.5 sec time window). RMS amplitudes are in microstrain (με).

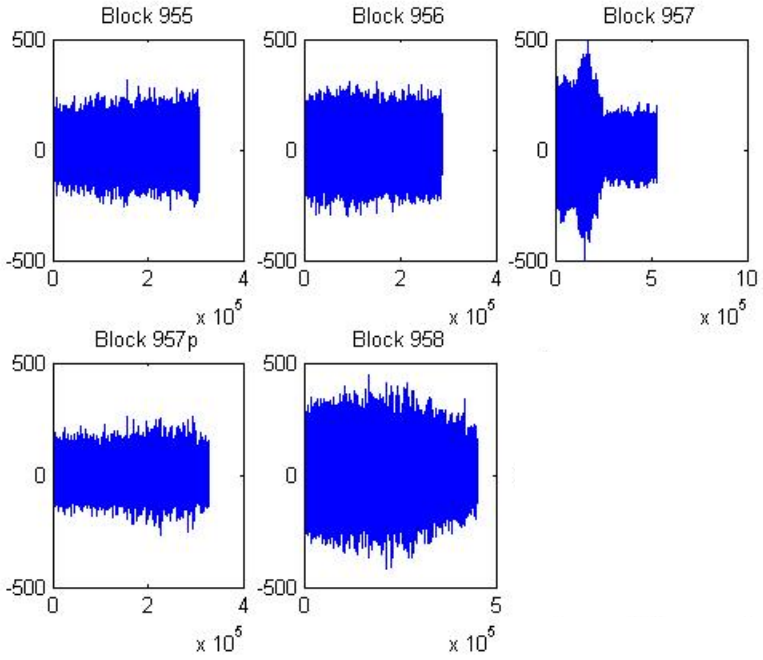

Figure 4-16: Strain histories for Flight Stage 6 for all BTA tests in microstrain (με) versus sample number.

The Swales spectrum is obtained through rainflow counting of a short window (of 0.4, 1 or 4 sec duration) in which the maximum RMS is observed. Figure 4-15 indicates that this window occurs approximately 10 sec into Test 958 and has an RMS value of 149.87. (Figure 4-15 shows the 0.5 sec window RMS values). The resulting strain spectrum on the basis of B132 is given in Table 4-4. The strain levels listed in Table 4-4 represent the middle of the strain ranges in the Swales report [ITA Phase 1 Report, Appendix D.2.4]. Stresses are obtained by the following multiplication: $\sigma = E\,\varepsilon$, where $E = 0.012 \times 10^6$ ksi.

Table 4-4: Nominal deterministic flight profile (cycle counts) provided by Swales Aerospace [ITA Phase 1 Report Appendix D.2.4]

Alternating Strain level με	Stage 1 (12 sec)	Stage 2 (26.5 sec)	Stage 3 (5 sec)	Stage 4 (9 sec)	Stage 5 (6.5 sec)	Stage 6 (389.5 s)	Stage 7 (61 sec)
396.31						9	
376.49						27	
336.86		1	3		7	274	33
297.23		6	19		38	1930	224
257.60		58	41		70	12995	507
217.97		398	60		88	53149	652
178.34	15	2162	158	54	153	91063	932
138.71	353	8547	867	965	509	103970	1927
99.08	3482	21808	4070	6462	3351	126163	19147
59.45	16712	32813	7583	14407	9803	190882	93325
33.69	7721	9507	1873	3771	3166	78865	34527
23.78	4868	5638	973	1951	1713	60718	19249
13.87	6146	7287	1026	2039	1879	100447	20251
3.96	3004	3920	455	833	819	72385	8522

Note that the maximum alternating strain level obtained during the window on which the rainflow count is based is 396 με, whereas the overall maximum strain recorded during Test 958 is 449 με (a 13% difference). Most of the fatigue damage is accumulated during Flight Stage 6 because it has both the highest stresses and highest cycle counts for this spectrum.

4.4.3 Uncertainty Quantification of the Load Spectrum

Uncertainty in the load spectra arises from four primary sources:

- Uncertainty in the duration of each Flight Stage
- Uncertainty in the cycle count for each amplitude bin
- Uncertainty in the magnitude of each amplitude
- Modeling uncertainty about the similarity between the strains experienced during the BTA tests and during the actual Shuttle missions.

The extent to which the uncertainty of each of these sources is included in the overall model is described below. The so-called "uncertainty factors" in the original Boeing analysis

were not included since the flight stages of the new spectrum are different than for the Boeing analysis. Presently, the precise function of these uncertainty factors on the loads is not known.

4.4.3.1 Flight Stage Duration Uncertainty

The cycle counts are directly related to the Flight Stage description derived by NASA-Goddard and shown in Table 4-5. To date, insufficient data were available to SwRI to quantify the uncertainty on Flight Stage duration. Therefore no estimate regarding variability of the flight stage durations between various Shuttle missions has been included in the current probabilistic model.

Table 4-5: Flight Stages description for STS-110 [ITA Phase 1 Report, Appendix D.2.2]. STS-110 serves as the basis for both NESC-2 and NESC-3 spectra.

Flight Stage	Description	start time	end time	duration
1	lift off to 104 %	0	12	12.0
2	104 % pre ramp down	12	38.5	26.5
3	ramp down	38.5	43.5	5.0
4	bucket	43.5	52.5	9.0
5	ramp up	52.5	59	6.5
6	accelerated	59	448.5	389.5
7	3G down	448.5	509.5	61.0

The Boeing spectrum (also referred to as NESC-1) consisted of 8 Flight Stages for the downstream flowliner. Currently, no information is available regarding the degree of uncertainty on the number of flight stages and the duration of each stage. Such information can readily be incorporated in the probabilistic analysis when it becomes available.

4.4.3.2 Cycle Count Per Bin Uncertainty

The baseline stress spectrum is based on the cycle count during a short time window in a single test for a single strain gauge. Figure 4-17 shows the rainflow cycle counts for B132 and B161, normalized with respect to the maximum RMS strain observed during a 0.4sec window. The maximum RMS strain is 396 με for B132 and 491 με for B161. Generally fairly little difference is observed in the relative rainflowed strain counts between B132 and B161, which are located in adjacent ligaments. The strain gauges B132 and B161 were used as reference points for the NESC-2 and NESC-3 spectrum, respectively. Figure 4-17 also indicates that significant cycle count differences exist for the largest strains/stresses in the load history.

The spectrum derived from a short time window is subsequently repeated during the entire flight stage. This effectively assumes that the strain is a perfectly periodic function of time with period equal to the window size. Figure 4-12 to Figure 4-16 suggest that at least for some BTA tests the strain histories are not only non-periodic but also non-stationary.

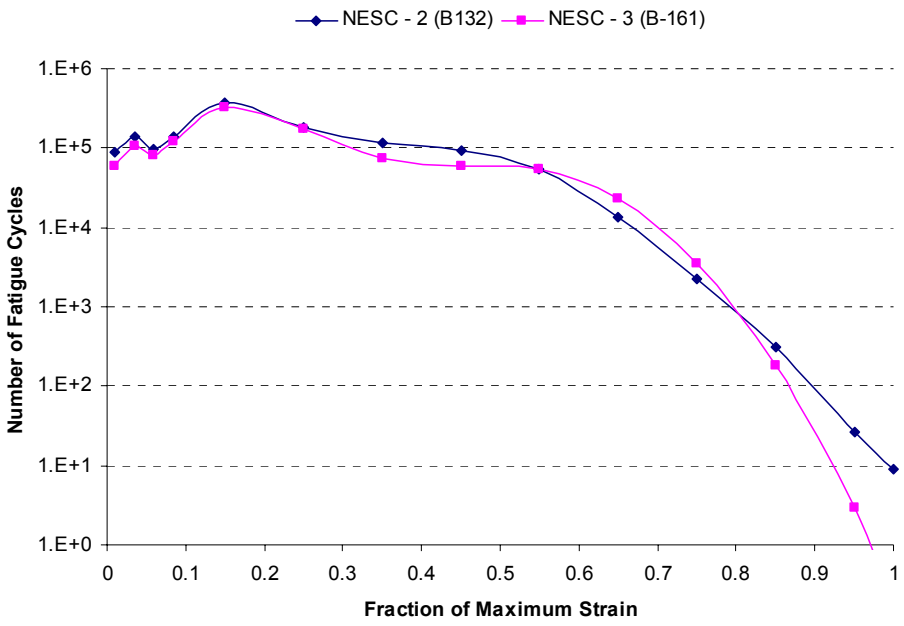

Figure 4-17: Strain spectrum derived from strain gauges B132 and B161 [ITA Phase 1 Report, Appendix D.2.4]

4.4.3.3 Amplitude Magnitude Uncertainty

To maintain conservatism in the deterministic analysis, Swales selected for each Flight Stage the test that had the highest RMS value, and the worst 0.4 sec time window during that test for the rainflow counting. This window and its associated high load level were then repeated for the entire duration of the flight stage.

The present probabilistic analysis uses the deterministic spectrum developed by Swales in Phase 1 [ITA Phase 1 Report, Appendix D.2.4] as a baseline. Since the strain levels for deterministic spectrum were determined on the basis of RMS values, this analysis will follow Swales' Phase 1 approach for consistency.

It should be noted that this approach is consistent with the assumptions made during the Phase 1 analysis. These assumptions are valid only if the process is stationary and only if a single vibration mode is active. Further analysis of the strain gauge recordings during Phase 2 by both SwRI and Swales has indicated that these assumptions are not satisfied. SwRI recommends updating the probabilistic model once the detailed results of this work become available as outlined in Section 6.

It is clear from the RMS plots (Figure 4-12 through Figure 4-15) that the strain level fluctuates from test to test. Figure 4-18 through Figure 4-23 show the empirical probability distribution (plotted on normal probability paper) of the RMS levels (computed over 0.5 sec time windows) for each of the 7 Flight Stages. Due to lack of data, a lognormal distribution with 25% COV was assumed for Stage 4; this coefficient of variation is comparable to the value obtained for the other Flight Stages. The empirical distributions are well approximated by either a normal or a lognormal distribution. Some of the distributions exhibit extreme outliers. For

instance, Figure 4-23 for Stage 7 has outliers above 80 με, which are not well reflected in the fitted distribution. It is justifiable to exclude these points from the fit since the time history and RMS history (Figure 4-24) suggest that the time window should probably be shortened by 0.5 sec. For most Flight Stages, significant scatter is observed. The fitted probability density functions and their parameters are listed in Table 4-6.

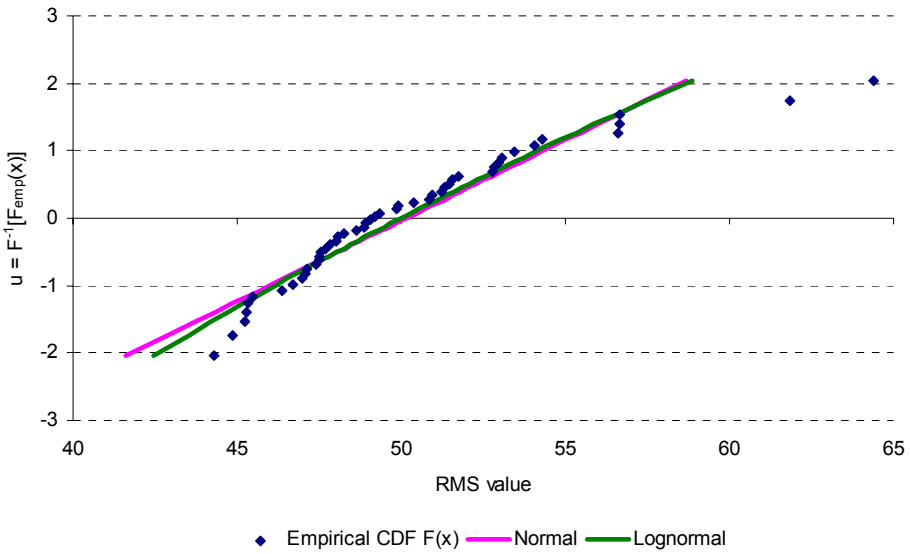

Figure 4-18: RMS load amplitude distribution for Stage 1.

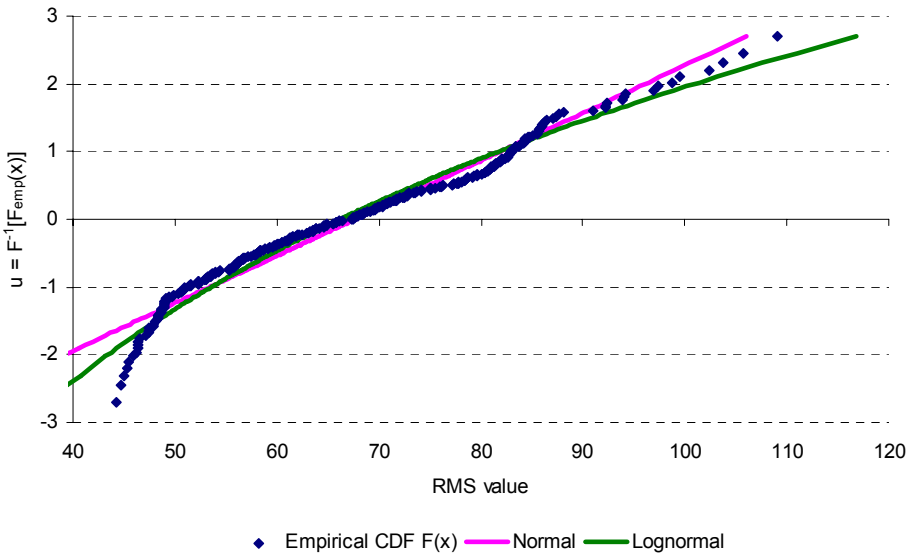

Figure 4-19: RMS load amplitude distribution for Stage 2.

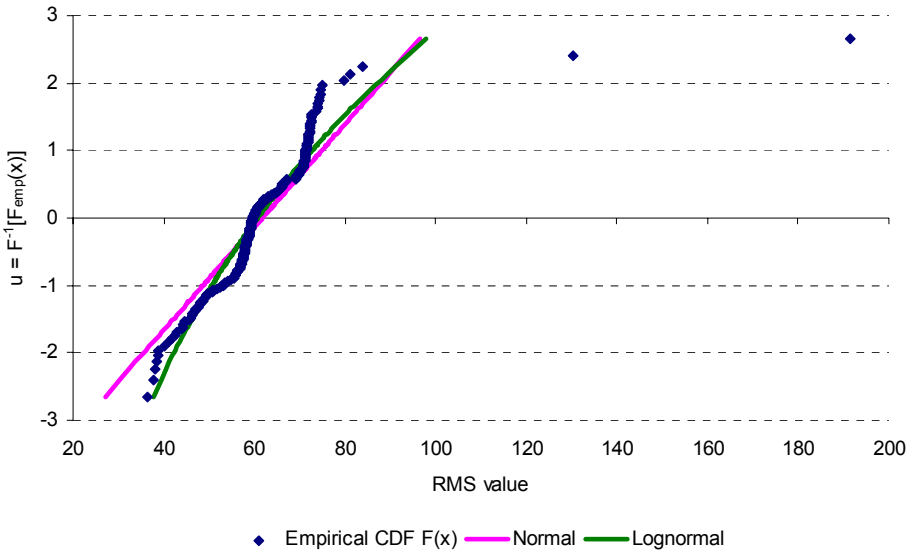

Figure 4-20: RMS load amplitude distribution for Stage 3.

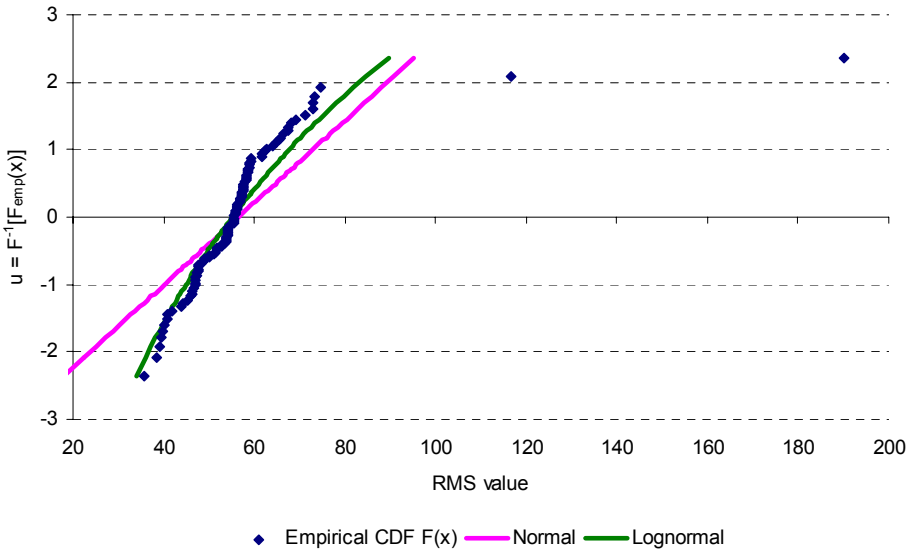

Figure 4-21: RMS load amplitude distribution for Stage 5.

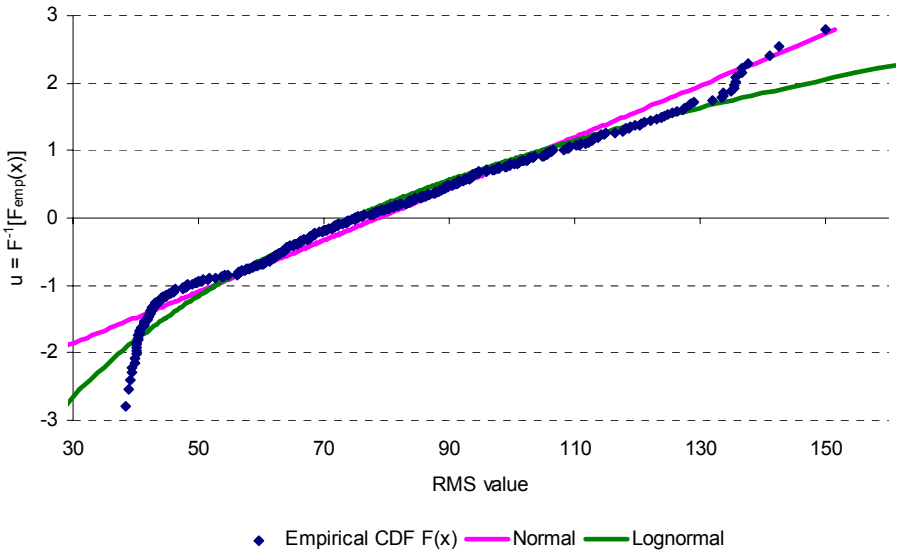

Figure 4-22: RMS load amplitude distribution for Stage 6.

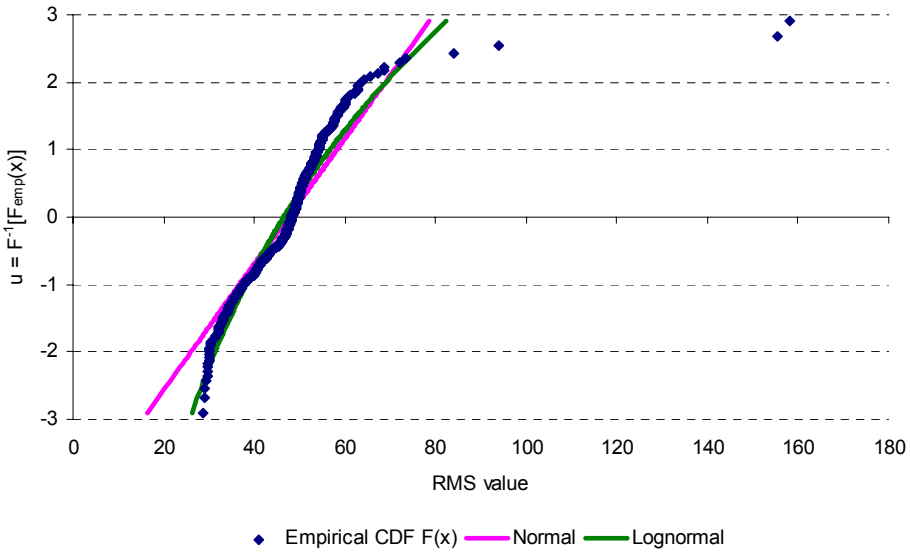

Figure 4-23: RMS load amplitude distribution for Stage 7.

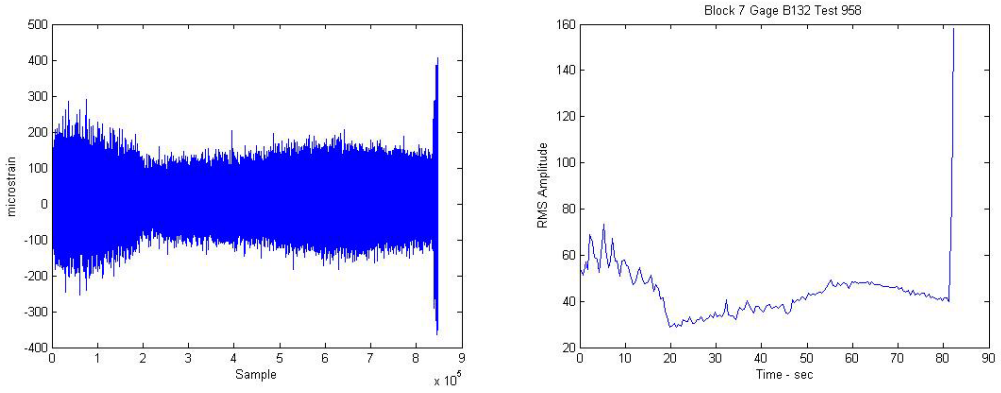

Figure 4-24: Time histories for Stage 7 - Test 958; Strain Gage B132.

Table 4-6: PDFs for load intensity uncertainty.

	Number of RMS data	Median	Standard deviation	Coefficient of Variation	PDF type
Stage 1	48	50.16	4.17	8.3%	Lognormal
Stage 2	280	67.65	14.24	21.1%	Lognormal
Stage 3	244	61.76	13.09	21.2%	Lognormal
Stage 4	-	-	-	25% (assumed)	Lognormal
Stage 5	108	56.54	16.38	29.0%	Lognormal
Stage 6	372	78.63	26.13	33.2%	Truncated Normal
Stage 7	530	47.47	10.73	22.6%	Lognormal

On the basis of the deterministic rainflow analysis, Stage 6 has been identified as the most damaging Flight Stage. Although the RMS level during Test 958 was 106.7 με (see Figure 4-15), the overall median RMS strain level for all 5 tests in Stage 6 is only 78.63 με (Table 4-6). Figure 4-25 shows the substantial variation in RMS level for different tests as well as during a single test for Stage 6. The stress levels in the deterministic spectrum are derived on the basis of Test 958. It can therefore be concluded that the median stress level can be reduced by the ratio of the median RMS level over all tests and the RMS level during the worst test. The reduction factors on the median stress are listed in Table 4-7. The substantial reduction for Stage 6 can be attributed to the short duration of the time window with near maximum RMS values (Figure 4-14).

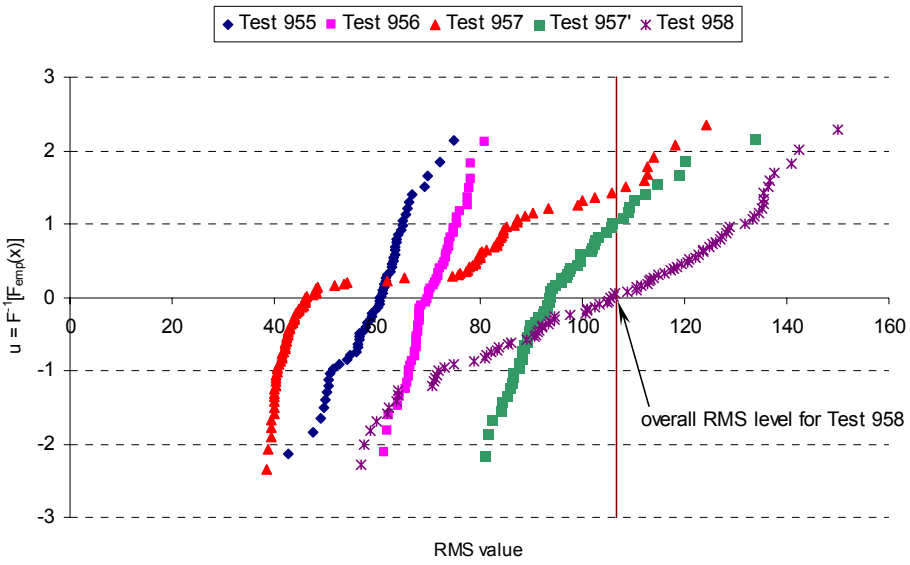

Figure 4-25: RMS distribution for various tests in Stage 6.

Table 4-7: Reduction factors for median stress level.

	Max overall RMS	Median RMS level	Reduction factor
Stage 1	52.92	50.16	0.95
Stage 2	82.69	67.65	0.82
Stage 3	67.13	61.76	0.92
Stage 4	-	-	1 (assumed)
Stage 5	60.23	56.54	0.94
Stage 6	106.66	78.63	0.74
Stage 7	52.73	47.47	0.90

The new median strain spectrum is shown in Figure 4-26 by the green circles. It is important to note that since Stage 6 experiences the largest reduction in median load level, the highest median strains no longer occur during Stage 6, but during Stages 3 and 5. One can therefore no longer a priori conclude that Stage 6 is the most damaging stage.

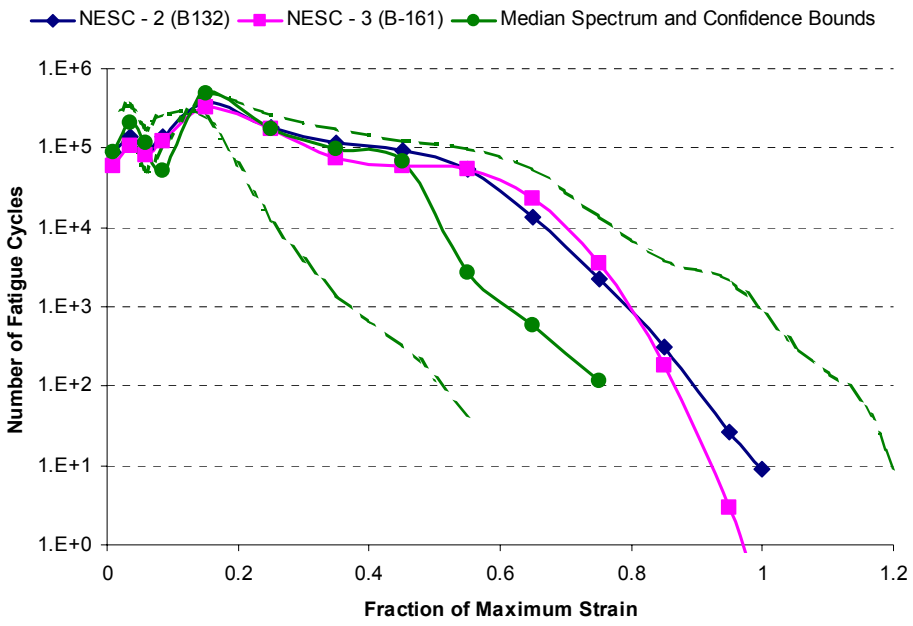

Figure 4-26: Comparison of median probabilistic and deterministic strain spectra. The bounds on the probabilistic spectrum are determined by assuming that each Flight Stage is at its 95% confidence level.

The probabilistic model has replaced the conservatism from the deterministic spectrum with explicit uncertainty quantification. The median strain spectrum at strain gauge B132 in Figure 4-26 is converted into a sample stress spectrum at a particular crack site through the following equation:

$$\sigma_{site} = L \quad TF_{site|B132} \quad E \quad \varepsilon_{med} \tag{4.9}$$

In this equation L is a lognormally or normally distributed load uncertainty factor with median 1 and COV as per Table 4-6, E is the Young's modulus (0.0312 x 10^6 ksi) and $TF_{site|B132}$ is the mode dependent transfer factor which accounts for the spatial variation of the stress along the flowliner perimeter. Transfer factors are the subject of the next section.

4.4.4 Transfer Factors

The rainflowed spectrum in Figure 4-26 describes the cycle count for stresses at the strain gauges. These mid-ligament strains are transformed into stresses at the crack locations by means of transfer factors.

Due to the fact that one ligament is approximately 1" long and all others are 0.75" long, the axi-symmetry is disturbed and it is expected that the various modes will lock in due to these geometric imperfections. Each of the 38 slots will therefore experience different load levels and this section describes our approach to take this location dependence of the transfer factor into account. This location dependence of the transfer factors is an essential component of the reliability assessment of the entire flowliner system.

Multiple structural vibration modes are active during the various Flight Stages. The present analysis is based on the assumption that only a single vibration mode is active during each Flight Stage. SwRI used the same vibration modes in the NESC-2 spectrum as the NIA/NASA Langley team; these are shown in Table 4-8.

Table 4-8: List of assumed dominant vibration modes per Flight Stage in NESC-2 spectrum for the downstream flowliners.

Flight stage	Vibration Mode
1	5ND
2	5ND
3	C4ND
4	C4ND
5	C4ND
6	5ND
7	C4ND

Figure 4-27 through Figure 4-30 show the axial stresses along the inner and outer diameter for the 2 vibration modes assumed to be dominant in the NESC-2 spectrum (5ND and C4ND) for the downstream flowliner. These stresses were computed using NASTRAN and made available to SwRI by Swales Aerospace. The transfer factors that relate the stress at strain gauge B132 to the stress at the crack site depend on both the slot number and the mode shape.

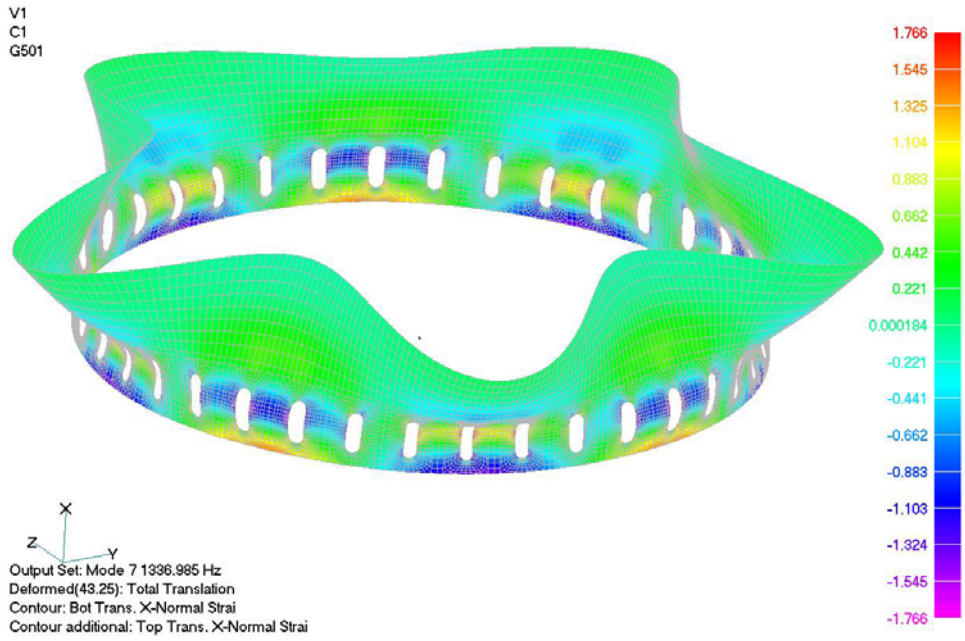

Figure 4-27: Axial stress along the flowliner ID for the 5ND Mode [courtesy of Swales Aerospace].

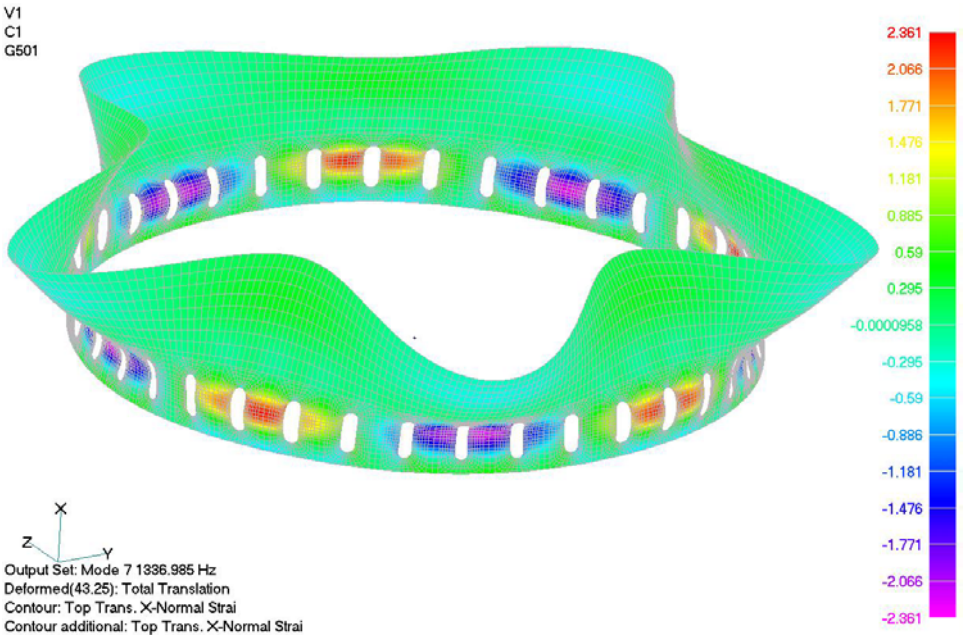

Figure 4-28: Axial stress along the flowliner OD for the 5ND Mode [courtesy of Swales Aerospace].

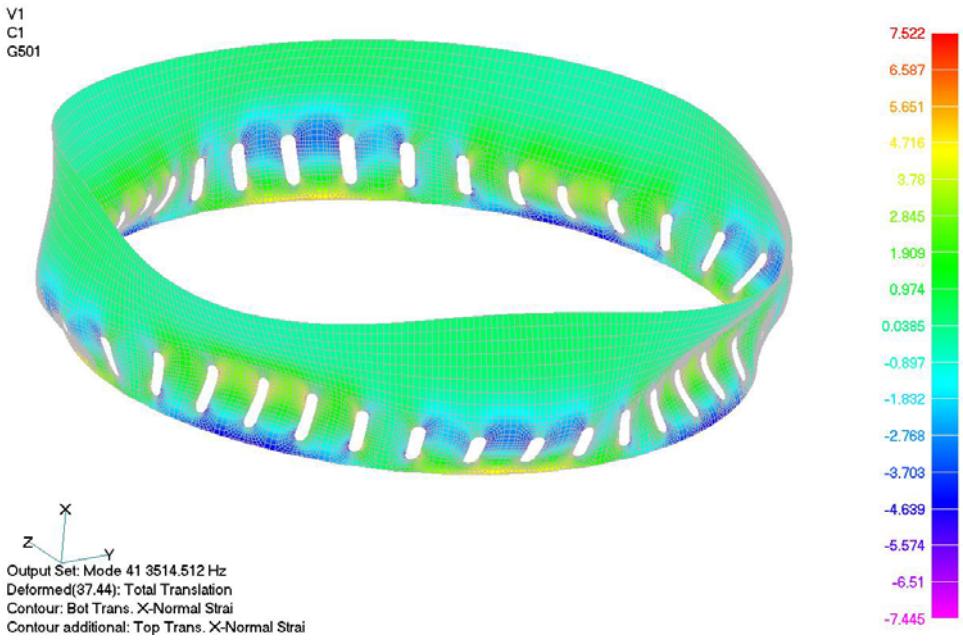

Figure 4-29: Axial stress along the flowliner ID for the C4ND Mode [courtesy of Swales Aerospace].

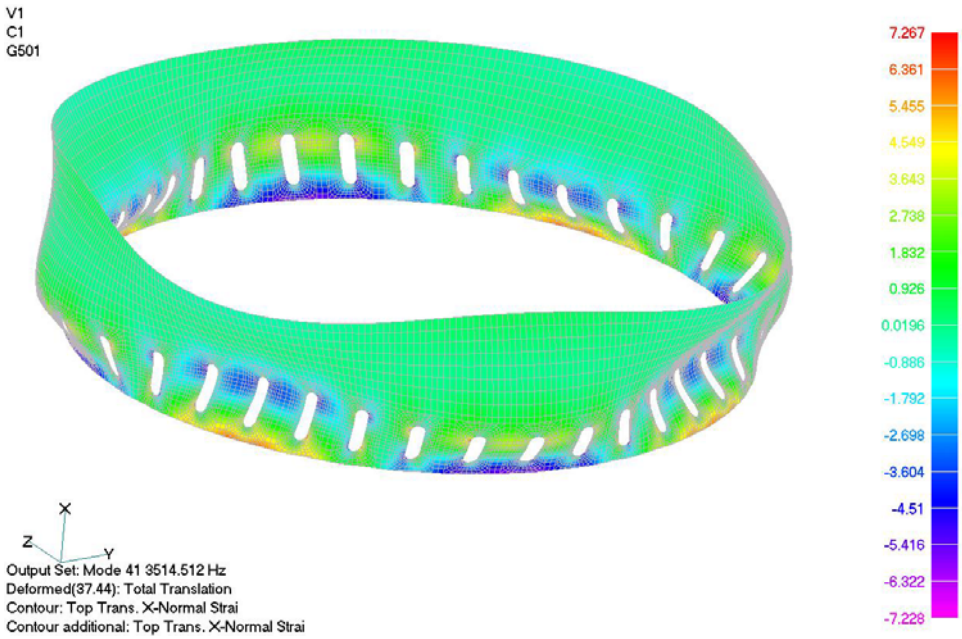

Figure 4-30: Axial stress along the flowliner OD for the C4ND Mode [courtesy of Swales Aerospace].

From the NASTRAN results, the transfer factors between the B132 location and each of the ligaments was computed for both the 5ND and C4ND modes for the crack site Location B at both the left and right end of the ligament and along both the inner and outer diameter (Figure 4-31 and Figure 4-32):

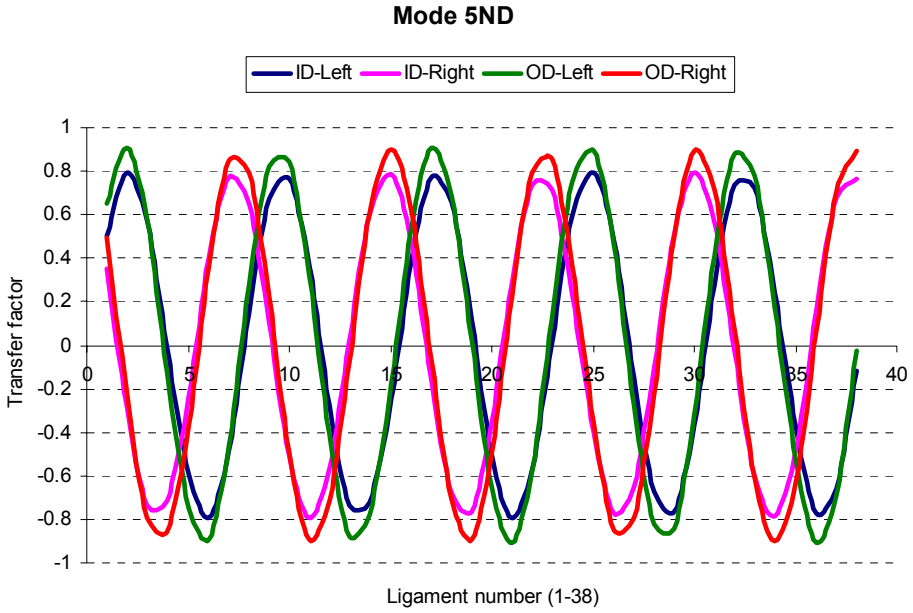

Figure 4-31: Transfer factor for mode 5ND at crack site B and various potential crack locations.

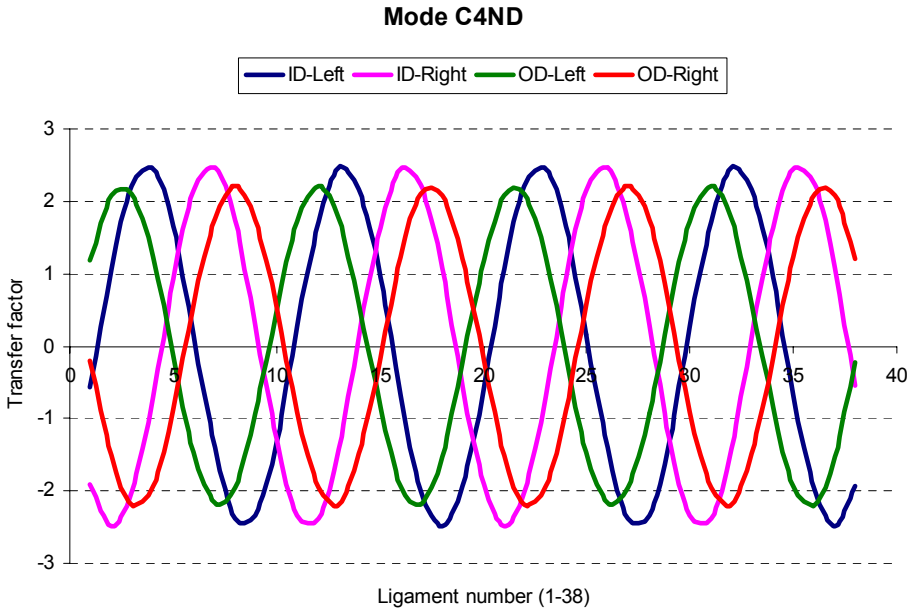

Figure 4-32: Transfer factor for Mode C4ND at crack site B and various potential crack locations.

$$TF(M, ID \mid OD, location) = \frac{\varepsilon_{M,ID|OD,location}}{\varepsilon_{M,B132}} \tag{4.11}$$

Where M is vibration Mode, ID is inside diameter at Location B, OD is outside diameter at Location B, and location is either right or left, as illustrated in Figure 4-33.

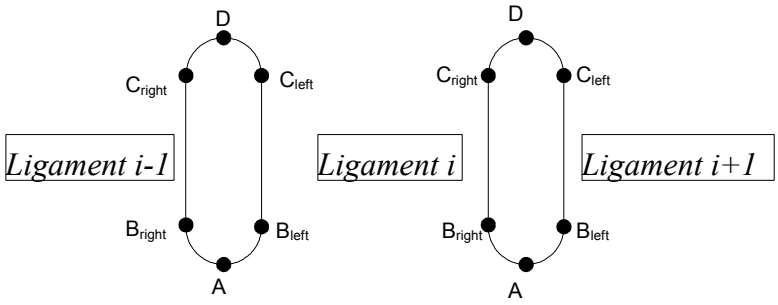

Figure 4-33: Crack site location nomenclature.

Figure 4-31 illustrates that there is little difference between the stresses along the ID and OD for Mode 5ND. Membrane action seems to be the primary loading mechanism for this mode and only very shallow gradients exist through the thickness of the ligament. For Mode C4ND in Figure 4-32, the anti-symmetric component is identical along ID and OD, but for the symmetric component a pronounced change is observed in the flowliner thickness direction.

Since the geometric variability of the flowliner is ignored, no uncertainties are associated with the modal analysis and the transfer factors. The Swales transfer factor does not depend on the location and is intended for a deterministic analysis of the worst location. It compares the maximum strain at the crack site to the maximum strain at the strain gauge locations:

$$TF(M, ID \mid OD) = \frac{\max\limits_{all\ ligaments} \varepsilon_{M,ID|OD}(location)}{\max\limits_{all\ strain\ gauges} \varepsilon_{M}(strain\ gauge)} \tag{4.12}$$

The maximum transfer factors computed for crack site B using Eq. (4.12) are compared with the Swales and Boeing transfer factors in Table 4-9. The 3ND mode, which is used in the NESC-1 and several certification spectra, is included in this table. The transfer factors are not identical to the Swales transfer factors [ITA Phase 1 Report, Appendix D.2.3] because the location of maximum strain at gauge B132 does not always coincide with the node that marks the transition between the semi-circle and the straight edge of the slot (Figure 4-33). The SwRI results are based on averages for the two elements that share the nodes 1, 20, 101, … (Figure 4-34), whereas Swales used the maximum strain in the neighborhood of crack site ‘B’.

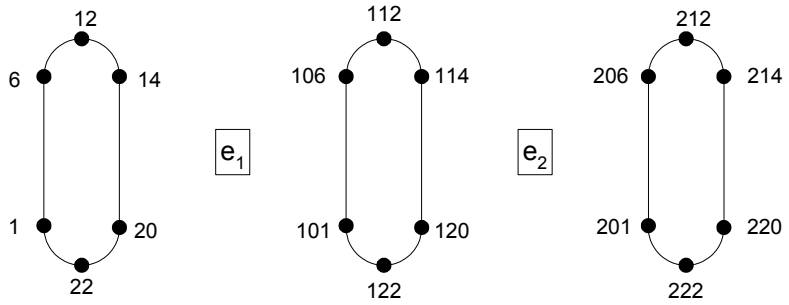

Figure 4-34: Node numbers in NASTRAN model.

To compensate for this discrepancy, the location-dependent transfer factors in Figure 4-31 and Figure 4-32 were multiplied by 1.16, 1.38, and 1.22 for Modes 5ND, C4ND and 3ND, respectively.

Table 4-9: Comparison of maximum transfer factors TF for crack site "B"

Mode Shape	Boeing	Swales	Eq. (4.12)
5ND	0.6	0.67	0.58
C4ND	2.4	3.41	2.46
3ND	1.2	1.38	1.13

4.4.5 Stress Gradients

In addition to the stresses at each of the potential crack sites, the crack growth analysis requires the local spatial stress distribution. The precise distributions are not easily discerned from Swales' NASTRAN plots. A shell dynamics analysis was performed at NIA/NASA Langley [James et al, 2004] and the Langley team sent SwRI 'worst case' gradients for each of the participating modes.

Symmetric and anti-symmetric gradient basis functions were generated to mimic these mode-dependent gradients (Figure 4-35). The steepness of the stress gradients in the symmetric and anti-symmetric components matches the 'worst case' gradients, which were provided by NIA/NASA Langley. For each slot, linear combinations of these basis functions were derived such that the combined gradient matches the transfer function values at the left and right end of each ligament as follows:

$$\alpha_{M,ligament,ID|OD} = \frac{TF_{Left,M,ligament,ID|OD} + TF_{Right,M,ligament,ID|OD}}{2}$$
$$\beta_{M,ligament,ID|OD} = \frac{TF_{Left,M,ligament,ID|OD} - TF_{Right,M,ligament,ID|OD}}{2} \qquad (4.13)$$

The respective contributions of the symmetric and anti-symmetric gradient factors for all ligaments are shown in Figure 4-36 for Mode 5ND and in Figure 4-37 for Mode C4ND. As indicated by the subscripts in Eq. 4.13, the α and β coefficients are computed for each mode on

the left and right edges of each ligament along both the ID and OD. The stress gradient along the ligament length is determined by α, β and the basis functions shown in Figure 4-35. Linear interpolation between the OD and ID stresses was used to compute the stress gradient in the through-ligament direction. For illustration purposes, the resulting modal stress fields for all 38 ligaments are shown in Figure 4-38 through Figure 4-75. It should be noted that these are alternating stress fields, and that the stresses reverse sign in each half-cycle.

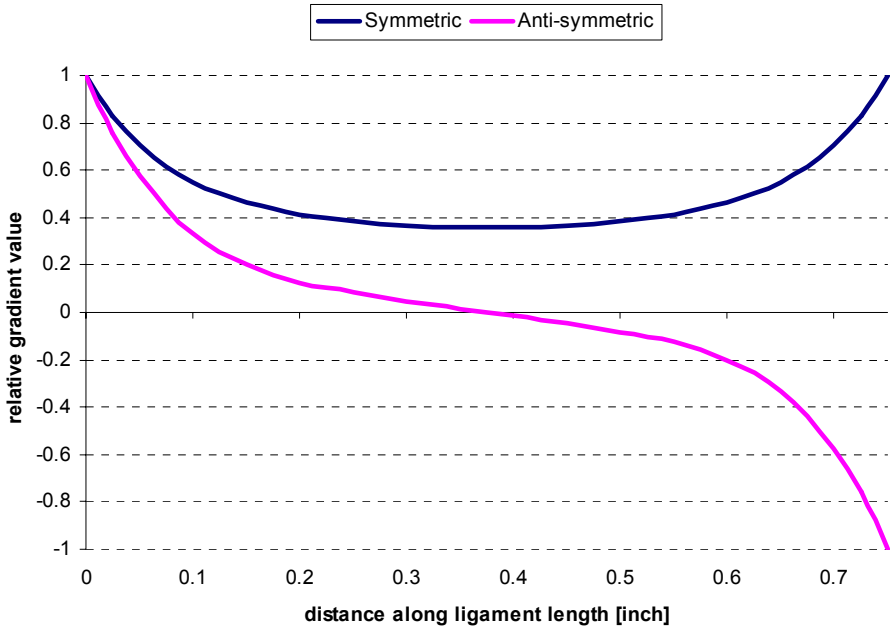

Figure 4-35: Gradient basis functions.

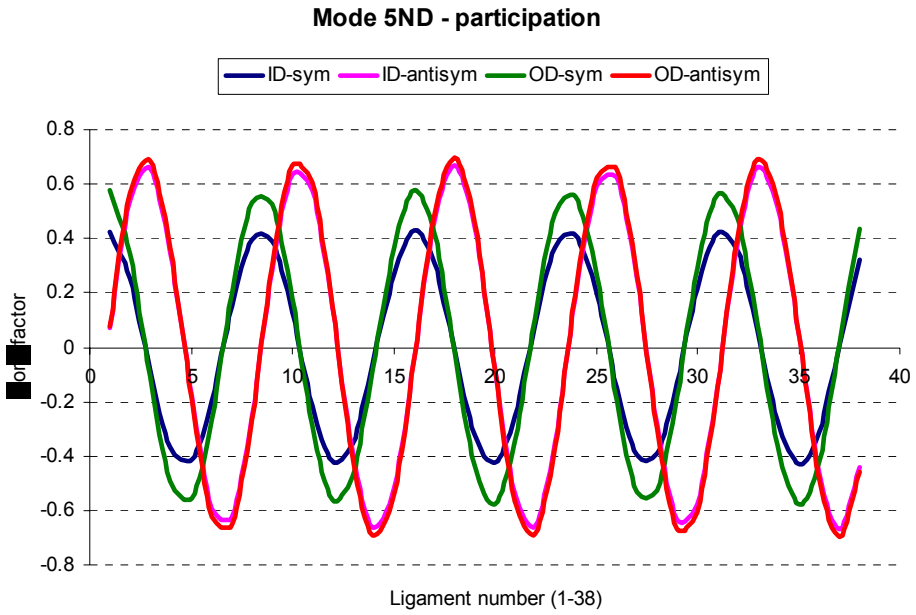

Figure 4-36: Contribution of symmetric and anti-symmetric gradient to total stress distribution.

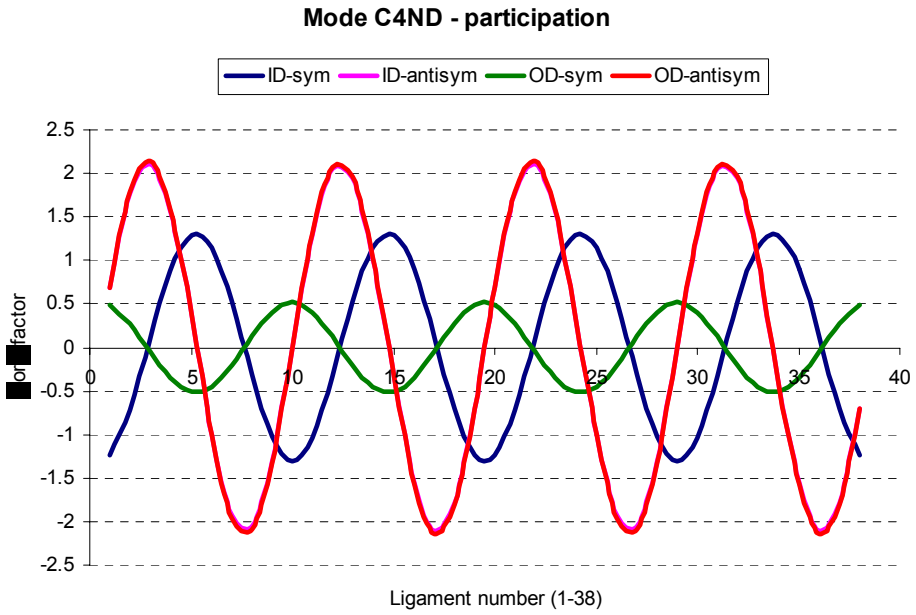

Figure 4-37: Contribution of symmetric and anti-symmetric gradient to total stress distribution.

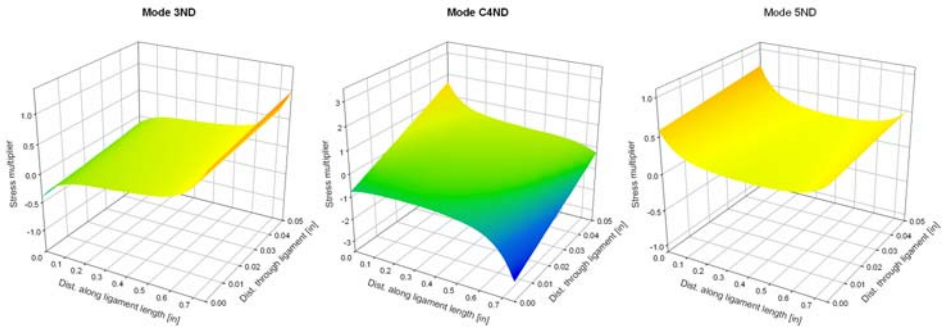

Figure 4-38: Local stress fields for ligament 1.

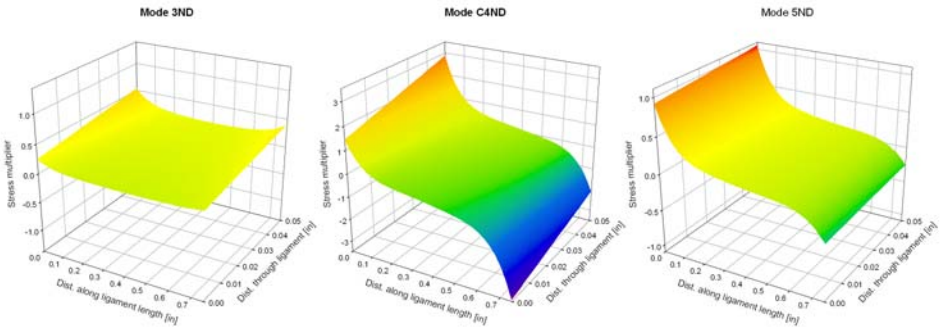

Figure 4-39: Local stress fields for ligament 2.

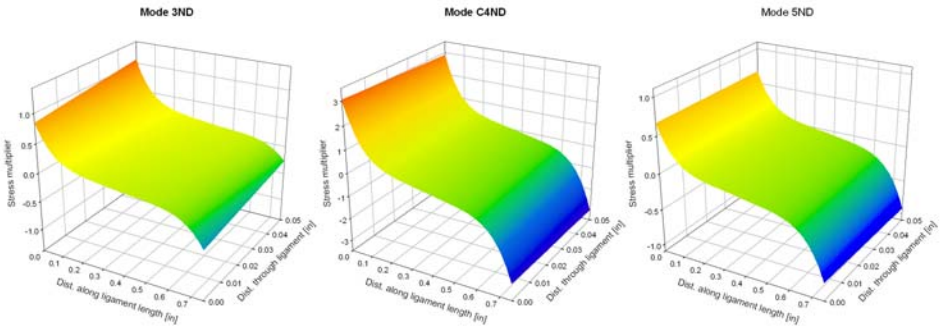

Figure 4-40: Local stress fields for ligament 3.

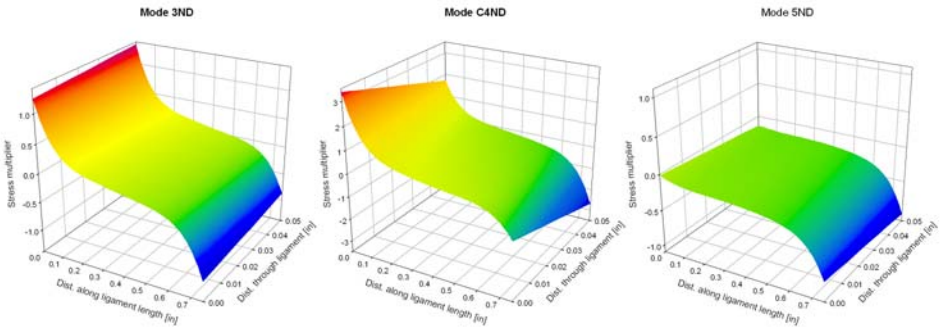

Figure 4-41: Local stress fields for ligament 4.

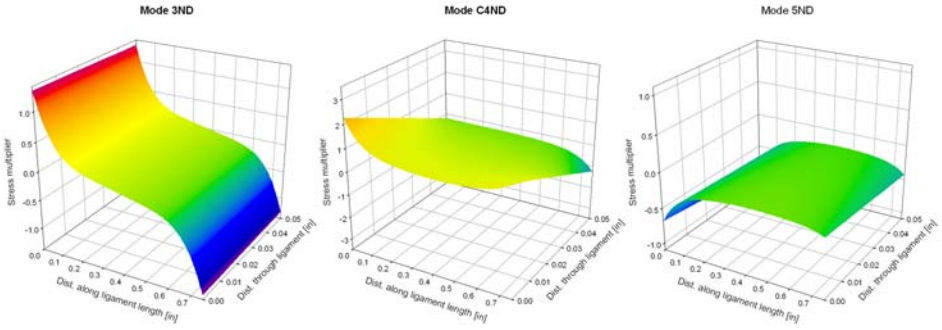

Figure 4-42: Local stress fields for ligament 5.

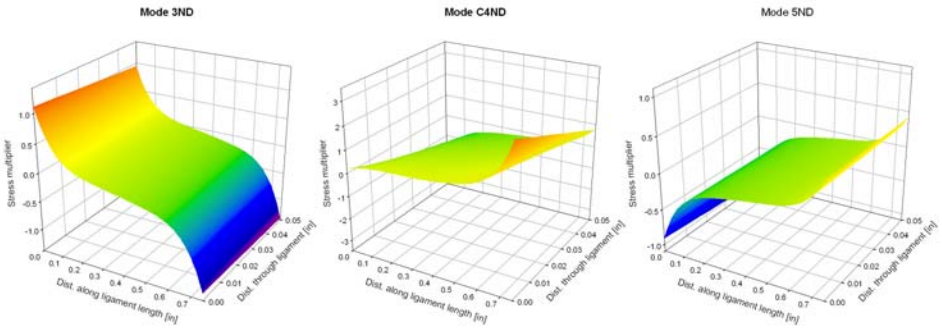

Figure 4-43: Local stress fields for ligament 6.

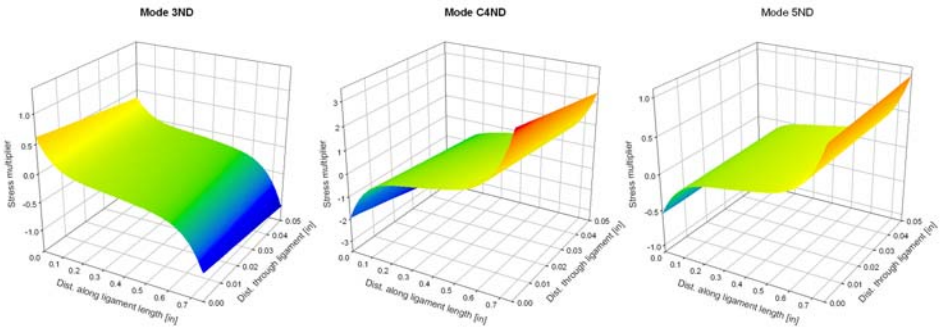

Figure 4-44: Local stress fields for ligament 7.

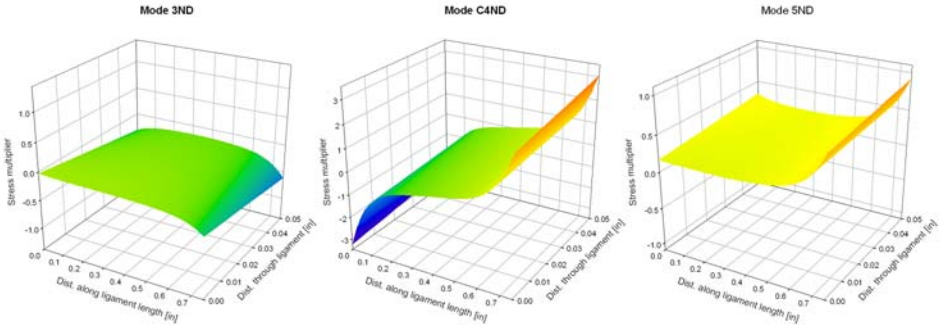

Figure 4-45: Local stress fields for ligament 8.

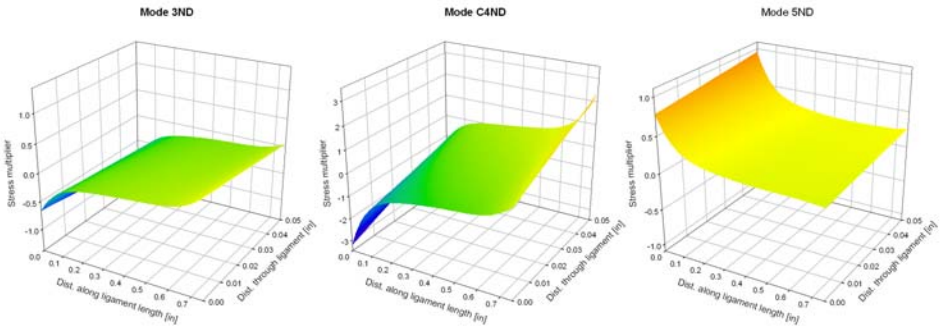

Figure 4-46: Local stress fields for ligament 9.

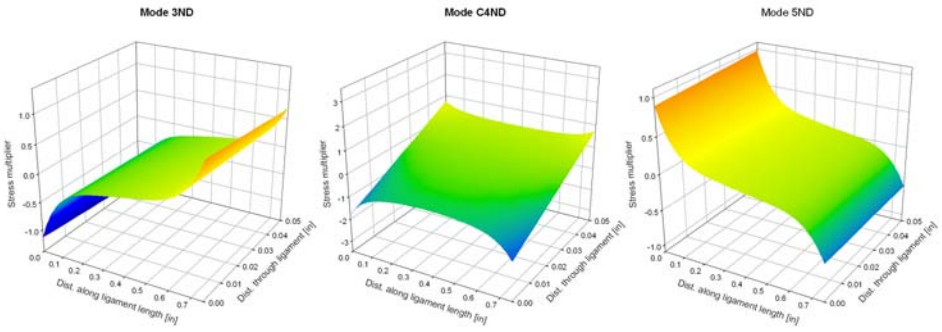

Figure 4-47: Local stress fields for ligament 10.

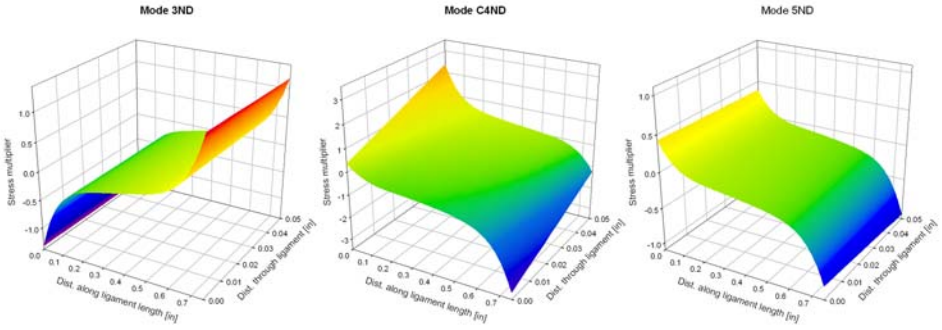

Figure 4-48: Local stress fields for ligament 11.

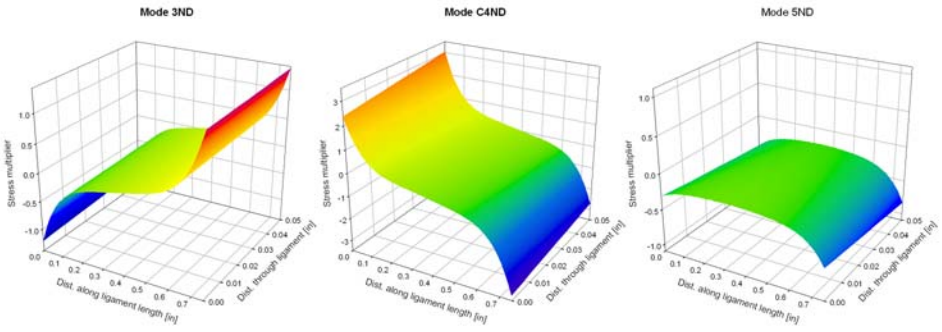

Figure 4-49: Local stress fields for ligament 12.

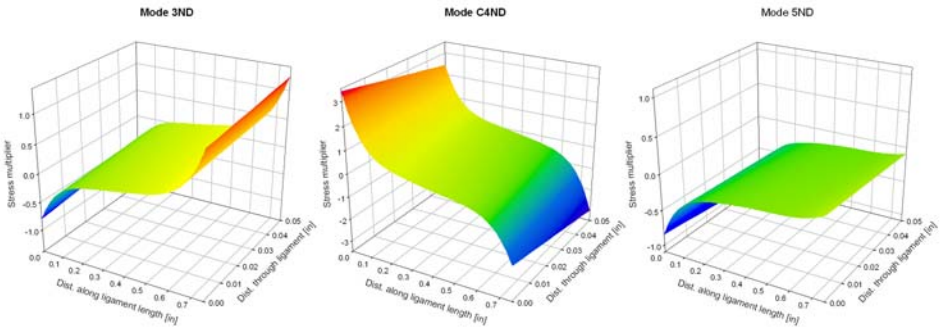

Figure 4-50: Local stress fields for ligament 13

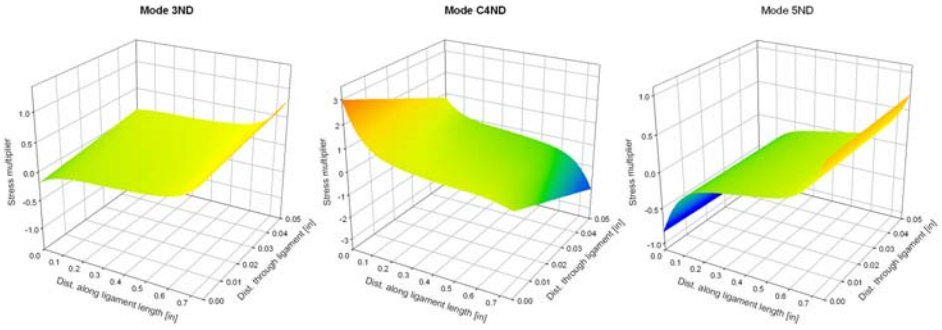

Figure 4-51: Local stress fields for ligament 14

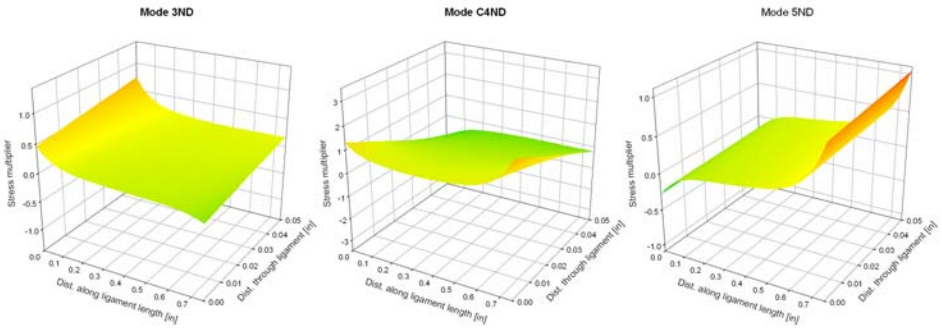

Figure 4-52: Local stress fields for ligament 15

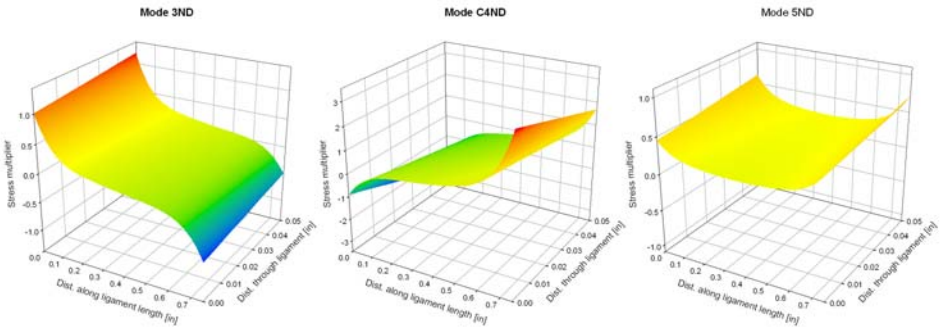

Figure 4-53: Local stress fields for ligament 16

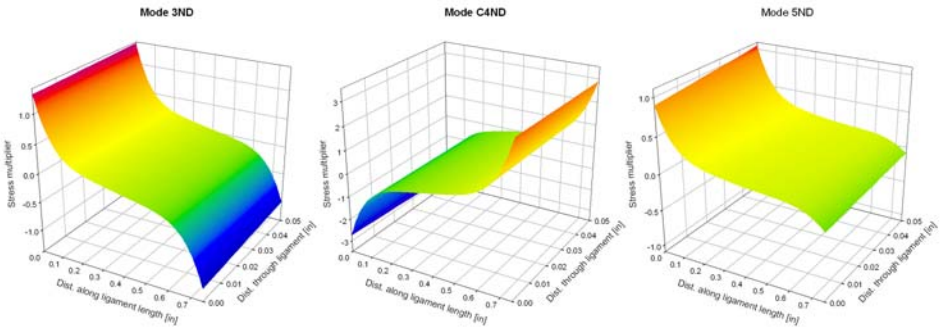

Figure 4-54: Local stress fields for ligament 17

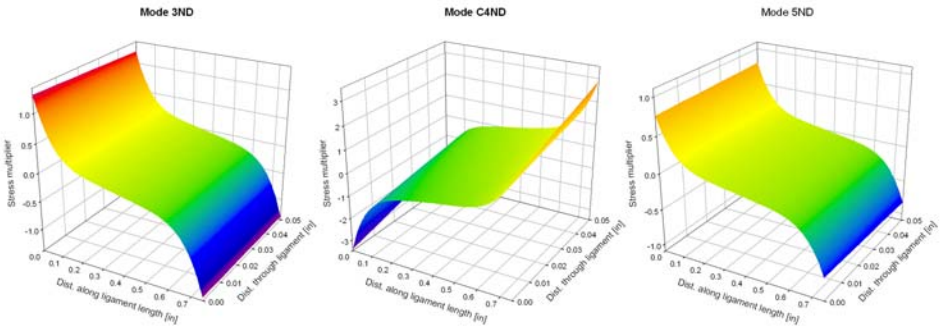

Figure 4-55: Local stress fields for ligament 18

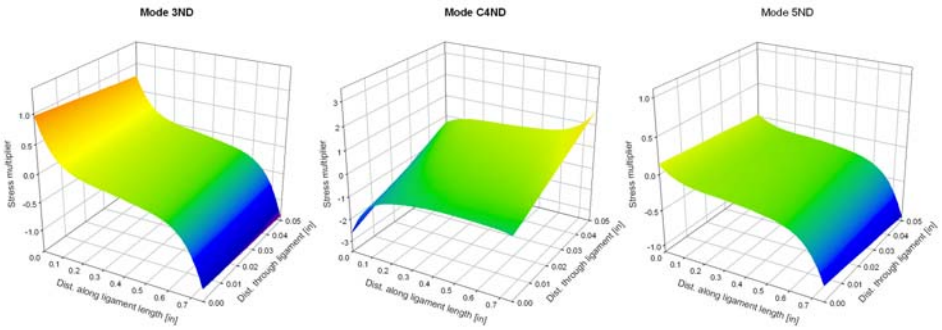

Figure 4-56: Local stress fields for ligament 19

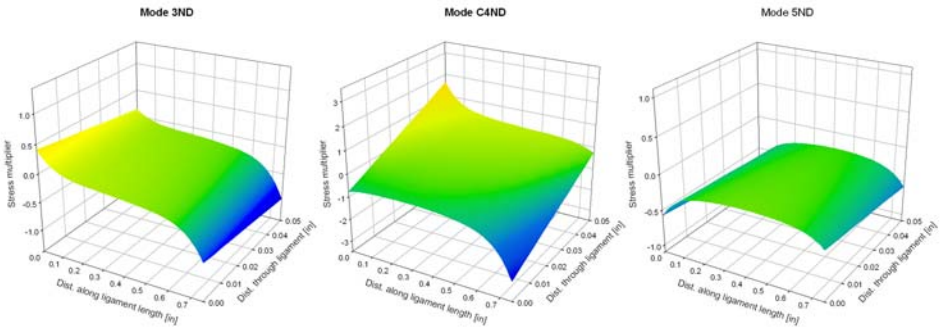

Figure 4-57: Local stress fields for ligament 20

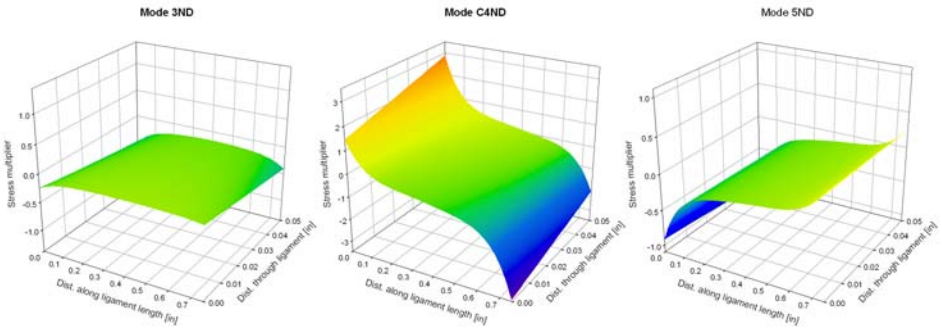

Figure 4-58: Local stress fields for ligament 21

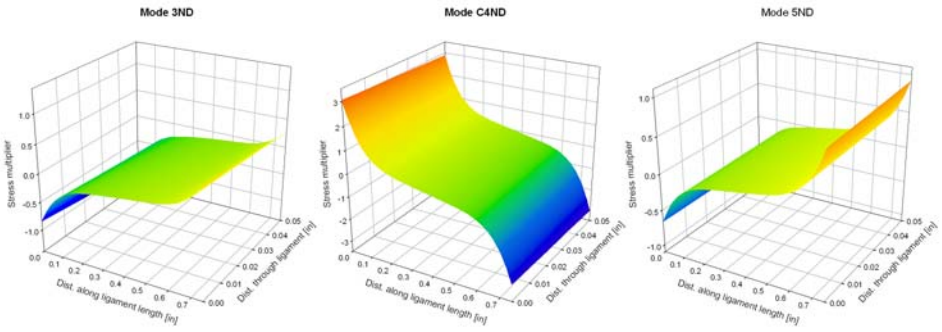

Figure 4-59: Local stress fields for ligament 22

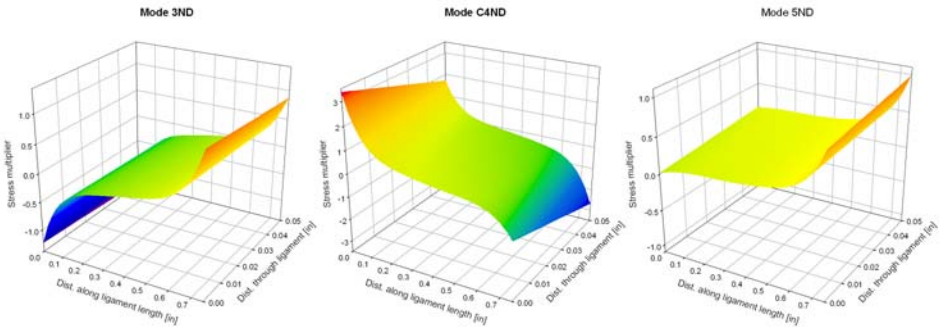

Figure 4-60: Local stress fields for ligament 23

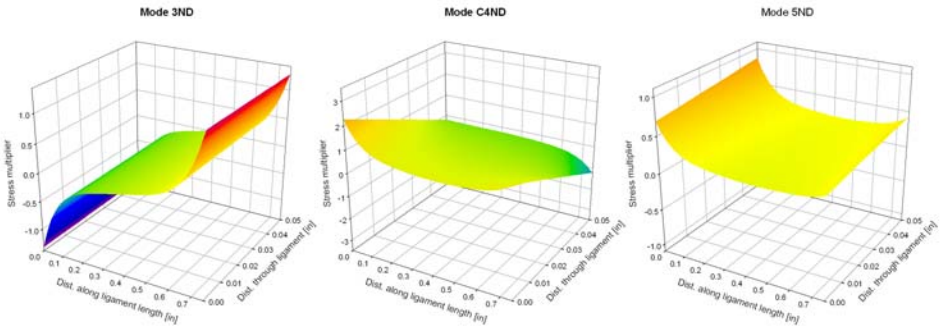

Figure 4-61: Local stress fields for ligament 24

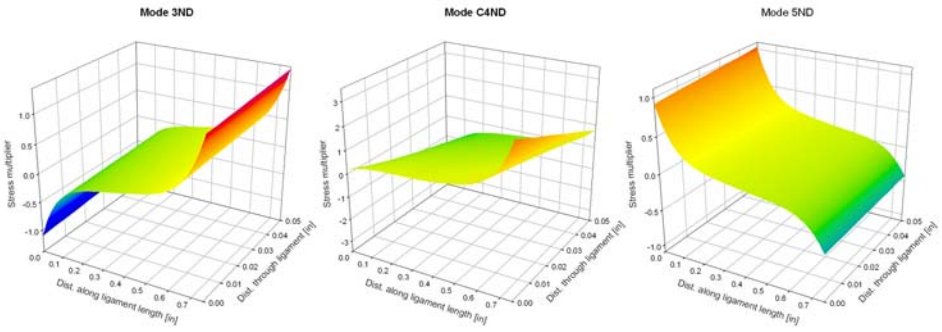

Figure 4-62: Local stress fields for ligament 25

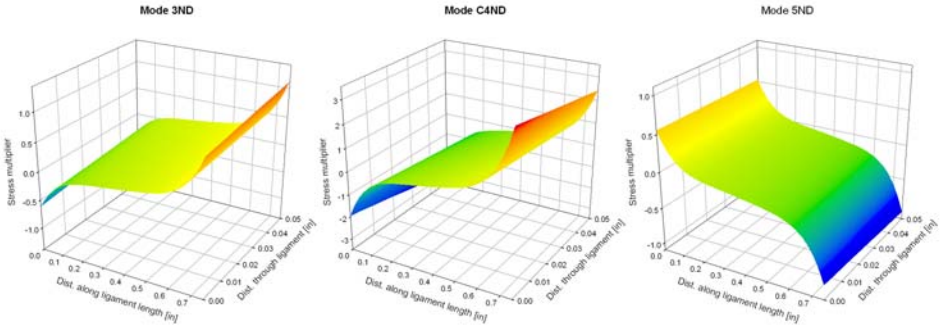

Figure 4-63: Local stress fields for ligament 26

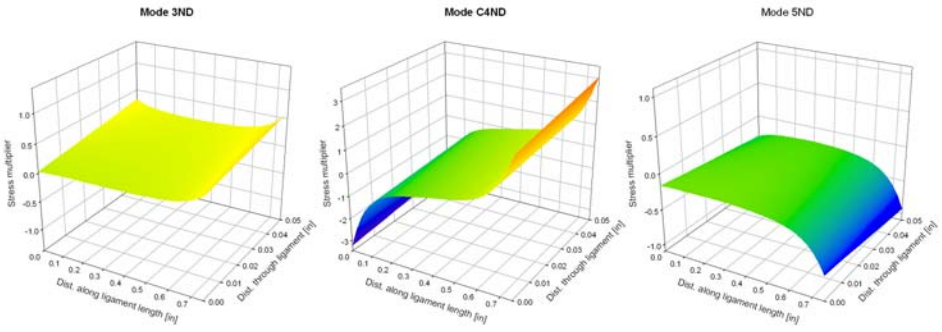

Figure 4-64: Local stress fields for ligament 27

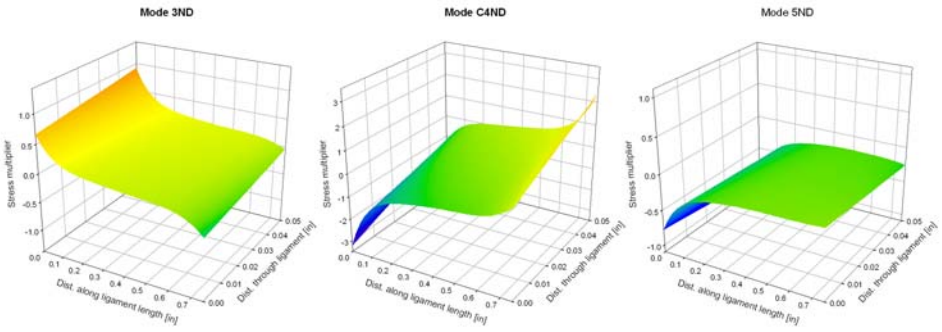

Figure 4-65: Local stress fields for ligament 28

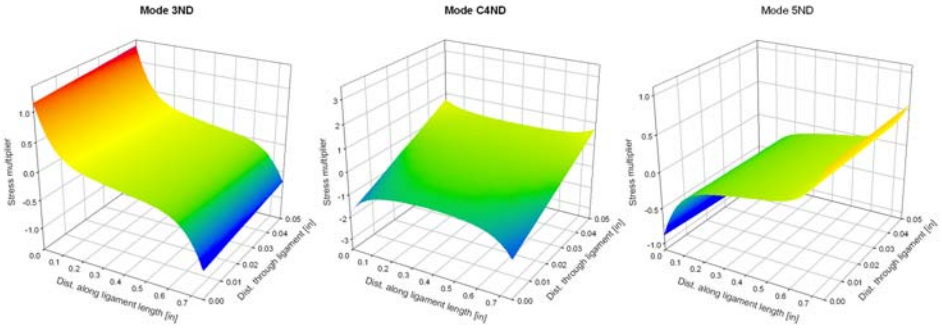

Figure 4-66: Local stress fields for ligament 29

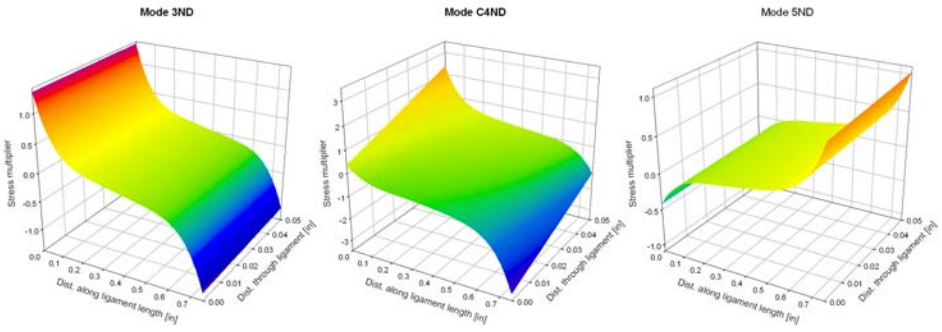

Figure 4-67: Local stress fields for ligament 30

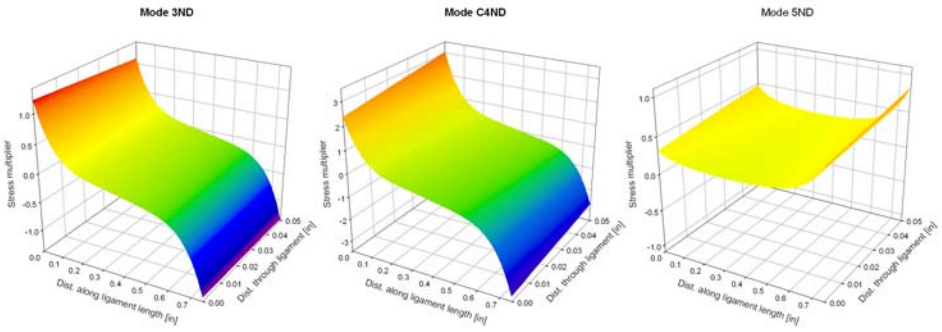

Figure 4-68: Local stress fields for ligament 31

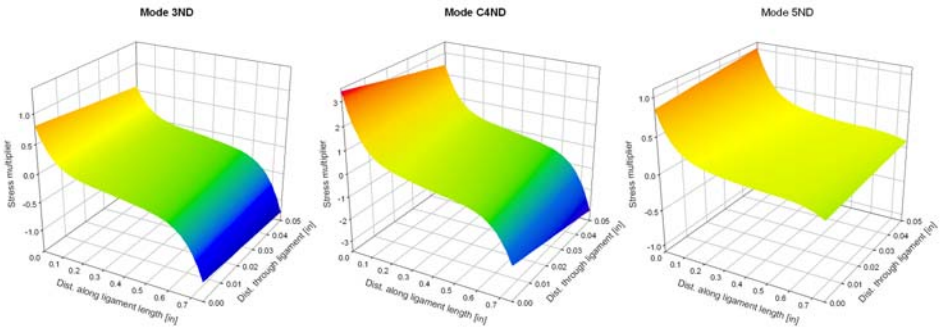

Figure 4-69: Local stress fields for ligament 32

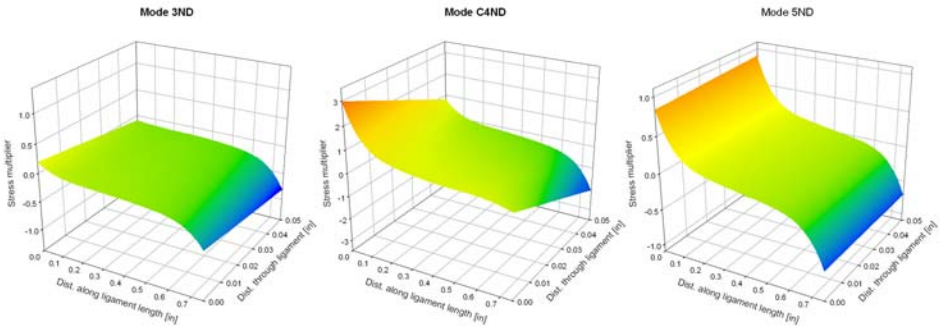

Figure 4-70: Local stress fields for ligament 33

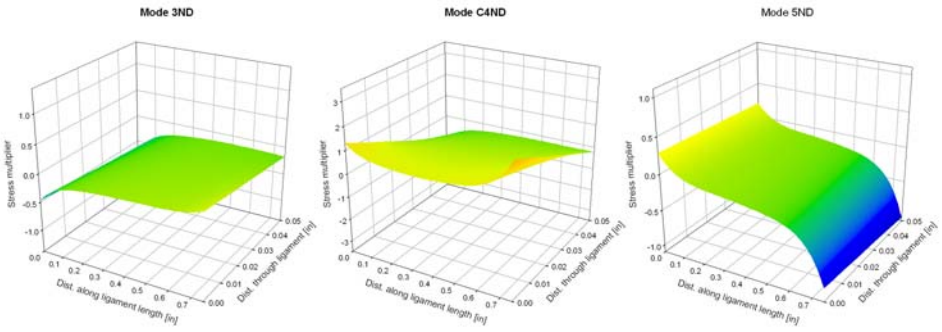

Figure 4-71: Local stress fields for ligament 34

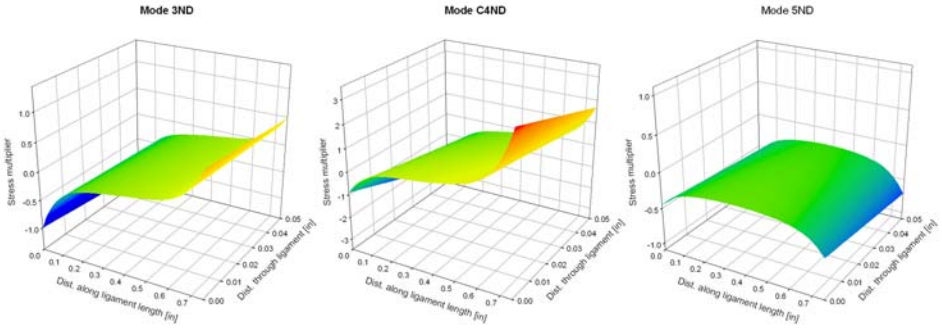

Figure 4-72: Local stress fields for ligament 35

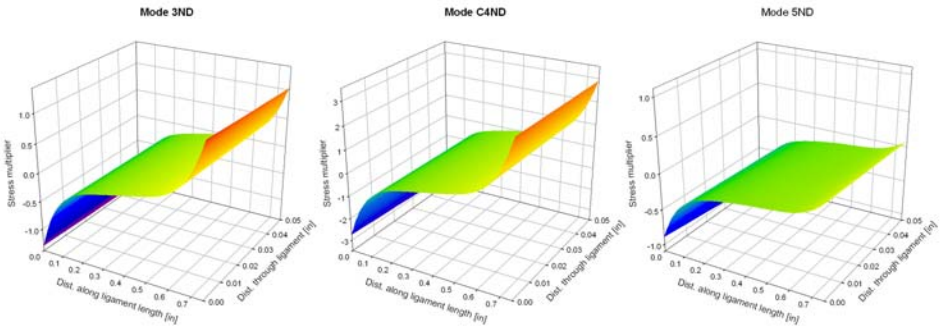

Figure 4-73: Local stress fields for ligament 36

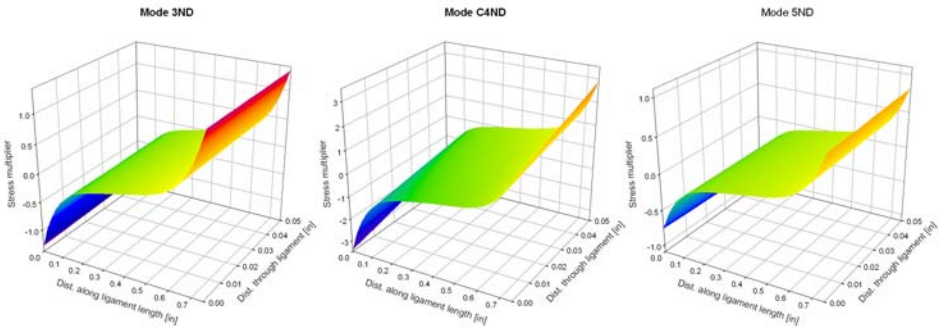

Figure 4-74: Local stress fields for ligament 37

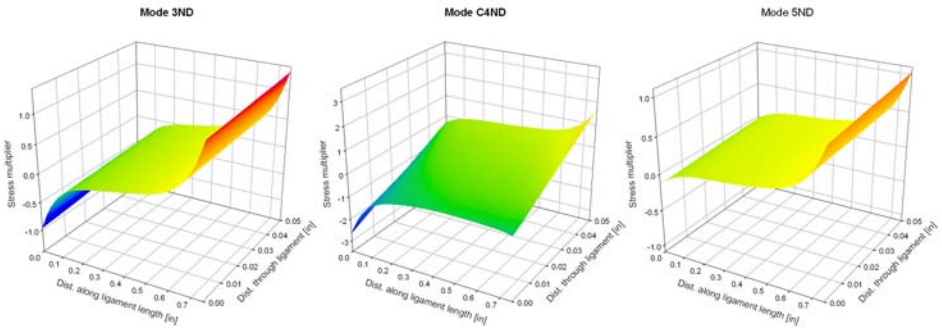

Figure 4-75: Local stress fields for ligament 38

5. PROBABILISTIC FATIGUE CRACK GROWTH ANALYSIS RESULTS

5.1 System Reliability Problem

The downstream flowliner consists of 38 ligaments, which all experience different stresses. The relative magnitude of the alternating stresses is determined by the mode-dependent transfer factors. In a deterministic analysis, the shortest lives are obtained in the ligaments with maximum alternating stress. Because of the large uncertainty associated with the initial crack size, material properties, and the stresses at each location, one cannot predetermine which slot is most likely to result in failure. Larger initial cracks may originate at lower stress locations, yet still result in a shorter life than a small initial crack at a higher stress location. It is therefore possible that due to the scatter in initial defect size some of the ligaments with less severe stresses could still make a significant contribution to the overall failure probability.

The system risk assessment takes the variable loading on all 38 ligaments of the downstream flowliner into account. Crack growth followed Scenario 2 (see Section 3) in which the crack begins with a corner crack and transitions to a through-crack in response to the local stress gradient. As in the deterministic model in Section 2, failure of the flowliner is defined as crack growth through 95% of the ligament length at any location. NESSUS keeps track of the critical life as well as which ligament is the most critical. This approach allows the computation of the relative contribution of each slot to the total failure probability.

It is possible for cracks to initiate at any of the four corners of the ligament between adjacent slots. Since the mean stress is tensile at the inner diameter and compressive on the outer diameter, there is insignificant probability of corner cracks growing from the OD positions. The analysis has therefore been limited to an assessment of both the left and right corner along the ID of all ligaments; cracks are likely to initiate at these locations since the residual stresses are tensile at the ID (and compressive at the OD). In addition, only cracks at Location B are considered since information on the dynamic stress gradients is currently only available at this location.

Since the dynamic stresses vary along the perimeter of the flowliner, the probability of fracture is different for each ligament. Figure 5-1 shows the contribution by each ligament to the system failure probability for the NESC-3 spectrum (defined in the next section). It is expected that the ligaments with the lowest life in the nominal, deterministic analysis will have the highest contribution to the total failure probability. Conversely, the failure probability contribution of each ligament is expected to be inversely proportional to the fatigue life under nominal conditions. The contribution factors shown in Figure 5-1 (for cracks at the left corner along the ID) generally track the inverse of the nominal, deterministic fatigue life as shown in Figure 5-2.

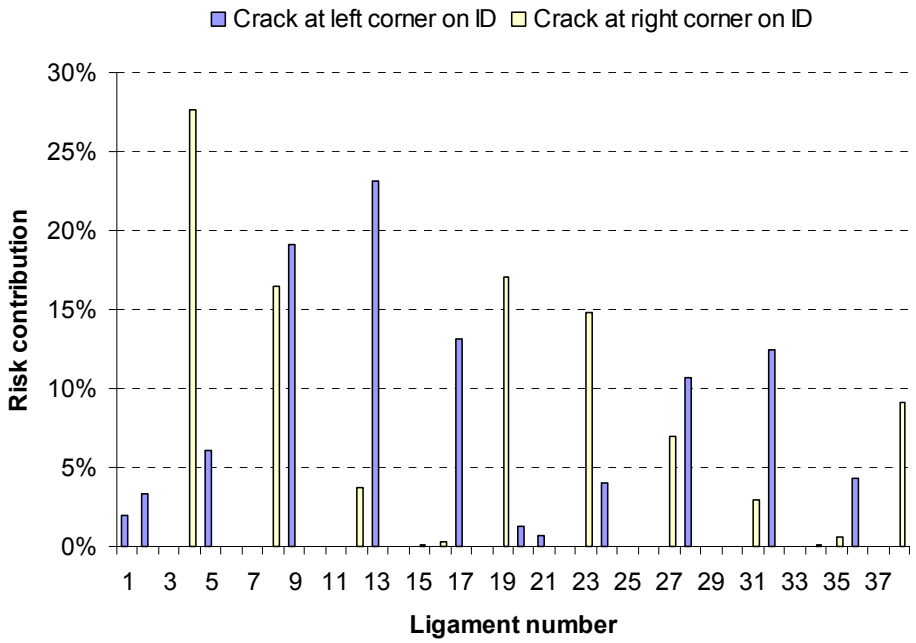

Figure 5-1: Contribution to system failure probability for each ligament using NESC-3 spectrum

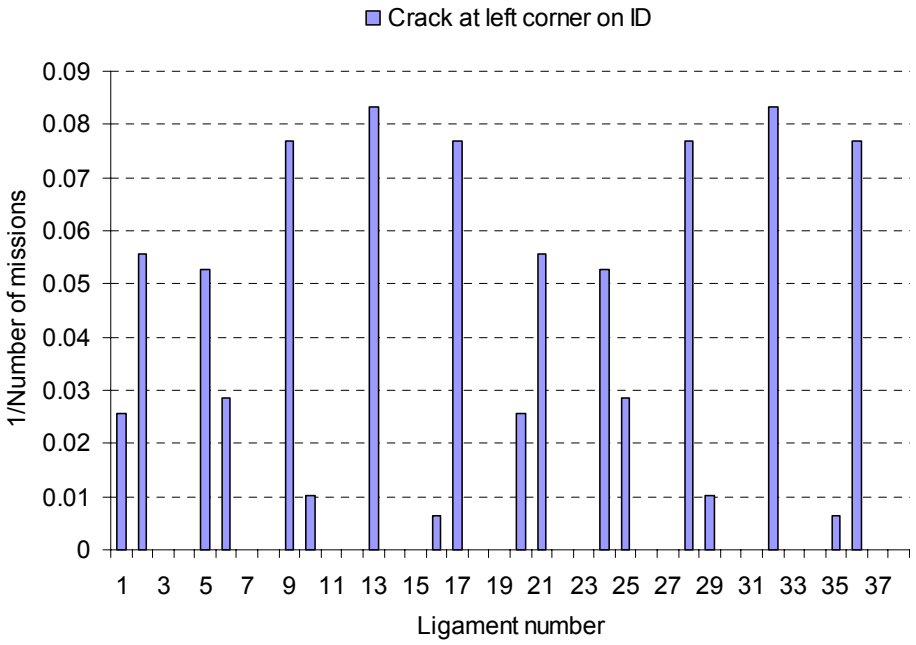

Figure 5-2: Inverse fatigue life at left ID corner for 0.02 in. initial flaw and median load levels and crack growth parameters.

Although different slots contribute to the failure probability depending on whether the crack originates at the left or the right corner, the left tail of CDF for the total mission life, which is of most interest in this application, is not significantly different for different crack locations. This is shown in Figure 5-3 for the NESC-2 spectrum and in Figure 5-4 for the NESC-3 spectrum. These spectra have been developed and provided by NIA/NASA LaRC [James et al, 2004].

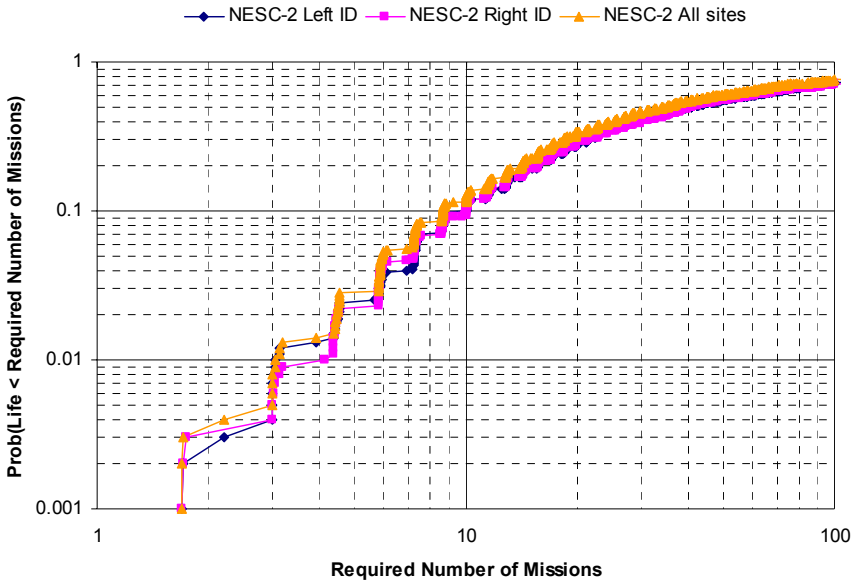

Figure 5-3: Life PDF as function for each crack origination site along the ID ligament (NESC-2).

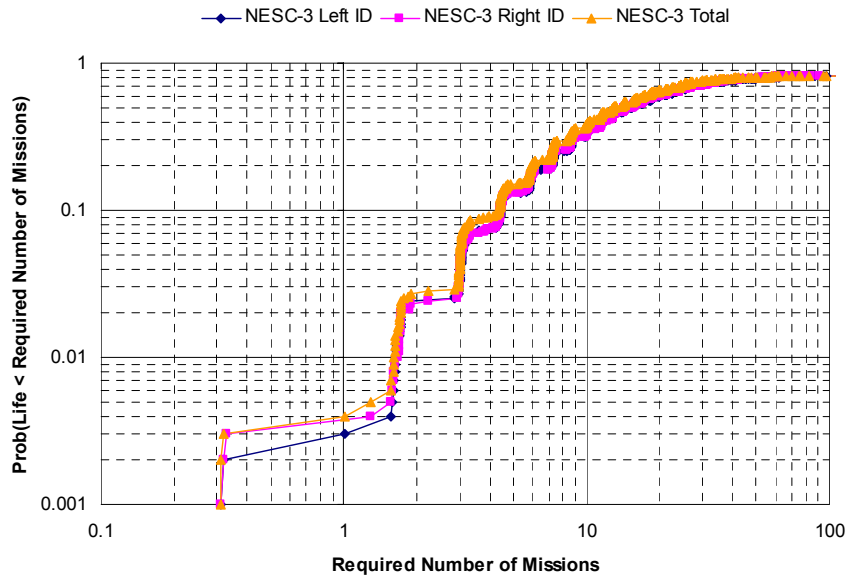

Figure 5-4: Life PDF as function for each crack origination site along the ID ligament (NESC-3).

5.2 Overview of Analysis Scenarios

The fatigue life is affected by several sources of uncertainty, which are described in Section 4:

- Mean and alternating stress level
- Initial defect size
- Crack growth material properties

For some of these sources no consensus estimates have yet been reached. In these cases we either used a conservative approach or analyzed various scenarios. For instance, a conservative approach was taken to model the mean (residual) stress [ITA Phase 1 Report, Appendix D]. A deterministic mean tensile stress level of 70 ksi was assumed along the ID, along the OD the mean stress is equal but compressive.

Since several spectra have been used by the ITA Team and Project Office for the alternating stresses, the probabilistic analysis were performed for many of these spectra:

- NESC-2 load spectrum: derived by NASA LaRC on the basis of the Swales rainflow count from the B132 strain gauges from the BTA test articles. All of the seven flight stages are assumed to be independent of each other. Note that the NESC-2 spectrum has 1.827 million cycles in 64 load blocks, whereas the Swales spectrum has only 1.296 million cycles in 78 load blocks.
- Reduced NESC-2 spectrum: the median load levels have been adjusted to reduce the conservatism associated with picking the worst time window of the worst test. Section 4 describes the approach to quantify the uncertainty on the load spectrum. All 7 flight stages are assumed independent.
- Correlated reduced NESC-2 spectrum: same median stress levels and uncertainty as the reduced NESC-2 spectrum. All load stages are assumed fully correlated.
- NESC-3 load spectrum: this spectrum is identical to NESC-2 except for a multiplier (1.238) that applies to all load levels. Each of the 7 flight stages is assumed independent.
- Certification spectrum: the deterministic analysis in Section 3 identified the downstream certification spectrum associated for the case Engine #3 out (dn_1.17_E3_engine_out.txt) as the case with the least amount of missions to failure. Note that the failure probability associated with this scenario is conditional upon the loss of engine #3. The probability of losing an engine has been estimated to be approximately 1/800 [Harris, 2004]. Thus, the total failure probability associated with the loss of engine scenario is:

$$P_{Total} = p(Life<4 \mid \text{Engine \#3 out}) \times p(\text{Engine \#3 out}) \tag{5.1}$$

For each of the above spectra the variance in RMS strains was determined on the basis of the observed variance during all applicable test intervals (see Section 4).

As described in Section 4, three lognormal POD curves have been used to study the effect of the initial defect size distribution. The first curve has a median value of 20 mils for the initial crack size. Its 99th percentile was set at 75 mils. The second curve has a median of 40 mils and a 99th percentile at 0.15 inch. The third and final curve has a median of 75 mils and a 99th percentile at 0.28 inch.

The effect of uncertainty in the fatigue crack growth properties has been considered as well. Two cases are considered: a nominal uncertainty model, described in Section 4 and an increased scatter model. The increased scatter model attempts to simulate the effects of heat-to-heat variability in the lower end of the crack growth curve. To this extent, the standard deviation on the orientation of the left leg (i.e. θ_1) has been doubled.

5.3 Baseline Flowliner System Risk Results

The probabilities of not meeting the required number of missions with the baseline NESC-2 and NESC-3 spectra are shown in Figure 5-5. Fractional missions are counted on the basis of number of completed load steps. Within each flight stage the load steps are sorted in decreasing alternating stress order. Since most damage occurs in the early load steps, the CDF curves are stair-stepped [Hudak et. al. 2004].

Perhaps the most important feature of the CDF curves is the slope, since it indicates how quickly the failure probability changes as a function of the required number of missions. If the CDF curve is quite steep, the failure probability rapidly drops orders of magnitude as the required number of missions is decreased. In this case if the average life is N_f missions (with $N_f > 1$ representing a safety factor), the probability of not meeting a single mission would be relatively small. However, if the CDF is flat, the probability of exceeding a single mission may be of a similar order of magnitude than the 50% risk associated with the median life N_f. As such the slope of the CDF curve is related to the required safety factor. To ensure adequate safety for a single mission, a larger safety factor n will be required for a flat CDF curve than for a steep CDF curve.

For this analysis the median value of the load spectrum was set equal to the nominal values used in the deterministic analysis by NIA/NASA Langley. The uncertainty on the loads, initial crack size and crack growth properties are as per Section 4. The POD with median flaw size equal to 20 mils was used to model the initial crack size.

The probability that the flowliner fatigue life does not exceed 4 missions is approximately 1.4% for NESC-2 and 7.5% for the NESC-3 spectrum. For NESC-3 the probability of failure during a single mission is approximately 1/300. These results were obtained using 5000 Monte Carlo simulations. The CDF of 95% sampling confidence intervals for the failure probability estimates are shown in Figure 5-5. Note that the median lives (corresponding to an exceedance probability of 50%) are very similar to the life predictions in the deterministic analysis. Specifically, compare medium results in Figure 5-6 with minimum lives from Table 3-5 (NESC-2) and Table 3-6 (NESC-3) for Scenario 2. This provides a verification of the integration of the fatigue modeling in the probabilistic algorithms.

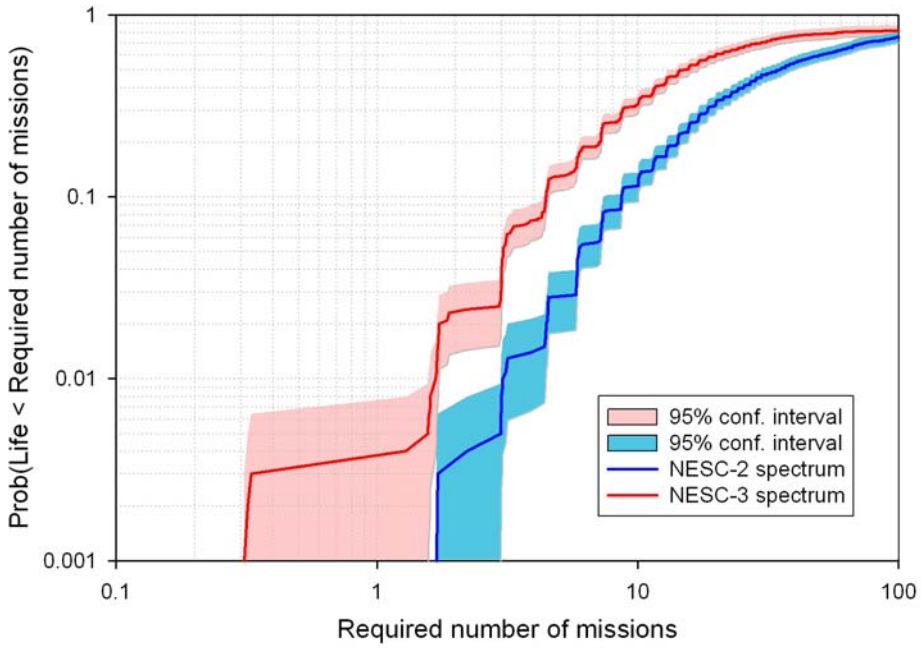

Figure 5-5: Baseline results for NESC-2 and NESC-3 spectrum.

5.4 Effect of the Load Spectrum on the Flowliner Risk

As explained in Section 4, the probabilistic load modeling can justifiably remove some of the conservatism in the nominal load spectrum while explicitly accounting for the variability of the loads. With this load level reduction, the probability of not achieving 4 missions is approximately 0.0004 for the NESC-2 spectrum with reduced median load levels. These results were computed using 5000 Monte Carlo samples and the narrower confidence bounds (compared to results in Figure 5-3) are also shown in Figure 5-6.

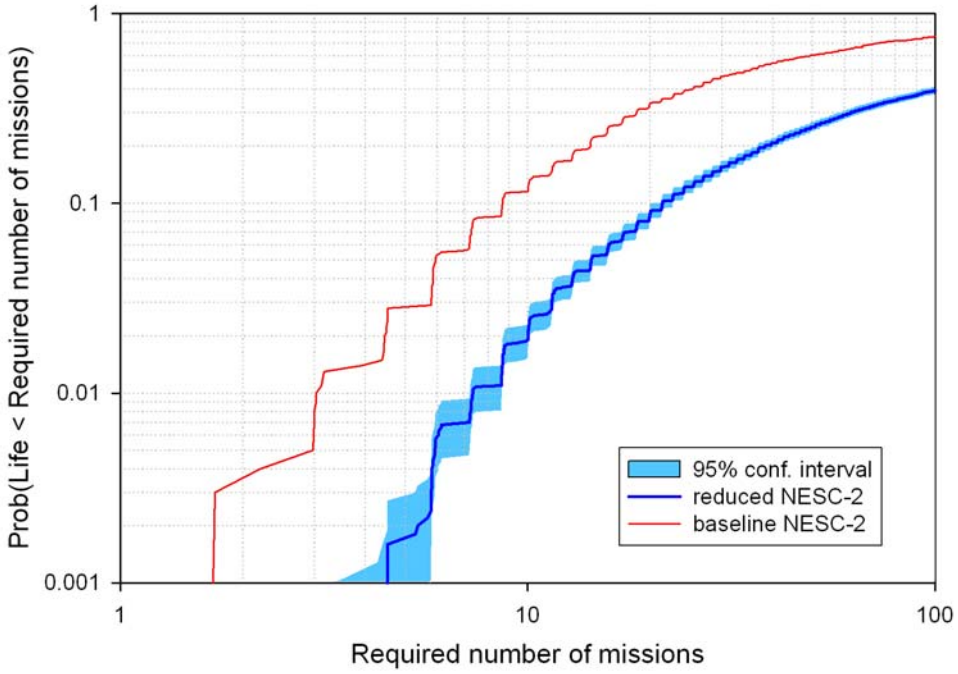

Figure 5-6: Effect of median load reduction in probabilistic analysis (reduced NESC-2) vs. conservative high-load level in baseline NESC-2.

The median load reduction factor was computed on the basis of the RMS strains provided by the ITA Team and will be revised once the multi-modal loads analysis has been completed by the team. Therefore the precise value of the reduction factor is not well known at the present time. The difference between the blue and red curve in Figure 5-6 nonetheless give an indication of the effect of removing some of the conservatism in the median load levels while explicitly accounting for the variability in the loads. It is not unreasonable to assume that the final reduction on the median load levels, based on the multi-model analysis, may still reduce the total flowliner failure probability by an order of magnitude.

Although the red curve in Figure 5-6 was obtained assuming that the peak stresses act during the entire flight segment durations (see Section 4) one cannot be assured that this curve represents a conservative estimate of the failure probability since the effect of considering multiple modes versus a single mode in the stress analysis is unknown.

The relative sensitivity of the failure probability to changes in the parameters of the PDF describing the random variables is shown in Figure 5-7. The sensitivities were obtained by averaging the derivatives with respect to the mean and standard deviation of the n_F failed Monte Carlo samples (limit state function is 4 missions; α_i represents either the mean or the standard deviation):

$$\frac{\partial p_F}{\partial \alpha_i} = \frac{1}{n_F} \sum_{i=1}^{n_F} \left[\frac{1}{f_X(x)} \frac{\partial f_X(x)}{\partial \alpha_i} \mid \text{life} < 4 \text{ missions} \right] \tag{5.2}$$

It is immediately clear that failure probability is most sensitive to changes in the uncertainty characterization of Flight Stage 6. This is caused by the confluence of 3 contributing factors:

1. The largest stresses occur during Flight Stage 6 (see Figure 5-8)
2. The most cycles in the spectrum occur in Flight stage 6
3. The largest amount of load variability is associated with Flight Stage 6 (see Section 4)

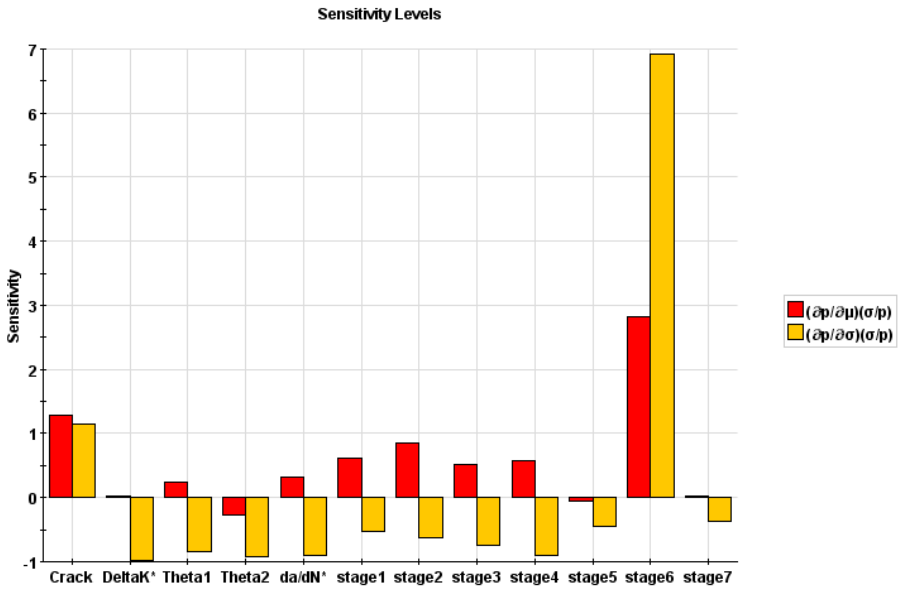

Figure 5-7: Probabilistic sensitivities for reduced NESC-2 spectrum, lognormal POD with median of 20 mils and baseline crack growth uncertainty model.

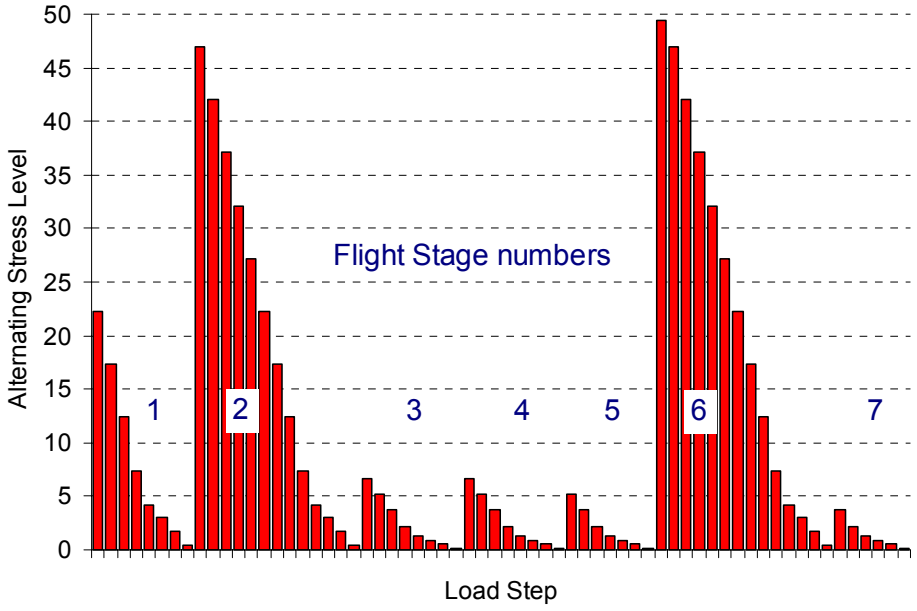

Figure 5-8: Load history for NESC-2 spectrum

It is not known a priori whether there is a statistical dependence of the stress levels between the different flight stages or load steps. For instance, it is not known whether higher than average stress levels in Flight Stage 3 (ramp down), typically lead to higher (or lower) than average stress levels in Flight Stage 5 (ramp up). The extent to which knowledge about the deviation from the average stress in a particular flight stage or load step is useful information to discern the stress level in a different flight stage or load step is measured by the linear correlation coefficient.

In the probabilistic model used herein, full correlation between all load steps within the same flight stage is assumed. The loads between different flight stages are assumed to be uncorrelated. However, the precise amount of correlation in the stress levels between the seven Flight Stages has not been documented at this time. Figure 5-9 shows the results of a parametric study, assuming either fully correlated or fully uncorrelated loads between the seven Flight Stages. The results indicate that a full correlation of all load levels results in a slightly higher probability of premature failure (up to a factor two). Note that the sampling confidence bounds for both correlation scenarios overlap, which is an indication that the effect is not very pronounced. The lack of significant difference between the correlated and uncorrelated load models is due to the overwhelming impact of Flight Stage 6 on the total failure probability.

Figure 5-10 shows the probabilistic sensitivities for the reduced NESC-2 spectrum with the fully correlated loads. Since all Flight Stages are correlated, only a single probabilistic load sensitivity is computed and its value is essentially identical to the sensitivity for Flight Stage 6 in the uncorrelated case.

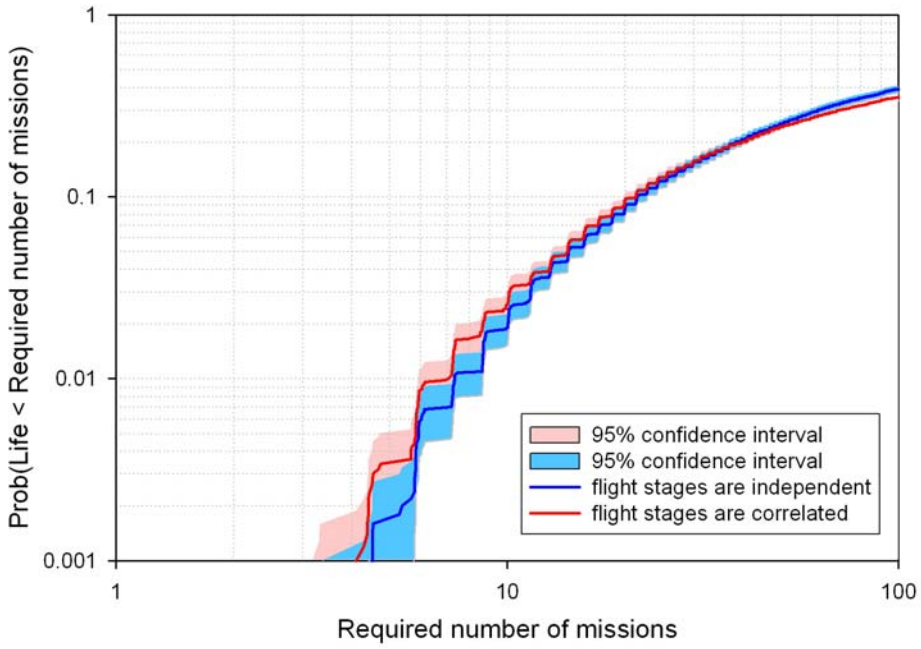

Figure 5-9: Effect of correlation between flight stages on the failure probability (reduced NESC-2 spectrum).

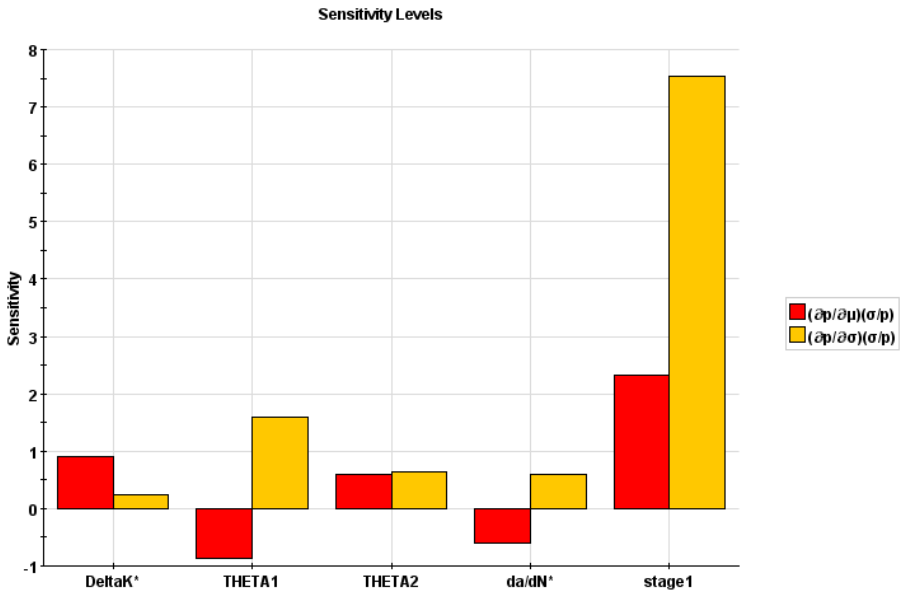

Figure 5-10: Probabilistic sensitivities for reduced NESC-2 spectrum assuming full correlation between flight stages.

5.5 Effect of the Initial Crack Size

The impact of the initial crack size distribution on the total failure probability was studied as well. Three lognormal Probability of Detection (POD) curves were used:

1. "regular POD": median at 0.020 in and 99^{th} percentile at 0.075 in
2. "large POD" : median at 0.075 in and 99^{th} percentile at 0.280 in
3. "intermediate POD" : median at 0.040 in and 99^{th} percentile at 0.15 in

Figure 5-11 and Figure 5-12 show the effect of increasing the initial defect size for the NESC-3 and the reduced NESC-2 spectra, respectively. These spectra were selected since they represent the upper and lower failure probability bounds for the various spectra considered.

Depending on the choice of POD curve, the probability of failure within one mission varies by more than an order of magnitude for both the NESC-3 spectrum (Figure 5-11) and the reduced NESC-2 spectrum (Figure 5-12). If the large POD is used as the initial crack size distribution, the probability of failure within a single mission is as high as 6% for the NESC-3 spectrum (see Figure 5-11). If no inspection were to occur between flights, the probability of failure within four missions would be 40%. If the regular POD curve is used, the probability of failure within four missions drops to 10%.

For the reduced NESC-2 spectrum (see Figure 5-12) the failure probabilities are reduced to about 0.5% probability of failure during the first mission and 2% for failure within the first four mission the reduced NESC-2 load spectrum for the large POD. The probability of failure within four missions drops from 2% for the large POD to 0.24% for the intermediate POD and to 0.05% for the regular POD.

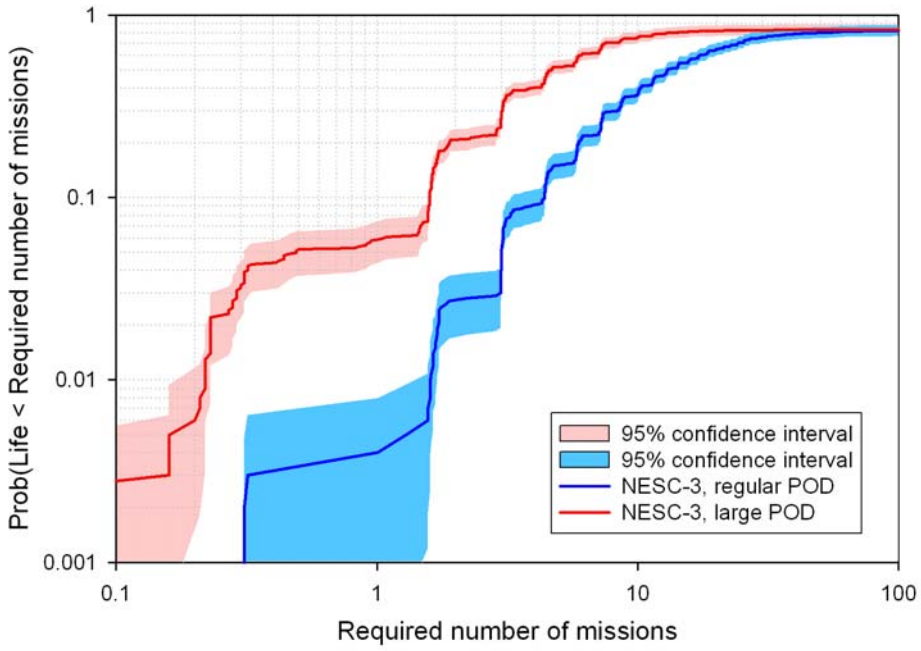

Figure 5-11: Effect of initial flaw size distribution on flowliner fatigue failure probability for the baseline NESC-3 spectrum.

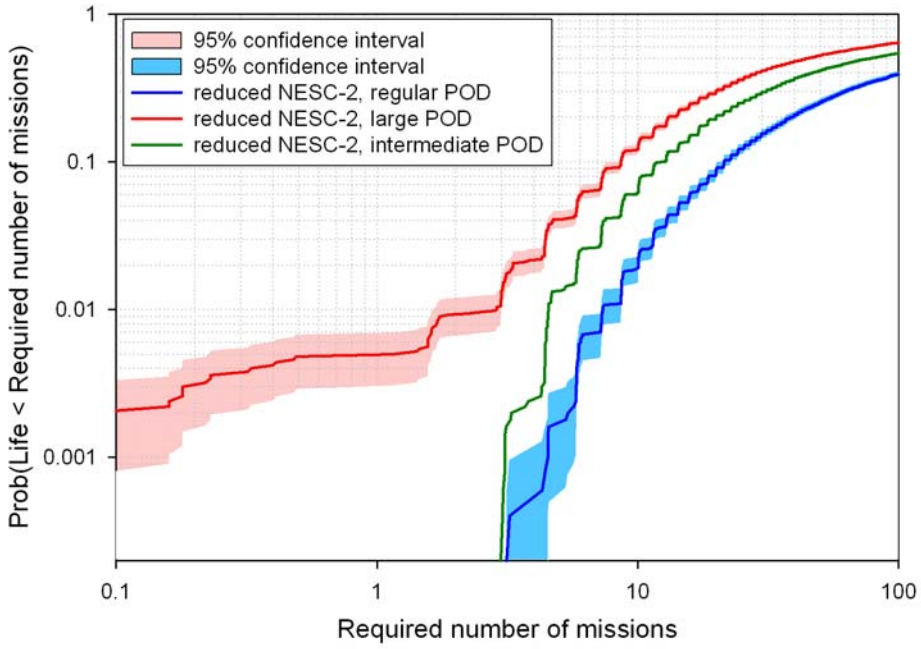

Figure 5-12: Effect of initial flaw size distribution on flowliner fatigue failure probability for the reduced NESC-2 spectrum.

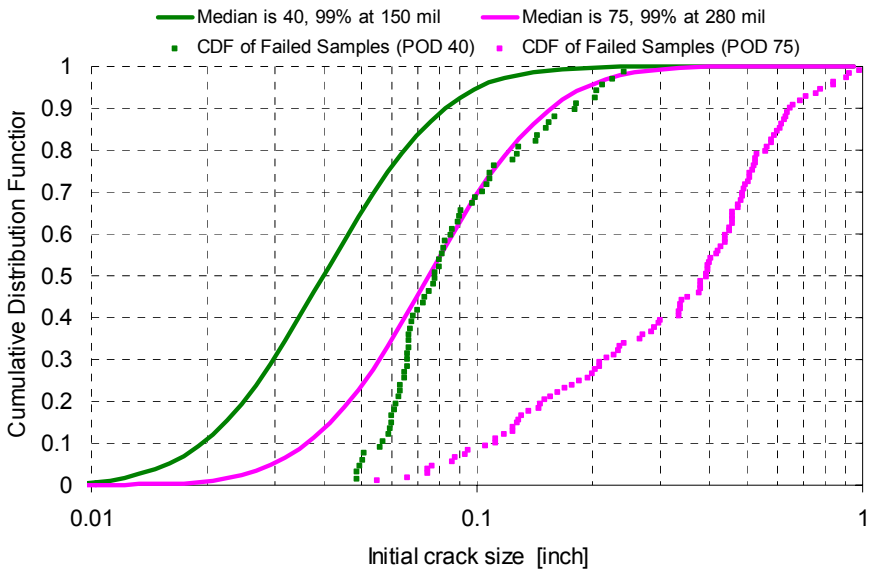

Figure 5-13: Comparison of original crack size distribution with median of 40 and 75 mils with corresponding CDFs of failed samples for the reduced NESC-2 spectrum

It is instructive to look at the conditional failure densities. These are the marginal PDFs of all failed samples from the Monte Carlo analyses. The conditional marginal failure distributions provide valuable insight into the most likely failure combinations. They indicate the range of the model that is most likely to cause failure and is therefore most important from a reliability point of view. Figure 5-13 reveals that for the large POD curve (with a median of 75 mils), the flowliner failures generally occur for larger than average initial crack sizes. In only about 10% of failures the initial crack size was less than the median crack size.

For the large POD the probability of having an initial crack that exceeds 95% of the entire ligament length is about 3.7×10^{-5}. During 5000 Monte Carlo simulations of all 38 ligaments, 190,000 (= 38 x 5000) crack sizes are simulated. One therefore expects to see about seven (= 190,000 x 3.7×10^{-5}) simulations with instantaneous failure. The empirical CDF of the failed samples in Figure 5-13 shows that in about eight samples the initial crack size is so large that immediate failure occurs and is in line with the expected behavior. This result therefore illustrates the importance of an accurate selection of the upper tail of the POD and confirms that care needs to be taken in specifying the initial crack size.

5.6 Effect of Scatter in Crack Growth Rate Properties

The fatigue crack growth material model, presented in Section 4, quantifies the effect of various sources of uncertainty on the scatter in the crack growth parameters. Because the heat-to-heat variability is not included in this assessment, a separate run was performed with increased scatter on the crack growth properties. Specifically, the standard deviation on the orientation of the left leg (*i.e.*, θ_1) was doubled. This increased the 95%-range for ΔK_{th} from 5.8-8.3 ksi$\sqrt{}$in. to 4.9 - 9.2 ksi$\sqrt{}$in.

The resulting failure probabilities were virtually identical to the cases with the baseline scatter model. The probability of failure within four missions is 1.62% and the probability of failure within the first mission is 0.44%. These numbers were obtained using 5000 Monte Carlo samples. The confidence bounds of the cases with baseline and increased crack growth scatter overlap considerably. This relative lack of influence of the uncertainty in near threshold crack growth properties on the failure probability is largely due to the fact that the uncertainty in the loading spectrum dominates the failure probability of the flowliner, as illustrated in Figures 5-7 and 5-16.

5.7 Certification Spectra

NASA Langley provided SwRI with seven certification spectra, which roughly fall in three categories: "nominal" conditions, failed engine conditions, and 2 spectra where the FCV failed. The deterministic analysis in Section 3 identified that the failed engine scenarios resulted in the smallest mission lives. The most critical spectrum is 1.17_E3_engine_out.

This load spectrum is characterized by an initial load step with about half a million cycles (about 1/3 of the total number of cycles) at a relatively high stress level. A median load reduction (as outlined in Section 4) was applied to this spectrum. This reduces the median load in the dominant first load step by 5%. The scatter associated with the first load step is also as per Section 4, i.e., 8%.

In this scenario, the probability of failure with the first mission is about 25%, and the probability of failure within four missions is 80%. To achieve a total failure probability number, this conditional probability must be multiplied by the probability of losing a single engine. This failure probability has been estimated by NASA to be 1/800 [Harris, 2004]. The resulting unconditional failure probability for this scenario is of the same order as that for the reduced NESC-2 spectrum.

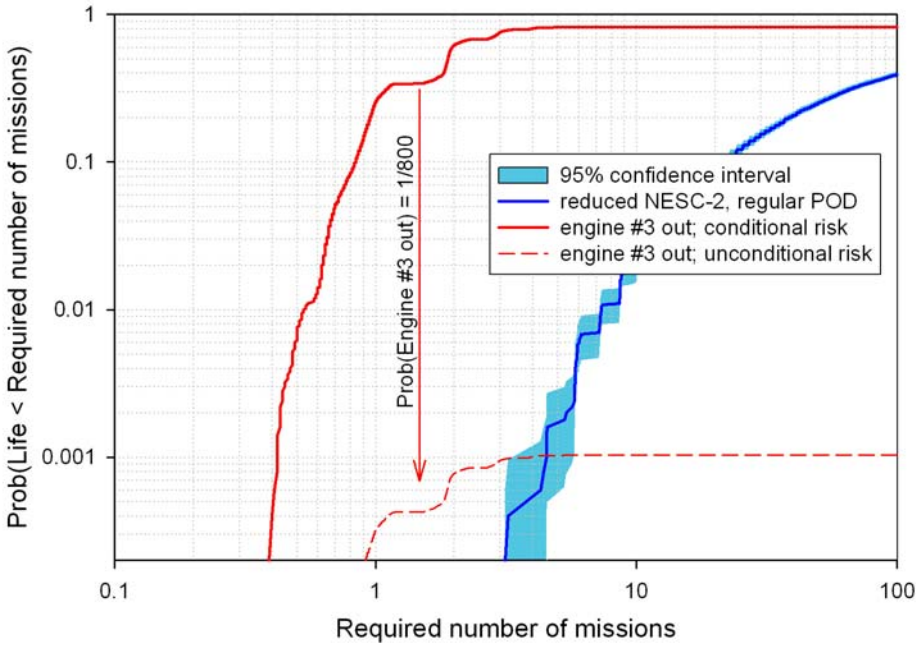

Figure 5-14: Comparison of "reduced NESC-2" and "Engine #3 out" spectra.

The curve for Engine #3 out scenario is characteristic of high-cycle fatigue. Specifically, if the stresses are high enough for crack growth to occur, failure follows quite rapidly. It is also worthwhile noting that although both the certification spectrum and the reduced NESC-2 case have a similar failure probability in the range of 4 to 5 missions, the failure probability for failure within the first mission differs by orders of magnitude. Consequently, if one wanted to ensure similar safety for both scenarios with the single mission limit state, a much higher safety factor on life would be required than for the blue curve because of the flatness of the red CDF curve (Figure 5-14). This situation illustrates that in high cycle fatigue applications it may be more appropriate to apply a safety factor on the threshold stress intensity factor, rather than on fatigue crack growth life.

Another critical spectrum is labeled "1.3 E2 Nominal with +3σ trajectory". This spectrum consists of seven Flight Stages and a total of 188 load steps. In this load spectrum, the most severe stresses are observed in Flight Stages 2 and 4. The median load reduction, outlined in Section 4, was applied to this spectrum. This reduced the median loads in Stage 2 by almost 20% but there was no reduction to the median load level in Stage 4. The coefficient of variation for the stress amplitudes is between 20% and 25% for both of these Flight Stages (see Section 4). The failure probability for the entire flowliner under this scenario and the "reduced NESC-2" spectrum are compared in Figure 5-15. The probability of failure within the first mission is approximately 2.5%. If no inspections occur in between flights, the probability of failure within 4 missions climbs to just over 50% (note that the deterministic analysis in Section 3 computes a life of 4 missions). Figure 5-16 confirms the dominant effect of the stress amplitude and scatter

in Flight Stages 2 and 4 on the failure probability. The failure probability is slightly more sensitive to changes in the crack size POD than to changes in the material uncertainty model.

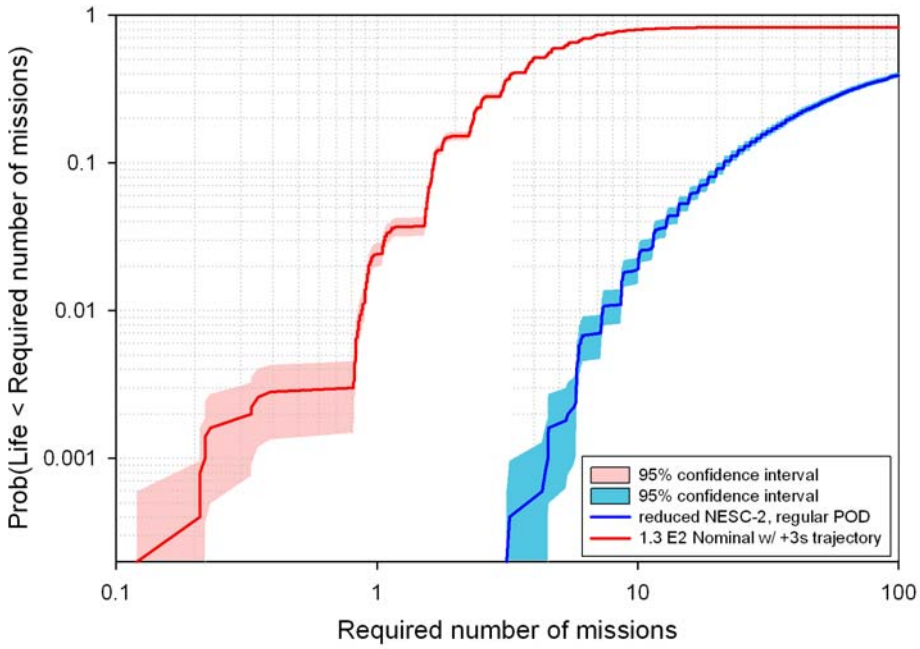

Figure 5-15: Comparison of "reduced NESC-2" with regular POD and "1.3 E2 Nominal with +3σ trajectory" spectra

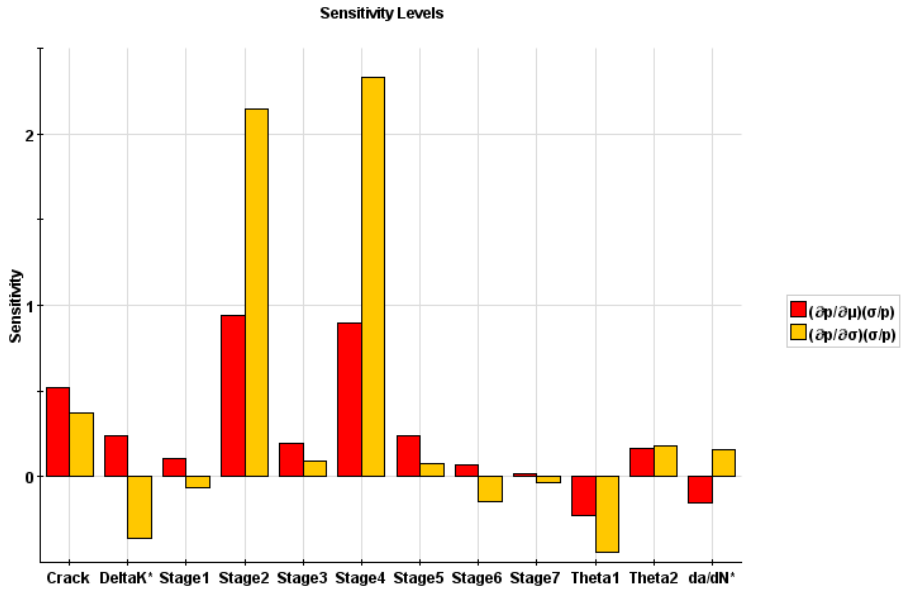

Figure 5-16: Sensitivity of Failure Probability to changes in mean and standard deviation of each of the random variables for the "1.3 E2 Nominal with +3σ trajectory".

5.8 Summary of Probabilistic Analyses

A summary table of all analyses is given in Table 5-1. The initial crack size is assumed to be given by the POD. Unless noted otherwise, the POD has a median of 20 mils and 99th percentile at 75 mils. The 'large POD' case refers to a lognormal POD with median at 75 mils. The crack growth parameter scatter is as defined in Section 4. The cases marked "large material scatter" indicate a doubling of the uncertainty on θ_1, the scatter on the lower part of the crack growth curve, to account for heat-to-heat variability.

Table 5-1: Summary of failure probabilities

Scenario	Prob(Life < 1 mission)	Prob(life < 4 missions)
1. Baseline NESC-2	< 0.001	0.014
2. Baseline NESC-3	0.003	0.075
3. Reduced NESC-2	< 0.0001	0.0004
4. Baseline NESC-3, large POD	0.058	0.400
5. Reduced NESC-2, large POD	0.005	0.022
6. Reduced NESC-2, regular POD, large material scatter	< 0.0001	0.0006
7. Reduced NESC-2, large POD, large material scatter	0.004	0.02
8. Engine failure (conditional)	0.257	0.803
9. Engine failure (unconditional)	0.0004	0.001
10. 1.3 E2 Nominal with +3σ trajectory	0.024	0.512

6. DISCUSSION

The Phase 1 work performed by SwRI under the present ITA focused on a definition of key elements of the flowliner cracking problem, conducted preliminary scoping analyses, and formulated a framework for development of more robust deterministic and probabilistic fatigue crack growth models [Hudak et al, 2004]. The current Phase 2 effort has developed and implemented the more robust models and applied them to the assessment of the probability of failure of the flowliner as a function of loading spectra, inspection sensitivities, and variation in material properties. Key aspects of the development and application of these models are discussed below and limitations are highlighted, first for the deterministic model and then for the probabilistic model.

6.1 Discussion of Deterministic Fatigue Model and Results

A deterministic fatigue crack growth program called Flowliner Fatigue Life (FFL) has been developed that has the capability of treating corner and through-thickness cracks in bivariant stress fields similar to those experienced at upstream and downstream flowliner slots. The program employs the weight function (WF) approach to calculating SIFs, and contains a library of WF solutions for evaluating the SIF of cracks at Locations A, B, C and D on the slots. The program was designed to interface with the NESSUS computer code to facilitate probabilistic calculations of the reliability of flowliners to survive a specified number of missions.

The unique requirements for assessing the fatigue life of flowliners made it necessary to develop the FFL code rather than employ the NASGRO computer program. These requirements included the need to:

1. Determine SIFs for corner and through thickness cracks subject to arbitrary bivariant stressing;
2. Address the possibility of fatigue cracking failures at all the 38 slots in each of the upstream and downstream liners;
3. Allow for transitioning from a corner crack to a through thickness crack during fatigue growth;
4. Allow for potential stress redistribution due to shakedown from plastic relaxation of peak stresses;
5. Provide versatility with respect to representing the distribution and treatment of mean stresses arising from residual welding and system stresses;
6. Directly interface the deterministic fatigue crack growth module with the NESSUS code, avoiding the computational inefficiencies associated with reading data from input files and writing to output files, which was the mechanism used to interface NASGRO with NESSUS in the preliminary Phase 1 analysis.

The FFL program is able to address all of the above requirements.

6.1.1 Validation of Weight Function Solutions and FFL Code

The WFs included in the FFL library of solutions have been validated by comparing the WF-based SIF calculations with the results of SIFs calculated using finite element methods. This validation exercise was performed for all the crack models contained in FFL. These crack models are:

- Axially oriented corner and through thickness cracks at Locations A and D on a slot

- Circumferentially orientated corner and through thickness cracks at Locations B and C on a slot.

In the case of through-thickness cracks, SIFs determined using the WF for an arbitrary univariant stress distribution through the ligament are combined with the SIF solutions for through-wall bending to represent the SIF solutions corresponding to the actual bivariant stressing.

The corner crack WF were found to be in excellent agreement with independent, 3-D finite element solutions performed at SwRI using ABAQUS as shown in Table 2-3, as well as in Figures 2-13 through 2-16 for crack Locations A, B C, and D. The through crack WF solutions were also found to be in excellent agreement with ABAQUS finite element results as shown in Figure 2-24.

The through-crack WF solutions were also compared to 2-D shell finite-element solutions developed at NASA-LaRC. In both cases results were for local dynamic stress gradients determined from modal analysis. Direct comparison of results from these two solution methods were difficult to interpret since the SwRI's SIF solutions were specific points on the crack front while the NASA-LaRC results were from a 2-D shell analysis involving a virtual crack closure method that averages SIF values along the crack front. As shown in Figure 3-2, the NASA finite element results were in overall reasonable agreement when compared with SwRI's WF solution based on using the stresses at the mid-thickness location. In fact, agreement was excellent for crack lengths of less than 0.1 in., where fatigue cracks spend most of their lives, but diverged with increasing crack length.

Comparison of NASA-LaRC and SwRI results is further complicated by the fact that the FFL code only addresses fatigue crack growth under Mode I loading (where the stressing is normal to the crack plane). Two other loading modes also exist—Mode II and Mode III—that result from shear stressing of a crack in plane and out of plane. The fatigue life computations performed by NASA-LaRC for initial through thickness cracks based on SIF solutions derived from the virtual crack closure technique include contributions from all three modes. NASA-LaRC combined these mixed mode contributions into an effective cyclic SIF. This is likely to be a conservative approach because Mode II and III stressing may not be as damaging as Mode I, and the measured Mode I crack growth rates used in the NASA-LaRC computations may not apply. In addition, and more importantly, the contribution of Mode II and III to the effective cyclic SIF only becomes significant for through cracks that exceed 0.1" in length, as shown in James et al (2004). Normally the majority of a fatigue life is expended in growing cracks that are small.

The impact of using mode I SIFs to evaluate lifetimes of upstream and downstream liners compared to using combined modes I, II and III SIFs is around a factor of 2, as can be seen by the results in Table 3-2. The results in this table were generated using the SIFs derived by NASA-LaRC to enable a direct comparison between predicted lifetimes of mode I loading and modes I, II and III. This difference would be expected to be significantly reduced in cracking at liner slots modeled by initial corner cracks because a greater fraction of the lives of these cracks will be spent in propagating them when they are small (<0.05") and for such cracks the influence of modes II and III on the effective SIF is likely greatly reduced compared to the influence these modes will have on through cracks.

A comparison between lifetime results predicted using the mode I WF approach in FFL (as opposed to NASA-LaRC's mode I SIF solutions) with NASA-LaRC's results for combined Mode I, II and III is shown in Table 3-3. As can be seen from Table 3-3 for cracks in downstream liners subjected to NESC-2 spectrum, the difference in missions to failure predicted for initial through cracks assuming either only Mode I loading compared to taking into account *a la* NASA-LaRC the actual combined mode loading is still around a factor of 2. However, for the upstream liners, the Mode I WF approach predicts lives that are 3-4 times shorter than those predicted by NASA-LaRC assuming combined Mode I, II and III SIFs. This is because in this case SIFs determined using the WF method are significantly higher than those computed by NASA-LaRC.

6.1.2 Crack Shape Evolution and its Effect on Fatigue Life

The crack models contained in FFL enable three crack propagation scenarios to be simulated, as shown schematically in Figure 3-4. In the first scenario, the initial crack is assumed to be a corner crack. After crack growth and penetration of the wall of the liner, the crack continues to propagate through the ligament at the c-tip as a corner crack but with the depth at the a-tip fixed at 97.5% of the flowliner thickness. In the second scenario, a corner crack is allowed to transition into a straight-fronted through-thickness crack when penetration of the liner wall is predicted. In the third scenario, the initial crack is assumed to be a through-thickness crack and to propagate to failure as a through crack. These three different scenarios were found to predict drastically different fatigue lives, as demonstrated by the results presented in Section 3. For example, an initial corner crack of size 0.02" at the ID position of Location B on slot number 5 subjected to the certification spectrum FCV_Failed_Open is predicted to survive 373 missions based on the first scenario, but only 4 missions based on the second scenario.

Figure 3-5 shows the observed cracking behavior in the MPTA test conducted at NASA-MSFC for crack Location B. This figure demonstrates that the scenario that actually occurs in practice falls somewhere in between the first and second scenarios described above. In the MPTA test, as shown in Figure 3-5, an initial corner crack has grown through the liner wall and then continued to grow through the ligament between two slots along the ID and OD. After penetrating the liner wall, the crack front remains curved; thus, although the corner crack has transitioned into a through crack, the through crack does not attain a straight crack front. As can be seen from the foregoing results for the first and second cracking scenarios which bound the actual cracking behavior, there could be an order of magnitude difference between the predicted

number of missions for failure obtained by assuming a corner crack transitions into a straight-fronted through-crack versus assuming the front remains curved. These results show the degree to which the predicted missions to failure are sensitive to the manner in which crack growth is modeled after crack transitioning is predicted.

Another important aspect of the deterministic fatigue analyses reported in Section 3 for cracks at Location B on liner slots is the demonstrated ability of the current FFL-based analysis, when combined with current best estimates for the cyclic stress distributions at the slots, to accurately model crack shape development before a corner crack penetrates the liner wall. The FFL code predicts that ligament cyclic stress distributions that are essentially univariant through the ligament and have only a small variation through the liner wall will result in initially quarter circular cracks maintaining their shapes during fatigue crack growth. The MPTA cracking illustrates that corner cracks that are initially quarter circular will remain approximately quarter circular during propagation through the thickness. The FFL results presented in Figure 3-6(a) show that this is predicted to be the case for the slots most at risk from cracking when subjected to the NESC-2 spectrum. The same will also be true for the predicted severest slots subjected to the most life limiting certification spectra, 1.17 E3 Engine Out, 1.28 E1 Engine Out and FCV Failed Open. The most damaging slot locations (2, 5, 6, 9, 13 and 17) under the certification spectra are also ranked as most damaging under the NESC-2 spectrum, and will experience similar cyclic stresses that are characterized as having little through thickness variation (i.e., a small through-thickness bend component).

The analysis results given in Section 3 confirm the findings of NASA-LaRC that some of the certification spectra (*e.g.*, 1.17 E3 Engine Out, 1.28 E1 Engine Out and FCV Failed Open) are significantly more severe than either the NESC-2 or NESC-3 spectra. For example, if slot 17 is assumed to have an initial through-crack of length 0.05 in. at Location B, then the failure is predicted in one mission under certification spectrum 1.17 E3 Engine Out (see Table 3.14). This prediction is not changed if the less onerous assumption is made of a corner crack of initial size 0.02 in. is present at slot 17 that is allowed to transition on penetrating the wall into a through crack. Under the NESC-2 spectrum, the equivalent number of missions to failure at slot 17 assuming initial through thickness and corner cracks are 20 and 32, respectively (see Table 3-5). However, if cracking at slot 17 is modeled as a corner crack that is not allowed to transition to a straight-fronted through crack but maintains a curved crack front after transitioning (first propagation scenario), the slot is predicted to survive at least 1000 missions under the certification spectrum 1.17 E3 Engine Out, and to have grown through the ligament to a length of 0.433" after that time. Thus, the predicted severity of the certification spectra can be a function of how crack growth and transitioning is modeled.

Fortunately, however, the low computed lives in the deterministic analysis for the above fault conditions such as "One-Engine-Out" or "FCV Failed Open", are mitigated in the probabilistic analysis, which also considers the conditional probability of these fault conditions actually occurring in a given flight. For example, as shown in Section 5.8, the fact that the probability of having a "One-Engine-Out" condition is 1/800 resulted in the actual (unconditional) probability of failure for this loading spectrum to be about the same as that for NESC-2, based on the uncertainty modeling of Section 4.

6.1.3 Effect of Residual Stress on Flowliner Fatigue Life

Welding residual stresses exist in the flowliner from two sources: 1) the welded attachment of the flowliner to the end-flange during initial fabrication of the feedline, and 2) the recent weld repair of cracks following their discovery in the flowliner. However, the magnitude and distribution of these residual stresses are largely unknown.

Moreover, SwRI experience with welding residual stresses in other applications—such as offshore structures used in oil and gas exploration—suggests that residual stresses are often highly variable. For example, measured residual stress from a circumferential seam weld in a pipe can vary from significant compression to tensile values as high as the yield stress of the material. Consequently, when analyzing welded structures it is commonly assumed that crack nucleation will occur at the location corresponding to the highest combination of tensile residual stress and superimposed cyclic stress. Thus, in fracture mechanics analyses of welded structures it is common engineering practice to account for high tensile residual stresses by employing fatigue crack growth rate data generated at high mean stress, or R-ratio, instead of explicitly treating the residual stresses in the crack driving force [Hudak, 1985].

This approach is particularly appropriate in high cycle fatigue situations where the critical crack size corresponding to crack instability has little or no influence on the fatigue life. Since this is the case in the flowliner, the residual stresses were accounted for indirectly by employing fatigue crack growth rate date that are free from crack closure effects and thereby are representative of high-R fatigue crack growth data. These data are given in SwRI's Phase 1 Report [Hudak et al, 2004], along with the procedure for establishing these crack closure-free data.

Consideration is being given by the ITA Team and/or Program Office to measurement of welding residual stress in the flowliner to end-flange attachment weld. Similar measurements could also be performed for simulated weld repairs. If and when quantitative information on both the magnitude and distribution of the residual stresses at the crack locations become available they could readily be analyzed using the tools developed in the current study, i.e., FFL interfaced with NESSUS.

6.1.4 Operative Fatigue Damage Mechanism(s)

The deterministic and probabilistic analyses performed in the current study subscribe to the argument that the primary damage mechanism is high cycle fatigue [ITA Phase 1 Report, Section 8.1] due to flow-induced vibrations.

Nevertheless, the possibility of supplemental damage from low cycle fatigue associated with thermal stresses has also been considered. Thermal stresses due to initial filling of the fuel system with LH2 before each launch are too small to be of concern for all locations except crack Location A [Warren, 2004]. Thermal stresses are maximum in this region due to the proximity of high thermal mass of the thick end-flange welded to the comparatively thin flowliner. Assuming that the welding residual stresses near Location A are greater than 50% of the materials' yield strength, then the thermal stress superimposed on the welding residual stress

could lead to fatigue lives as low as 10,000-20,000 cycles, based on the fatigue data summarized by Bonacuse [Phase 1 Report, Appendix D4]. Since the number of launches (thermal stress cycles) for any given orbiter is less than 100, one can conclude that LCF is not, in and of itself, life-limiting for the flowliner. However, it is important to recognize that under these high stresses it is possible to nucleate microcracks very early in life. These microcracks could facilitate the early onset of HCF—in much that same way that microcracks due to punching the flowliner slots likely contributed to the original observed engineering-sized cracks.

Thus, some type of interaction between HCF and LCF is possible at Location A. However, this possibility is indirectly taken into account in the fracture-mechanics- based fatigue crack growth analysis performed in the current study since the analysis assumes that cracks are initially present. Moreover, the initial crack size assumed in both the deterministic (a=c=0.020 in.) and probabilistic (crack size distribution given by the POD curve) analyses are larger than would be the size of microcracks generated by LCF.

6.1.5 Potential Influence of Hydrogen Environment on Flowliner Fatigue Life

High pressure hydrogen is known to degrade fatigue properties of IN 718 at temperatures around room temperature [Jewett et al, 1971]. Whether or not these effects can occur at cryogenic temperatures and for the loading conditions that occur in the flowliner is presently unknown. The effect of hydrogen embrittlement on the fatigue life of the flowliner has not been taken into account in either the current deterministic or probabilistic fatigue crack growth calculations since fatigue crack growth rate data would have been required in LH2 at –423°F.

One can hypothesize several reasons why hydrogen embrittlement would not be expected to occur in the environment and operating conditions of the flowliner, as follows: 1) the mobility of hydrogen is anticipated to be very low at –423°F, thus, the dissociative surface reaction necessary to produce the atomic hydrogen needed to enter the metal is unlikely; 2) the low mobility would impede the diffusion of hydrogen to local stress concentrations within the metal that are believed necessary for hydrogen embrittlement to occur; 3) the fatigue loading frequencies that are excited by the flow-induced vibrations (1000-4000 Hz) are typically too fast to allow the time-dependent transport and embrittlement reactions to occur over a given loading cycle.

However, it is important to recognize that there are no hard data either to support or refute the above hypotheses. In response to this need, the NESC's Materials Super Problem Resolution Team is planning a test program at NASA-LaRC to assess whether or not LH_2 is detrimental to fatigue crack growth in IN718 [Materials SPRT Minutes, 2004]. In view of the lack of definitive data surrounding this issue, combined with the fact that the integrity of the flowliner is crucial to the safe return to flight of the orbiter fleet, we fully endorse the generation of these data.

6.2 Discussion of Probabilistic Fatigue Model and Results

During Phase 2 several significant improvements were made to the probabilistic modeling. First, a probabilistic analysis was performed on the entire downstream flowliner

including all 38 slots. This approach enables the flowliner to be analyzed as a system by considering variations in stress amplitude at each potential crack site location along the flowliner perimeter in the assessment. This was accomplished by treating both the spatial variation and mode dependence of the transfer factors.

Secondly, an improved statistical description of the crack growth rate material properties was developed. This improved model avoids the problems encountered during Phase 1 with statistical characterization of the fatigue crack growth rates because of the estimation of the asymptotic nature of the previous models in the near threshold regime. It also explicitly considers the statistical correlation between consecutively measured crack growth rates on replicate specimens.

The current analysis also included significant improvements to the stress modeling. Specifically, the fracture mechanics analysis is now based on dynamic stress amplitudes and associated gradients (provided to SwRI by NIA/NASA-LaRC) instead of the remote tension and bending assumptions used in Phase 1. In addition, substantial sources of conservatism in the load modeling were identified and eliminated. For example, the deterministic rainflow counting was previously performed on the most severe time window of the most severe test (in terms of RMS strain amplitudes). The probabilistic analysis justifiably removes the conservatism associated with using the "worst case" stresses while explicitly accounting for the variability of the stresses.

Application of the enhanced probabilistic model has also demonstrated that loading spectrum—including the local dynamic stress amplitudes and associated gradients—is the most significant random variable governing the reliability of the flowliner. Both the mean values as well as the variance of the dynamic stresses significantly influence the number of missions that can be tolerated before flowliner failure occurs. The uncertainty model for the dynamic stresses was based on a detailed analysis of the strains gage data measured during the GTA tests conducted at NASA-MSFC. However, an unanticipated consequence of this analysis is that data are not consistent with the assumption used by the ITA Team and Program Office in developing the loading spectra that a single mode dominates the loading spectrum in a given Flight Stage. These results are briefly summarized below and their consequence to the flowliner assessment is discussed.

It is instructive to approach this discussion by considering that the derivation of the loading spectrum consisted of two parts:

1. The strain gauge recordings from BTA articles consisting of the mid-ligament strains, measured during multiple tests runs. These measurements are used to compute a strain spectrum using a rainflow analysis, and

2. Translation of the strain gauge results at mid-ligament to the stresses at the crack sites of interest. This is achieved by using Finite Element modal analysis, which is calibrated to the measured strains. Results are expressed in terms of transfer factors, which are the ratio of the local strain at the crack site to the measured strain at the mid-ligament.

Each of these elements of the loading spectrum development will be discussed separately below.

6.2.1 Strain Spectra

The current spectra that were provided by the ITA Team and Program Office assumes that a single mode dominates at any given Flight Stage and that mode switching can only occur on going from one Flight Stage to another. Spectral analysis of strain data by both SwRI and Swales indicates that multiple modes are active at the same time. This is shown in Figure 6-1 where several peaks exist in the power spectral density (PSD). The waterfall plot on the left of this figure shows a color coded PSD as function of time. The pink color corresponds to peaks in the aggregate PSD on the right, which is for the entire test. Since multiple modes can be active and contribute significantly to the flowliner excitation at the same time it is imperative that the strain signal be broken down into its modes so that each mode can be analyzed separately.

Moreover, the plot on the right in Figure 6-1 is an accurate representation of the actual PSD only if the process is stationary—*i.e.*, if the color bands in the waterfall plot on the left extend throughout the entire test duration. For a non-stationary process, the color bands may abruptly start or stop. It is clear from the waterfall plot that the process is in fact non-stationary.

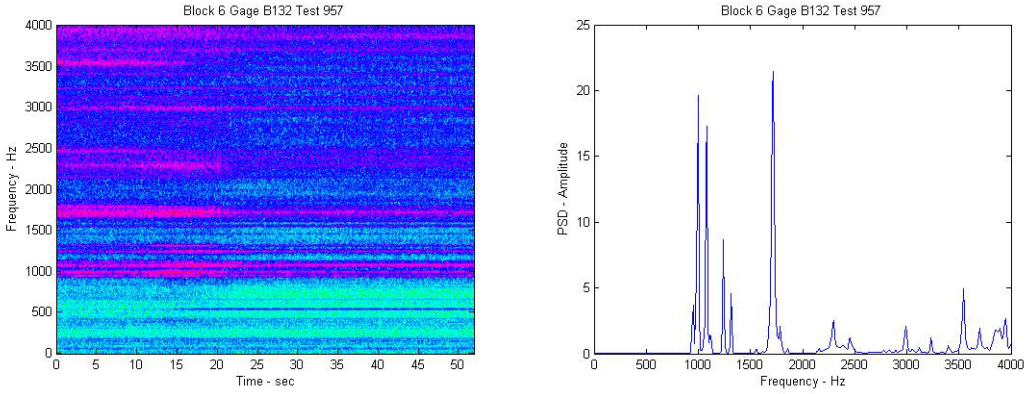

Figure 6-1: Waterfall and PSD for entire Flight Stage 6 - Test 957.

The non-stationary nature of the strains is manifested in two ways. First, the active mode changes during the Flight Stage as shown in the waterfall plot in Figure 6-1. This is more clearly shown in Figure 6-2 and Figure 6-3 where the results from Figure 6-1 are separated into two nearly-stationary sub-stages corresponding to two different time intervals.

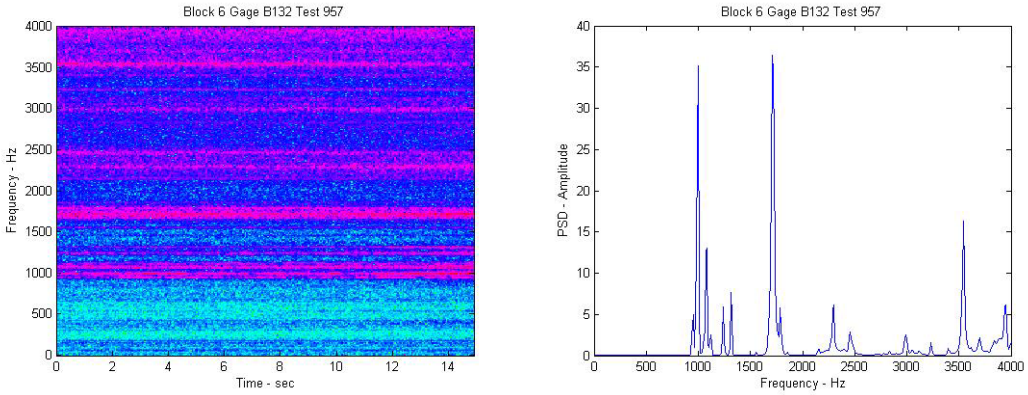

Figure 6-2: Waterfall and PSD for first 15 seconds (Flight Stage 6).

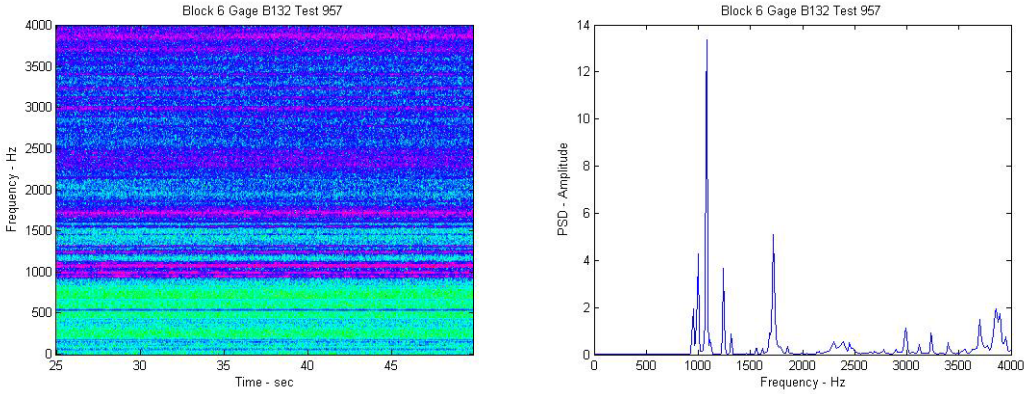

Figure 6-3: Waterfall and PSD for between 25 and 50 seconds (Flight Stage 6)

Secondly, not all tests result in the same power spectrum. For instance, for Flight Stage 7 in Test 958 shown in Figure 6-4, three different regimes are present, each exciting different frequency bands (Figure 6-5 through Figure 6-7). This test result shows that one cannot assume constant modes during the currently defined flight stages. Similar behavior was observed for all tests in Flight Stage 5 (Figure 6-8). The C4ND mode (3.3kHz) is used in the currently recommended spectrum for this flight stage. However, the waterfall plots in Figure 6-8 show that this mode is only active during the last half of Test 955 and the first third of Test 957.

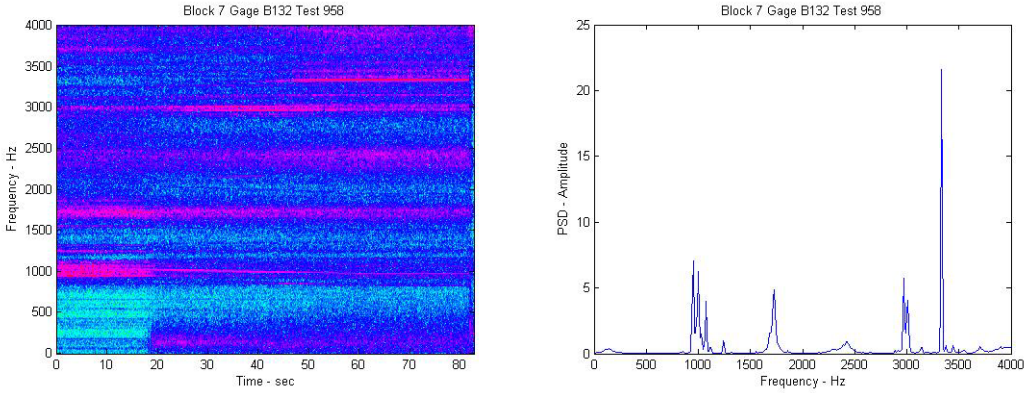

Figure 6-4: Waterfall and PSD for entire 82 sec window (Flight Stage 7).

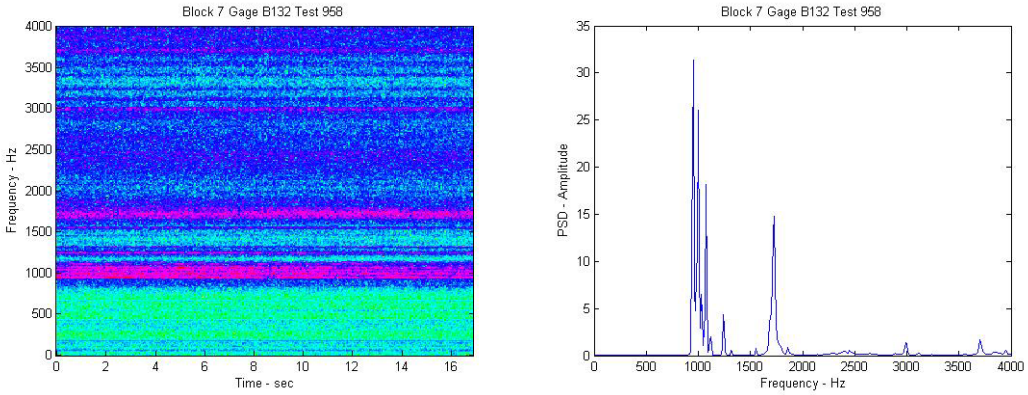

Figure 6-5: Waterfall and PSD for first 17 seconds (Flight Stage 7).

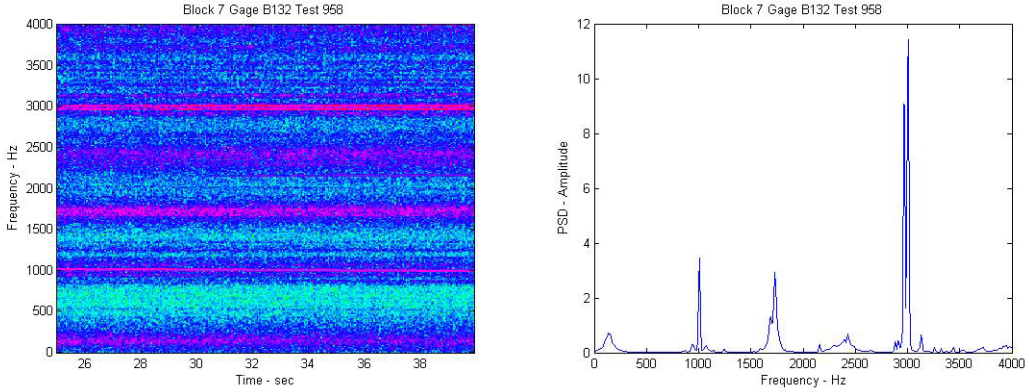

Figure 6-6: Waterfall and PSD between 25 and 40 seconds (Flight Stage 7).

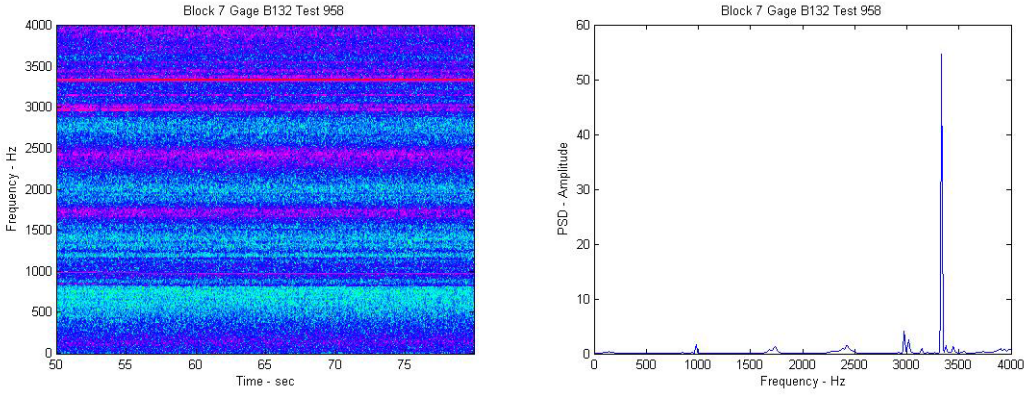

Figure 6-7: Waterfall and PSD between 50 and 80 seconds (Flight Stage 7).

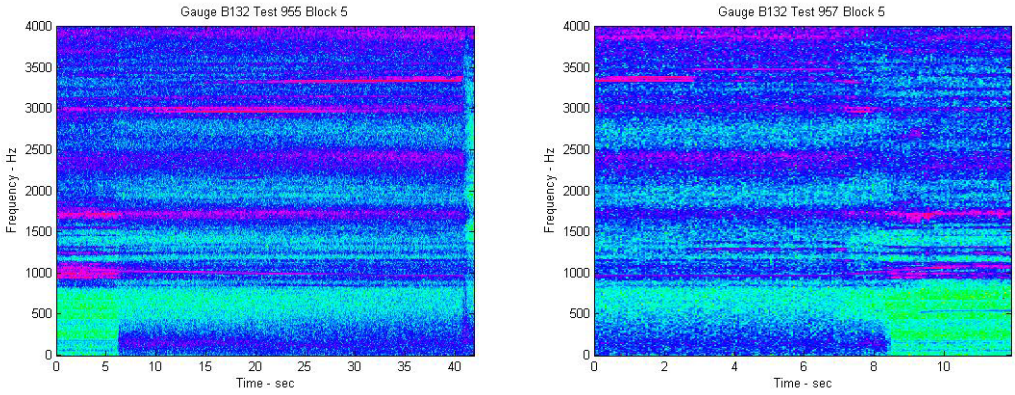

Figure 6-8: Waterfall plots for Flight Stage 5.

In addition, the rainflow cycle counting provided by the currently recommended spectrum is based on analysis of time-histories from short time windows (either 0.4, 1 or 4 seconds) selected from periods during which the RMS strain is maximum. This count is subsequently assumed to be repeated during the entire flight. Scaling up the rainflow results is correct only if the process is stationary, which does not appear to be the case based on the above results.

There are also instances where the rainflow results appear to have been assigned to an incorrect mode. For example, as shown in Figure 6-9, the highest RMS strain for Flight Stage 7 is obtained after either approximately 8 seconds, or at the very end of the test. However, based on results in Figure 6-10, it would appear that the signal at the very end of the test is an aberration and should be discarded. As previously shown in Figure 6-5, distinct pink bands occur at time t = 8 sec and the dominant frequencies are near 1000Hz and 1700Hz. Nevertheless, the currently recommended spectrum for Flight Stage 7 employs the C4ND mode at 3300 Hz. It is inconsistent to rainflow count a 1000Hz signal and subsequently assign these load pairs to a 3300Hz mode. This can be rectified by including all operative modes in the analysis.

A final point is that the NESC-2 and NESC-3 spectra have a quite different cycle count (1.83 million cycles in both cases) than the Swales spectra derived for B-132 (1.3 million cycles) and B-161 (1.1 million cycles). This discrepancy needs to be resolved.

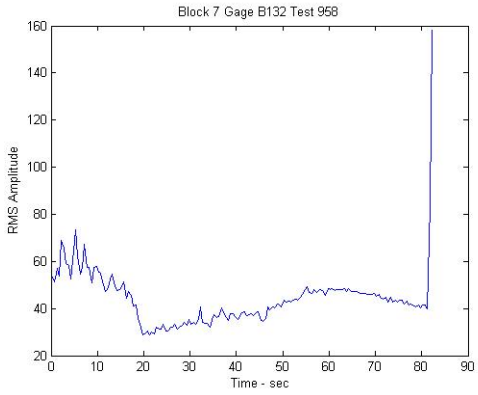

Figure 6-9: RMS for Flight Stage 7 in Test 958 and waterfall plot of final second.

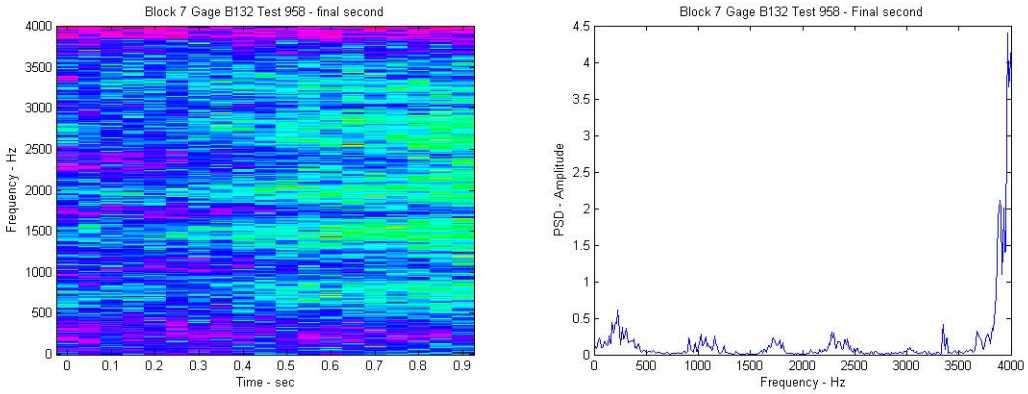

Figure 6-10: Waterfall plot and PSD of final second of Flight Stage 7 in Test 958.

6.2.2 Transfer Factors

It is also interesting to note that, as shown in Figure 5-5, the currently recommended NESC-3 spectrum is significantly more damaging than the NESC-2 spectrum—possible because the stress amplitudes in NESC-3 are a factor 1.238 times those in NESC-2. This number appears to have arisen from the ratio of the maximum strains observed in the rainflow windows for strain gauge B132 (396με) and B161 (491με). However, since these strain gauges are located at different ligaments, it is not surprising that a different strain was recorded for B132 and B161 due to the periodic nature of the mode shape. Consequently, it would appear that there is little justification for applying such a scaling factor to the spectrum.

The dependence of the strain gauge measurements on their location can be eliminated by normalizing the strains for both B132 and B161 with respect to their respective maximum strains. When this is done, as is shown in Figure 6-11, the strain spectra for both locations are virtually identical, as would be expected. Since NESC-2 and NESC-3 are both based on the same flight stages and test results, it would appear that the different stress levels contained in NESC-2 and NESC-3 have arisen from a faulty transfer of mid-ligament strains to crack site stresses.

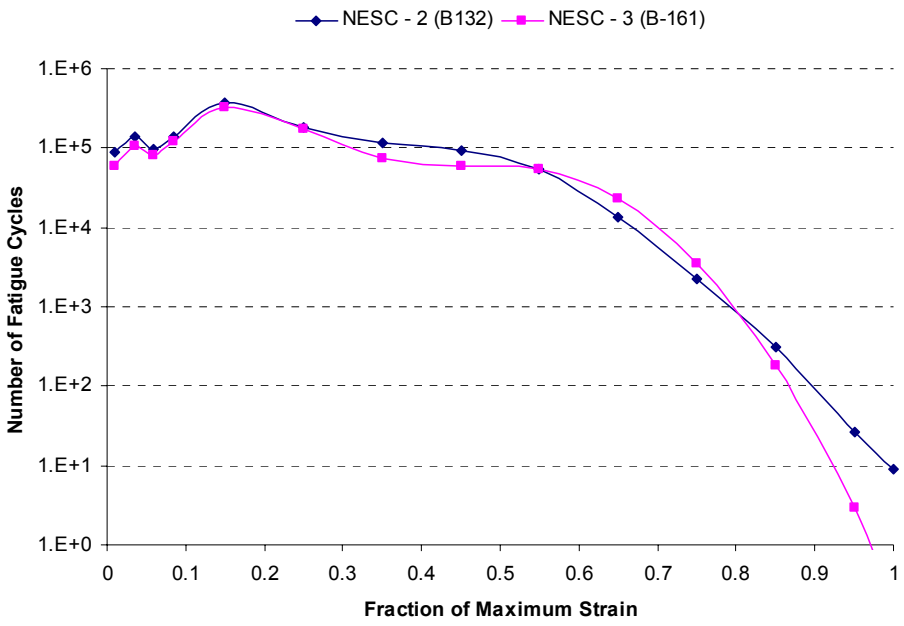

Figure 6-11: Strain spectrum derived from strain gauges B132 and B161 [Swales Aerospace, ITA Phase 1 Report - Appendix D.2.4]

A second point to be made here is related to the presence of multiple vibration modes. The transfer factors are computed on a per mode basis but subsequently multiplied by the 'total strain signal at B132' to compute stresses at the crack site location. Since the present analysis has identified the fact that the strain signal contains multiple modes, it is inconsistent to relate mode specific quantities to aggregate quantities. Once all relevant modes have been identified, the strain gauge data need to be filtered around all the relevant modes so that individual contributions can be identified and then superimposed.

Because the dynamic analysis of stress amplitudes and subsequent fatigue damage is highly non-linear, it is impossible to ascertain whether the single mode assumption in the presently recommended loading spectra is conservative or non-conservative. Consequently, the reliability of the flowliner is clouded by this uncertainty. It is therefore paramount to investigate the effect of the multiple vibration modes on the fatigue life, particularly for the Flight Stage 6, which has the highest cycle count (longest duration).

Given that the modes and modal participation factors appear to change over time, Flight Stages need to be separated into sub-Flight Stages, and different rainflow spectra need to be determined. The probabilistic analysis could then select the appropriate mix of modal participation factors to account for this time dependence.

In addition, since the current fracture mechanics analyses have demonstrated that the stress gradients over the flowliner ligaments are critically important, the gradients computed using various FE models should be compared in detail and a consensus reached as to which give the most accurate stresses.

7. SUMMARY AND CONCLUSIONS

The current report summarizes a probabilistic damage tolerance analysis performed by SwRI to analyze observed cracking at flowliner slots in the hydrogen feed lines to the space shuttle main engines. Both deterministic and probabilistic models were developed to analyze this problem. Both models used critical input from the NASA Program Office and the NESC Independent Technical Assessment Team including observed crack geometries and orientation, material properties at the cryogenic operating temperature of the flowliner, and the dynamic stress history induced by flow-induced vibrations combined with static stresses. The following summary and conclusions are based upon the deterministic and probabilistic analyses performed in this assessment. Based on these conclusions, several recommendations are also provided in Section 8.

7.1 Deterministic Modeling and Assessment

1. A deterministic damage tolerance model and associated Flowliner Fatigue Life (FFL) software was developed based on linear elastic fracture mechanics and two crack models: corner cracks and through-wall cracks. Unlike previous crack models used by NESC Team members, the corner crack model enables crack growth with two degrees of freedom thereby allowing the crack to change shape as it grows in response to the local stresses at the flowliner slots.

2. Crack driving forces were expressed in terms of the range of stress intensity factor (SIF). The weight function (WF) method was utilized to develop new SIF solutions for axial (Locations A and D) and circumferential (Locations B and C) corner and through-thickness cracks emanating from the flowliner slots.

3. The WF method enabled bi-variant SIF solutions to be developed that accounted for variations in stresses across the uncracked ligament between flowliner slots, as well as through the thickness of the flowliner. Combining these WF solutions with knowledge of the uncracked stress fields enabled SIF to be obtained for cracks at six different locations/orientations at the flowliner slots.

4. The weight function solutions enabled SIF solutions to be implemented for the unique dynamic stress gradients that occur at each of the 38-flowliner slots as the result of dynamic simulations of flow-induced vibrations.

5. The developed WF-based SIF solutions for corner cracks enables predictions of the crack shape evolution as the crack grows in the flowliner. Predicted crack shapes are in agreement with those observed in an MPTA tests thereby attesting to the accuracy of the WF-based SIF solutions and their ability to capture salient features of the dynamic analysis.

6. The WF-based SIF solutions were also compared with analogous SIF solutions based on 2-D FEM shell analyses performed at NASA-LaRC and found to be in reasonable agreement. The resulting SIF differences gave computed lives that were within a factor of two, which is not unexpected for fatigue crack growth analysis of complex geometries and loading histories, such as the flowliner. This level of variability is less that that associated with uncertainty in loading history, defects, and materials properties.

7. Deterministic fatigue crack growth life calculations were found to be very sensitive to crack shape assumptions; for example, for the NESC-2 Loading Spectrum and flowliner Location B, a 0.02 in.-quarter-circular corner crack that was allowed to evolve in shape in response to dynamic stress gradients resulted in lives greater than 1000 missions with apparent crack growth and arrest in the range of 0.32 in. to 0.41 in. for the worst cases, whereas a 0.05 in. through-cracks results in lives as short as 8 missions. Similar variations in predicted lives were observed with calculations performed using two crack models to simulate transitioning behavior from a part-penetrating crack to a through-wall crack depending on whether the transitioned crack was assumed to have a curved or a straight crack front.

8. Deterministic fatigue crack growth calculations for cracks at Location B in the down stream flowliner indicate that the NESC-2 Loading Spectrum provided by the ITA Team is on average two-to-four times more damaging than the NESC-3 Loading Spectrum.

9. Deterministic fatigue crack growth life calculations for Certification Loading Spectra provided by the Orbiter Program Office with either through-cracks of 0.05 in. or edge-cracks of 0.02 in. at Location B in the downstream flowliner gave lives ranging from 3 to 34 for various "nominal" spectra and between 1 and 3 for various "fault" spectra, the most severe of which were for loss of one engine on liftoff (see conclusion 19d for a probabilistic assessment of this problem).

10. The current model does not explicitly include the effect of welding and fit-up residual stress since quantitative information on the magnitude and distribution of these residual stresses is not currently available. Instead, residual stresses are addressed indirectly by conservatively using fatigue crack growth rate properties applicable to high mean stress. Should residual stress data become available they could be explicitly included in the fatigue crack growth life calculations.

11. Although the current model is capable of accounting for plastic shakedown of stresses at the flowliner slots, this feature was not activated in current calculations since yielding does not occur due to the relatively high strength of the original flowliner material. In contrast, yielding would be expected to occur in the weld-repaired material since its strength is considerably lower

than that of the base metal (e.g., 73 ksi vs. 148 ksi at room temperature). However, this analysis would also require information on welding residual stresses, which are not presently available.

7.2 Probabilistic Modeling and Assessment

12. A probabilistic damage tolerance model was developed for the flowliner by integrating the deterministic FFL fatigue crack growth software with SwRI's NESSUS Version 8.1. The corner crack model with crack growth and shape governed by two degrees of freedom was selected as the best option from the available crack models in FFL and crack transitioning to a straight-fronted through-thickness crack was allowed. Embedding FFL in NESSUS resulted in two orders of magnitude speed-up in computations compared to those in Phase 1, which used an external link between NESSUS and NASGRO.

13. The probabilistic model treated the following random variables: magnitudes of the cyclic stress amplitudes for each flight stage, fatigue crack growth material properties, and defect distribution resulting from periodic in-service inspection as characterized by Probability of Detection (POD) curves.

14. Uncertainty in the magnitudes of the cyclic stress amplitudes was determined based on variability in strain gage measurements during BTA tests, while uncertainty in fatigue crack growth properties was determined based on measure da/dN (ΔK) at the service temperature (-423ºF); a series of POD curves were hypothesized based on expert opinion since measured POD curves are not available, although they are under development.

15. A new model for treating uncertainty in fatigue crack growth rates was developed and implemented based on the three regimes of fatigue crack growth. This physically based model resulted in an enhanced characterization of uncertainty in fatigue crack growth material properties—particularly in the near-threshold regime where difficulties had been encountered in implementing prior models in probabilistic analysis due to their asymptotic nature.

16. The flowliner system reliability problem was solved using Monte Carlo simulation and included all 38 flowliner slots for hypothesized cracks at Location B in the downstream flowliner. This location was the focus of the study since detailed input data on loading spectrum and dynamic stresses were not available for other crack locations. Nevertheless, the model is capable of treating these other cases although additional effort would be required to quantify the necessary uncertainty models.

17. Probabilistic sensitivity factors were developed to prioritize the importance of input random variables in governing the fatigue life. The magnitudes of the cyclic stress amplitudes were found to be by far the most important variable;

in particular, the probability of failure is very sensitive to changes in both the mean and standard deviation of the cyclic stress amplitude for Flight Stage 6. Crack detection was the second most important variable; crack growth rate material properties and Loading Stages 1 through 4 were of lesser importance, and their relative importance could not be differentiated from each other.

18. Computed Probability of Failure (POF) for ten different scenarios are summarized in Table 7-1 in terms of the probability of a flowliner surviving one mission and four missions. Key comparisons are summarized below.

    a) Similar to the deterministic analysis, Loading Spectrum NESC-3 is 4-5X more damaging than NESC-2 (Scenario 1 vs. 2).

    b) The greatest potential for reducing the probability of flowliner failure is to increase the POD; specifically, increasing the POD from [75 mils at 50%, 280 mils at 99%] to [20 mils at 50%, 75 mils at 99%] would decrease the POF by 5-15X for the NESC-3 Loading Spectrum (Scenario 3 vs.4), and by 55X for the Reduced NESC-2 (Scenario 3 vs. 5).

    c) There is little impact of doubling the variance on the near threshold properties to account for heat-to-heat variability (Scenarios 3 vs. 6, and 5 vs. 7).

    d) The Certification Spectrum with "one engine out" results in a 26% probability of having a life of less than one mission, and a 80% probability of having a life of less than four missions, conditional on one engine actually failing. However, considering the fact that engine failure has a probability of 1 in 800, the actual (unconditional) probabilities are reduced to 0.0004 and 0.001 of having a life of less than one or four missions, respectively (Scenario 8 vs. 9).

    e) The nominal certification spectrum with +3 σ trajectory gives the highest probabilities of failure – a 2.4% probability of having a life of less than one mission, and a 51% probability of having a life of less than four missions. If this trajectory were a rare occurrence, the actual (unconditional) probabilities would decrease accordingly (Scenario 10).

19. The strain gage data from Flight Stage 6 exhibit clear evidence that multiple vibration modes are active (see Section 6.2). These data conflict with the assumption in the loading spectra being used by the ITA Team and Program Office that a single mode dominates in each flight stage. Unaccounted for vibrational modes in the flight spectra could alter the probability of failure predictions for the loading spectra reported above (see Recommendation #1 in Section 8).

Table 7-1: Summary of computed failure probabilities for ten analysis scenarios including different loading spectra, inspection PODs. and materials property scatter.

Scenario	Prob(Life < 1 mission)	Prob(life < 4 missions)
1. Baseline NESC-2	< 0.001	0.014
2. Baseline NESC-3	0.003	0.075
3. Reduced NESC-2	< 0.0001	0.0004
4. Baseline NESC-3, large POD	0.058	0.400
5. Reduced NESC-2, large POD	0.005	0.022
6. Reduced NESC-2, regular POD, large material scatter	< 0.0001	0.0006
7. Reduced NESC-2, large POD, large material scatter	0.004	0.02
8. "One engine out" spectrum (conditional)	0.257	0.803
9. "One engine out" spectrum (unconditional)	0.0004	0.001
10. 1.3 E2 Nominal with $+3\sigma$ Trajectory	0.024	0.512

8. RECOMMENDATIONS

1. The probabilistic sensitivity analysis clearly shows that uncertainties in the predicted flowliner fatigue lives are predominantly controlled by uncertainties in the values of the mean and standard deviation for the cyclic stress amplitudes. Attempts should be made to characterize these quantities more accurately. As discussed in Section 6, all spectra presently being used by the ITA Team and Program Office assume that a single mode dominates during each Flight Stage. Spectral analysis of strain data from the GTA tests by SwRI and Swales indicates that multiple modes can be active at the same time. There are also indications that the response is non-stationary—*i.e.*, it can change over time. It is unclear what affect these unaccounted for modes and non-stationary response might have on the flowliner probability of failure. Consequently, different rainflow-counted spectra should be developed for each sub-Flight Stage. The probabilistic analysis could then select the appropriate mix of modal participation factors to take these additional modes and time-dependence into account.

2. The fracture mechanics based fatigue crack growth analysis has indicated that an accurate estimation of the stress gradients over the ligament is also critically important. Several different finite element models have been employed to determine these local stress gradients within the ITA Team and Program Office The probabilistic analysis in the current study used the gradients provided by NASA-LaRC. Therefore, the gradients computed using various FE models should be compared in detail and a consensus reached by either the ITA Team or the Program Office as to which are the most appropriate for fatigue analyses.

3. As indicated in the probabilistic sensitivity analysis, achieving low probabilities of failure in the flowliner (POF = 0.001 to 0.0001) are critically dependent upon being able to detect cracks during in-service inspection with adequate sensitivity—*e.g.*, 20 mil cracks with 50% POD and 75 mil cracks with 99% POD were assumed in the current analyses. Although actual POD curves are not presently available for the inspection techniques being considered for in-service inspection of the flowliner, they are presently under development. When available, these POD curves should be used to perform an updated probabilistic analysis of the flowliner since they are likely to differ from those assumed in the current analysis, and it is known that the POF is sensitive to changes in the upper tail of the POD distribution.

4. The current analyses have employed fatigue crack growth data that were generated using liquid helium to achieve the flowliner service temperature of –423ºF. Consequently, it is implicitly assumed that liquid hydrogen has no detrimental effect on the fatigue crack growth rate properties at –423ºF. Although hydrogen is known to embrittle materials at higher temperatures, crack growth data are not presently available in liquid hydrogen at cryogenic

temperatures. Critical experiments should be performed to assess whether or not liquid hydrogen degrades the fatigue crack growth rate properties in the near threshold regime under conditions relevant to flowliner cracking.

9. REFERENCES

Allen, Phillip A., 2004, "Flowliner Stress Intensity Solutions", NASA-MSFC Presentation, Feb. 26.

ASTM E647, "Standard Test Method for Measurement of Fatigue Crack Growth Rates," Annual Book of ASTM Standards, Vol. 03.01

Elliot, K.B., "Development of the Fatigue Loading Spectrum," Page 7, Appendix D.2, to the Independent Technical Assessment of the Orbiter LH2 Feedline Flowliner Cracking Problem Phase 1 Final Report, July 20, 2004.

Favanesi, J.A., Clemmons, T.G., and Lambert, T.J., 1994, "Fracture Mechanics Life Analytical Methods Verification Testing," *NASA CR 4602*.

Fujimoto, W.T., 2000, "A Weight Function Approach for Tracking the Growth of Surface and Radial Cracks through Residual Stress Fields or Bi-Variant Stress Fields," *Proc. 2000 USAF Aircraft Structural Integrity Program Conference*, San Antonio, Texas.

Harris, D.O., Bianca, C.J., Eason, E.D., Salter, L.D., and Thomas, J.M., 1987, "NASCRAC: A Computer Code for Fracture Mechanics Analysis of Fatigue Crack Growth," *Proc. 28th Structures, Structural Dynamics, and Materials Conference*, Monterey, California, Part 1, pp. 662-667.

Harris, Charles E., 2004, ITA Face to Face Meeting, May 4-6, NASA-LaRC.

Hudak, S.J. Jr., Huyse, L., Riha, D.S., Chell, G.G., Lee, Y-D., McClung, R.C., Gardner, B., Thacker, B.H., 2004, "Preliminary Probabilistic Fracture Mechanics Analysis of LH2 Flowliner For The Space Shuttle Main Engine, ITA Phase 1 Report, NASA-NESC, May 28.

Hudak, S.J. Jr., Burnside, O.H., and Chan, K.S., 1985. "Analysis of Corrosion Fatigue Crack Growth in Welded Tubular Joints", ASME Transactions, Journal of Energy Resources Technology, Vol. 107, pp. 212-219.

James, M.A., Dawicke, D.S., Brzowski, M.B., Raju, I.S., Elliot, K.B., and Harris, C.H., "Coupled Crack Growth and Structural Dynamics Analysis," Appendix D3.1, Independent Technical Assessment of the Orbiter LH2 Feedline Flowliner Cracking Problem, Phase I Report, 2004.

Jewett, R.P., Walter, R.J., Chandler, W. T., Frohmberg, R. P., 1971, "Hydrogen Embrittlement of Metals – A NASA Technology Survey, NASA CR-2163.

Kendall, M., Stuart, A., and Ord, J.K., *Kendall's Advanced Theory of Statistics (3 Vols.)*, 5th Edition, Oxford University Press, New York, 1987.

Materials SPRT Minutes, 2004, August 31.

McClung, R.C., Enright, P.E., Lee, Y-D., Huyse, L.J., and Fitch, S.H.K.,2004, "Efficient Fracture Design for Complex Turbine Engine Components," *Proc. ASME Turbo Expo 2004,* Vienna, Austria.

MIL-HDBK 1823, 1999, *Nondestructive Evaluation System Reliability Assessment*, U. S. Department of Defense, April 30.

NASGRO Reference Manual, 2003, Version 4.02, NASA Johnson Space Center and Southwest Research Institute.

Orynyak, I.V., Borodii, M.V., and Torop, V.M., 1994, "Approximate Construction of a Weight Function for Quarter-Elliptical, Semi-Elliptical and Elliptical Cracks Subjected to Normal Stresses," *Engineering Fracture Mechanics*, **40**, pp. 143-151.

Orynyak, I.V. and Borodii, M.V., 1995, "Point Weight Function Method Application for Semi-Elliptical Mode I Cracks," *International Journal of Fracture*, **70**, pp. 117-124.

Saxena, A., Hudak, S.J., Jr., and Jouris, G.M., 1979, "A Three Component Model for Representing Wide Range Fatigue Crack Growth Rate, Behavior," *Engineering Fracture Mechanics*, Vol. 12, No. 1, pp. 103-115.

Saxena, A., and Hudak, S.J., Jr., 1980, "Evaluation of the Three Component Model for Representing Wide-Range Fatigue Crack Growth Rate Data," *Journal of Testing and Evaluation*, JTEVA, Vol. 8, No. 5, pp. 113-118.

Seber, G.A.F., and Wild, C.J., 2003, *Nonlinear Regression*, Wiley Series in Probability and Statistics, John Wiley & Sons, Hoboken, NJ.

Warren, J., 2004, Boeing Presentation, March 18.

Warren, J., "Residual Stresses Testing and Status," Presentation at Technical Interchange Meeting, June 22, 2004.

Zhao, W., Newman J.C., Jr., Sutton, M.A., Wu X.R., and Shivakumar, K.N., 1995, "Analysis of Corner Cracks at Hole by a 3-D Weight Function Method with Stresses from Finite Element Method," *NASA TM 110144*.

REPORT DOCUMENTATION PAGE

Form Approved
OMB No. 0704-0188

1. AGENCY USE ONLY (*Leave blank*)	2. REPORT DATE	3. REPORT TYPE AND DATES COVERED
	June 2005	Final Contractor Report

4. TITLE AND SUBTITLE

Probabilistic Fracture Mechanics Analysis of the Orbiter's LH_2 Feedline Flowliner

5. FUNDING NUMBERS

WBS–22–104–08–41
NAS1–00135

6. AUTHOR(S)

Stephen J. Hudak, Jr., Luc Huyse, Graham Chell, Yi-Der Lee, David S. Riha, Ben Thacker, Craig McClung, Brian Gardner, Gerald R. Leverant, Jim Unruh, and Jason Pleming

7. PERFORMING ORGANIZATION NAME(S) AND ADDRESS(ES)

Southwest Research Institute
6220 Culebra Road
San Antonio, Texas 78238

8. PERFORMING ORGANIZATION REPORT NUMBER

E–15052

9. SPONSORING/MONITORING AGENCY NAME(S) AND ADDRESS(ES)

National Aeronautics and Space Administration
Washington, DC 20546–0001

10. SPONSORING/MONITORING AGENCY REPORT NUMBER

NASA CR—2005-213585

11. SUPPLEMENTARY NOTES

This report prepared for and managed by Glenn Research Center as a task of Langley Contract NAS1–00135. Project Manager, Peter J. Bonacuse, Power and Electrical Propulsion Division, NASA Glenn Research Center, organization code RSL, 216–433–3309.

12a. DISTRIBUTION/AVAILABILITY STATEMENT

Unclassified - Unlimited
Subject Category: 39

Available electronically at http://gltrs.grc.nasa.gov

This publication is available from the NASA Center for AeroSpace Information, 301–621–0390.

12b. DISTRIBUTION CODE

13. ABSTRACT ***(Maximum 200 words)***

Work performed by Southwest Research Institute (SwRI) as part of an Independent Technical Assessment (ITA) for the NASA Engineering and Safety Center (NESC) is summarized. The ITA goal was to establish a flight rationale in light of a history of fatigue cracking due to flow induced vibrations in the feedline flowliners that supply liquid hydrogen to the space shuttle main engines. Prior deterministic analyses using worst-case assumptions predicted failure in a single flight. The current work formulated statistical models for dynamic loading and cryogenic fatigue crack growth properties, instead of using worst-case assumptions. Weight function solutions for bivariant stressing were developed to determine accurate crack "driving-forces". Monte Carlo simulations showed that low flowliner probabilities of failure (POF = 0.001 to 0.0001) are achievable, provided pre-flight inspections for cracks are performed with adequate probability of detection (POD)—specifically, 20/75 mils with 50%/99% POD. Measurements to confirm assumed POD curves are recommended. Since the computed POFs are very sensitive to the cyclic loads/stresses and the analysis of strain gage data revealed inconsistencies with the previous assumption of a single dominant vibrant mode, further work to reconcile this difference is recommended. It is possible that the unaccounted vibrational modes in the flight spectra could increase the computed POFs.

14. SUBJECT TERMS

Space shuttle orbiters; Metal fatigue; Crack propagation; Fracture mechanics; Stochastic processes; Reliability

15. NUMBER OF PAGES

160

16. PRICE CODE

17. SECURITY CLASSIFICATION OF REPORT	18. SECURITY CLASSIFICATION OF THIS PAGE	19. SECURITY CLASSIFICATION OF ABSTRACT	20. LIMITATION OF ABSTRACT
Unclassified	Unclassified	Unclassified	